AEOLIANITES AND PALAEOSOLS IN ISRAEL:

LUMINESCENCE CHRONOLOGY AND RELATIONSHIP WITH EASTERN MEDITERRANEAN CLIMATES

Anette Engelmann

A thesis submitted to the
University of Gloucestershire
In accordance with the requirements of the degree of
Doctor of Philosophy in the Faculty of Environment and Leisure

January 2004

Declaration

I declare that the work in this thesis was carried out in accordance with the regulations of the University of Gloucestershire and is original except where indicated by specific reference in the text. No part of the thesis has been submitted as part of any other academic award. The thesis has not been presented to any other education institution in the United Kingdom or overseas.

Any views expressed in the thesis are those of the author and in no way represent those of the University of Gloucestershire.

Cheltenham, January 2004

Anette Engelmann

Nature exhibits not simply a higher degree
but an altogether different level of complexity.
The number of distinct scales of length of natural patterns
is for all practical purposes infinite.

Benoit B. Mandelbrot, The Fractal Geometry of Nature, Freeman, 1982

Abstract

Aeolianites and palaeosols on the Mediterranean coastal plains of Israel were investigated with luminescence dating in order to explore the sedimentological evidence for climate change in the area and the response to it. The dated samples were taken from sites between the towns of Haifa and Netanya South, which are located in a quarry near the town of Habonim and further towards the coast, in a quarry North of the town of Hadera and further towards the coast as well as at the coastal cliff and in a sewage gully by the town of Netanya South. The aims of this study were to correlate aeolianite and palaeosol exposures along the Mediterranean coast, to establish a chronology for a climatological interpretation, and also whether aeolianite formation and palaeosol development could be correlated with major climate events of the Late Pleistocene in the Eastern Mediterranean. Over 80 samples were collected from various sites, covering exposures from North to South and also from East to West. They were dated with infrared optical stimulated luminescence (IR-OSL) and thermoluminescence (TL). In addition radiofluorescence spectra were obtained from some of the samples and also their equivalent doses were determined with infrared radiofluorescence (IR-RF). The chronology established through the luminescence dating results showed that aeolianite formation and palaeosol development in the Carmel and Sharon coastal plains are connected with the cyclical occurrence of enhanced rainfall over the Mediterranean. These conditions, which also cause the Mediterranean sapropels to form, are characterised by a sudden increase of precipitation. The rainfall lessens over the time of the episode but temperatures increase. It is likely that most of the soils in the coastal plains developed during the humid conditions of the rainfall episodes, while sand accumulation and aeolianite formation took place during the arid conditions at the end of the rainfall episodes or shortly afterwards. A new climate-event-stratigraphical model for the correlation of the deposits is suggested.

Acknowledgements

My sincerest thanks go to Prof. Frank Chambers, University of Gloucestershire, Cheltenham. Without his continuing and effective support, interest, encouragement and his fine subtle guidance, this study would not have been completed.

Acknowledgements are also given to Prof. Manfred Frechen, Leibniz Institute for Applied Geosciences, GGA, Hannover, Germany, for his helpful advice and support during this study and to Dr. Simon Lewis, Queen Mary, University of London for his encouragement and helpful advice.

Thanks go to Prof. Wolfgang Boenigk, Geological Institute, University of Cologne, Germany, who accompanied one field trip to Israel and assisted in the sampling of the Netanya South Cliff section. He also allowed the gamma spectrometry to be carried out in Cologne. Thanks also go to Prof. Avraham Ronen, Zinman Institute of Archaeology, University of Haifa, Israel, who introduced the members of the project to several sites in the Israeli coastal plains. Dr. Alexander Tsatskin, Zinman Institute of Archaeology, University of Haifa, Israel, provided physical help during the sampling of the pedocomplexes at Habonim Quarry and Hadera Power Station Quarry. I am thankful for this and his comments on pedological points in the field. Many thanks also go to fellow students in the project: Dr. Alexander Neber and Dipl.-Geol. Birgitt Dermann provided physical help during the sampling. Birgit Dermann also assisted with the rock cutting of some samples in Cologne. Alexander Neber sampled the four HAB-II samples. I am grateful to Dr. Anja Zander, University of Marburg, Germany and to Dr. Frank Preusser, University of Bern, Switzerland for fruitful discussions and help in Cologne. Dr. Frank Preusser took care of the measurements of the gamma spectrometry samples.

Dr. Naomi Porat, Geological Survey, Jerusalem, Israel, is given many warm thanks for her helpful advice and her continuing encouragement and support during the time of the study. Dr. Toralf Trautmann, former Institute for Applied Physics, University of Mining and Technology, Freiberg, Germany, now Bosch Company, Stuttgart, Germany, encouraged me to carry out radiofluorescence dating on my samples and supervised measurements on samples from the Netanya South cliff section. Thanks to the enthusiasm and endless effort of Dr. Gunter Erfurt, Deutsche Solar AG, Freiberg, it

was possible to measure a second set of samples already in the newly built automated radioluminescence reader. To him and to Dr. Matthias Krbetschek, Saxony Academy of Science, Quaternary Chronology Section, I am deeply indebted for their continued interest in the measurement of my samples and their help at all times. I am also thankful to Prof. Werner Stolz and to Prof. Sepp Unterricker, both of Freiberg, who welcomed the research visits. To all colleagues and friends at the Saxony Academy of Science, Quaternary Chronology Section and the Institute for Applied Physics I give warmest thanks for the very pleasant working atmosphere and hospitality.

Due recognition is given to Prof. Ferdinant Dejeht and Dr. Robert Dolhen, Institute for Nuclear Chemistry, Catholic University of Louvain-la-Neuve, Belgium, who supported this work by allowing me to irradiate the samples with a ^{60}Co gamma source. I am especially thankful to Dr. Robert Dolhen for his trust in me to work with the source.

Dr. Phil Toms, UGGI., University of Gloucestershire, Cheltenham, UK, was always open to discussion and gave helpful advice on the beta counting. Dr. Geoff Duller, Institute of Geography and Earth Sciences, Aberystwyth, kindly provided me with a copy of the program Analyst. Prof. Mebus Geyh, Bannetze-Hannover/Germany provided useful comments on my data. Dr. Alex Zylberman, Survey of Israel, allowed the redrawing and printing of parts of the Israeli topographic map 1 : 100 000.

To Debra Marshall, Roy Hickey, Jane Nicholls, Heather Coeur, Dr. John Daniell, Dr. Gesine Lorenz, Susanne Kratzer and the Lambrechts family belong many and warmest thanks for their friendship and support. Dr. Andrei Sarua supported me in every possible way for which I am very happy and most grateful. I thank my parents Anneliese und Wilhelm Engelmann, Bendorf, Germany for their continued support in all matters.

Financial support has been received from the German Israeli Foundation for Scientific Research and Development (GIF) and the Project "Pleistocene sand migration and cyclical desertification in the Mediterranean coastal plain of Israel" (No. I 435). GIF supported the author with some accommodation costs for the first sampling, the shipping of all samples from Haifa, Israel, via Rotterdam, Netherlands, to Cologne, Germany, and the travel and accommodation costs of the second sampling and employment as "Wissenschaftlicher Mitarbeiter" (Research Fellow) in the first half year. A three year maintenance bursary was received from the Geography and Environmental Management Research Unit (GEMRU), University of Gloucestershire. The attendance

of the '9th International Luminescence and ESR Conference' in Rome, Italy was possible through the support of the Graduate School, Cheltenham & Gloucester College of Higher Education (now University of Gloucestershire) and BRITISH ENERGY. I am most thankful for the New Research Workers Award from the Quaternary Research Association, UK which helped to cover travel and accommodation costs for the second research visit to Freiberg, Germany. EUROTUNNEL provided a complimentary ticket for a channel crossing for one of the irradiations in Louvain-la-Neuve, Belgium. The St. Paul and St. Mary Fund, University of Gloucestershire, supported my attendance at the 'UK Luminescence and ESR Seminar' in Glasgow 2001. The University of Gloucestershire re-imbursed some of the costs incurred during this research.

Contents

List of figures and photos

List of tables

Introduction

History of the Ph.D. research

The PhD was started in June 1998 at the Geological Institute of the University of Cologne, Germany, and was part of the German-Israeli-Foundation (GIF) project "Pleistocene sand migration and cyclical desertification in the Mediterranean coastal plain of Israel" (GIF-project No. I 435) between the Geological Institute of the University of Cologne, Germany, and the Zinman Institute of Archaeology of the University of Haifa, Israel. The GIF-project began in 1997. Two field trips to Israel were carried out for sampling. The first sampling campaign was from 13th to 31st May 1997. Samples from sites along the motorway from Haifa to Tel Aviv were taken. The second sampling took place from 16th March to 3rd April 1998. Further samples along the motorway in the Carmel coastal plain and at the coastal cliff in the Sharon were collected. When the PhD was started, I was employed in the project as a "Wissenschaftliche Mitarbeiter" at the Geological Institute of the University of Cologne. After half a year the PhD was transferred to the Geography and Environmental Management Research Unit (GEMRU) at the Cheltenham & Gloucester College of Higher Education, since October 2001 University of Gloucestershire, Cheltenham, UK.

Supervisors of the PhD research

During the different phases in the course of the PhD research the following people supervised me. In phase one from June 1998 to December 1998 at the Geological Institute, University of Cologne, Germany, my first supervisor was Prof. Wolfgang Boenigk, Department of Quaternary Science, University of Cologne, Germany. My second supervisor was Priv.-Doz. Dr. Manfred Frechen, at this time at GEMRU, Cheltenham & Gloucester College of Higher Education, Cheltenham, UK. During the second phase from January 1999 to April 2001 at GEMRU, Cheltenham & Gloucester College of Higher Education, Cheltenham, UK, my first supervisor was Priv.-Doz. Dr. Manfred Frechen, GEMRU, Cheltenham & Gloucester CHE, Cheltenham, UK. My second supervisor was Dr. Simon G. Lewis, School of the Environment, Cheltenham & Gloucester CHE, Cheltenham, UK, who changed during this time to Queen Mary College, University of London, London, UK. Third supervisor was Prof. Frank Chambers, GEMRU, Cheltenham & Gloucester CHE, Cheltenham, UK. In the third

phase from May 2001 to January 2004 at GEMRU, Cheltenham & Gloucestershire CHE, Cheltenham, UK, my first supervisor was Prof. Frank Chambers, University of Gloucester, Cheltenham, UK, my second supervisor was Priv.-Doz. Dr. Manfred Frechen, Institute for Applied Geosciences, GGA, Hannover, Germany, and my third supervisor was Dr. Simon G. Lewis, Queen Mary College, University of London, London, UK. For an overview over supervisors and their locations please see Table a.

Table a: List of location of PhD research, supervisors and their locations.

Phase and time	Location of PhD research	Supervisor 1 and location	Supervisor 2 and location	Supervisor 3 and location
Phase 1 from June 1998 to December 1998	Geological Institute, University of Cologne/Germany	Prof. W. Boenigk, Department for Quaternary Science, Geological Institute, University Cologne/Germany	Priv.-Doz. Dr. M. Frechen, GEMRU, Cheltenham & Gloucester CHE, Cheltenham, UK	
Phase 2 from January 1999 to April 2001	GEMRU, Cheltenham & Gloucester CHE, Cheltenham, UK	Priv.-Doz. Dr. M. Frechen, GEMRU, Cheltenham & Gloucester CHE, Cheltenham, UK	Dr. S. G. Lewis, School of Environment, Cheltenham & Gloucester CHE, Cheltenham, UK, then Queen Mary, University of London, London, UK	Prof. F. Chambers, GEMRU, Cheltenham & Gloucester CHE, Cheltenham, UK
Phase 3 from May 2001 to January 2004	GEMRU, Cheltenham & Gloucester CHE, then University of Gloucestershire, Cheltenham, UK	Prof. F. Chambers, GEMRU, Cheltenham & Gloucester CHE, then University of Gloucestershire, Cheltenham, UK	Priv.-Doz. Dr. M. Frechen, GGA, Hannover, Germany	Dr. S. G. Lewis, Queen Mary, University of London, London, UK

Structure of PhD thesis

Chapter 1 gives an introduction into the working area and the Israeli aeolianites. A brief overview of tectonic structures with reference to the Israeli coast follows. The geography and present-day climate factors are described and the genetic models of Israeli coastal sand dunes are introduced in a literature review. Chapter 2 states the aims and objectives of the study. Chapter 3 introduces the nomenclature of aeolianites and palaeosols in Israel and contains descriptions of the study sites. Chapter 4 introduces aspects of luminescence dating in a literature review. Chapter 5 describes the methods used in this study. Chapter 6 describes the analytical results. Chapter 7 contains the

discussion of the results and their interpretation. The Conclusions summarise the findings of this study, the limitations and possible future research. References and Appendices follow.

CHAPTER 1

Fossil coastal sand dunes in the southeastern Levant

The chapter aims to give a general overview of the working area with examples from the Carmel and Sharon coastal plains. The geological cycle of fossil coastal sand dunes is described. Tectonic structures of the Eastern Mediterranean and the Israeli coastal plains in particular are discussed. A brief summary of the geography of Israel and present-day climate factors follows. Finally the research history of the Israeli coastal sand dunes and their genetic models are going to be looked at.

1.1 Israeli aeolianites

Seen from the point of global distribution the Israeli lithified coastal sand dunes are part of one of the four predominant locations of carbonate aeolianite on Earth. Major tracts are found in the northern hemisphere around the Mediterranean and in middle America/Bahamas and in the southern hemisphere in southern Africa and western and southern Australia. Apart from this, single outcrops of carbonate aeolianites are known mainly from islands in the Atlantic (BROOKE 2001). DARWIN (1851) published his observations of lithified coastal sand dunes on the island of St. Helena from his research trip with the ship Beagle in 1836 (in BROOKE 2001). Another example of isolated aeolianites is reported in LIETZ and SCHWARZBACH (1971) from the island of Porto Santo (Madeira archipelago), not mentioned by BROOKE (2001).

The geological interest of this study focusses on the fossil coastal dune sands in the coastal plains of Israel between the towns of Haifa and Tel Aviv. These fossil coastal dune sands appear as elongated morphological features more or less parallel to the modern coastline (Chapter 1.7.1) (Fig. 1.1a).

In the literature lithified dune sands are often referred to as 'aeolianites'. For use and definitions of the term 'aeolianite' in literature and in this study please see Chapter 3.1.1. The following paragraphs outline general features and degrees of development of aeolianites and give examples from northern Israel where possible. This is intended to give a first impression of the working area in relation to a general geology of aeolianites. The special geology of the Israeli aeolianites and their soils and the description of the individual sample sites are given in Chapter 3.

Like all geological structures, fossil coastal dune sands undergo the inevitable geological cycle of genesis and weathering. General features for coastal sand dune formation, their lithification and deterioration are shown in Figure 1.1b. If a major sediment source is available for the supply of offshore sands, then currents and wave action can bring these sands ashore.

Figure 1.1a: Area of interest and major tracks of coastal lithified dune sands (after FRECHEN et al. 2001).

From there winds pick up the sand and blow them into dunes until a series of mobile sand dunes exists. Mediterranean-type climates, which alternate between cool, wet winters and hot, dry summers, encourage the stabilisation of the dune surfaces

through the invasion and growth of vegetation. At the same time these climates are responsible for the cementation of the dunes through precipitation of calcium carbonate around the sand grains. During winter rains the *in situ* carbonate is dissolved because of the slightly acidic water percolating between the sand grains. The following summer, when it gets drier, the dissolved carbonate precipitates as a coating or cement around the grains. This starts at the lower parts of the dunes and stabilises them from below. Contemporaneously a humic soil develops through the vegetation, which stabilises the dune surface. The soil increases the acidity of the groundwater which promotes further leaching. Underneath the humic layer a thin zone of quartz sand is left as the insoluble remnants of the leached sand. The processes of dissolution and concentration of carbonate are mainly found at the base of the humic layer. If it is a well developed soil and there is sufficient carbonate supply these processes can produce a hard layer of calcrete, which protects the softer calcarenite beneath it from erosion (own field observations and after MCNAMARA 1986).

In the further process of deterioration of aeolianites plant roots take advantage of fissures in the calcrete subsoil layer and penetrate the softer sediments below. Water seeping away uses these channels and thereby leaches calcium carbonate from the sand around and precipitates it around the plant roots. In a further stage the roots rot away leaving rizolithes as evidence for these processes. The channels widen and deepen into solution pipes with continued leaching and lengthy weathering. Along with these processes soil development proceeds and the soil deepens progressively. The subsurface carbonate successively dissolves with the leaching process continuing over geological time periods. More resistant parts of aeolianites remain longer. After continuous weathering and soil erosion the remains of these processes are uncovered (own field observations 1997, 1998 and after MCNAMARA 1986). The weathered unconsolidated available sediment is often included in the next formation of aeolianite, and so the process can be described as a cycle of lithified sand dune formation and deterioration (Figure 1.1b).

These general features of aeolianites and their environment can be observed in the study area. Some introductory examples are given here. A detailed description of the study area and the studied sections follows in Chapter 3.

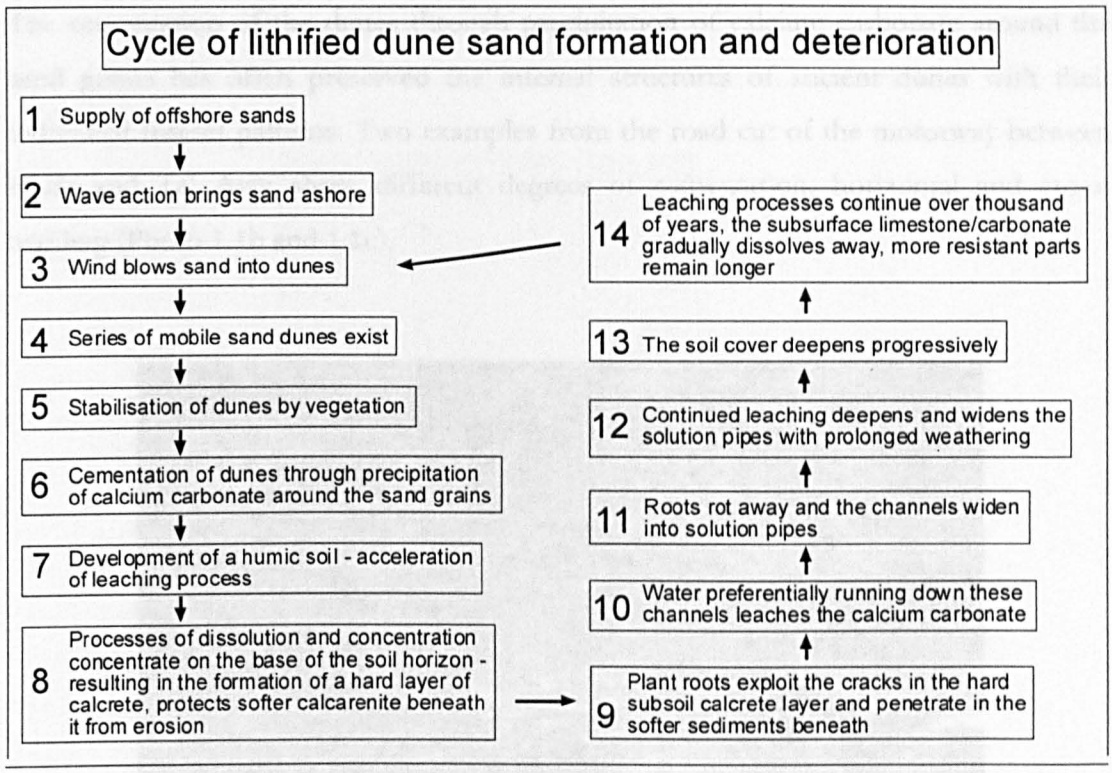

Figure 1.1b: Cycle of coastal lithified sand dune formation and deterioration (cp. MCNAMARA 1986).

The vegetation at the recent sand dune fields near Hadera or Netanya South demonstrates impressively how vegetation invades dune fields and stabilizes them on the surface (Photo 1.1a).

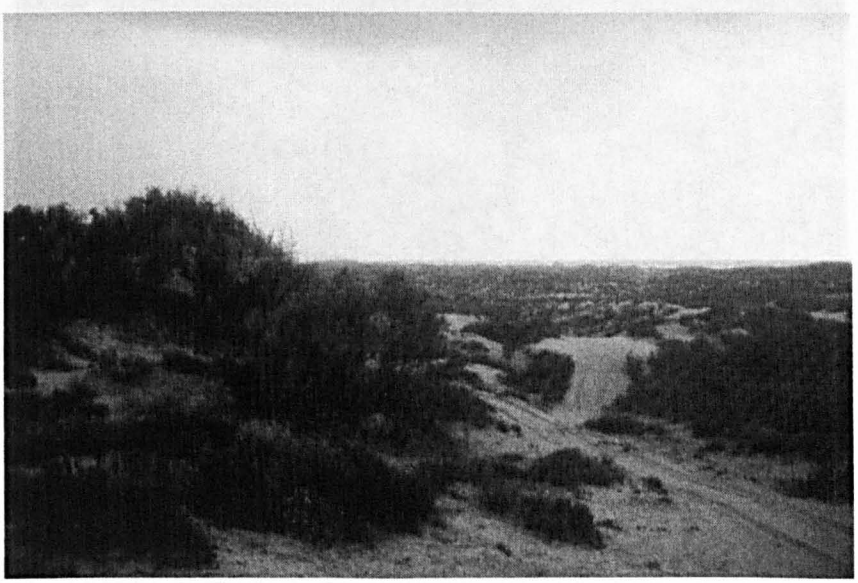

Photo 1.1a: Vegetation stabilising the surface of a recent dune field near Hadera.

The cementation of the dunes through precipitation of calcium carbonate around the sand grains has often preserved the internal structures of ancient dunes with their individual foreset patterns. Two examples from the road cut of the motorway between Haifa and Tel Aviv show different degrees of cementation, horizontal and cross-bedding (Photo 1.1b and 1.1c).

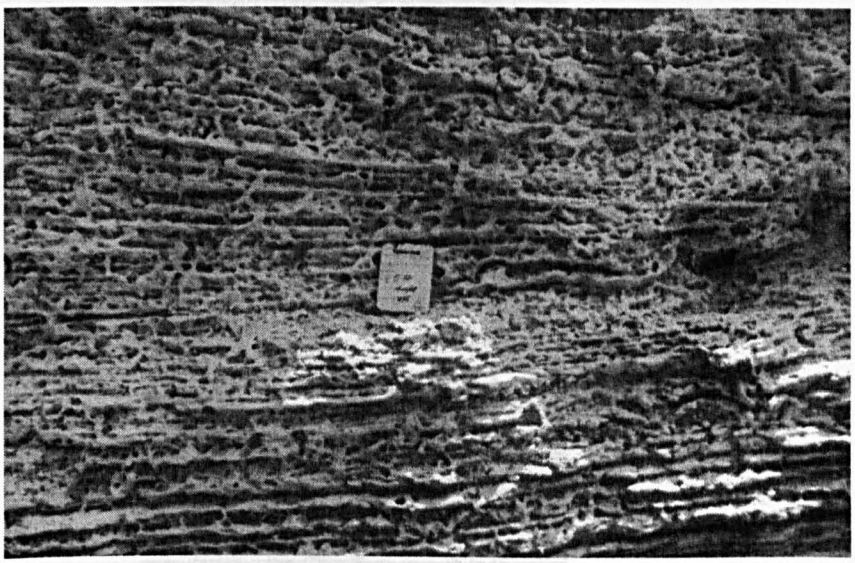

Photo 1.1b: Aeolianite at the motorway road cut by En-Ayyala. Single forests are still clearly distinguishable although strongly cemented. Metal sign (7.5 x 10 cm) for scale.

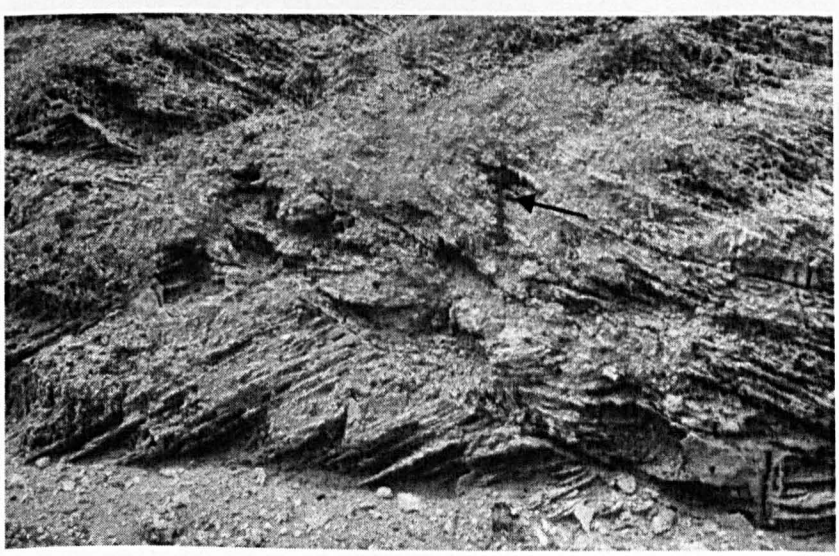

Photo 1.1c: Cross-stratification at an aeolianite by En-Ayyala at the motorway roadcut between Haifa and Tel Aviv. Geological hammer (see arrow) for scale.

An example of a soil sandwiched between two bodies of aeolianites can be seen at the motorway road cut between Haifa and Tel Aviv near En-Ayyala (Photo 1.1d).

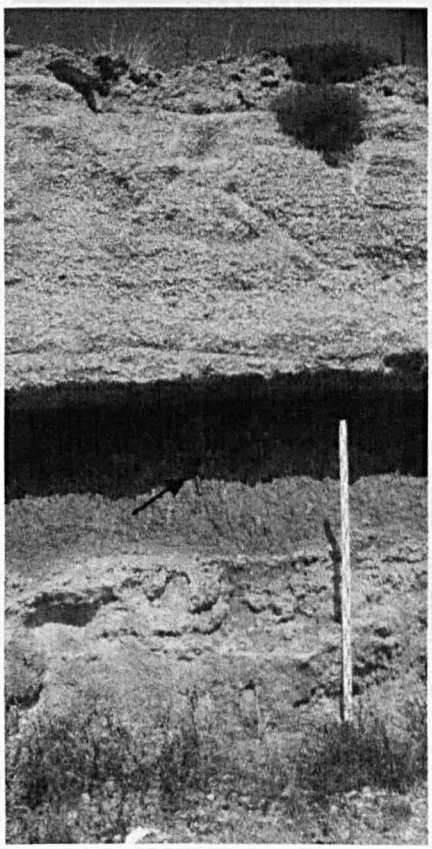

Photo 1.1d: A red soil can be observed sandwiched between two bodies of carbonate aeolianite at the motorway roadcut near En-Ayyala. Geological hammer (see arrow) and surveyor's staff (2 m) for scale.

The increased acidity in groundwater is the reason for leaching processes taking place at the contact zone at the bases of humic layers with the underlying aeolianite. Many examples of leaching processes can be found along the motorway road cut or in aeolianites further towards the sea (Photo 1.1e and 1.1f).

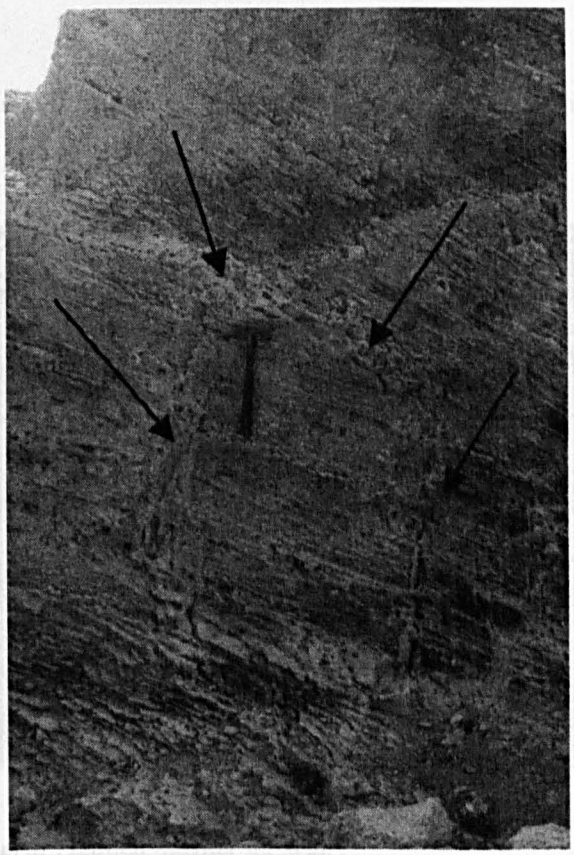

Photo 1.1e: Leaching features in an aeolianite at the motorway road cut by Qara North. Geological hammer for scale.

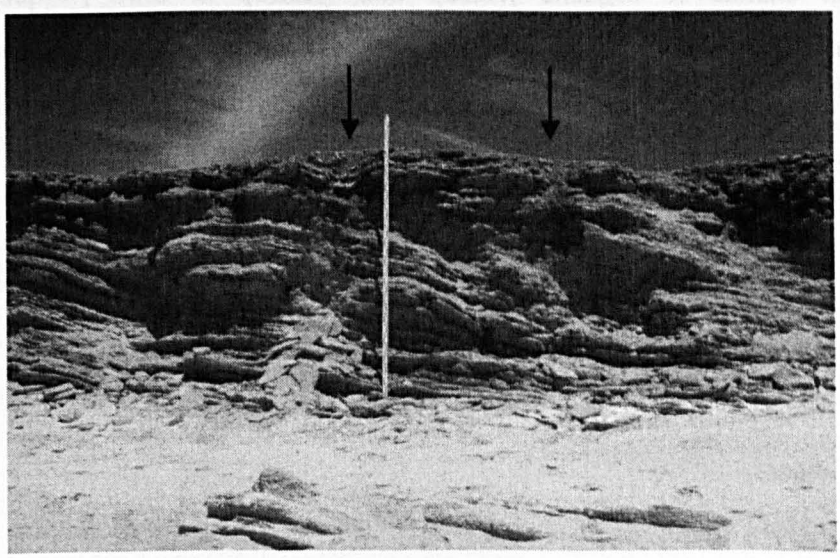

Photo 1.1f: Two solution pockets have formed in the upper part of the aeolianite at the seashore near Hadera (south of the power station) through leaching out the carbonate and they are filled with red palaeosol. Surveyor's staff (3m) for scale.

Rizolithes can be observed in a weak soil e.g. in a quarry near Hadera (Photo 1.1g).

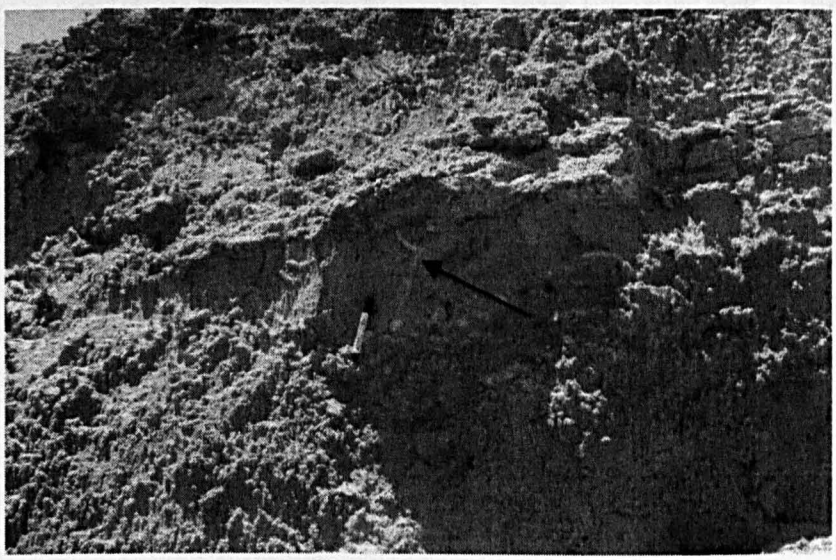

Photo 1.1g: The photo shows a rizolithe in a lens of a weak soil at Power Station Quarry (cp. Chapter 3.2.2) near Hadera. Marker for scale.

The above described cycle of coastal lithified sand dune formation and deterioration can be interrupted and start again at any stage. This depends on factors like changes in sediment supply, both in quantity and quality, changes of climate factors like precipitation and temperature *et cetera.* This results often in complex sediment and soil sequences, but leaving also with this, very detailed climate records.

1.2 Geology

The tectonic pattern of Israel and the Levant is complex as the structural geology of this region is influenced by the surrounding four major systems of the African Craton in the South, the Mediterranean Basin in the West, the Alpine Orogenic Belt in the North and the Arabian Plate in the East. The movements of these four systems relative to each other are responsible for the present structural configuration of the Near East (HOROWITZ 1979) (cp. Figure 1.2a).

Figure 1.2a: Elements of the structural geology of Israel, Sinai and the Levant (after NEEV 1975).

Israel

Parts of the African Craton, the Arabo-Nubian Massif, are found in Israel in the area of Elat and in the southern part of Sinai, from where it extends south on both sides of the Red Sea. East of the Arava valley, in Jordan, it is exposed as far North as the Dead Sea. The Arabo-Nubian Massif was formed in the Late Precambrian and is surrounded by younger platform sediments, mainly of fluviatile or shallow marine facies. The sedimentary cover in Israel becomes thicker towards the Northwest. In the South of Israel a significant part of the sedimentary sequence is continental, but the northern and western part of Israel are covered by shelf deposits, e.g. fossiliferous limestones and similar rocks. Towards the West the western coastal plain and the shelf areas are covered by deep-sea sediments, such as marls and clays. There is no information on the distribution of rocks older than the Triassic, as in the western and northern parts of Israel the Palaeozoic is buried deeply (HOROWITZ 1979).

A major s-shaped fold belt extends to the West in the Negev and the Sinai and to the East in Lebanon and Syria, which folds the Levant into a series of anti- and synclines. Three main folding phases along the same lineaments (not the same axes) could be distinguished, a pre-Jurassic system (FREUND *et al.* 1975 in HOROWITZ 1979), a Late Mesozoic through Early Cenozoic system (BENTOR and VROMAN 1951 in HOROWITZ 1979) and a Late Eocene – Oligocene folding phase (GVIRTZMAN 1970 in HOROWITZ 1979). Through the Miocene the folding continued (GARFUNKEL and HOROWITZ 1966 in HOROWITZ 1979), but did not always affect all of the previously folded structures (FREUND and ZAK 1973 in HOROWITZ 1979).

Superimposed on the folded structures in central Israel during the Quaternary upwarping took place along a North-South direction (HOROWITZ 1979). This lineament is also conspicuous along the downthrown area of the coastal plain (NEEV 1975). The region in the East of the Jordan – Arava Rift Valley is upwarped along a line of the same direction (HOROWITZ 1979).

At the eastern border of Israel the Jordan – Arava Rift Valley stretches south to the Gulf of Elat and the Red Sea Rift System. Towards the North the fault system is continued through the Lebanon and Syria until it reaches southern Turkey. Although the main streak of this fault system runs North-South a number of minor faults deviate in other directions to account for volume problems of advancing structures (HOROWITZ 1979).

Older than the Jordan – Arava Rift Valley fault system is the so-called "Erythrean System". It stretches northwest – southeast and has caused, besides other structures, the Yizre'el Valley and the elevated block of Mount Carmel. HOROWITZ (1979) dates the Erythrean System back to the Earliest Pliocene.

Apart from the major fault systems mentioned, a huge number of small-scale faults exists, which are East – West orientated and cross the North – South running lineaments of the folded and upwarped structures. In the North of Israel, in Galilee, they are a major landscape feature, whereas in the South, in the Negev they are hardly observed. The age of these faults ranges from the Triassic onwards (FREUND *et al.* 1975, MIMRAN 1972 in HOROWITZ 1979) to the Quaternary and some are even active today (HOROWITZ 1979).

All the above mentioned fault systems consist of normal faults and are exclusively down to gravity faulting as a compensation for the uplift of this region. Compressional features could not be observed (HOROWITZ 1979).

In contrast to that, another fault system with East – West direction, is known from the Negev and its continuation from Jordan (BARTOV 1974 in HOROWITZ 1979), over the Sinai into Egypt, where it extents underneath the Nile Delta (SAID 1975). This fault system consists of dextral strike-slip faults and shows apart from normal faulting also compressional features, which are "mainly displayed as a series of equidimensional domes" (HOROWITZ 1979 p. 48). The faults are of post-Miocene up to Earliest Pliocene age and the overall shear distance of these faults is of several kilometres (HOROWITZ 1979).

Eastern Mediterranean

The Levantine Basin, as defined by NEEV (1975), covers the space west of an old structural line (hinge line), that has been active since the pre-Jurassic (GVIRTZMAN and KLANG 1972 in HOROWITZ 1979). This line runs generally North-South and follows at the central part of the coastal plain, the Israeli shoreline. Further South the hinge line runs east of the shoreline and bends at the Sinai coastal plain towards the West. North of the central Israeli coastal plain, it follows South of Haifa Bay the direction of the "nose" of Mount Carmel, about North-North-West and extends seawards. Further to

the North it runs again parallel to the shoreline of the coast of Lebanon and Syria (HOROWITZ 1979).

The Levantine Basin is adjoint to Israel and Lebanon in the East, Sinai in the South and Cyprus in the North-West. Physiogeographically the following elements structure the basin: West from the Levantine Shelf several parallel fold structures accompany the Pelusium Line and the Levantine Platform extends West and towards the Erastosthenes Seamount. The platform shows two different facies, in the South the Late Miocene evaporites could geophysically not be logged ("Belt of no M"), while in the North their diapires are pronounced (Diapir Belt). In the South of the basin the Bardawil Escarpment stretches across, north of the Nile Delta and the Sinai Shelf. The main structures of the Levantine Basin are orthogonal to each other and either parallel the Levantine coast in the East or the coast of North Africa in the South of the basin (HOROWITZ 1979).

Wide synclinoric and anticlinoric structures, layed out *en échelon*, can be observed as much as 150 km offshore the Levantine coast with varying amplitudes up to several kilometres (HOROWITZ 1979).

The Roman settlement of Pelusion on the offshore bar of the Bardawil Sebkha gave its name to the so-called Pelusium Line. This line runs about 50 – 60 km offshore parallel to the Levantine coast and follows a Southwest direction, crossing the Suez Canal and the Nile river, crossing into the African continent. NEEV (1975) and NEEV *et al.* (1987) suggested that this lineament represents a compressional zone which divides the Central Levantine and Arabian Plate from the Mediterranean Plate.

Another structural important feature is the Bardawil Escarpment. The fault zone has a vertical throw of about 1 km. Parallel to the Escarpment runs the boundary of the two belts with the facies differentiation, which is thought to be controlled tectonically (HOROWITZ 1979).

In the North the Levantine Basin gradually changes through Cyprus into the fold belt of Turkey, Greece and Crete, which might constitute an uplifted part of the midocean ridge of the Tethys. The crust of the Levantine Platform is specified to be oceanic to semioceanic (NEEV 1975).

The age of the structural movements of the Levantine Basin is reconstructed by GVIRTZMAN (1970 in HOROWITZ 1979) mainly from drillings on the Israeli coast. The

tectonic activity of the major fold systems in the Levantine Basin looks to have taken place since the pre-Jurassic and have controlled the facies of the sediments since then (HOROWITZ 1979).

It is pointed out by GVIRTZMAN (1970 in HOROWITZ 1979) that the basement of the coastal plain of Israel is faulted in an *en échelon* pattern stretching north – south. (HOROWITZ 1979) puts this down to a misidentification of Miocene and Pliocene strata by Gvirtzman and argues that subsurface step faults that might be observed are of Late Miocene to Early Pliocene age. This view is supported by the folding of Late Miocene evaporites in the Mediterranean, the Red Sea and the Gulf of Suez and that in the Earliest Pliocene also the Bardawil Escarpment was formed.

Two phases of structural movements can be singled out in the Levantine Basin. Firstly, a phase of folding took place along North – South extended directions. This phase began at least in the early Mesozoic and intermittently took place until the Early Tertiary. Secondly, a phase of faulting took place along North/East – South/West and East – West extended lines. This tectonic activity commenced at the beginning of the Pliocene and is in a small scale still active today (HOROWITZ 1979).

Late Quaternary tectonic activity in the Mediterranean coastal plain

From data of boreholes and geophysical research GVIRTZMAN (1970 in HOROWITZ 1979) suggested two systems of pre- and post-Miocene faults along the coastal plain: a longitudinal one, running generally parallel to the present coastline, and the other faults bearing parallel to the Erythrean system.

According to HOROWITZ (1979) the fault system of the coastal plain is problematic. He states that no faults can be observed definitively as they would be covered by younger sediments. He also comments that the structure of the coastal plain can be the result of folding and channelling, without any faulting at all. HOROWITZ comments that the information brought forward by GVIRTZMAN would not be sufficient enough to place so many faults along the coastal plain. He therefore favours the hypothesis of ITZHAKI (1955 in HOROWITZ 1979) of folding and downwarping of the coastal plain.

NEEV *et al.* (1973) looked at the height above sea level of *Glycymeris* beds and dated some specimens of *Glycymeris violacescens* by radiocarbon. They also observed the ancient

Herodian harbour at Caesarea and reported parts of the breakwaters of the harbour to be submerged since its construction by 10 to 15 metres. They concluded that the coastal zone from Ashqelon to Caesarea was downwarped and submerged under the Mediterranean Sea. In a later event the offshore littoral zone in the West of the assumed North-South running fault line (which crosses also the Herodian harbour) remained submerged, while the area East of the fault line was uplifted to its present position. NEEV *et al.* (1973) assume this to have probably occurred later than 700 a BP, but at the earliest at 3,800 a BP. Eustatic reasons for the deposition of the *Glycymeris* beds are rejected by the authors with the argument that there is no evidence for a transgressive sea level that reached far inland (NEEV *et al.* 1973).

More recent publications by MART and PERECMAN (1996) and by GALILI and SHARVIT (1998) re-assess the problem of neotectonic activity in the coastal plains of Israel. MART and PERECMAN (1996) conclude from high-resolution seismic reflection surveys that coast-parallel faults displace both the submerged aeolianite, which runs along the coastal zone, and the submerged Herodian breakwaters. The observed faults have offsets of 1 – 3 m, downthrowing the seaward flank and leaving the landward flank stable. The neotectonic activity along the Mediterranean coast of Israel is seen as a consequence of the Pliocene – Quaternary subsidence of the southeastern Mediterranean basin (MART and PERECMAN 1996).

GALILI and SHARVIT (1998) re-examined coastal archaeological structures and geological indicators for neotectonic activity along the Israeli coast from North to South. They found that coastal pools, channels and quarries are found today at sea level or very close to it and are still able to function. As regards the submerged and collapsed breakwater of the Herodian harbour at Caesarea they point out that the submerged western part of the breakwater was built on an unconsolidated interdune (inter-aeolianite) surface, while the still functioning part is located on the aeolianite ridge in the coastal zone. The western part of the breakwater was therefore exposed to marine erosion, with the settlement of the foundations into the sediment (GALILI and SHARVIT 1998). They also comment that it was a common ancient building practice of harbours and similar architectural structures, to lower into the water huge blocks of stone (50 x 10 x 9 feet or bigger) until the foundations had risen to water level, as was described by the Roman historian Josephus Flavius about the construction of the Caesarea harbour (GALILI and SHARVIT 1998). Therefore the submerged parts of the western breakwater of the Herodian

harbour cannot count as an argument for tectonic subsidence. Apart from the discussion about the breakwaters of the Caesarean harbour GALILI and SHARVIT (1998) suggest that the step-like feature which can be observed in the seismic profiles of MART and PERECMAN (1996) is suspicious because it is just at the western edge of the submerged aeolianite ridge and it may be sub-bottom topographic profile of the western boundary of the aeolianite ridge rather than a tectonic fault. GALILI and SHARVIT (1998) conclude from their observations along the Israeli coast that the coast is stable and there were no neotectonic movements during historical times.

Many others have contributed to the discussion of neotectonic activity along the Israeli Mediterranean coast earlier. Two schools of thought have emerged, the "activists" and the "stable-ists" (Table 1.2.1 a).

Table 1.2.1 a: List of authors who support ("Activists") or oppose ("Stable-ists") neotectonic activities along the coastal plain of Israel.

"Activists"	"Stable-ists"
NEEV *et al.* (1973)	GALILI and SHARVIT (1998)
NEEV *et al.* (1987)	
MART and PERECMAN (1996)	

However, regarding the North-South running faults along the Mediterranean coast of Israel, it seems to be safe to assume that the aeolianites onshore are not affected by neotectonic movements, as the onshore zone plus the eastern part of the coast lies in a tectonically stable terrain, different from western parts of the coast and the shelf (MART and PERECMAN 1996).

1.3 Geography and climate factors

1.3.1 Physical geography

The State of Israel lies at the southeastern end of the Mediterranean Sea. Israel is from North to South about 400 km (250 miles) long and extends at its widest point from East to West about 121 km (75 miles). Its borders are in the Northeast to Syria, in the East and Southeast to Jordan, in the Southwest to Egypt, in the West and Northwest to the Mediterranean Sea and in the North to Lebanon. Israel covers an area of 20,700 km^3 (7,992 square miles). This does not include 7,477 km^3 (2,887 square miles) of the Israeli-occupied or semiautonomous territories in the Golan Heights (in the Northeast), the West Bank and East-Jerusalem (in the East) and the Gaza Strip (in the Southwest) (EB 1997).

Four physiogeographically regions of Israel can be distinguished (EB 1997):

The Mediterranean coastal plain at the most western part of the country, which is about 185 km (115 miles) long and measures only 32 km (20 miles) across at its widest point.

The mountainous region, which extends from the northern border along the Israeli-occupied West Bank and reaches into central Israel.

The Rift Valley stretches out along the eastern boundary of the country to the Gulf of Aqaba in the South. The Rift Valley contains the Dead Sea, which 400 m (1,312 feet) below sea level is the lowest point on the surface of the Earth.

The large region of the Negev desert, which occupies almost the entire southern half of Israel.

1.3.2 Relief and drainage

The Mediterranean coastal plain is a very narrow strip, only widening in the South. The Galilee Mountains in the North of the country build the highest part of Israel. The highest point in the mountains of Galilee is Mount Meron (Jebel Jarmaq) at 1,208 m (3,963 feet). The mountain region ends to the East in an escarpment which overlooks the Rift Valley. The Plain of Esdraelon (Emeq Yizre'el) runs about Northwest – Southeast, separates the Galilee mountains from the Samarian and Judean hills and joins the coastal plain with the Rift Valley. From the hills of Samaria and Judea the Mount

Carmel range extends in a Northwest direction and nearly reaches the coast at Haifa. The highest peak in the range is at 546 m (1,791 feet) (EB 1997).

In the East the Rift Valley forms a long fissure in the crust of the Earth which extends from beyond the Israeli northern borderland along the length of the country to the South and the Gulf of Aqaba. The river Jordan gushes forth at the frontier between Israel and Jordan. At Dan in the North it is 152 m (500 feet) above sea level and from there it flows South into the Hula Basin ('Emeq Hula) at about sea level and onwards into the Yam Kinneret (Sea of Galilee, Lake Tiberias), which is 210 m (689 feet) below sea level. The Jordan continues into the Dead Sea. In the South the Negev desert builds a triangle-shaped piece of land which points to Eilat (Elat) at the Gulf of Aqaba (EB 1997).

The main drainage is through the river Jordan and its tributaries. Two other important rivers are the river Yarqon and the river Qishon. The Yarqon runs into the Mediterranean Sea at Tel Aviv and the Qishon flows through the western part of the Esdraelon Plain (Yizre'el Valley) and empties into the Mediterranean Sea at Haifa. For the most part all other streams are seasonal and flow through streambeds called wadis (EB 1997).

1.3.3 Late Pleistocene palaeoclimatic record of the eastern Mediterranean

Information about the late Pleistocene palaeoclimate in Israel and the Levante derives from terrestrial and marine records and the link between them. Climate proxies from these records allow an accurate and detailed reconstruction of the palaeo-environmental conditions of the area.

Terrestrial records

BAR-MATTHEWS *et al.* (2000) investigated oxygen and carbon isotope records of speleothems from the Soreq cave in Israel (Figures 1.3.3a and 1.3.3b). The speleothems were dated with thermal ionisation mass spectrometry (TIMS) U-series dating. The method yields a high precision and uncertainties under 2 ‰ (2 sigma) were observed in all samples but one from the Soreq cave (cp. BAR-MATTHEWS *et al.* 2000). The investigated speleothems of the Soreq cave overlap with their age ranges and form a

continuous record of the last 140 ka. From these well-dated speleothems stable isotope records of $\delta^{18}O$ and $\delta^{13}C$ were established from 3800 samples, yielding also a high accuracy.

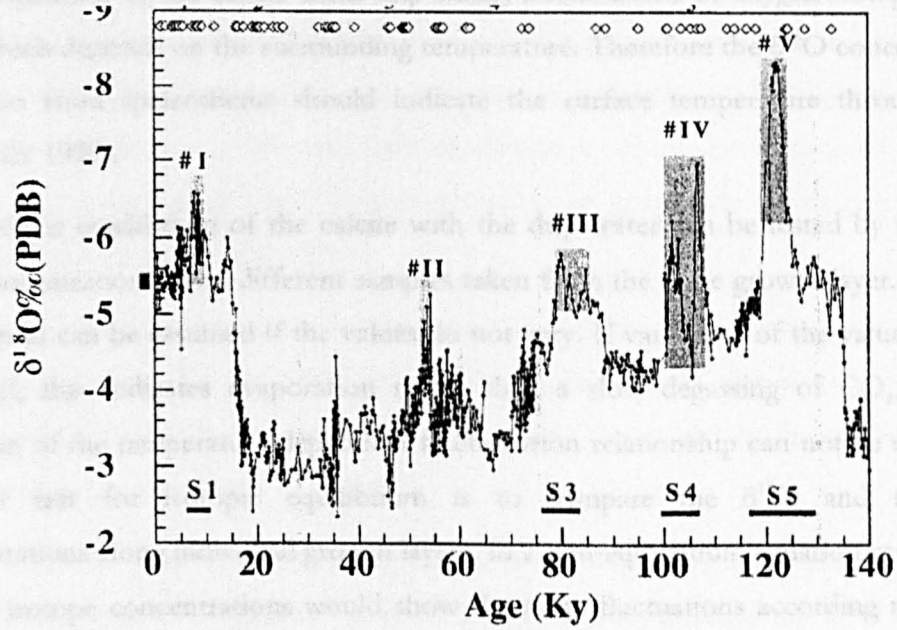

Figure 1.3.3a: Oxygen isotope data of speleothems of the Soreq Cave in Israel (from BAR-MATTHEWS et al. 2000). Age (Ky) = Age (ka).

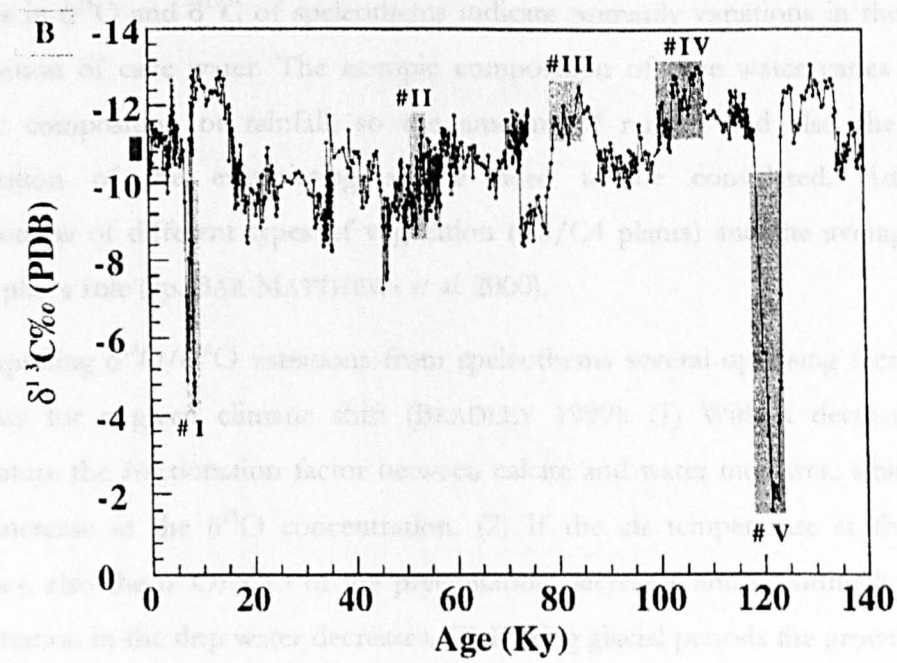

Figure 1.3.3b: Carbon isotope data of speleothems of the Soreq Cave in Israel (from BAR-MATTHEWS et al. 2000). Age (Ky) = Age (ka).

Variations of the $\delta^{18}O$ concentration of carbonate layers from speleothems along their growth axis can be used as proxies of palaeotemperatures. Air and water movements in a cave need to be slow, so that a thermal equilibrium can be established between the bedrock and the air in the cave, reflecting the mean annual surface temperature. During the precipitation of the calcite from drip water, fractionation of oxygen isotopes takes place which depends on the surrounding temperature. Therefore the $\delta^{18}O$ concentration of calcite from speleothems should indicate the surface temperature through time (BRADLEY 1999).

The isotopic equilibrium of the calcite with the drip water can be tested by analysing $\delta^{18}O$ concentrations from different samples taken from the same growth layer. Isotopic equilibrium can be assumed if the values do not vary. If variations of the values can be observed, this indicates evaporation rather than a slow degassing of CO_2, and an alteration of the temperature-dependent fractionation relationship can not be excluded. Another test for isotopic equilibrium is to compare the $\delta^{18}O$ and the $\delta^{13}C$ concentrations along individual growth layers. In a non-equilibrium situation carbon and oxygen isotope concentrations would show the same fluctuations according to kinetic factors by which they are controlled. If there is no correlation between the two isotopes, equilibrium during the precipitation of the carbonate speleothems can be assumed (BRADLEY 1999).

Changes in $\delta^{18}O$ and $\delta^{13}C$ of speleothems indicate primarily variations in the isotopic composition of cave water. The isotopic composition of cave water varies with the isotopic composition of rainfall, so the amount of rainfall and also the isotopic composition of the evaporating source need to be considered. Additionally contributions of different types of vegetation (C3/C4 plants) and the average annual rainfall play a role (cp. BAR-MATTHEWS *et al.* 2000).

In interpreting $\delta^{18}O/\delta^{16}O$ variations from speleothems several opposing factors come into play for a given climatic shift (BRADLEY 1999): (1) With a decreasing cave temperature the fractionation factor between calcite and water increases, which results in an increase in the $\delta^{18}O$ concentration. (2) If the air temperature at the surface decreases, also the $\delta^{18}O/\delta^{16}O$ of the precipitation decreases and accordingly the $\delta^{18}O$ concentration in the drip water decreases. (3) During glacial periods the growth of $\delta^{18}O$ depleted continental ice-sheets results in an increase of $\delta^{18}O$ concentration in sea water and also in the precipitation.

At first variations in the $\delta^{18}O$ concentrations from speleothems were interpreted as the result of variations in the $\delta^{18}O$ concentration of precipitation with lower $\delta^{18}O$ values indicating colder conditions (e.g. DUPLESSY *et al.* 1970, 1971). EMILIANI (1972) observed that the $\delta^{18}O$ concentrations from speleothems, interpreted by DUPLESSY *et al.*, were inverse to $\delta^{18}O$ concentrations from oceanic foraminifera indicating palaeotemperatures. EMILIANI (1972) concluded that variations of $\delta^{18}O$ concentrations from speleothems were not controlled by the $\delta^{18}O$ concentrations of precipitation, but by temperature-dependent fractionation. This was later confirmed by the measurement of inclusion waters from speleothems. The $\delta^{18}O$ concentrations of speleothem calcite increase with falling temperatures (BRADLEY 1999).

Records of $\delta^{18}O$ concentration of speleothems of the Soreq are interpreted accordingly (e.g. BAR-MATTHEWS *et al.* 1997, 2000). Investigations on inclusion waters from speleothems of the Soreq cave and two other caves in Israel confirmed the interpretation (cp. MCGARRY *et al.* 2004).

BAR-MATTHEWS *et al.* (1997) established also the relationship between mean annual rainfall (mm), the $\delta^{18}O$ (SMOW) concentration (‰) of rain and the $\delta^{18}O$ (SMOW) concentration (‰) of cave water for the Soreq cave (Figure 1.3.3c). The relationship between $\delta^{18}O$ (SMOW) concentration (‰) of cave water and the $\delta^{18}O$ (PDB) concentration (‰) of low magnesium calcite (LMC) from the speleothems after O'NEIL *et al.* (1969) is also given there (Figure 1.3.3d).

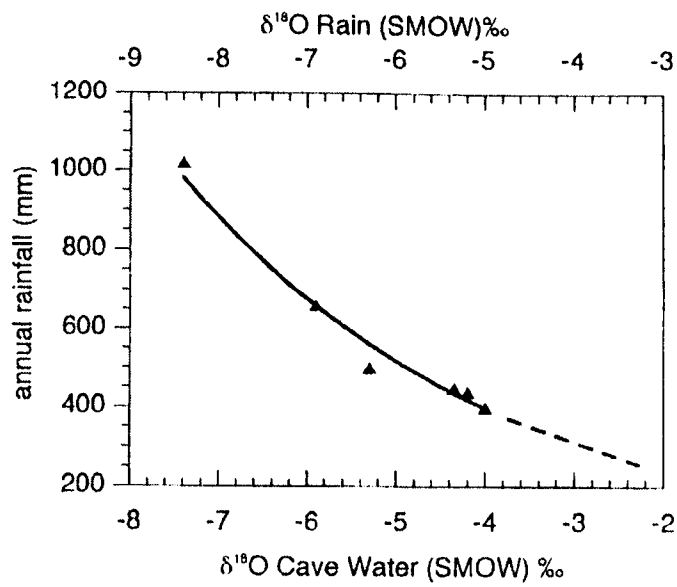

Figure 1.3.3c : Relationship of $\delta^{18}O$ (SMOW) (‰) of rain and of Soreq cave water as function of the annual rainfall (mm) (from BAR-MATTHEWS et al. 1997).

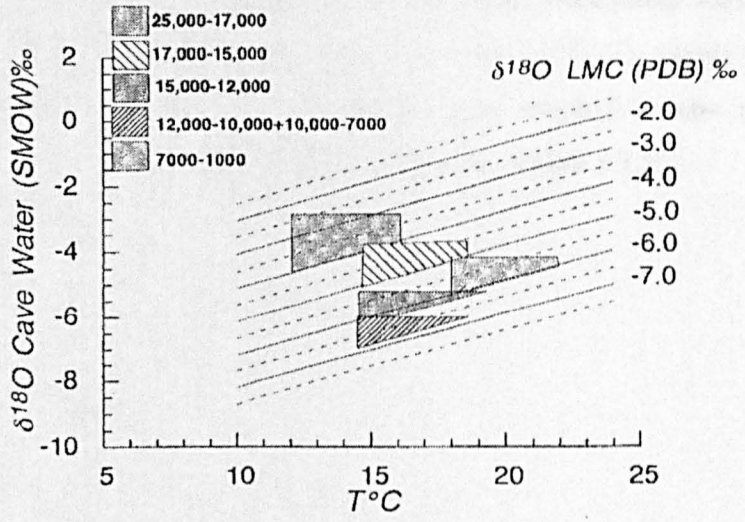

Figure 1.3.3d: Relationship after O'NEIL et al. (1969) between $\delta^{18}O$ (SMOW) concentration (‰) of cave water and the $\delta^{18}O$ (PDB) concentration (‰) of low magnesium calcite (LMC) from speleothems (from Bar-Matthews et al. 1997).

The $\delta^{13}C$ (PDB) (‰) concentration of speleothems in the Soreq cave depend on the contribution of the surrounding rock (dolomite), the contribution of CO_2 from soils depending on C_3/C_4-type vegetation and on CO_2 degassing and carbonate precipitation processes (BAR-MATTHEWS *et al.* 1997). Owing to differing photosynthesis of different plant species, depending on climatic conditions, isotopic fractionation of carbonate occurs. C_3 plants correspond to highest $\delta^{13}C$ depletion, and C_4 plants to lowest depletion of $\delta^{13}C$ (cp. BRADLEY 1999) (cp. Figure 1.3.3e).

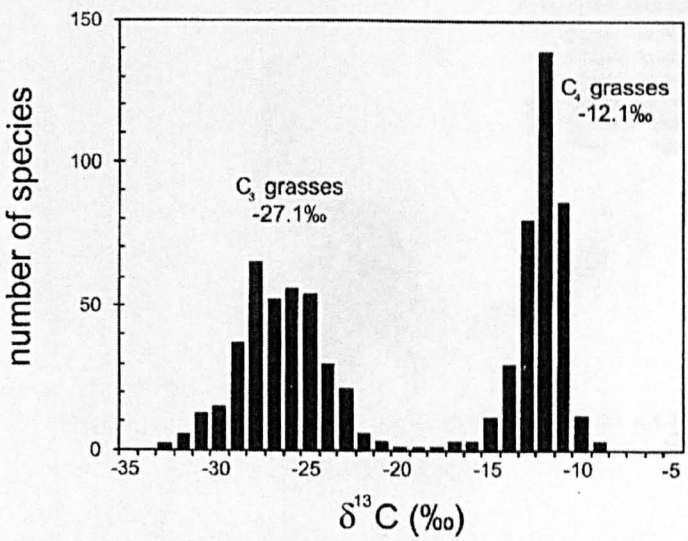

Figure 1.3.3e: Concentrations of $\delta^{13}C$ (‰) of C_3 and C_4 grasses (CERLING and QUADE 1993 cp. BRADLEY 1999).

C_3 plants are found predominantly in the northern hemisphere owing to the cool growing season, and this compares with a mixture of C_3/C_4 plants in tropical and temperate deserts, semi-deserts, dry steppes and tropical scrubs and woodlands (CERLING and QUADE 1993 cp. BRADLEY 1999) (cp. Figure 1.3.3f).

Figure 1.3.3f: The general distribution of C_3 and C_4 plants (CERLING and QUADE 1993 cp. BRADLEY 1999).

BAR-MATTHEWS *et al.* (1997) give the $\delta^{18}O$ ‰ (PDB) versus the $\delta^{13}C$ ‰ (PDB) concentrations of 400 data points measured on speleothems of the Soreq cave (Figure 1.3.3g).

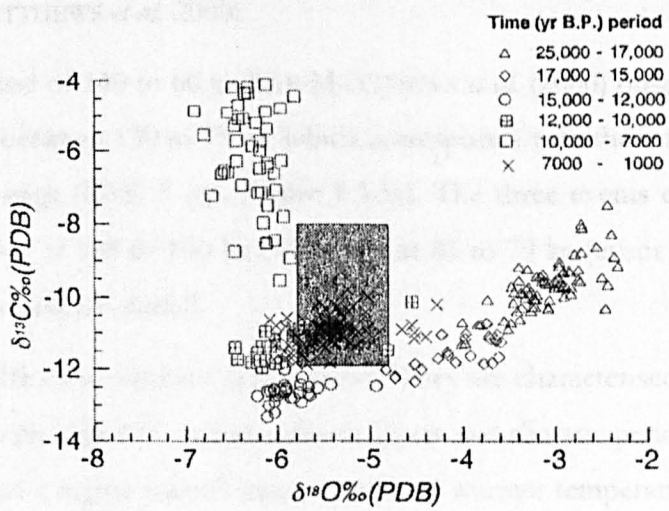

Figure 1.3.3g: Isotopic compositions $\delta^{18}O$ ‰ (PDB) versus $\delta^{13}C$ ‰ (PDB) of 400 data points measured on speleothems of the Soreq cave. The shaded area represents the present-day $\delta^{18}O$ versus $\delta^{13}C$ concentrations (from BAR-MATTHEWS et al. 1997).

From the $\delta^{18}O$ ‰ (PDB) and the $\delta^{13}C$ ‰ (PDB) concentrations and the speleothem growth habits BAR-MATTHEWS *et al.* (1997) estimated the $\delta^{18}O$ ‰ (SMOW) concentration of cave water, the temperature range (°C), the mean annual rainfall (mm) and then determined the vegetation type for the time period of 25 ka to present. This record from the Soreq cave was extended from 140 ka to the present by BAR-MATTHEWS *et al.* (1998a, 1998b, 1999 and 2000) (cp. Figures 1.3.3a and 1.3.3b).

For the time between 60 – 17 ka, which corresponds to the last glacial period, they observed quasi-periodic changes in the $\delta^{18}O$ and the $\delta^{13}C$ concentrations at a millennial time scale. The isotopic values were on average 2 ‰ higher than during the period from 17 ka to present. Maximum $\delta^{18}O$ values were observed at about – 2.2 ‰ and maximum $\delta^{13}C$ values at about – 8.5 ‰ and are recorded at 46, 35, 25 and 19 ka reflecting the coldest and driest conditions of the period (cp. Figures 1.3.3a and 1.3.3b) with mixed C_3 and C_4 type vegetation. When $\delta^{18}O$ and $\delta^{13}C$ values are at their lowest as during event #II at 54 ka, warmer and wetter conditions are indicated (cp. Figures 1.3.3a and 1.3.3b) (BAR-MATTHEWS *et al.* 2000).

Between 17 to 7 ka very sharp drops in the $\delta^{18}O$ concentration (– 2.2 to – 6.5 ‰) and the $\delta^{13}C$ concentration (– 8.5 ‰ to – 13 ‰) were observed, which show an interval of increasing temperature and annual rainfall (BAR-MATTHEWS *et al.* 2000). From 8.5 to 7 ka a very wet period (event #I) occurred with annual precipitation nearly double that of the present, during which $\delta^{18}O$ values were as low as – 6.5 ‰ and the $\delta^{13}C$ concentration showed maximum values of circa – 5.0 to – 4.0 ‰ (cp. Figures 1.3.3a and 1.3.3b) (BAR-MATTHEWS *et al.* 2000).

For the time period of 140 to 60 ka BAR-MATTHEWS *et al.* (2000) observed three further low $\delta^{18}O$ events between 130 to 75 ka, which corresponds with the interglacial period of marine isotopic stage (MIS) 5 (cp. Figure 1.3.3a). The three events occurred at 124 to 119 ka (event #V), at 108 to 100 ka (#IV) and at 85 to 79 ka (event #III) and indicate also periods of enhanced rainfall.

Events #V and #I show similar characteristics. They are characterised by very low $\delta^{18}O$ values together with high $\delta^{13}C$ values indicating very wet climatic periods. And it is likely that event #V had a higher rainfall intensity and/or warmer temperatures than event #I (BAR-MATTHEWS *et al.* 2000). During the glacial-interglacial transitions from MIS 6 to MIS 5 and from MIS 2 to MIS 1 the most pronounced isotopic changes occurred in the speleothems from the Soreq cave.

BAR-MATTHEWS *et al.* (2003) compared also proxy climate data from speleothems of the Soreq cave with the of the Peqiin cave and were able to show that because of the location of the caves and their comparable records, which the terrestrial climate records BAR-MATTHEWS *et al.* (1997, 1999, 2000 and 2003) presented, reflect not only local climatic changes but the of a wider area.

Marine records

Proxy climate information for the Levante derives also from marine cores and the oxygen isotope concentrations of foraminifera.

Oxygen isotope records from benthic foraminifera reflect variations of the $\delta^{18}O/\delta^{16}O$ concentrations of the oceans according to $\delta^{16}O$ depletions caused by the $\delta^{16}O$ reservoir of large ice-sheets during glacial times. The information from benthic foraminifera is considered as independent from surface-temperature variations of the oceans and their influence on the oxygen isotope fractionation processes, as there is a constant temperature of a few degrees Celsius at the sea-bottom (BRADLEY 1999). MARTINSON *et al.* (1987) compiled an astronomically tuned standard isotope curve from various oxygen isotope records based on benthic foraminifera from deep-sea cores around the world (cp. PISIAS *et al.* 1984) (Figure 1.3.3h). The record reflects the $\delta^{16}O$ depletions in oceanic waters caused through the large inland ice-sheets during glacial periods and summarises general climate variations in areas close to ice-sheets. Differing local climate variations of small areas or climate variations in areas distant from ice-sheets are not represented in the standard isotope curve.

Oxygen isotope records from planktonic foraminifera reflect apart from fluctuations of the ice-sheet volumes also local sea-surface temperature variations. KALLEL *et al.* (2000) investigated oxygen isotope records of core MD84-641 which is not far off the Israeli coast. For core MD84-641 the oxygen isotope records were obtained mainly from *Globigerinoides ruber* (*G. ruber*) as the dominant species in the Levantine basin but also from *Globigerina bulloides* when *G. ruber* were absent during cold periods (KALLEL *et al.* 2000). In these cores non-sapropel sediments alternate with sapropels. Sapropels are organic carbon rich horizons that have formed during oxygen depletion of deep sea waters (cp. Chapter 7.2.6). Sapropels occurred during glacial and also during interglacial

phases. The observed low $\delta^{18}O$ concentrations combined with low salinity values indicate freshwater input during sapropel formation (KALLEL *et al.* 2000).

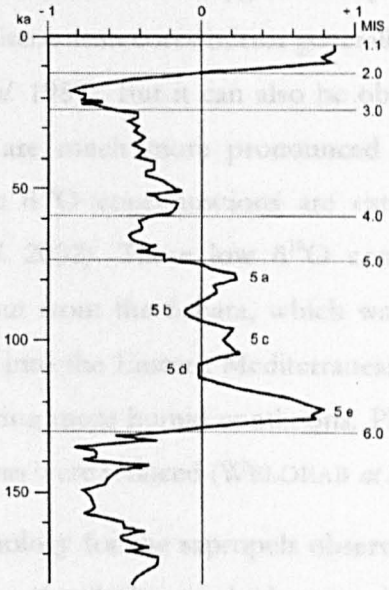

Figure 1.3.3h: Astronomically tuned SPECMAP record of oxygen isotope variations based on benthic foraminifera of deep-sea cores around the world (redrawn from MARTINSON et al. 1987).

WELDEAB *et al.* (2002) presents the oxygen isotope record from *G. ruber* from three eastern Mediterranean cores, from which core KL83 like core MD84-641 is directly off the Israeli coast (Figure 1.3.3i).

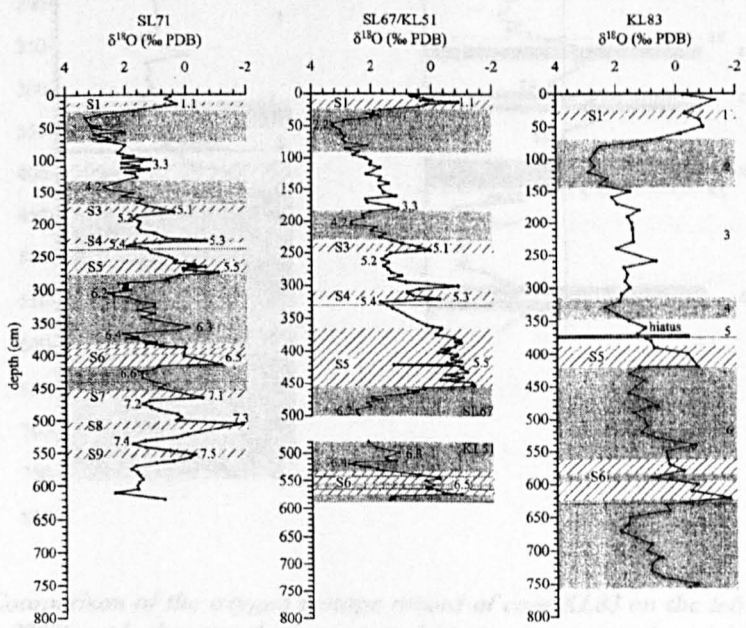

Figure 1.3.3i: Oxygen isotope records from Globigerinoides ruber of three eastern Mediterranean cores, from which core KL83 is just off the Israeli coast (from WELDEAB et al. 2002). Sapropels are indicated as S1 and S3-S9.

Because the fluctuations through variations of ice-sheet volumes are not isolated in these oxygen isotope records from fluctuations caused by varying sea-surface temperatures from local climates, the oxygen isotope records from planktonic foraminifera of eastern Mediterranean cores mirror generally the global standard-isotope curve (e.g. MARTINSON *et al.* 1987). But it can also be observed from core KL83 that glacial-interglacial changes are much more pronounced compared to the standard-isotope curve and that the $\delta^{18}O$ concentrations are extremely low during sapropel formation (WELDEAB *et al.* 2002). These low $\delta^{18}O$ concentrations together with a drastically reduced dust input from the Sahara, which was also not balanced through sediment influx from rivers into the Eastern Mediterranean during this time, indicate a denser vegetation cover during more humid conditions. Physical erosion and sediment removal from the source areas were reduced (WELDEAB *at al.* 2002).

In order to provide a chronology for the sapropels observed in core KL83 the oxygen isotope record can be compared with the standard oxygen isotope curve (Figure 1.3.3j).

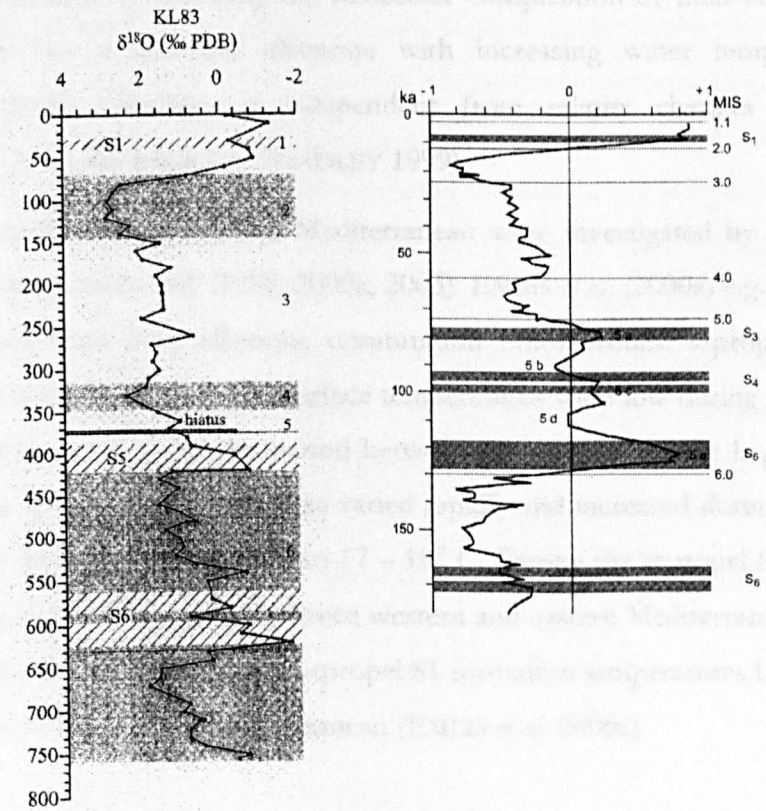

Figure 1.3.3j: Comparison of the oxygen isotope record of core KL83 on the left (from WELDEAB et al. 2002) and the standard oxygen isotope curve on the right (redrawn from MARTINSON et al. 1987). According to the sedimentation rate the oxygen isotope curve of core KL83 differs from the standard oxygen isotope curve. For sapropels S1 and S3 to S6 on the right cp. KALLEL et al. (2000).

KALLEL *et al.* (2000) subtracted further the oxygen isotope record of the benthic foraminifera *Cibicides wuellerstorfi* from the oxygen isotope record of the planktonic foraminifera *G. ruber* on core MD77-169 of the Andaman Sea, Bay of Bengal, Indian ocean. This resulted in a record reflecting mainly changes in the oxygen isotope concentrations of the surface water. From this KALLEL *et al.* (2000) were able to show that the Mediterranean sapropels coincided with a decrease in the surface salinity of the Andaman Sea and an increase in the strength of the Indian summer monsoon. Additionally, the sapropels coincide with peaks of the summer insolation of the northern hemisphere.

Altogether this shows that high summer insolation of the northern hemisphere was responsible for enhanced atmospheric transport of freshwater to both Asia and the Mediterranean basin (KALLEL *et al.* 2000).

Alkenone unsaturation ratios from marine phytoplankton can also be used to reconstruct palaeo-sea-surface-temperatures. Certain phytoplankton respond to temperature changes by changing the molecular composition of their cell membranes and produce less unsaturated alkenone with increasing water temperature. The information from alkenones is independent from salinity changes and isotopic composition of the sea water (cp. BRADLEY 1999).

Alkenone records for the Eastern Mediterranean were investigated by KALLEL *et al.* (1997, 2000) and EMEIS *et al.* (1998, 2000a, 2003). EMEIS *et al.* (2000a) e.g. calculated sea surface temperatures from alkenone unsaturation ratios around sapropel S1 (Figure 1.3.3k) and found that average sea surface temperatures were low during the last glacial and at about 11 – 15° C for the period between 16 – 13 ka. At the beginning of the Holocene the sea surface temperatures varied rapidly and increased during the sapropel S1 formation (between 9.5 – 6.6 ka) to 17 – 18° C. During the sapropel S1 formation a temperature gradient of 2 – 3° C between western and eastern Mediterranean sub-basins was maintained like today. After the sapropel S1 formation temperatures have fluctuated close to 20° C in the Eastern Mediterranean (EMEIS *et al.* 2000a).

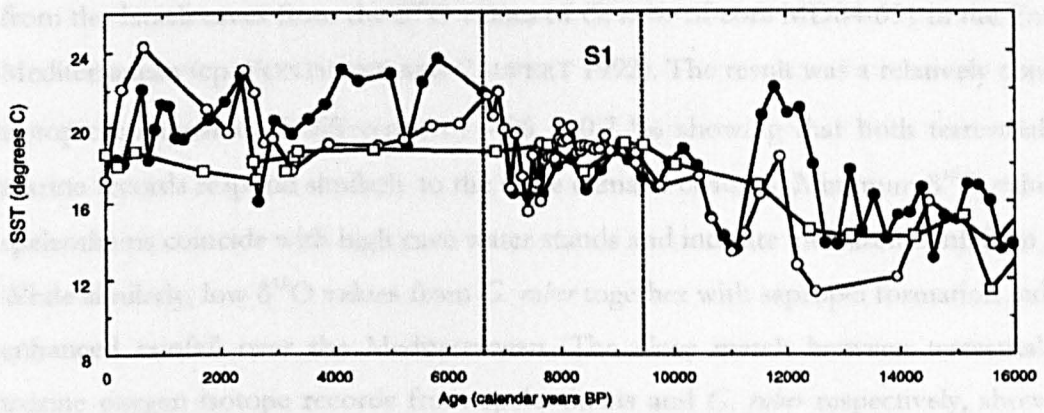

Figure 1.3.3k: Sea surface temperatures (SST) from alkenone unsaturation ratios of three Mediterranean cores, from which ODP core 967 is situated in the Levantine basin (open circles) (from EMEIS et al. 2000a).

EMEIS *et al.* (2003) calculated sea surface temperatures from alkenone unsaturation ratios after the equations given by MÜLLER *et al.* (1998) and TERNOIS *et al.* (1997) for the time intervals bracketing the sapropel events S10 – S3 and S1 for the eastern Mediterranean. Across the Pleistocene sapropel intervals, sea surface temperatures increased between 0.7° - 6.7° C. They also found that the oxygen isotope composition of sea water shows the $\delta^{18}O$ depletion during sapropel formation to be most pronounced at their base. This is in agreement with an initial input of monsoon-derived freshwater (EMEIS *et al.* 2003). From the calculated sea surface temperatures they were able to show that most sapropels coincide also with temperature increase. The exceptions are (1) the "glacial" sapropel S6 (176 – 170 ka), for which after an initial rapid warming colder sea surface temperatures are recorded, but along with a very strong $\delta^{18}O$ depletion, and (2) another period with a strong $\delta^{18}O$ depletion at the insolation maximum at around 150 ka but with cold sea surface temperatures, which is because of the cold sea surface temperatures not expressed as a sapropel, but coinciding with a strengthened monsoon (EMEIS *et al.* 2003).

Link between terrestrial and marine records

BAR-MATTHEWS *et al.* (2003) found that their $\delta^{18}O$ records from the speleothems of the Soreq and the Peqiin caves match excellently the $\delta^{18}O$ records from *G. ruber* in the Eastern Mediterranean. BAR-MATTHEWS *et al.* (2003) established the link between terrestrial and marine oxygen isotope records by subtracting $\delta^{18}O$ values of speleothems

from the Israeli caves from the $\delta^{18}O$ values of *G. ruber* of core MD84-651 in the Eastern Mediterranean (cp. FONTUGNE and CALVERT 1992). The result was a relatively constant isotopic compositional difference of –5.6 ± 0.7 ‰ showing that both terrestrial and marine records respond similarly to the same climatic changes. Minimum $\delta^{18}O$ values of speleothems coincide with high cave water stands and indicate increased rainfall on land. While similarly, low $\delta^{18}O$ values from *G. ruber* together with sapropel formation indicate enhanced rainfall over the Mediterranean. The close match between terrestrial and marine oxygen isotope records from speleothems and *G. ruber* respectively, show that both systems experience events of enhanced rainfalls simultaneously (BAR-MATTHEWS *et al.* 2003).

Through this link between terrestrial and marine oxygen isotope records it was now possible to use sea surface temperatures from alkenone unsaturation data as proxy for land temperatures at the caves and to calculate $\delta^{18}O$ values of palaeo-rainfall and the amounts (BAR-MATTHEWS *et al.* 2003). The $\delta^{18}O$ of *G. ruber* of three periods (cp. EMEIS *et al.* 1998, 2000a) match the $\delta^{18}O$ record from the speleothems well (Figure 1.3.3l).

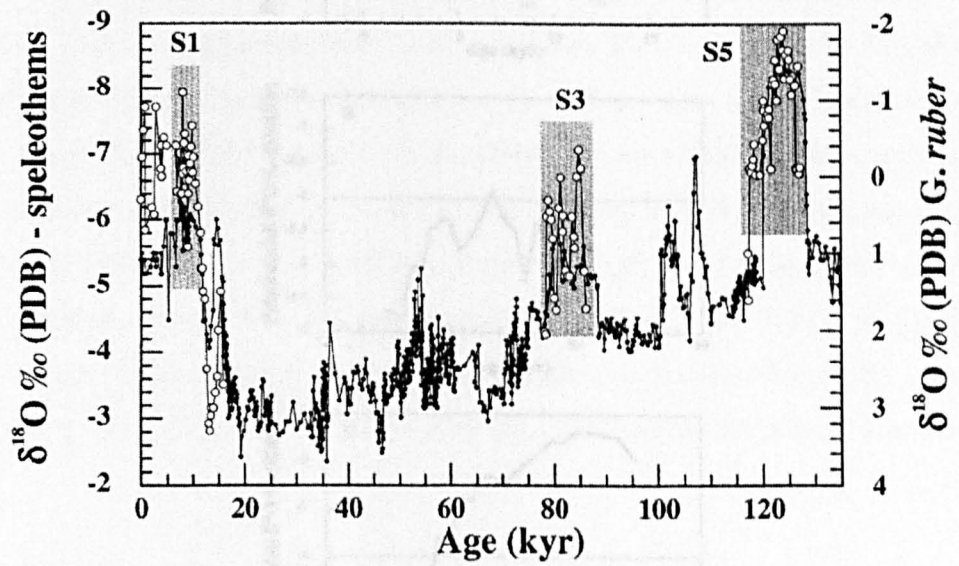

Figure 1.3.3l: Oxygen isotope records of G. ruber from ODP site 967 (open circles) (EMEIS et al. 1998, 2000a) and oxygen isotope records of speleothems (solid circles) against time (from BAR-MATTHEWS et al. 2003). Age (Kyr) = Age (ka).

The three well matching periods are between 128 – 117 ka during sapropel S5, between 85 – 78 ka during sapropel S3, both during marine isotope stage (MIS) 5, and a period during the Holocene between 16 ka to the present which includes sapropel S1.

For the three selected periods BAR-MATTHEWS *et al.* (2003) calculated first the $\delta^{18}O$ of cave water from the speleothems $\delta^{18}O$ values and the matched alkenone temperatures using the calcite-water equation of O'NEIL *et al.* (1969). Secondly, they subtracted 1 ‰, the difference of present-day rainfall to present-day cave water, to obtain the rainfall values (Figure 1.3.3m). The rainfall values from the Soreq cave area could then, thirdly, be converted into estimates of palaeo-rainfall amounts (Figure 1.3.3n) by assuming the modern relationship of annual rainfall amounts and the $\delta^{18}O$ values of the Soreq cave were also valid in the past (BAR-MATTHEWS *et al.* 2003).

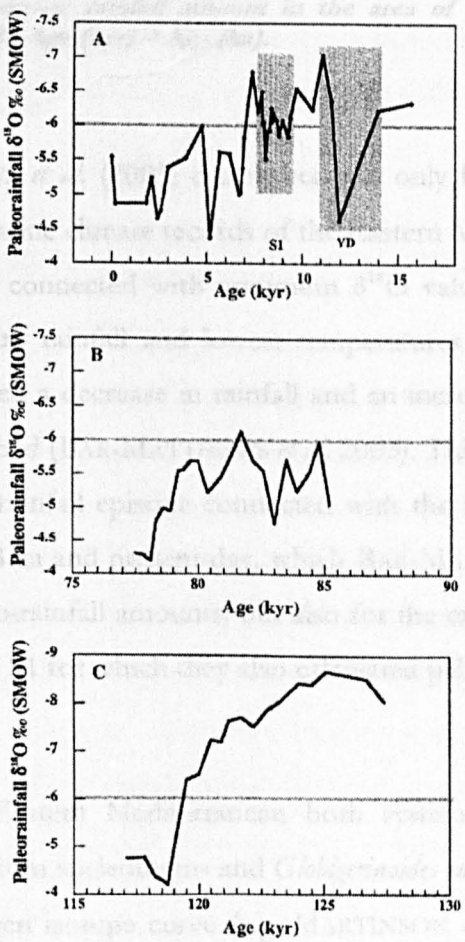

Figure 1.3.3m: Oxygen isotope palaeo-rainfall values (SMOW) for the three selected periods (from BAR-MATTHEWS et al. 2003). Age (kyr) = Age (ka).

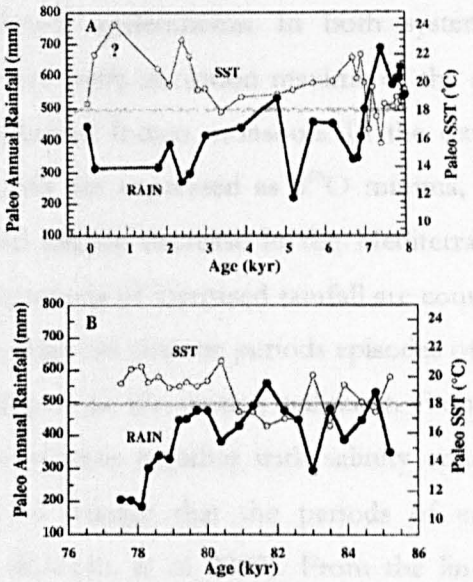

Figure 1.3.3n: Palaeo-rainfall (solid circles) and sea-surface temperatures (open circles) (SST from Emeis et al. 1998, 2000b) against time. Horizontal lines indicate modern temperature and average rainfall amount in the area of the Soreq cave (from Bar-Matthews et al. 2003). Age (kyr) = Age (ka).

With this BAR-MATTHEWS *et al.* (2003) established not only for the first time the link between terrestrial and marine climate records of the Eastern Mediterranean but showed that the rainfall episodes connected with minimum $\delta^{18}O$ values in both systems were characterised by maximum rainfall and lowest temperatures at the beginning of the event, which then followed a decrease in rainfall and an increase of temperatures until arid conditions were reached (BAR-MATTHEWS *et al.* 2003). This pattern is not only valid for the examples of the rainfall episode connected with the formation of sapropel S3 and the period between 8 ka and present-day, which BAR-MATTHEWS *et al.* (2003) used to demonstrate the palaeo-rainfall amounts, but also for the rainfall episodes connected with the sapropels S5 and S1 for which they also calculated palaeo-rainfall amounts.

To summarise: in the Eastern Mediterranean both systems, terrestrial and marine oxygen isotope records, from speleothems and *Globigerinoides ruber*, respectively, generally mirror the standard oxygen isotope curve (e.g. MARTINSON *et al.* 1987) although they show more pronounced glacial-interglacial transitions. Both systems react simultaneously to the climate variations in the same fashion, as it is possible to match oxygen isotope records from *G. ruber* from eastern Mediterranean cores with oxygen

isotope records from Israeli speleothems. In both systems indicated periods of enhanced rainfall are in tune with insolation maxima of the northern hemisphere and with periods of a strengthened Indian monsoon. In the oxygen isotope records the periods of enhanced rainfall are expressed as $\delta^{18}O$ minima, accompanying high cave water stands on land and salinity decrease in the Mediterranean Sea. In the marine environment most of the periods of increased rainfall are connected with the formation of sapropels, although during cold climatic periods episodes of enhanced rainfall are not always expressed as sapropels in the marine sediment. From the amplitudes of $\delta^{18}O$ depletions in the marine systems together with salinity concentrations and alkenone temperatures it seemed to emerge that the periods of enhanced rainfall show a monsoon-like character (KALLEL *et al.* 2000). From the link between terrestrial and marine records and the calculations of palaeo-rainfall amounts it was possible for BAR-MATTHEWS *et al.* (2003) to establish a pattern for the rainfall episodes, with enhanced rainfall and low temperatures at the beginning and a decrease in rainfall amounts and increase in temperatures to arid conditions during the episode.

1.4 Genetic models of the Israeli coastal sand dunes

The Israeli coast is part of the southeastern corner of the Levantine basin and the Nile littoral cell. The coastline between the Egyptian and Lebanese border stretches for about 230 km. The coastal plain of Israel shows a low relief and only in the North is the shore reached by two mountains, the Carmel Mountain and the mountains ridge at Rosh Haniqra, both Cenomanian (NIR 1985). In the South the width of the coastal plain is 40 km, while towards the North it narrows to only a few hundred metres. A long part of the coast is formed by a cliff which varies in height between 40 and 2 m. It is composed of Pleistocene rocks and sediments: aeolianites (carbonate-cemented quartz sandstone), red soils, other soils and sand at various stages of cementation. The aeolianites – locally called "kurkar" - and the intercalated red soils form elongated ridges, so-called "kurkar ridges". These ridges run more or less parallel to the present-day shoreline. The kurkar ridges are exposed in the coastal plain onshore or at the shallow shelf offshore and also offshore covered under Nilotic sediments. The ridges onshore are discontinuous as several ephemeral rivers (wadis) from the eastern mountains drain into the

Mediterranean Sea (NIR 1985). The ridges are composed mainly of quartz, heavy minerals and some accessory feldspar.

River Nile as sediment source for the Israeli coastal plain

The aeolianite ridges and other Quaternary sediments in the coastal plain of Israel attracted early interest. LÖWENGART (1928), ADLER (1934), PICARD and AVNIMELECH (1937), EMERY and NEEV (1960), YAALON (1967) and others, concluded that the aeolianite ridges were the result of sand, transported from the river Nile delta east- and northward by Mediterranean currents along the shore and blown onshore by landward winds (KARMELI *et al.* 1968). EMERY and NEEV (1960) confirmed by heavy mineral analysis that the sand on the beaches and in the dune sands of Israel is most likely to derive from the river Nile and is transported by longshore currents. Heavy minerals from the beach sands near the western mouth of the Nile river show a high content in augite (25 %) and hornblende (40 %). That is similar to the concentration in sediments in the lower part of the river Nile (EMERY and NEEV 1960). Because the Atbara river drains through the volcanic massive of Abyssinia/Ethiopian Plateau before it flows into the Nile river at about 1500 km upstream, it carries the high concentration of augite which can be observed. Near the Egyptian border to Libya beach sands contain high concentrations of zircon (39 %) (SHUKRI and PHILIP 1956a in EMERY and NEEV 1960), which is likely to derive from the Nubian sandstone. Towards the East between Port Said and Gaza the concentration of augite and hornblende lessens, whereas there are higher concentrations of zircon, rutile and garnet. This change is thought to come from the loss of weathered minerals during transport and from the mixing with new sand input from the Sinai sea cliffs and wadis (EMERY and NEEV 1960). This overall trend continues North of Gaza, where the concentration of augite decreases, while the concentration of hornblende (65 %) is high on Israeli beaches. That the amounts of tourmaline and zircon in Israeli beach sands are far less than in Libyan beach sands shows that the sediment discharge of the river Nile outweighs the sediment input from the African coast West of the Nile mouth (EMERY and NEEV 1960). A comparison between the heavy minerals contents of the beach sands and dunes with the kurkar ridges (aeolianites and their soils) shows that the kurkar ridges contain similar concentrations than the beach sands and dunes, with a high content of hornblende. The concentrations of epidote and zircon are higher in the aeolianites than in the recent

sands (beach and dunes), which points towards a weathering sequence of less stable minerals (e.g. augite, hornblende) and the resulting concentration of the more resistant minerals (e.g. zircon, rutile) (EMERY and NEEV 1960). In Egyptian aeolianites the same weathering sequence was noted (SHUKRI and PHILIP 1956b in EMERY and NEEV 1960). The analyses by EMERY and NEEV (1960) also made clear that the contribution of river sediments to the beaches of Israel is only minor with some local exceptions along the northern part of the Israeli coast. EMERY and NEEV (1960) conclude that because the river Nile is the only large river along the northern coast of Africa that is able to contribute significant amounts of sandy sediment into the Nile littoral cell, and beach sands west of the Nile delta show a different mineral composition than in the East, it seems reasonable that the river Nile is the main source for the "detrical and main fraction" (p. 10) of the beach sands of Israel. There may be some additional sediment contribution from the Sinai peninsula. Apart from the fringe of the general Mediterranean current which transports the sands east- and northward, there are also some wave-induced currents responsible for the sediment transport. Waves arrive on the Israeli coast from about 280° (azimuth of crest: 010). The curvature of the Israeli coast causes the wave-induced current in the North of the Israeli coast to return some sand to the central part of the coastal plain in a reverse transport movement from North to South. Where the longshore Mediterranean current towards the North and the northern wave-induced current towards the South meet, sand is particularly available on the beach to be blown inland and form a dune field (EMERY and NEEV 1960).

GOLDSMITH and GOLIK (1980) established a sediment transport model for the southeastern Mediterranean coast, as the gradual change of the shoreline orientation from West-East to South-North, the longest fetch in the Mediterranean of 2400 km in West-East direction and the main sediment source being the Nile delta in the West, provided a unique opportunity for such a study. They found that wave-induced currents are responsible for longshore transport of sediment. Between El Arish and Rafah the transport is to the Northeast and is very large. In the area between Rafah and Haifa nodes of converging transport directions exist which vary in location with the alteration of the wave approach direction. Owing to the concave form of the shoreline relative to the approaching waves, the net transport of quartz sand decreases from South to North (GOLDSMITH and GOLIK 1980). The zone at Haifa Bay operates as a sediment sink for sand from the river Nile or southerly local cliffs, because the wave energy of nearly all

approaching waves is much lower than for the rest of the coast. North of Haifa Bay from Akko to Rosh Haniqra the wave refraction is high because of the subaqueous Akhziv Canyon being near shore. The longshore transport of sediment varies greatly in orientation and quantity and the net transport along the shore is negligible (GOLDSMITH and GOLIK 1980).

Southeastern Mediterranean sediment transportation patterns, which were investigated through clay mineral distribution, confirmed the dispersal of Nile sediments along the coast towards the Northeast in an extended counter-clockwise gyre (STANLEY *et al.* 1998). But the sediment provenance of the river Nile in the Nile littoral cell and along the coastline towards the Northeast has changed in the last century since the construction of the two Aswan dams (Low Dam 1902, High Dam 1964) and modern coastal installations. The volume of silt and clay which passes the Nile delta after the closure of the High Dam is reduced to 15 % of the pre-1902 quantities. The reduction of the sediment supply through the river Nile causes along the southeastern coast of the Mediterranean erosion of the coastal cliffs and the Quaternary sediments of the seafloor (STANLEY *et al.* 1998). NIR (1973) estimated the erosion of the coastal cliff in Israel of about 3 – 4 cm/a over the last 6 ka. This value has changed dramatically to a present-day erosion rate of 20 – 40 cm/a (NIR, in press, in STANLEY *et al.* 1998).

Many others have contributed to the discussion of the currents in the southeastern Mediterranean and the sediment transport from the Nile delta along the Mediterranean coastline of the Levant (e.g. AVNIMELECH 1962, VENKATARATHNAM *et al.* 1972, CARMEL *et al.* 1984, GOLIK 1992, 1993, 1997, FRIHY 1994, SHOSHANY *et al.* 1996, SANDLER and HERUT 2000).

Deposition patterns behind the aeolianite ridges and their sediment facies and soils

Parallel to the studies of the sediment transport mechanisms of the Israeli Mediterranean coast, studies were also carried out to reveal the sedimentation history and principles behind the formation of the kurkar ridges in the coastal plains.

In the early 1960s ITZHAKI (1961) supposed a cyclical sedimentation of the kurkar-hamra-successions of the aeolianite ridges along the coastal plain. He states that in the coastal plain marine transgressive sediments would interdigitate with continental sediments and he distinguished four cycles during the Quaternary. A cycle starts with

terrestrial sediments, followed by the sedimentation of marine transgressive sediments in the West and alternating in the East with continental deposits. The cycle would come to an end with a regression phase which is attributed by ITZHAKI (1961) to leave sandy clays to cover the surface that form the hamra soils. The first cycle (would have) ended in the deposition of "Hamra I" during an early regression in the phase of the Ante - Penultimate Glaciation. The second cycle was completed with "Hamra II" and would have been deposited during the regression of the Penultimate Glaciation. The third cycle ceased with "Hamra III" and would have been deposited during the beginning of the Last Glaciation. The fourth cycle would be complete with the Postglacial (ITZHAKI 1961). No hamra soil was assigned to this cycle by ITZHAKI (1961). The oldest continental sandstones (kurkar) are exposed in the East of the coastal plain ITZHAKI (1961).

One of the key papers (in the 1960s) on the lithification of the aeolianites and their environmental significance is by YAALON (1967). He was able to show on partially consolidated dunes that a minimum of 8% $CaCo_3$ is needed for the process of the calcareous cementation of the sand to be continued and that the lithification is a result of cycles of wet and dry conditions, as are typical for a Mediterranean climate. Through percolating rainwater carbonaceous skeletal remains in the dune sand are dissolved and by evaporation of the water re-crystallisation takes place, which causes the dune to be consolidated by a carbonaceous cement from the top downwards. This process of lithification is very fast and by judgement of iron or pottery artefacts and bones takes tens to hundreds of years (YAALON 1967).

It could also be shown that the lamination which can be observed in the aeolianites of the kurkar ridges is caused by a particle differentiation during the formation of ripples on the dune surface. The differentiation is caused by the gravity and size of the grains. Carbonaceous skeletal fragments are usually of a coarser grain size and also lighter in density than the quartz sand and accumulate therefore on the crest of the ripples which is also observable on modern dunes. The resulting laminae of the dune structure are thicker or smaller, depending on the carbonate content in the unconsolidated dune. YAALON (1967) reasons that the preservation of the laminae in the indured aeolianites supports the observation made by FRIEDMAN (1964) that the dissolved carbonate is re-precipitated next to the place of dissolution.

YAALON (1967) documented that the environmental conditions under which calcareous dune sand would convert into consolidated aeolianite (kurkar) or into red Mediterranean soil (hamra), would solely depend on the carbonate content in the unconsolidated dune and on the amount of leaching, which depends on microclimatic conditions and the relief, and would appear to take place under general similar climatic conditions. Because the microclimatic and environmental conditions of precipitation and carbonate supply varies over space and time (EMERY and NEEV 1960), YAALON (1967) argues that the aeolianites or hamra soils should not be correlated with climatic phases during the Quaternary, if not based on independent information.

KARMELI *et al.* (1968) argue in opposition to ITZHAKI (1961), deduced from the homogenous dispersion of the clay in the soil layers, which is independent from the position relative in the ridge that the clay in the soils is of aeolian origin. Supporting the view of YAALON (1967) the authors stress that no climatic changes are necessary for the development of the different sediment facies of the aeolianite ridges in the coastal plain and that all facies types can be observed under the present-day environmental conditions in the coastal plain (KARMELI *et al.* 1968). ITZHAKI (1961) and KARMELI *et al.* (1968) are consistent with their views that the oldest aeolianites are exposed in the East of the coastal plain.

In the 1970s YAALON and LARONNE (1971) studied the internal structures of the Israeli aeolianites in relation to the palaeowinds. They concluded that according to the slipfaces of the studied aeolianites of Pliocene to Holocene age the palaeowind regime was similar to the present-day prevailing wind direction from West – Southwest. Further efforts were undertaken to shed further light on the palaeosols forming on aeolianites and dune sediments in the coastal areas of Israel (DAN and YAALON 1971, YAALON 1971). FARRAND and RONEN (1974) were the first to report that a kurkar ridge is not deposited in one sedimentary cycle, but is the outcome of several depositional periods. HOROWITZ (1975, 1979) advocated the view that the kurkar ridges in the coastal plain get older from West to East. RONEN (1975a) distinguishes sedimentary cycles in two kurkar ridges. The first ridge constitutes the coastal cliff and the second ridge is specially exposed at the motorway road cut between Haifa and Tel Aviv. In the first ridge along the coast he identifies 7 sedimentary cycles and in the second ridge he recognizes 5 sedimentary cycles, a cycle starting with a sand or an aeolianite unit and developing into a palaeosol. In the palaeosols of both ridges Mousterian, Epi-Palaeolithic, Neolithic or

Historic industries can be found. RONEN (1975a) holds a contrary view to HOROWITZ (1975, 1979) and concludes that both ridges would be in general contemporaneous and deposited during the Last Glacial and the Holocene. Further archaeological finds from the palaeosols in the Sharon and Carmel coastal plain were reported e.g. by RONEN *et al.* (1975) and RONEN (1977).

RONEN (1975b) reviews the archaeology and chronology of Israel. To explain the ridge-like morphology of the aeolianites in the coastal plain and the cyclicity in the sediments, he employs the following concept (cp. FARRAND and RONEN 1974). At the maximum point of transgression sand will be transported inland and is deposited as a longshore bar (barrier bar). With regression commencing the offshore sand belt between 0 and –40 m is exposed and maximal sand amounts are transported inland by wind. The deflation of sand from the offshore belt landwards continues until the source is consumed or covered by a new transgression. When the inland sedimentation of sand ceases to a certain threshold or completely, pedogenesis will commence and will continue until a further transgression is at its maximum (RONEN 1975b).

During the 1980s ISSAR (1980) sees the Israeli aeolianites as consolidated shore-dunes associated with the front or maximum of different transgressions. He distinguishes transgressive/regressive cycles for the marine Pleistocene of Israel and differentiates the three stages of the Calabro-Sicilian, the Tyrrhenian and the post-Tyrrhenian. According to ISSAR (1980) the aeolianites get older from West to East.

A submerged and excavated Neolithic village, named Newe Yam, gives evidence for a lowered sea level of minimal –5 m. Around 5 ka BC the population was forced to leave the village owing to a quick burial of the village with sand and an ensuing transgression WREschner (1983). Other submerged prehistoric archaeological sites were reported by RABAN (1983) and by GALILI *et al.* (1988).

MAGARITZ and GOODFRIEND (1987) studied the movement of the desert boundary in the Levant from the latest Pleistocene to the early Holocene and determined from various proxy data that during the deglaciation period in the semiarid region of the Levant, relatively wet conditions predominated between 15 – 11 ka, followed by a phase of extreme dry conditions from 11 – 10 ka and again wet conditions between 10 – 8 ka. The authors suggest that the period between 15 – 11 ka was considerably wetter than the phase between 10 – 8 ka evidenced by the formation of a calcareous horizon which cannot be observed during the Holocene (MAGARITZ and GOODFRIEND 1987).

GVIRTZMAN *et al.* (1984) identified six sedimentary cycles of interdigitating marine and continental sediments. He assumes that the sedimentary beds dip 45° toward the West, so the exposed kurkars get older from the West to the East (GVIRTZMAN *et al.* 1984).

BRUNNACKER *et al.* (1982) did heavy mineral analyses of the aeolianites in the southern coastal plain of Israel and confirmed in principle the findings of EMERY and NEEV (1960). The aeolianite formation was associated with regressional phases during the younger Pleistocene/Last Glacial. The aeolianites are less consolidated with increasing age from West to East (BRUNNACKER *et al.* 1982).

Further heavy mineral analyses on sediments of the aeolianites in the northern coastal plain by BOENIGK *et al.* (1985) showed a similar picture. Intercalated soils indicated three aeolian active phases.

GOLDBERG (1986) puts a chrono- and lithological summary together of stratigraphical sequences from the northern part of the Sinai and the western Negev by reviewing archaeological industries and differentiating between depositional and erosional events.

The research on the aeolianites in the Mediterranean coastal plain in Israel until the 1980s emphasises three points. Firstly, on the one hand, the deposition of aeolianites and the development of their palaeosols is solely dependent on micro-climatical and morphological conditions of the environment, and are hence independent from general climatic changes during the Quaternary. All sediment facies of the aeolianites occur under present-day conditions in the coastal plain (YAALON 1967, KARMELI *et al.* 1968). Secondly, contrariwise, the alternation between the deposition of aeolianite ridges along the Israeli coast and the genesis of palaeosols is connected with transgressive and regressive phases. Various authors differ between several sedimentary cycles during the younger Pleistocene and the Holocene. The formation of the aeolianites especially the ridges was mainly attributed to the holds of the transgressions and the successive regressions, as during this time the maximum amount of sand from the shore was for disposal; pedogenesis was attributed to the transgressional phase of a cycle (ITZHAKI 1961, FARRAND and RONEN 1974, RONEN 1975b, BRUNNACKER *et al.* 1982, BOENIGK *et al.* 1985). Others affiliated the formation of aeolianites with transgressive phases of sea stand (e.g. ISSAR 1980). Thirdly, the exposures of aeolianites are supposed to get older from West to East and each ridge is assigned to an individual accumulation phase

during the change of eustatic sea level (e.g. ITZHAKI 1961, KARMELI *et al.* 1968, HOROWITZ 1975, 1979, ISSAR 1980, BRUNNACKER *et al.* 1982, GVIRTZMAN *et al.* 1984).

In the transition to the 1990s ISSAR *et al.* (1989) explored the coherence of Nile river sediment discharge with the shift of the Inter-Tropical Convergence Zone (ITCZ) and the East African monsoon belt during the Last Glacial. The deflection of the monsoon belt to the North resulted in the rise of the water level of the Nile and an increased sediment supply to the Mediterranean (ISSAR *et al.* 1989).

GORING-MORRIS and GOLDBERG (1990) use radiocarbon dated prehistoric sites to condense the geomorphological history of the dune fields in the northern Sinai Peninsula and the western Negev desert. They found that the deposition of aeolian sands mainly over loess is somewhat earlier than the Last Glacial Maximum (LGM). This is likely to be due to the lower sea level and a therefore wider exposed Nile delta (GORING-MORRIS and GOLDBERG 1990).

Shortly after the GIF-project was started GVIRTZMAN *et al.* (1998) picked up the view already postulated by FARRAND and RONEN (1974) and by RONEN (1975b), that kurkar ridges in the central coastal plain were formed synchronously during the Last Glacial. GVIRTZMAN *et al.* (1998) introduce a revised stratigraphy in which they negate that the ridges get older from West to East and that the formation of a ridge is representing a certain sea-level (shoreline).

SIVAN *et al.* (1999) studied Quaternary deposits in the Galilee coastal plain in northern Israel. They confirmed that the aeolianites were formed as longitudinal ridges and contemporaneously. The deposits in the North were found to be of Tyrrhenian (transgressive event at marine isotope stage 7.1 and younger) to Holocene age. Red palaeosols are attributed to wet phases, aeolianites to dry phases and both to a low sea-level stand (SIVAN *et al.* 1999).

Pedology

YAALON (1992) gives a brief overview on the pedogenesis and the aeolianites in the coastal plain. He describes the aeolianites as calcareous sandstone whose sand originates in Ethiopia and is transported by the river Nile and longshore currents to the Israeli

coast. The degree of cementation of the aeolianites varies with the amount of available carbonate. For the hamra he recognises that it can apart from one soil also be a soil association. YAALON (1992) concludes that aeolianite formation takes place when high amount of carbonate are available and that hamra forms on parent material where the carbonate is leached out.

TSATSKIN and RONEN (1999) studied the Mousterian pedocomplex intercalated in the aeolianites at Habonim with micromorphology. They identified at least four discrete pedogenic phases indicating an increase in moisture partly through water logging (cp. Chapter 3.2.1 and 7.2.5).

Submerged aeolianites

Submerged aeolianites on the shelf offshore northern Israel were observed by geophysical and lithological means (EYTAM and BEN-AVRAHAM 1992, BELKNAP and MART 1999). BELKNAP and MART (1999) correlated the deposition of aeolianites with the sea-level low stand of MIS 2. The observed features suggest that the sea-level was at least 100 m lower than present. Both studies suggest Holocene tectonic activity of offshore faults in the area (EYTAM and BEN-AVRAHAM 1992, BELKNAP and MART 1999).

Negev

Late Pleistocene sediment sequences in floodplains and tels in the Negev desert and their relation to palaeoclimatic regimes were studied by ZILBERMAN (1993) and ZILBERMAN *et al.* (1994). YAIR *et al.* (1997) investigated the movement and percolation of water in longitudinal dunes in the western Negev. They distinguished patterns of spatial and temporal variabilities for an area with less than 100 mm annual rainfall.

Archaeology

An important archaeological site in the coastal plains of Israel is the Lower Palaeolithic site excavated in the Evron Quarry in Galilee (RONEN 1991). The finds were embedded in the upper parts of a hamra soil, which is considered to be the oldest hamra in the

coastal plain. Estimated ages range between 500 ka and 1000 ka (RONEN 1991). Other Lower Palaeolithic sites were excavated near Kibbutz Ruhama in the northern Negev (RONEN *et al.* 1998) and in the Sharon coastal plain near Kibbutz Eyal (RONEN and WINTER 1997). RONEN *et al.* (1999) date the pedocomplex in Habonim Quarry as Mousterian, owing to Levallois-Mousterian finds and radiothermoluminescence datings, which assign ages of MIS 5 – 4 to the pedocomplex. An important submerged pre-pottery Neolithic site (8100 – 7500 B.P.) Atlit-Yam was excavated by GALILI *et al.* (1993).

Stratigraphy and Sedimentology

GVIRTZMAN *et al.* (2000) established ^{14}C chronologies on shells of the landsnail *Xerophicta vestalis* found in Holocene deposits of the coastal plain. Climatically low moisture regimes with desertification and the dislocation of human settlements were correlated with sand accumulation, while pedogenesis and phases of human activity were attributed to moister periods (GVIRTZMAN *et al.* 2000).

The erosion and cliff retreat of the Sharon escarpment between Givat Olga and Tel Aviv was studied by PERATH and ALMAGOR (2000). The biggest quantity of aeolianites is removed by slumps and rockslides, depending on the wave climate and the erosion of the talus in front of the escarpment. Erosion through water run-off has only a minor influence on the cliff retreat (PERATH and ALMAGOR 2000).

GVIRTZMAN and WIEDER (2001) propose a soil-sequence stratigraphy for the coastal plain of Israel for the last 53 ka BP. They investigated the sediments with magnetic susceptibility, particle-size distribution, clay mineralogy and soil micromorpholoy and recognized thirteen proxy-climatic events, which were linked to dry and wet episodes. The climatic changes were compared to oxygen and carbon records of cave speleothems and to lake level records of Lake Lisan, which became since the Younger Dryas the Dead Sea. GVIRTZMAN and WIEDER (2001) distinguished a mature hamra soil developed between 40 – 12.5 ka BP, and loess which was deposited during the Younger Dryas from 12.5 – 11.5 ka BP and developed during the wet episode from 11.5 – 10.5 ka BP into a Grumosol; after a dry period of sand accumulation from 10.5 – 10 ka BP a further red hamra soil developed under moister and warmer conditions from 10 – 7.5 ka BP which is correlated to the sapropel S1 formation and other small-scale changes of

wet and dry conditions followed in the Late Holocene from 7.5 ka BP to present, which were recorded in the coastal sediments (GVIRTZMAN and WIEDER 2001).

SIVAN *et al.* (2001) ascertain changes in sea-level along the Israeli coast during the Holocene. They compare archaeological observations with a numerical model and found both in general agreement. The numerical model forecasted a sea-level of –13.5 ± 2 m, while the archaeological evidence assigns the sea-level to –16.5 ± 1 m for the time at 8 ka BP. At 7 ka BP the sea-level had risen to –7 ± 1 m; the numerical model and the archaeological data are congruent. At 6 ka BP the sea-level was lower than –3 to –4.5 m and stayed lower than at present until 2 – 3 ka BP. SIVAN *et al.* (2001) also conclude that the average vertical tectonic movement of the Carmel coast is less than 0.2 mm/a over the last 8 ka BP.

NEBER (2002) studied the sedimentological properties of Quaternary deposits in the coastal plain and distinguishes between several facies of aeolianites, sands, soils and beach rock. He classified the aeolianites in three groups (A, B, C) for the Carmel coastal plain and in three groups (D, E, F) for the Sharon coastal plain. The deposits are correlated with the help of physical datings in terms of climate change and the MISs and are intensively discussed in this study (cp. Chapter 7.2.4).

Physical dating

A number of physical dating studies were carried out over the years for sites in the coastal plains of Israel, concerning archaeological sites, aeolianite and palaeosol successions and also offshore deposits. The chronologies were established with ^{14}C, ESR and luminescence methods (MERCIER and VALLADAS 1994, PORAT and WINTLE 1994, MERCIER *et al.* 1995, RITTE *et al.* 1997, PORAT *et al.* 1996, 1999, GVIRTZMAN *et al.* 1998, 2000, VALLADAS *et al.* 1998, RONEN *et al.* 1999, ENGELMANN *et al.* 2001, FRECHEN *et al.* 2001, 2002, in press, NEBER 2002, PORAT and RONEN 2002, PORAT *et al.* 2003).

The earlier studies in the coastal plain showed the need for a robust dating framework, which might be provided with luminescence chronology. Part of this dating framework could meanwhile be established by the above mentioned studies.

CHAPTER 2

Aims and objectives of the study

The chapter states the aims and objectives of this Ph.D. study and puts it into the wider context of palaeoclimate studies.

2.1 Aims and objectives

An important part in correlating terrestrial records with palaeoclimates is to unfold the precise sedimentation history, like the "Pleistocene sand migration and cyclical desertification in the Mediterranean coastal plains of Israel". Such correlations are often only possible through climate proxies and physical dating methods. To uncover the chronological history of the terrestrial sedimentation records from the aeolianites and palaeosols in the Carmel and Sharon coastal plains in Israel luminescence dating was applied. The method was chosen, as luminescence dating is one of the Quaternary dating methods that covers at least the time span of the last glacial-interglacial cycle and is ideally applied to aeolian transported sediments, giving the age of deposition.

- The luminescence dating study should provide a reliable geochronological framework for the aeolianites and palaeosols at key sections in the Carmel and Sharon coastal plains.
- The comparison of data from this study with chronological results of other studies should enable the correlation of the deposits of the Carmel and Sharon coastal plain with each other. It was also hoped to provide an improved chronology for artefacts found in some of the intercalated palaeosols.
- The dating study was also intended to answer questions as to whether the development of aeolianites and palaeosols could be linked with Eastern Mediterranean climate changes during glacial-interglacial times.
- Apart from the more applied nature of this research, it was attempted on a smaller scale to compare classical multiple aliquot dating techniques (IR-OSL, TL) with the new radiofluorescence (IR-RF) dating technique.

Small scale palaeoclimate studies as from the GIF-project "Pleistocene sand migration and cyclical desertification in the Mediterranean coastal plains of Israel" add to the information about local climate responses e.g. during the last glacial-interglacial cycle. Palaeoenvironmental and palaeoclimate reconstructions play a crucial role in the determination of causal factors for climate change and for future climate prediction models.

CHAPTER 3

Study area

The chapter introduces in the Levant the established terms "kurkar" and "hamra" and defines them as used in this study. Further, the different facies of the Israeli dune sands – varying qualities of the aeolianites and varying pedology – are distinguished as observed in the field. Finally, the site descriptions follow with location, general composition, detailed field descriptions and interpretation of the geological units and location of the luminescence sampling points.

3.1 Nomenclature and special geology of the fossil sand dunes in the northern coastal plain

3.1.1 Nomenclature

Already in LÖWENGART (1928) the term "kurkar" is used and characterised as a local term to describe carbonaceous cemented sandstone. This sandstone is identified by LÖWENGART (1928, p. 504) clearly as lithified dune sand: "Der Kurkar läßt sich deutlich als verkrusteter Dünensand erkennen." LÖWENGART (1928) remarked that the lithification is often so weak, that from the drillings undertaken in the coastal plain, not kurkar, but loose sand would be conveyed. Following from there, the term "kurkar" defines an aeolian deposited sand lithified through a carbonaceous cement. This definition is congruent with the most common use of the term "aeolianite" (BROOKE 2001) and distinguishes from other forms of fossil dune sands (e.g. BELL 1991).

The term "kurkar ridge" is used in Israel and the Levant to describe the geological features exposed along the coast with a ridge-like morphology, taking the name from the main lithological units (aeolianites) and the morphological form. Although there are several palaeosols or loose sands intercalated between the aeolianites, the whole form is referred to as a "kurkar ridge".

This is not always clear in the literature, as the term "kurkar" is sometimes used with the meaning of "kurkar ridge". To avoid confusion, in this study the term "kurkar" is used as a synonym of "aeolianite", strictly as a lithological term. "Kurkar ridge" is used to refer to the morphological form, including different lithological units.

The soils in connection with the kurkar ridges in the coastal plain are often referred to as "hamra". The term "hamra" or "chamra" comes from the Arabic and means "red" (GOODALL and AL-BELUSHI 1998). Usually the term is used for red palaeosols or red sand (LÖWENGART 1928, GOODALL and AL-BELUSHI 1998). In the Israeli soil taxonomy "hamra" is defined as red and brown Mediterranean soils (DAN and KOYUMDJISKI 1979) (cp. Chapter 3.1.2). In this thesis the term "hamra" is used with that definition.

3.1.2 Special geology of aeolianites and their soils

Aeolianites

During the field campaigns it was possible to distinguish macroscopically between different types of aeolianites. The exposed rocks display variations in colour, grades of lithification through the recrystallisation of shell fragments, as well as different parent material.

In general the aeolianites along the motorway and for example in the quarry by Habonim show a stronger lithification (Figure 3.2.1b) than aeolianites further South, e.g. the "Dor Kurkar" in the Netanya cliff section (Table 3.2.3a). This general trend is likely to have evolved in connection with a general increased precipitation towards the North. The actual dune structures, like horizontal bedding from accretion deposits and foreset laminae of cross bedding from enchroachment deposits, can in most cases still be observed. Partly lithified dune sands display small layers (1 – 2 cm) of carbonaceously lithified sand, alternating with loose unconsolidated thicker layers (3 – 4 cm) of sand. Such aeolianite was observed in the quarry near the Hadera Power Station or at the seashore near the Hadera Power Station (Tables 3.2.2b, d). In aeolianites with a medium lithification the sand inbetween the stronger carbonaceous layers is also consolidated, but stronger and less lithified layers alternate and are especially distinguishable when physical erosion exposes the stronger lithified parts from the softer lithified layers. Higher degrees of carbonate lithification led to overall more massive aeolianites where the lithification still traces the original structures. The alternating layers are generally conjunct, showing on erosional surfaces small holes of 1 – 2 cm diameter of less lithification. Where the lithification is complete aeolianite is suited as building stone. Historic and modern examples can be observed at the Roman Caesarea and many modern houses in Haifa. The colour of the aeolianites in the Sharon and Carmel coastal plain varies from yellowish-ochre aeolianites (e.g. Habonim East wall, Table 3.2.1a) over light grey (e.g. Habonim North wall, Figure 3.2.1b) to whitish aeolianites (e.g. "Tel Aviv Kurkar", Table 3.2.3a). Some of these colour changes might be caused by varying contributions of haematite (α-Fe_2O_3) and goethite (α-FeOOH) minerals deriving from ferric compounds as weathering products from different contingents and distributions of heavy mineral assemblages in the parent material of the aeolianites. Other colour changes have their origins in a different bulk parent material. While most aeolianites observed in the coastal plains consist of quartz sand in a carbonaceous cement, some

have a higher proportion of biogenic clasts, shell fragments and ooids (e.g. "Tel Aviv Kurkar", Table 3.2.3a), which also leads to a brighter, whitish colour.
Sedimentological studies by NEBER (2002) on the aeolianites in the Carmel and Sharon coastal plains allowed distinction between various types of aeolianites and their detailed properties. However, for the dating study here it is sufficient to distinguish the sampled aeolianites through their macroscopical qualities observed during sampling in the field.

Soils

Associated with the aeolianites in the coastal plain of Israel are typical red Mediterranean soils, which shape the image of the landscape very distinctively because of their dark to foxy red colour. The red colour is obtained from haematite and partly maghaemite (γ-Fe_2O_3) minerals, which are in the subsoil, while the rich in humus topsoil contains mostly goethite with yellow-brownish colours (ANDRUSCHKEWITCH 1996). On the surface of aeolianites along the coastal plains the remains of past red soils can be observed, filling solution pockets or building thin layers on top, indicating past Mediterranean red soils which are eroded today. These red soils in Israel are known as hamras (luvisols). Apart from hamras various other soils like grumusols (vertisols), nazaz (pseudogley), regosols and arenosols are known in connection with the aeolianites and sandy sediments of the coastal plain (DAN and YAALON 1971, ANDRUSCHKEWITCH 1996, TSATSKIN and RONEN 1999).
Hamras in the sense of the Israeli soil classification correlate to rhodoxeralfs and haploxeralfs (DAN and KOYUMDJISKI 1979) of the U.S. soil taxonomy, used by the U.S. Department of Agriculture (USDA 1975). Xeralfs develop in climates where there is a xeric or an aridic to xeric moisture regime. During the summer months the soils are dry, while in winter the moisture progresses into the soil to deeper layers. On a non irrigated soil small grains, grapes and olives can be grown (USDA 1975). Hamras are red (rhodoxeralfs) or red-brown non-calcic sandy clay loams (haploxeralfs) (DAN and YAALON 1971, DAN and KOYUMDJISKI 1979). They are also known as chromic luvisols (FITZPATRICK 1980).
Geographically associated with xeralfs are xererts, the latter belonging to the order of vertisols (USDA 1975). In Israel soils classified as Grumusols are equivalent to chromoxererts and pelloxererts of the U.S. taxonomy (DAN and KOYUMDJISKI 1979, USDA 1975). Xererts in general appear in Mediterranean type climates. The alternation

of cool wet winters with warm dry summers causes these soils to crack. The cracks are open for up to three month after the summer solstice in most years and closed for up to three months after the winter solstice (USDA 1975). Chromoxererts are distinguished by a subhorizon in the upper 30 cm which shows a colour (other than black, grey or white). They are typical for gentle to strong dipping slopes with good water run-off conditions. Chromoxererts are typically mottled soils. Because of illuvial (argillic) horizons observed in certain depths in chromoxererts it is assumed that with time old soils generate a fine enough texture for vertisols to develop in them (USDA 1975). Pelloxererts are characterised by their grey to black colour of all subhorizons in the upper 30 cm. They appear on plane surfaces. Xerets allow closed grass or savanna vegetation (USDA 1975).

Nazazs in the Israeli classification correspond to albaqualfs of the U.S. taxonomy (DAN and KOYUMDJISKI 1979, USDA 1975). Basically they are pseudogleys (DAN and YAALON 1971). Ground water reaches seasonally into the illuvial horizon which is in direct contact with a bleached zone above it, with usually no transition zone in between. The bleached horizon can dry out during the summer months and an oscillating water table is essential for their genesis (USDA 1975). The soils are also known as planosols (FITZPATRICK 1980).

Weak soils observed in connection with the kurkar ridges and dune fields in the coastal plain emerge on lithified and loose dune sands as parent material and are sometimes refered to as "Café au Lait", because of their colour. "Café au Lait" seems to concern a regosol of the Israeli classification, xerorthents and torriorthents of the U.S. taxonomy (DAN and KOYUMDJISKI 1979, USDA 1979). Xerorthents and torriorthents belong to the order of entisols. These are young soils that have not developed a B horizon and cannot be contained in any other order. Xerorthents are at a distance from ground water of at least 1.5 m, they are of moderate depth and are apparently not silica-cemented. Their surface horizon (epipedon) is usually ochric (contains less than 1 % organic matter, is light in colour and thin) and lies on sediment or soft rock (USDA 1975). Torriorthents are saline regosols with a thin vegetation cover of xerophytic scrubs and ephemeral grasses and forbs (DAN and KOYUMDJISKI 1979, USDA 1975).

ANDRUSCHKEWITCH (1996) distinguished between regosols developing on aeolianites and arenosols developing on loose sand as parent material. Arenosols are young soils with an upper mineral Ah horizon of 10 to 15 cm thickness. The horizon is slightly stained through organic matter (FITZPATRICK 1980). The B horizon is coarse sandy in

texture, has a uniform colour and may be more than 2 m thick (FITZPATRICK 1980). In the FAO classification regosols comprise arenosols (KUNTZE *et al.* 1994).

Typical catenas for the central coastal plain were described for the area of Netanya by DAN *et al.* (1968) and ANDRUSCHKEWITCH (1996). On hilltops arenosols, regosols and hamras (luvisols) can be found, which can have stagnic properties. On upper slopes occur cambisols, regosols and arenosols, without stagnic properties going over to middle slopes with mainly arenosols and regosols. At the lower slopes the stagnic properties increase again, leading to the development of luvisols (hamras) and planosols (pseudogleys) (ANDRUSCHKEWITCH 1996). Depressions are characterized by planosols (pseudogleys) and also by vertisols (ANDRUSCHKEWITCH 1996, DAN *et al.* 1968). ANDRUSCHKEWITCH (1996) characterises also two chronosequences for loose dune sand and aeolianite parent materials on highlands in the coastal plain. The sequence on loose dune sand begins with the development of an arenosol. It comes to decalcification, accumulation of fines and rubification. The development continues in a luvisol, with lessivation, accumulation of fines and rubification taking place and precipitation of secondary carbonates. The luvisol is followed by a stagnic luvisol in which redoximorphic features start to develop. The end of the sequence results in a pseudogley (planosol) where the redoximorphic features are well accomplished and partly secondary carbonates are precipitated (ANDRUSCHKEWITCH 1996). The chronosequence on aeolianites as parent material develops from regosols to cambisols. In the beginning decalcification takes place, followed by accumulation of fines and rubification. The sequence develops in luvisols (hamras) with shifting of clay, the beginning of redoximorphic features and the precipitation of secondary carbonates. The sequence on aeolianites is also complete with the development of pseudogleys (planosols) with well accomplished redoximorphic features and partly precipitated secondary carbonates (ANDRUSCHKEWITCH 1996).

3.2 Site descriptions

The description of the sample sites follows from North to South. Where possible East-West transects over the kurkar ridges were sampled. This was the case at Habonim and at the vicinity of Power Station Quarry near the town of Hadera (Figures 3.2.1a, 3.2.2a). For criteria of sampling compare Chapter 5.1.1.

3.2.1 Habonim Quarry, Dor-Habonim Nature Reserve Middle Ridge, Dor-Habonim Nature Reserve Coast

Habonim Quarry

The site of Habonim is situated west of the Tel Aviv – Haifa motorway and north of the town of Habonim (Figures 1.1a and 3.2.1a). The quarry lies west of the so-called « third ridge » (by counting from West to East) which is exposed along the coast.

Figure 3.2.1a : Map of the site locations of Habonim Quarry (HAB), Dor-Habonim Nature Reserve Middle Ridge (HDM) and Dor-Habonim Nature Reserve Coast (HDC). Latitudes and longitudes according to New Israel Grid. Redrawn from the Topographic Map 1 : 100,000 (SURVEY OF ISRAEL 1999a).

The sampled section was situated in the East wall of the quarry, consisting of a palaeosol complex in a shallow interdune depression (TSATSKIN and RONEN 1999,

RONEN *et al.* 1999) sandwiched between aeolianites. Samples (HAB) were taken from there and also from the North wall (Figure 3.2.1 b). Successive quarrying activities exposed a West – East transect, where different aeolianites and a soil could be sampled (HABII) (cp. NEBER 2002) (Figure 3.2.1c).
The pedocomplex of the section sampled in the East wall of the quarry (Figure 3.2.1b) was also investigated in detail with micromorphological and other techniques by TSATSKIN and RONEN (1999). A detailed description of the section is given in Table 3.2.1a.

Sample HAB4 was taken about 1.25 m further North from the sampled section in the pedocomplex. Sample HAB14 was taken 4 m further North. A further sample (HAB15) was taken about 50 m south of the sampled pedocomplex from the location where a flake from flint was found. The flint was embedded in the upper part of the gleyed horizon above the vertisol, 15 cm underneath its upper contact to the above sand horizon. The horizons on this location are all less thick, as the pedocomplex wedges out to the South. Sample HAB15 is from the same horizon as sample HAB12.
Sample HAB16 was taken from the lower aeolianite of the East wall about 25 m North of the above decribed pedocomplex. The horizon is described as sand of yellowish colour with irregular carbonaceous concretions and many shell fragments.

Dor-Habonim Nature Reserve Middle Ridge

A sample (HDM) was taken from the aeolianite at the relative surface of the so-called « second ridge », just west of the railway-crossing and north of the access road to the Dor-Habonim Nature Reserve.

Dor-Habonim Nature Reserve Coast

Another kurkar sample (HDC) was taken from an aeolianite in the Dor-Habonim Nature Reserve west of the car park. The Dor-Habonim Nature Reserve is situated about 3 km south from Habonim to Tel Dor (N 32° 37', E 34° 55') (NRA 2004).

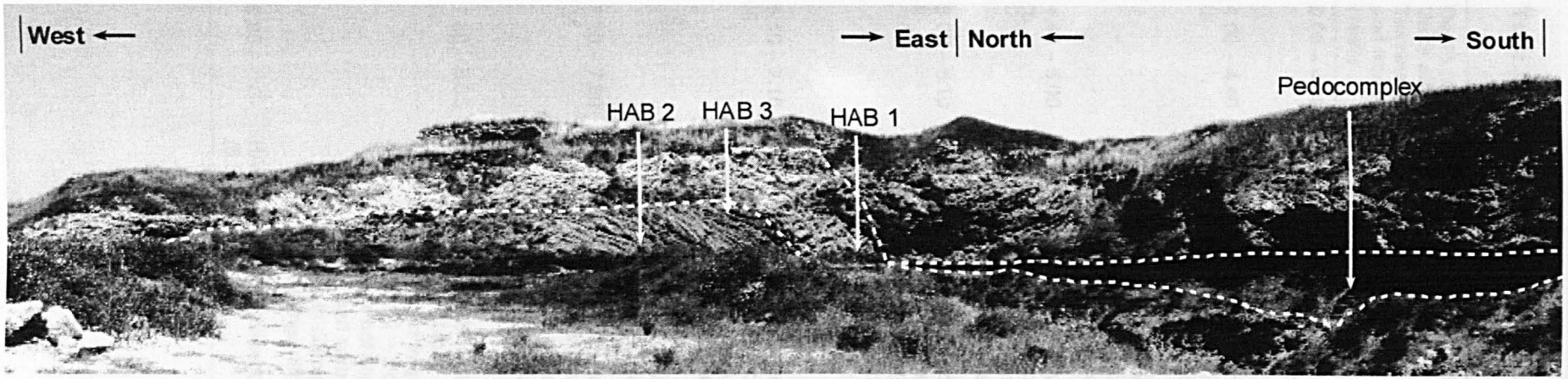

Figure 3.2.1b : Photo of Habonim Quarry, East and North wall with sample locations for samples HAB.

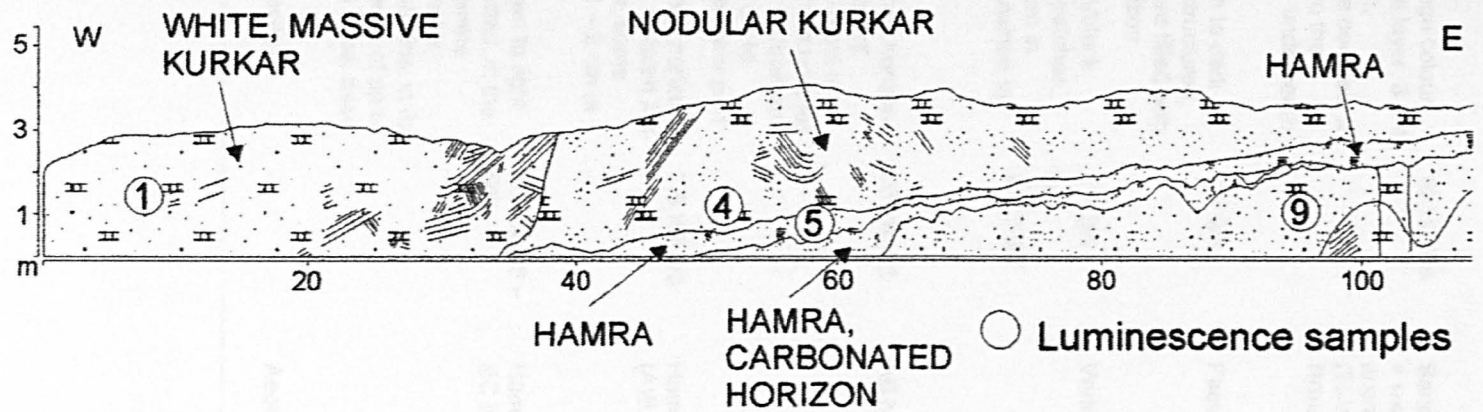

Figure 3.2.1c : Sketch of Habonim quarry, West-East profile after successive quarrying, with sample locations for samples HABII (changed after NEBER 2002).

Table 3.2.1a : Detailed description of the section in the East wall of Habonim quarry and location of the luminescence samples.

Depth (m), Units after TSATSKIN and RONEN (1999)	Sample name and depth (m)	Field description (16/05/1997)	Munsell notation dry (TSATSKIN and RONEN 1999)	Interpretation (cp. TSATSKIN and RONEN 1999)
0.00 – 4.00	HAB14 (3.60 m)	Lower part : Sand, strongly lithified through carbonaceous cement, massive		Aeolianite (kurkar)
4.00 – 4.40 Ia	HAB13 (4.20 m)	Sand, clayey, ochre/orange colour, not cemented, Carbonate layer, 3 – 4 cm thick, at about 4.10 m, discontinuous, Carbonate nodules, 2 – 4 cm in diameter, above the carbonate layer isolated, underneath the layer frequently	10 YR 7/8	Sand, clayey, « weak accretionary soil » (TSATSKIN and RONEN 1999)
4.40 – 5.00 Ib	HAB12 (4.50 m)	Clay/Silt, sandy, greenish to dark brown colour, prismatic structured, manganese cutans, fissure filled with sand from the above horizon	5 Y 5/1	Pseudogley
5.00 – 6.10 II	HAB11 (5.25 m) HAB10 (5.55 m) HAB9 (6.05)	Sand, clayey, dark brown/black colour, slickensides, Mn-patches, Carbonate nodules, 0.5 cm in diameter, Continuous transition to horizon below	5 Y 3/1 to 2.5 Y 3/2	Vertisol
6.10 – 7.10 III	HAB8 (6.25) HAB7 (6.75)	Sand, clayey, less clay than horizon above, brown colour, frequent carbonate nodules with 0.5 cm in diameter, isolated carbonate nodules with diameters 2 – 4 cm, Carbonate incrustations with 5 – 10 cm in diameter frequently in the lower part	10 YR 4/6	AB horizon
7.10 – 7.80 IV	HAB6 (7.45) HAB5 (7.75)	Sand, clayey, less clay than horizon above, red/brown colour, isolated Mn-patches 1 cm in diameter, some carbonate nodules with 1 – 2 cm in diameter	7.5 YR 4/6	Hamra (A)B horizon
7.80 – 8.85 IV	---	Sand, middle to fine, brown to light orange colour, not cemented, in the upper part frequent carbonate nodules 1 – 2 cm in diameter, nodules not conjunct, crotovina, in the lower part carbonate geodes of up to 10 cm in diameter on the base, base increasingly lithified	10 YR 6/6 – 6/8	Hamra BC horizon
8.85 -	HAB4 (8.90)	Sand, lithified by carbonaceous cement		Aeolianite (kurkar)

3.2.2 Hadera Power Station Quarry, South of Power Station, Seashore Power Station

Hadera Power Station Quarry

The sampled section (samples PSQ) lies in a quarry about 4 km north from the centre of Hadera, East of the motorway and the main road number 4 between Haifa and Tel Aviv, just Northeast of Nahal Hadera Junction of the main road number 4. The quarry is situated in the so-called "third ridge" surrounded by the modern dune field at Hadera, from which the Power Station of Hadera is visible towards the Northwest (Figure 3.2.2a).

Figure 3.2.2a : Map of the site locations of Hadera Power Station Quarry (PSQ), South of Power Station (SOP) and Seashore Power Station (SPS). Latitudes and longitudes according to New Israel Grid. Redrawn from the Topographic Map 1 : 100,000 (SURVEY OF ISRAEL 1999b).

The main section in the quarry exposes a strongly lithified aeolianite (kurkar), followed towards the top by a pedocomplex of nearly 3 metres thickness, which is itself covered by recent dune sand. For a detailed description see table below (Table 3.2.2a).

Table 3.2.2a : Detailed description of the section in the East wall of Hadera Power Station quarry and luminescence sample locations.

Depth (m)	Sample name and depth (m)	Field description (23.05.1997)	Interpretation
0.00 – 0.30	---	Sand, light ochre colour, boundary to lower horizon blurred	Sand
0.30 – 1.30	PSQ8 (0.50) PSQ7 (1.00)	Sand, clayey, dark black-grey to brown-grey colour, prismatic structure, Mn-coatings 2 mm in diameter, in the lower part from about 1.10 – 1.30 m foxy red stains 1 cm in diameter, also lighter marks (redox-reaction), gradually transition to lower horizon	Vertisol
1.30 – 1.90	PSQ6 (1.55)	Sand, clayey, dark red-brown colour, prismatic structure, Mn-coatings	Hamra/Vertisol
1.90 – 2.80	PSQ5 (2.10) PSQ4 (2.50)	Sand, foxy red colour, at 2.30 m crotovina with 10 cm diameter of burrow filled with light orange-brown material, adjacent material darker red, between 2.30 – 2.80 m colour of sediment more light orange	Hamra
2.80 – 3.20	PSQ3 (3.05)	Sand, light orange and dark brown colour, mottled, isolated Mn-coatings, carbonaceous (HCl positive)	Hamra
3.20 -	---	Sand, strongly lithified through carbonaceous cement, massive	Aeolianite (kurkar)

From the section on the East wall the pedocomplex wedges out in a few metres towards the North, where older parts of the stratigraphical sequence are exposed. Sample PSQ 1 was taken about 20 m North from the upper part of the aeolianite on one of the North walls of the quarry (Figure 3.2.2a). This aeolianite can be laterally traced to be stratigraphically placed below the described pedocomplex. Sample PSQ 2 was taken from loose dune sand deposited on top of the soil complex. The sand had an ochre colour and mostly fine sand altered with thin layers of coarse sand showing some stratification. The thin coarser layers also contained shell fragments. The loose dune sand was about 1.40 m thick and sample PSQ 2 was taken at 0.75 m below the surface. Only a few metres Northwestwest on a further East wall of the quarry, sample PSQ 12 was taken from a lower part of the lower aeolianite one metre above the quarry surface (Figure 3.2.2b). In another North wall and a West wall of the quarry a weak sandy soil is displayed in lenses between aeolianites (Figure 3.2.2b). The weak soil was sampled in a section in the West wall (Table 3.2.2b).

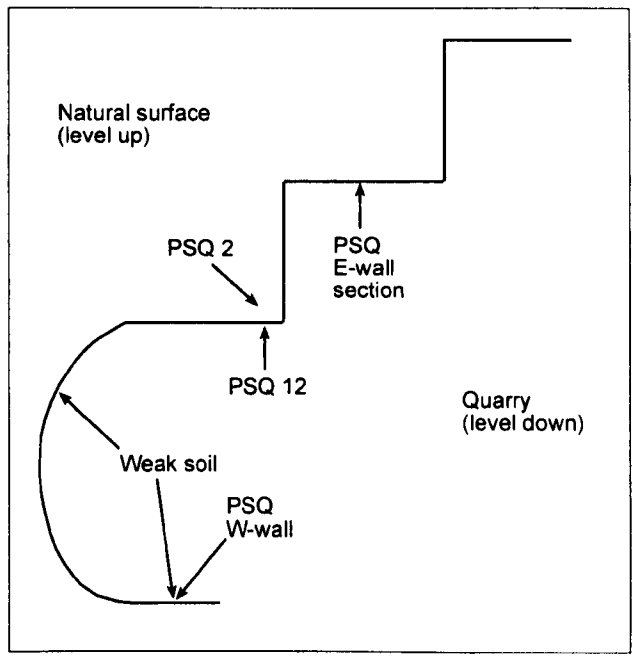

Figure 3.2.2b: Sketch of the situation of the quarry walls of Hadera Power Station quarry (without scale).

Table 3.2.2b : Detailed description of the section in the West wall of Hadera Power Station quarry and luminescence sample locations.

Depth (m)	Sample name and depth (m)	Field description (23.05.1997)	Interpretation
0.00 – 0.45	PSQ9 (0.25)	Sand, partially and irregularly lithified by a carbonaceous cement	Aeolianite (kurkar)
0.45 – 0.65	PSQ10 (0.55)	Sand, middle to fine, ochre colour, with remains of shells of landmolluscs,	Weak soil (Regosol/Arenosol?)
0.65 –	PSQ11 (0.85)	Sand, partially and irregularly lithified by a carbonaceous cement	Aeolianite (kurkar)

South of Power Station

A further section was sampled in the so-called "second ridge" south of Power Station (samples SOP). The section is reached by driving on the motorway in a southbound direction and turning west straight from the motorway into a small track just after passing Junction Qesarya and a couple of trees and bushes. Following the track in a general western direction leads to the sampled section, which lies about halfway between the motorway and the coast in the vicinity of a modern dune field (Figure 3.2.2 a). The section is described in detail below (Table 3.2.2c).

Table 3.2.2c : Detailed description of the section south of Power Station and luminescence sample locations.

Depth (m)	Sample name and depth (m)	Field description (24.05.1997)	Interpretation
0.00 – 0.50	SOP1 (0.25)	Sand, foxy red, carbonate concretions, gradual transition to lower horizon	Hamra (C horizon)
0.50 – 2.50	SOP2 (2.40)	Sand, lithified through carbonaceous cement, single foreset patterns of former dune in cementation preserved, strongly dipping, frequent rizolithes	Aeolianite (kurkar)
2.50 – 3.10	SOP3 (2.60)	Sand, light ochre	Weak soil (Regosol/Arenosol?)
3.10 – 3.40	---	Sand, lithified through carbonaceous cement, wedging out to both sides (lens)	Aeolianite (kurkar)
3.40 – 4.30	SOP4 (3.60)	Sand, light ochre	Weak soil (Regosol/Arenosol?)
4.30 –	SOP5 (5.30)	Sand, lithified through carbonaceous cement, single foreset patterns of former dune in cementation well preserved, slightly dipping	Aeolianite (kurkar)

Seashore Power Station

Further towards the West a gently southward dipping kurkar – hamra sequence could be sampled (samples SPS) directly on the seashore South of the wharf of the Hadera Power Station (Figure 3.2.2a). Through the southward inclination and the erosion along the beach only parts of the sequence are exposed at a time in one place. The sequence was sampled in two locations (Table 3.2.2d and 3.2.2e), which are about 150 – 200 m apart from each other. The slight inclination of the sediments causes the oldest exposure to be in the North. Also from between the two onshore sections a beach rock (SPS 3) was sampled from just underneath the waterline.

Table 3.2.2d : Detailed description of the northern part of the section at the seashore south of the wharf of Power Station and luminescence sample locations.

Depth (m)	Sample name and depth (m)	Field description (26/05/1997)	Interpretation
0.00 – 0.60	SPS1 (0.50) from hamra soil in filling	Sand, partly lithified by carbonaceous cement, single foreset patterns of former dune well preserved, flat bedded, clear contact to the underlying horizon, Solution pocket reaching into the horizon below. Filling: Sand, dark foxy red, mixed with aeolianite material, reaching into the horizon below	Aeolianite (kurkar)with solution pockets filled with pedosediment of an eroded hamra soil
0.60 –	SPS2 (1.60)	Sand, partly lithified by carbonaceous cement, single foreset patterns of former dune well preserved, gentle dipping	Aeolianite (kurkar)

Table 3.2.2e : Detailed description of the southern part of the section at the seashore south of the wharf of Power Station and luminescence sample locations.

Depth (m)	Sample name and depth (m)	Field description (26/05/1997)	Interpretation
0.00 – 0.70	SPS8 (0.25) SPS7 (0.60)	Sand, light ochre colour, embedded at 0.15 m band of *Glycymeris spec.*, at 0.30 m band of shell fragments, at 0.50 m band of well rounded pumice up to 5 cm in diameter	Sand
0.70 -	SPS6 (0.80) SPS5 (1.20)	Sand, middle to fine, foxy red, from 0.70 – 1.00 m weak prismatic structure, contact to the upper horizon very clear (unconformity)	Hamra

3.2.3 Netanya South Cliff, Wadi Netanya South

Netanya South Cliff

Along the coastal cliff in the Sharon coastal plain various lithological units are well exposed through coastal erosion (cp. PERATH and ALMAGOR 2000). For dating, the lithological units were sampled from the coastal cliff south of the town Netanya South (Figure 3.2.3a).

Figure 3.2.3a : Map of the site locations of Netanya South Cliff (NET) and Wadi Netanya South (WNS). Latitudes and longitudes are given according to New Israel Grid. Redrawn from the Topographic Map 1 : 100,000 (SURVEY OF ISRAEL 1999b).

The section is composed of a lower aeolianite on which a well established regosol could develop. Towards the top follow several metres of aeolianite, intercalated by lenses of weak sandy soils (regosols, arenosols). Above the aeolianite follows a thick hamra, on top of which a whitish aeolianite (hardpan) was deposited, which builds the solid surface of the cliff top. Sand with a weak developed soil follows. A detailed description and sample positions are given in Table (3.2.3a).

Table 3.2.3a : Detailed description of the southern section at the coastal cliff near Netanya South and luminescence sample locations.

Depth (m)	Sample name and depth (m)	Field description (20/03/98)	Stratigraphical names after GVIRTZMAN *et al.* (1998)	Interpretation
0.00 – 0.30	NET 24 (0.10)	Sand, middle to fine, dark ochre colour, shells of landmolluscs	---	Regosol/Arenosol
0.30 – 1.00	NET 23 (0.90)	Sand, middle to fine, ochre colour, shell fragments of landmolluscs, crotovina 2 – 3 cm diameter	Ta'arukha Sands	Regosol/Arenosol
1.00 – 4.40	NET 22 (1.30) NET 21 (4.10)	Bioclasts (shell fragments), middle and coarse, and Sand, middle, pale ochre-whitish colour, massive, strongly lithified with carbonaceous cement, on erosional surface bedding structure explicit, single layers more lithified and weathered out than rest	Tel Aviv Kurkar	Aeolianite (kurkar), Hardpan
4.40 – 7.00	NET 20 (4.60) NET 19 (6.60)	Sand, some fines, red – brown colour, in the upper 1 m slightly mottled through redox-patches, former root traces filled with ochre coloured sand, also frequently shells of landsnails in the upper 1 m, below 1 m more sparse, the upper 70 cm very strongly consolidated	Netanya Hamra	Hamra
7.00 – 21.50	NET 18 (7.80) NET 17 (11.00) NET 16 (16.00) NET 15 (20.50)	Sand, fine, ochre colour, loose, alternating with calcified layers, layering 1 – 4 cm thick, partly the original dune structure (foresets) recognisable, in the lower part isolated shell fragments of 1 – 2 cm length, in the upper part no bioclasts	Dor Kurkar	Aeolianite (kurkar)
21.50 – 21.90	NET 14 (21.60)	Sand, fine, ochre colour, isolated fine shell fragments, soil in upper part stronger developed		Regosol/Arenosol
21.90 – 22.70	NET 13 (22.30)	Sand, fine, ochre colour, parts lithified by carbonaceous cement alternating with layers of loose sand	Dor Kurkar	Aeolianite (kurkar)

Table 3.2.3a : Continued.

Depth (m)	Sample name and depth (m)	Field description (20/03/98)	Stratigraphical names after GVIRTZMAN *et al.* (1998)	Interpretation
22.70 – 23.40	NET 12 (22.80)	Sand, fine, ochre colour, isolated fine shell fragments, soil in upper part stronger developed, shells of landmolluscs		Regosol/Arenosol
23.40 – 25.10	NET 11 (24.30)	Sand, fine, ochre – yellowish colour, with bioclasts but articulately less than in kurkar below, sand layer 2 – 4 cm thick, alternating in the lower 50 cm with thin calcified layers of 0.5 cm thickness, clasts in calcified layer quartz sand up to 1 mm diameter plus frequent coarser shell fragments of ~ 2 mm diameter, in the upper part strongly calcified, rizolithes and carbonate concretions, dune structure destroyed	Dor Kurkar	Aeolianite (kurkar)
25.10 – 26.40	NET 10 (25.70)	Sand, fine, ochre colour, but lighter than the regosol/arenosol below, gradual transition from underlying horizon in the lower 50 cm, isolated fine shell fragments, soil in upper 70 cm stronger developed (darker colour), isolated shells of landmolluscs (*in situ*?)		Regosol/Arenosol
26.40 – 32.40	NET 9 (27.10) NET 8 (29.40) NET 7 (31.80)	Sand, fine, ochre – yellowish colour, with bioclasts but articulately less than in kurkar below, sand layer 2 – 4 cm thick, alternating with thin calcified layers of 0.5 cm thickness, clasts in calcified layer quartz sand up to 1 mm diameter plus frequent coarser shell fragments of ~ 2 mm diameter	Dor Kurkar	Aeolianite (kurkar)
32.40 – 33.70	NET 4 (32.70) NET 3 (33.30)	Sand, fine, ochre colour, with remains of shells of landmolluscs, small carbonate concretions in the lower centimetres, in the upper part darker (soil stronger developed)	Nasholim Sands	Regosol
33.70 – base of section at 37.50	NET 2 (34.30) NET 1 (35.10)	Sand, middle to fine, with frequent bioclasts, light ochre to ochre colour, lithified through carbonaceous cement, former dune structure (foresets) still visible, frequent rizolithes in the upper part, stronger lithified structures accentuated through erosion of the rest	Ramat Gan Kurkar	Aeolianite (kurkar)

About 100 m towards the North from the above described section (Table 3.2.3a) the lowermost aeolianite is exposed with a greater thickness. Two further samples were taken (Table 3.2.3b).

Table 3.2.3b : Detailed description of the northern section at the coastal cliff near Netanya South and luminescence sample locations.

Depth (m)	Sample name and depth (m)	Field description (20/03/98)	Stratigraphical names after GVIRTZMAN *et al.* (1998)	Interpretation
0.00 – base of section at 18.00	NET 6 (12.00) NET 5 (14.50)	Sand, middle to fine, with frequent bioclasts, light ochre to ochre colour, lithified through carbonaceous cement, former dune structure (foresets) still visible, frequent rizolithes in the upper part, stronger lithified structures accentuated through erosion of the rest	Ramat Gan Kurkar	Aeolianite (kurkar)

Wadi Netanya South

In an open domestic sewage gully which carved into the recent local dune field and Holocene sediments between a southern part of the town Netanya and the beach (Figure 3.2.3a), several Holocene sections with alternating sand and soil horizons were described and sampled. The gully was arbitrarily named "Wadi Netanya South" (samples WNS). For dating two sections which comprise the main horizons were chosen (Tables 3.2.3c, d).

The first section (Table 3.2.3c) comprises a weak soil (regosol/arenosol) at the bottom of the wadi, followed by a hamra. On top of the hamra follows a carbonaceous horizon, which is followed by a regosol and sand.

Table 3.2.3c: Detailed description of the eastern section at Wadi Netanya South and luminescence sample locations.

Depth (m)	Sample name and depth (m)	Field description (25/05/1997)	Interpretation
0.00 – 1.50	---	Sand, light ochre colour, clear boundary to horizon below	Sand
1.50 – 1.90	---	Sand, middle to fine, dark brown colour, shells of land snails, some shells of molluscs, isolated in bands, gradual transition to horizon below	Regosol (A horizon)
1.90 – 2.50	---	Sand, middle to fine, light ochre colour	Regosol (C horizon)
2.50 – 2.75	---	Carbonate concretions, several centimetres in diameter, irregular forms, partly conjoined, inbetween loose ochre coloured sand	Caliche?
2.75 – 3.50	WNS20 (3.00)	Sand, ochre colour, frequent and dense carbonaceous concretions 1 cm in diameter, lower contact clear but undulating	Caliche?
3.50 – 4.30	WNS19 (3.65) WNS18 (4.25)	Sand, middle to fine, foxy red colour, from 3.50 – 3.70 m somewhat darker, browner in colour, below orange foxy red colour, gradual transition to horizon below	Hamra (B/C horizon)
4.30 – 5.25	WNS17 (4.75)	Sand, middle to fine, ochre to orange colour, lighter than lower part of horizon above, gradual transition to horizon below	Hamra (C horizon)
5.25 – basement of wadi at 7.25	WNS16 (6.00)	Sand, Café-coloured	Weak soil (Regosol/Arenosol)

At the second section the carbonaceous horizon is exposed on the basis, on top of which follows a regosol, at least one further soil and the recent sand (Table 3.2.3d).

Table 3.2.3d: Detailed description of the western section at Wadi Netanya South and luminescence sample locations.

Depth (m)	Sample name and depth (m)	Field description (25/05/1997)	Interpretation
0.00 – 1.00	WNS15 (0.70)	Sand, ochre colour, stratified, clear boundary to lower horizon, boundary marked by shells of landsnails	Sand, recent
1.00 – 1.40	WNS14 (1.15)	Sand, middle to fine, dark grey brown colour, humous, no clay in fingertest, frequent shells of landsnails diffuse contributed, relative clear boundary to horizon below	Soil (A horizon) Regosol
1.40 – 1.90	WNS13 (1.60)	Sand, middle to fine, middle brown and towards the lower part red brown colour, many well preserved shells of landsnails	Soil (B horizon?)
1.90 – 2.40	WNS12 (2.00)	Sand, middle to fine, dark grey brown colour, humous, dispersed shells of land snails, contact to upper horizon sharp and marked by band of land snail shells, gradual transition to horizon below	Regosol (A horizon)
2.40 – 2.70	WNS11 (2.55)	Sand, middle to fine, brownish colour, gradual transition to horizon below	Regosol (A/C horizon)
2.70 – 3.60	WNS10 (3.20)	Sand, middle to fine, ochre colour, dispersed shells of land snails, sharp lower contact	Regosol (C horizon)
3.60 – base of section at 4.00	---	Carbonaceous concretions, several centimetre in diameter, dense, inbetween sand, ochre colour	Caliche?

CHAPTER 4

Aspects of luminescence dating

The chapter gives an introduction into the physical phenomenon of luminescence. The solid state physical process is described with the help of a general band model, the principle of how luminescence can be used for dating is explained, a brief historical note outlines some developments of luminescence dating, there is a section on natural dosimeters and the signals emitted by potassium-rich feldspars, also other aspects like natural optical bleaching, artificial irradiation, thermal pre-treatment, anomalous fading, equipment, dose characteristics, equivalent dose determination, normalisation and dosimetry concerning sediment dating are described.

4.1 Physical phenomenon of luminescence and dating principle

4.1.1 Physical phenomenon of luminescence and its description through band models

Luminescence is a spontaneous emission caused by an energy supply, where the absorbed excitation energy, from the material capable of luminescence (luminophor), is not added to the radiant heat of the body, but will be saved as potential energy. This is in contrast to thermal radiation, where the absorbed energy adds to the lattice oscillations of the atoms (phonons). The stored potential energy can be emitted as a whole or partially. Therefore luminescence does not follow Planck's thermal radiation law, but is an additional emission, which appears as a surplus over the thermal radiation of a certain body at a certain temperature (RIEHL 1971).

The term luminescence needs to be distinguished from other light emissions that are not thermal radiation, but are not luminescence either. This concerns for example the Čerenkov-effect or some light-scatter-effects. Luminescence is in contrast to such effects caused by the excited states in the atom or the molecule. Because the lifetime of such states is at least 10^{-8} s, it is only possible that the luminescence emission follows after 10^{-8} s of the excitement. With for example the Čerenkov-effect or light-scatter-effects no such delay exists and the time between cause (irradiation) and effect (radiation) is in the order of the period of oscillation of a wavelength of light, that is about 10^{-14} s (RIEHL 1971).

Some of the kinetics of luminescence processes can be explained with the help of band models. In band models processes are described at the atomic level, which are collective processes concerning wider areas than single atoms or molecules. The energy states of bound (valence) and free (conduction) electrons are arranged on top of each other in hierarchical levels (bands). The valence band describes the energy state of electrons that are bound to their own or neighbouring nuclei, while the energetically higher conduction band describes energy states of free electrons, which would theoretically be available for conduction. The absence of an electron in the valence band is described as a hole. The valence band in insulators and semi-conductors is, in contrast to metals, separated from the conduction band by a so-called band gap. The band gap is a forbidden zone in a perfect crystal where no energy states are allowed. At room temperature most electrons in insulators are situated in the valence band and are not

available at the conduction band. The luminophors used for dating, like feldspars and quartz minerals, are non-metals and belong generally to the group of insulators. But through the embedding of foreign atoms, impurities in the crystal lattice generate metastable energy states in the band gap, which can cause a luminescence emission (cp. RIEHL 1971).

Electrons in atoms and molecules of sediments are excited through ionising radiation of the natural radioisotopes. In principle three modes of light emitting transitions can be described (RIEHL 1971):

1) The simplest case is the excitation of an electron into a higher energetic state without abandoning the atom or molecule (monomolecular reaction). As the electron is not free, no photoconductivity takes place. Stimulation and emission take place in the same atom or molecule (excitation centre). The return of the electron into its basic state, accompanied by photon emission, is a monomolecular reaction of the so-called first order.

2) In other cases electrons are removed from their original place. Free electrons can move in the electric field (conduction) and their recombination into the basic state is a reaction of the so-called second order. Free electrons in the conduction band are able to recombine with holes emitting light.

3) Electrons can also be captured by a trapping centre (trap). Traps and luminescence centres are usually crystal impurities, which show in comparison with the rest of the lattice a positive excess charge and therefore attract electrons. Traps and luminescence centres are energetically placed between the valence and conduction band creating energy terms in the band gap. Traps are energetically near the conduction band and luminescence centres are usually near to the valence band. If a free electron is captured by a trap its recombination with a luminescence centre can be delayed. Electrons can stay in traps (metastable state) for geological time scales. In order to remove an electron from the local potential minimum of a trap for example optical or thermal energy supply is necessary. The electron can recombine with a luminescence centre, emitting light. Usually the recombination takes place over the conduction band (Figure 4.1.1). This process is used for luminescence dating (cp. Chapter 4.1.2).

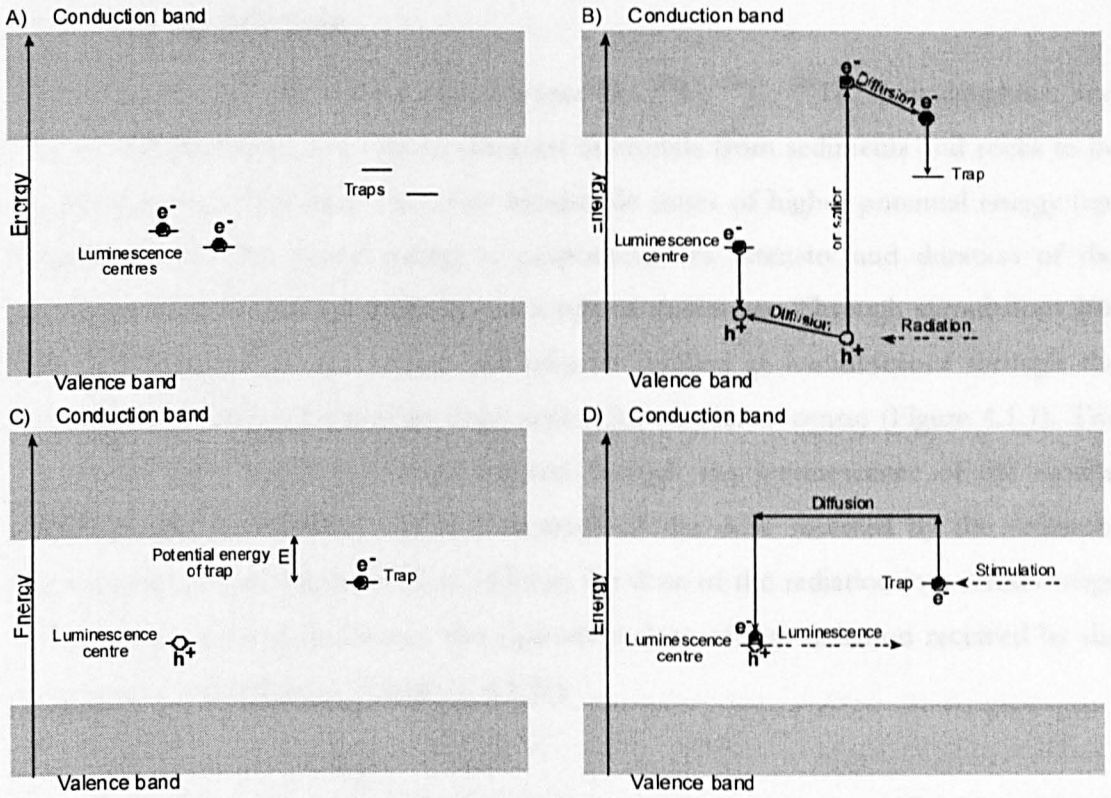

Figure 4.1.1: Schematical band model for the luminescence process (changed after Aitken 1985). A) Basic state. B) Excitation. C) Storage. D) Stimulation and luminescence. For explanation please see text below.

A) The crystal is in a basic state. The energetically higher traps are empty; the energetically lower luminescence centres are filled with electrons.

B) Ionising radiation removes electrons from the valence band and lifts them through the supplied energy into the conduction band, where they are distributed through diffusion, until captured by an electron trap. The ionisation also causes a positive hole in the valence band, which moves also through diffusion, until it meets an energetically low enough luminescence centre, which is filled with an electron. The electron recombines with the hole and empties with this the luminescence centre.

C) The electron remains in the trap. The crystal stores with this the energy, which was supplied by the ionising radiation.

D) Through stimulation (supply for example of optical or thermal energy) the electron in the trap is able to overcome the potential energy difference and is lifted into the conduction band. From there the electron can recombine with an energetically lower free luminescence centre. At the recombination the surplus of energy of the electron is emitted as light quanta (luminescence).

4.1.2 Dating principle

Irradiation through the natural radioisotopes like ^{235}U, ^{238}U, ^{232}Th, their daughters and ^{40}K, as well as cosmic rays, causes electrons in crystals from sediments and rocks to be transferred from their basic state into metastable states of higher potential energy (cp. Chapter 4.1.1). The stored energy is proportional to intensity and duration of the irradiation and the mineral grain acts as a natural dosimeter. Through stimulations like light and temperature this energy can later be recalled as luminescence through the recombination of electrons from traps with a luminescence centre (Figure 4.1.1). The amount of light quanta (photons) emitted through the luminescence of the natural dosimeter can be detected and is a measure of the dose received by the sediment through the natural radiation. If, in addition the dose of the radiation in a certain range of time, the dose rate, is known, the equivalent dose of that radiation received by the sample can be determined (Equation 4.1.2a).

$$Equivalent\ dose = \int_{0}^{Age} Dose\ rate_{(t)} * dt \qquad \text{(Equation 4.1.2a)}$$

If the dose rate over the time of integration is constant, the age of a sample can be obtained from the quotient of equivalent dose and dose rate (Equation 4.1.2b).

$$Age(a) = \frac{Equivalent\ dose(Gy)}{Dose\ rate(Gy/a)} \qquad \text{(Equation 4.1.2b)}$$

One essential requirement for dating the time of sedimentation is that the atoms and molecules at this time are in their basic state; no potential energy should be stored in the matter from previous depositions, which would later be measured as additional luminescence on top of the luminescence from the energy absorbed since sedimentation (cp. Chapter 4.5).

4.2 Historical aspects of luminescence dating

Historical observations of luminescence and related phenomena are collected in AITKEN (1998). Bioluminescence of fireflies and bacteria and phosphorescence of the sea are mentioned in Chinese literature 3000 years ago, Aristotle (384-322 BC) and Pliny the Younger (61-112) describe luminescent rubies, Catherine of Aragon (1485-1536) possessed a ring with a stone which shined in the dark, Vincenzo Cascariolo, Bologna, recorded the phosphorescence of baryt ($BaSO_4$) in 1603 and Sir Robert Boyle reported in 1663 to the Royal Society about (phototransfered) thermoluminescence of a diamond which he had beforehand warmed with his body (AITKEN 1985, HARVEY 1957 in AITKEN 1998).

Before sensitive light detectors (photomultipliers) were developed in the middle of the last century luminescence was used to distinguish between different minerals taking advantage of the fact that a mineral after stimulation always emits light of a characteristic wavelength (AITKEN 1985, 1998). DANIELS *et al.* (1953) suggested thermoluminescence for geological and archaeological age determination. First dating studies using thermoluminescence were carried out in archaeology on ceramics (e.g. GRÖGLER *et al.* 1960, KENNEDY and KNOPF 1960, AITKEN *et al.* 1964, ICHIKAWA 1965, MAZESS and ZIMMERMAN 1966, RALPH and HAN 1966, AITKEN *et al.* 1968, MEJDAHL 1969 in AITKEN 1985). Subsequently thermoluminescence dating was applied to other materials like burnt flintstone or volcanic materials (GÖKSU *et al.* 1974, WINTLE 1973, GUÉRIN and VALLADAS 1980 cp. AITKEN 1985).

4.2.1 Dating sediments with thermoluminescence and optical stimulated luminescence

Relative dating of Ukrainian sediments with thermoluminescence (TL) was reported by MOROZOV (1968 in AITKEN 1998). WINTLE and HUNTLEY (1979) dated sediments from a deep-sea core with thermoluminescence and showed that the resetting of the luminescence signal is carried out through bleaching of sunlight. The reason for the resetting of the luminescence signal was not clear in earlier studies and was thought to be related to grinding (cp. WINTLE and HUNTLEY 1979, WINTLE 1997). WINTLE (1981) was the first to date terrestrial western European sediments using thermoluminescence. SINGHVI *et al.* (1982) applied the method on dune sands. Via thermoluminescence dating it was subsequently possible to work out successions of sediment stratigraphies

(e.g. WINTLE and BRUNNACKER 1982, WINTLE and HUNTLEY 1982, JUVIGNÉ and WINTLE 1988, WINTLE and PACKMAN 1988, WINTLE 1987, 1990, WINTLE *et al.* 1984, ZÖLLER *et al.* 1988, 1994, FRECHEN 1991, 1992, 1994, a.o.).

Parallel to the development of thermoluminescence dating the application of optical stimulated luminescence was investigated as a dating tool for sediments (HUNTLEY *et al.* 1985, SMITH *et al.* 1986, GODFREY-SMITH *et al.* 1988, RHODES 1988). HÜTT *et al.* (1988) and HÜTT and JAEK (1989) were the first to date potassium-rich feldspars with infrared optical stimulated luminescence (IR-OSL). Reviews on optical dating are given in AITKEN (1992, 1994). Combined luminescence dating of IR-OSL and TL as the routine approach to date sediments was predominantly carried out on loess and loess-like sediments (e.g. AKTAS and FRECHEN 1991, FRECHEN *et al.* 1995, FRECHEN and PREUSSER 1996, FRECHEN *et al.* 1997, FRECHEN and DODONOV (1998), FRECHEN 1999a, 1999b, FRECHEN and YAMSKIKH 1999, FRECHEN *et al.* 1999, ENGELMANN 1997, ENGELMANN *et al.* 1999, ZANDER 2000, ZANDER *et al.* 2000, FRECHEN *et al.* 2001).

While during the 1990s dating studies on fine grain samples were carried out mostly on multiple tens of subsamples (multiple aliquots methods) (cp. WINTLE 1997), first single aliquot methods (up to a few subsamples) for coarse grain samples were introduced. Additive protocols for coarse grain feldspars were developed by DULLER (1991, 1994) and GALLOWAY (1996). MURRAY *et al.* (1997) introduced a single aliquot additive dose protocol for quartz. Regenerative approaches for feldspar (DULLER 1991) and for feldspar and quartz (SARA, single aliquot regenerative and added dose protocol) (MEJDAHL and BØTTER-JENSEN 1994) were developed. Though single aliquot approaches promised certain advantages over multiple aliquot methods, various cycles of irradiation, preheat and stimulation of the natural dosimeter have complicated implementation of the approaches for dating. Different correction methods were developed to overcome the loss of stable signal during repeated preheat cycles and changes in sensitivity towards radioactive radiation (DULLER 1994, MEJDAHL and BØTTER-JENSEN 1994, GALLOWAY 1996). The by then developed single aliquot approaches were better suited for young (Holocene) samples than older (Last Glacial) ones (cp. DULLER 1995). Further regenerative protocols for quartz were developed by MURRAY and ROBERTS (1998) (SAR, single aliquot regenerative dose protocol) and FOLZ and MERCIER (1999a, 1999b) (single aliquot regenerative dose protocol involving bracketing regenerative doses). In the SAR protocol by MURRAY and ROBERTS (1998)

changes in sensitivity were overcome using the OSL response to a given test dose and the 110° C thermoluminescence peak was used for corrections of sensitivity changes. MURRAY and WINTLE (2000) improved the SAR protocol of MURRAY and ROBERTS (1998) and the simplified SAR protocol of MURRAY and MEJDAHL (1999) by correcting the natural and regenerative OSL signals for changes in sensitivity using only the OSL response to a certain test dose (10 – 20 % of the equivalent dose) and testing that the applied test dose would always result in the same population of trapped charge carriers. MURRAY and WINTLE (2000) concluded that the improved SAR protocol is sufficiently robust for the dating of quartz. WALLINGA *et al.* (2000a) applied the SAR protocol to potassium-rich feldspar grains, but encountered the underestimation of the equivalent dose caused by an increased trapping probability of electrons through thermal treatment (WALLINGA *et al.* 2000a, b).

4.2.2 Radiofluorescence dating

As the term "radioluminescence (RL)" used in the early studies concerning infrared-radiofluorescence (IR-RF) dating of potassium-rich feldspars also comprises other physical phenomena (e.g. radiophosphorescence) than only the actually observed fluorescence, the dating technique was re-named to the physically more precise expression "radiofluorescence (RF)" (ERFURT and KRBETSCHEK 2003a).

Since the dose-dependency of single emission peaks in radiofluorescence spectra was recognised, radiofluorescence was suggested for sediment dating (TRAUTMANN *et al.* 1998, TRAUTMANN 1999). At first visible radiofluorescence (VIS-RF) was suggested as a dating tool for plagioclases (TRAUTMANN *et al.* 1998), but recognition that VIS-RF signals of only some plagioclases are sensitive to bleaching through sunlight made this dating possibility less attractive for routine dating applications. The following detection and investigation of radiofluorescence spectra reaching into infrared wavelengths, proved the infrared emission at 865 nm suitable for dating potassium-rich feldspars (TRAUTMANN 1999, TRAUTMANN *et al.* 1999). A new localised transition model was suggested to explain the observed radiofluorescence properties (TRAUTMANN 1999, TRAUTMANN *et al.* 1999, TRAUTMANN *et al.* 2000a, TRAUTMANN 2000). KRBETSCHEK *et al.* (2000) explored methodological aspects of radiofluorescence sediment dating and radiofluorescence properties of single feldspar grains were investigated by TRAUTMANN *et al.* (2000b). Radiofluorescence spectra for quartz and other materials were summarised by KRBETSCHEK and TRAUTMANN (2000). To facilitate further investigations of

radiofluorescence measurements and to ease routine dating applications with the method, a fully automated multi-spectral reading system was developed (ERFURT *et al.* 2003). Additionally to that ERFURT and KRBETSCHEK (2003a) introduced an infrared radiofluorescence single-aliquot regenerative dose (IRSAR) protocol for dating coarse grain potassium-rich feldspars and studied physical aspects of the infrared radiofluorescence of potassium-rich feldspar as well as methodological aspects to sediment dating (ERFURT and KRBETSCHEK 2003b).

4.3 Natural dosimeters

Luminescence properties are seen in a wide range of minerals like for example gypsum, zircon and others (e.g. RIEHL 1971, WINTLE 1973, WINTLE 1997, KRBETSCHEK *et al.* 1997), yet a natural dosimeter requires to be able to store the received radiation energy over geological times without loss or change, to be bleached through natural means like sunlight or heat, to emit under stimulation a sufficiently intense (bright enough) signal and to be adequately available in the geological context. Since feldspar and quartz generally meet these requirements and are the two most abundant minerals in the Earth's crust they are commonly used for luminescence sediment dating. Both minerals are geologically most versatile and appear in many different geological systems showing a number of varieties and modifications. Differences in luminescence properties of feldspar resulting from numerous modifications in chemical composition and structure are investigated in detailed studies (cp. KRBETSCHEK *et al.* 1997, DULLER 1997). The chemical and structural diversity of quartz regarding varying luminescence dating properties is less intensively explored than that of feldspars (cp. KRBETSCHEK *et al.* 1997). This might be because the systematic of the most common feldspars is usually depicted in a ternary system between the endmembers orthoclase (microcline, sanidine), albite and anorthite, emphasising the chemically discontinuous composition of alkali-feldspars and the chemically continuous composition of plagioclases. In contrary to feldspars the systematic of the quartz group is only partly depicted in a P-T-phase diagram, emphasising structural rather than chemical differences. In luminescence dating with feldspars, usually potassium-rich feldspars are separated using differences in the density of chemically distinguishable feldspars (cp. Chapter 5.3.1). The potassium-rich feldspar dosimeter in this case still comprises differences in chemical composition around the endmember of the ternary system, potassium-feldspar, and its chemical substitutes, but also structural differences deriving from high temperature and high

pressure phases (e.g. sanidine, microcline). In dating applications with quartz no structural or chemical differences are made as such. In the table below luminescence dating properties of potassium-rich feldspars and bulk quartz are compared (Table 4.3). The dosimeter used in this study is potassium-rich feldspar (cp. Chapter 5.2).

Table 4.3: Luminescence dating properties of potassium-rich feldspars and bulk quartz.

Properties	Potassium-rich feldspars	Bulk quartz
Saturation dose	High saturation dose (ca. 3000 Gy) (depending on environmental dose rate)	Lower saturation dose (smaller age range depending on environmental dose rate)
Bleaching	Optical response to sunlight is quick, but not as quick as quartz	Quick optical response to sunlight
Optical signal intensity	Bright	Less bright
Possible draw backs	Anomalous fading, Optical absorption	Sensitivity changes, Thermal quenching, Mixed signal from bulk quartz mixture

4.4 Signals from potassium-rich feldspars

More than half of the natural occurring minerals are luminescent and most emit under stimulation signals at various wavelength. As in this study potassium-rich feldspars are used as natural dosimeters their luminescence emissions are introduced below. Colours for certain wavelengths are given after the German Industry Norm (Deutsche Industrie Norm, DIN 5031) (cp. KRBETSCHEK *et al.* 1997, AITKEN 1998). The detection range of photomultiplier and optical filters used in front of the photomultiplier detection window determine the spectral detection range used for dating (cp. Chapter 5.3.3).

4.4.1 Thermoluminescence signals from potassium-rich feldspars

In the review by KRBETSCHEK *et al.* (1997) strong thermoluminescence emission bands of potassium-rich feldspars are observed at 275-290 nm, 325-330 nm, around 400 nm (390-415 nm) and at 730 nm. Medium strong radiation is detected around the above mentioned wavelengths but also towards lower energies at 450 nm, 485 nm, 510 nm, 525 nm, 565 nm, 600 nm, 660 nm, 700 nm and 765 nm. This ties in with the main thermoluminescence emission bands of feldspars at 275-290 nm and at 320-340 nm both in the far and near ultra-violet spectral region, respectively, and at 390-440 nm in the violet to blue. The near ultra-violet and the violet to blue emission bands form the main components in spectra from potassium-rich feldspars (KRBETSCHEK *et al.* 1997).

4.4.2 Optical stimulated luminescence signals from potassium-rich feldspars

Strong optical emission of potassium-rich feldspars is observed around 385 nm and at 400-410 nm. Medium strong optical emission of potassium-rich feldspars is detected at 320-340 nm, at 440 nm (370-440 nm), at 530 nm, at 550-560 nm and above 700 nm (cp. KRBETSCHEK *et al.* 1997). Main optical emission bands of feldspars in general are observed at 320-340 nm in the ultra-violet, at 390-440 nm in the violet to blue and at 550-570 nm in the yellow-green. The violet to blue emission, in particular around 400-410 nm (violet), builds the main component in infrared stimulated spectra from potassium-rich feldspars and is commonly used for IR-OSL dating (KRBETSCHEK *et al.* 1997).

4.4.3 Radiofluorescence signals from potassium-rich feldspars

Several materials emit radiofluorescence signals (cp. KRBETSCHEK and TRAUTMANN 2000). Radiofluorescence emission of feldspars is observed at 410 nm in the violet, at 560 nm in the yellow-green, at 730 nm in the red and at 865 nm in the infrared. The radiofluorescence emission of potassium-rich feldspars in the infrared (865 nm) can be used for dating (e.g. TRAUTMANN 1999, TRAUTMANN *et al.* 1999, TRAUTMANN *et al.* 2000b).

4.5 Natural optical bleaching

Resetting the luminescence signal back to zero through sunlight, prior to deposition of the natural dosimeter, is a prerequisite of luminescence sediment dating. Any inherited luminescence signal from radiation during a previous deposition would result in age overestimation. Therefore the optical bleaching response towards (sun)light of the dosimeter used for dating is tested. The knowledge of the response times of the different luminescence signals (cp. Chapter 4.4) towards light allows to evaluate if a dosimeter from a certain sediment is likely to be bleached under consideration of the geological deposition process.

Sunlight which is received on the Earth's surface generally varies (i) in intensity because of cloud cover variability and (ii) in spectrum with the changing orientation of the Earth towards the Sun over a day or for example the seasons of a year, for a certain geographical location. Natural sunlight is therefore difficult to employ as an

experimental parameter, which is required to stay constant in its intensity and spectrum, to observe and compare its effects on bleaching of the luminescence signals over time (seconds, minutes, hours, geological time scales). For this reason most bleaching tests are carried out with artificial sunlight using laboratory lamps which emit a spectrum close to natural sunlight. The results of bleaching tests are assumed to be comparable to a similar bleaching behaviour of the sediment during the time of deposition.

Experiments on fine grain loess show that natural sunlight bleaches both the IR-OSL and TL signal faster than artificial laboratory light from an OSRAM Ultra Vitalux 300 W UV lamp (e.g. ENGELMANN 1997). Similar results as for fine grain aeolian sediments were observed for signals of coarse grain potassium feldspars of the Israeli aeolianites (FRECHEN *et al.* 2002). Distinctions in the bleaching behaviour towards natural and artificial sunlight result from differences in the emitted light spectra and in particularly most likely of the ultraviolet portion. The bleaching tests in this study were carried out with a HÖNLE SOL2 bleaching unit (cp. Chapter 5.3.4). The unit simulates a spectrum close to that of natural sunlight (BARAY and ZÖLLER 1994, WINTLE 1997) and is several times more intense (HÖNLE product information (6.5 times), WINTLE 1997).

Monitoring IR-OSL and TL signal intensities after various bleaching times showed in a number of studies that the IR-OSL signal is bleached faster than the TL signal and while the IR-OSL signal can be reduced to zero the TL signal decreases only to a finite value. These properties of optical and thermal stimulated luminescence towards their bleaching behaviour were first observed in optical studies with green (514 nm) laser light by GODFREY-SMITH *et al.* (1988). From the experiments it could be concluded that the optical signals derive from recombining electrons from highly light sensitive traps and that their contribution towards the TL signal is negligible, while the main part of the TL signal originates from recombining electrons of significantly less light sensitive traps (GODFREY-SMITH *et al.* 1988).

Optical bleaching times for infrared radiofluorescence (IR-RF) signals with direct sunlight lie within one to three hours (TRAUTMANN 1999) and within minutes with artificial laboratory light (KRBETSCHEK *et al.* 2000). Overall the optical bleaching times of IR-RF signals are somewhat longer than of IR-OSL signals and lie between bleaching times of IR-OSL and TL signals.

4.6 Artificial irradiation

Artificial irradiation of the dosimeter used for dating is performed in the laboratory to simulate the accumulation of dose in the natural environment (cp. Chapter 4.1.2, Chapter 4.13). In this way response of the dosimeter to a well defined dose can be studied (cp. Chapter 4.10). In luminescence dating practice usually two types of irradiation, either gamma or beta (electron) irradiation, are used. The laboratory irradiation with higher doses compared to natural irradiation causes a thermally unstable signal to occur which needs to be removed before measurement (cp. Chapter 4.7). Further anomalous fading is observed in some minerals, particularly feldspars, after artificial irradiation (cp. Chapter 4.8).

4.6.1 Gamma irradiation

Gamma irradiation is carried out with sources external to the luminescence readers (cp. Chapter 5.3.2). The nuclide ^{60}Co is commonly used for irradiation and sources can be accessed in scientific or medical institutions. ^{60}Co is an unstable nuclide which has a half-life of 5.3 a and decays with emission of an electron (β particle) and gamma rays with six discrete energies to the stable isotope ^{60}Ni (EUROPEAN COMMUNITIES JOINT RESEARCH CENTRE 1999).

4.6.2 Beta irradiation

Since luminescence readers were equipped with beta sources irradiation is possible in luminescence readers themselves. Beta irradiation in luminescence readers is usually carried out with ^{90}Sr sources. The nuclide ^{90}Sr is a pure beta emitter and decays with a half-life of 28.8 a to the radioactive nuclide ^{90}Y. ^{90}Y is also a pure beta emitter and decays with a half-life of 64.10 h to the stable isotope ^{90}Zr (GAMMEL 1997).

Irradiation in the radiofluorescence reader is carried out with ^{137}Cs sources (ERFURT *et al.* 2003). The nuclide ^{137}Cs decays under three beta emissions and one gamma line to the stable isotope ^{137}Ba. The half-life of ^{137}Cs is 30.2 a.

4.7 Thermal pre-treatment

Artificial irradiation causes a thermally unstable luminescence signal to occur, which needs to be separated from the luminescence signal measured for dating. The signal is considered to be unstable at a certain temperature over geological time scales due to electrons recombining from shallow traps. Shallow traps are more likely to eject electrons than deeper traps, because the degree of thermal vibration needed to eject an electron from a deep trap is higher than to eject an electron from a shallow trap. Also, the probability of an electron being ejected at a certain temperature and in a certain time is higher for shallow than for deeper traps. Therefore, the lifetime of trapped electrons depends on temperature and the depth of the trap. The so-called plateau test can be used to find the temperature region, in which the measured electrons are thermally stable and for which the probability of electrons de-trapping is negligible for geological time scales during the burial of the natural dosimeter (AITKEN 1985).

The thermally unstable component can in contrast to anomalous fading (cp. Chapter 4.8) be removed if an appropriate preheat procedure is applied. Preheats used in studies for quartz could not be applied to feldspar dating. According to LI (1991) a suitable preheat procedure for potassium-rich feldspars can be chosen over a preheat plateau by altering the preheat times at a certain preheat temperature using the ratio of the natural signal divided by the natural plus irradiated signal. A plateau indicates the same thermal stability of natural and natural plus irradiated signal and hence a sufficient preheat. Additionally, thermal decay rates for the natural and the natural plus irradiated signal can be measured (LI 1991). With the development of single aliquot methods preheat plateaus were obtained by altering the preheat temperature and keeping the preheat time constant (e.g. MURRAY *et al.* 1997, MURRAY and WINTLE 2000, WALLINGA *et al.* 2000a, b).

4.8 Anomalous fading

One phenomenon associated with luminescence feldspar dating, in opposition to quartz, is the effect of anomalous fading. The expression describes the loss of signal during storage after artificial irradiation without further stimulation. Anomalous fading was first observed by WINTLE (1973) in thermoluminescence measurements on feldspars of volcanic lava from sanidines from rhyolites near Naples, Italy, and from plagioclases

from basalts from Iceland and the Massive Central, France. SPOONER (1992, 1994) also confirmed anomalous fading in IR-OSL measurements on feldspars. The phenomenon is commonly associated with feldspars deriving geologically from mineral assemblages with a volcanic background. The fast cooling volcanic environment prohibits perfect structural ordering of the crystal lattice and the crystals precipitate in more disordered structures. Structural disorder is brought forward to be a reason for anomalous fading (HUNTLEY and LAMOTHE 2001). Physically anomalous fading is explained through electrons tunnelling through the potential energy barrier of their traps (e.g. VISOSEKAS 1985, VISOSEKAS *et al.* 1994). Anomalous fading would result in age underestimation of the dated sediment and is therefore routinely tested in IR-OSL and TL dating applications with feldspars. There have also been suggestions to overcome anomalous fading in dating applications by storing samples at elevated temperatures (cp. WINTLE 1997, HUNTLEY and LAMOTHE 2001). HUNTLEY and LAMOTHE (2001) suggested that anomalous fading in the IR-OSL dating of young feldspars (low dose region) could be overcome by establishing the rate of fading which according to the theory of quantum-mechanical tunnelling can be described by a time depending logarithm (VISOSEKAS 1985) and corrected by extrapolation. On the other hand ZINK and VISOSEKAS (1997) and VISOSEKAS and ZINK (1999) proposed to use the TL emission at 710 nm in the near infrared for dating alkali feldspars, as this emission seems not to be affected by anomalous fading. Yet this approach is only possible with photomultipliers sensitive in this wavelength area and which are able to distinguish between the 710 nm emission and thermal radiation background, hence not with standard dating equipment.

4.9 Measuring equipment

Since luminescence measurements can be effectively used for sediment dating and other dating applications the development of automated luminescence readers was introduced. Today equipment for the measurement of optical stimulated luminescence and thermoluminescence is commercially available for example from RISO NATIONAL LABORATORIES, Roskilde, Denmark, LITTLEMORE, Oxford or DAYBREAK NUCLEAR AND MEDICAL SYSTEMS, Branford, U.S.A..

BØTTER-JENSEN (1997) provided an overview of the instrumentation available from RISØ for optical stimulated luminescence and thermoluminescence measurements. For

an automated infrared and visible radiofluorescence reader Dr. Gunter Erfurt, TU Freiberg, Germany can be approached.

4.9.1 Optical luminescence and thermoluminescence readers

The luminescence readers used in this study are the RISØ models TL-DA-12, which was upgraded for OSL measurements, and TL/OSL-DA-15 at the University of Gloucestershire Geochronology Laboratories (UGGL). Both machines are equipped with a ^{90}Sr beta source (cp. Chapter 4.6.2), a photomultiplier tube, a heating unit and optical stimulation units (IR-OSL, G-OSL). A rotating sample holder carries 24 or 48 aliquots, respectively and transports one subsample at the time to the appropriate irradiation or measurement position. The systems are controlled with the RISØ software TL/OSL for Windows, Version 1.13, 1996. A more detailed description can be found in BØTTER-JENSEN (1997).

4.9.2 Radiofluorescence reader

A newly developed automated radiofluorescence reader which can detect emissions in the visible range and in the infrared was developed following the recognition that infrared radiofluorescence can be used for Late Pleistocene sediment dating (cp. Chapter 4.2.2). The instrument is described in detail by ERFURT *et al.* (2003). The radiofluorescence reader is based on a commercially available DAYBREAK 1100 TL reader system, which was re-designed and modified. The new instrument is equipped with a sample holder which can carry up to ten samples at one time and ten ^{137}Cs sources for excitation (cp. Chapter 4.6.2) which are located on a platter underneath the sample holder. Sample holder and source platter can be turned out of phase, so that no irradiation is possible. The radiofluorescence emission of the samples are guided through an optical fibre cable and filters in an automated filter wheel to the photomultiplier (HAMAMATSU GaAs:Cs type R943-02) which is housed in a thermoelectric cooler for reduction of the dark count. The photomultiplier is sensitive between 160 to 930 nm. The instrument has also a unit to stimulate optical luminescence and a bleaching unit built in. All devices can be automatically controlled with a program written for this purpose (ERFURT *et al.* 2003) (Figure 4.9.2). Photos of the new instrument can be seen on the DAYBREAK webpages (DAYBREAK NUCLEAR 2004).

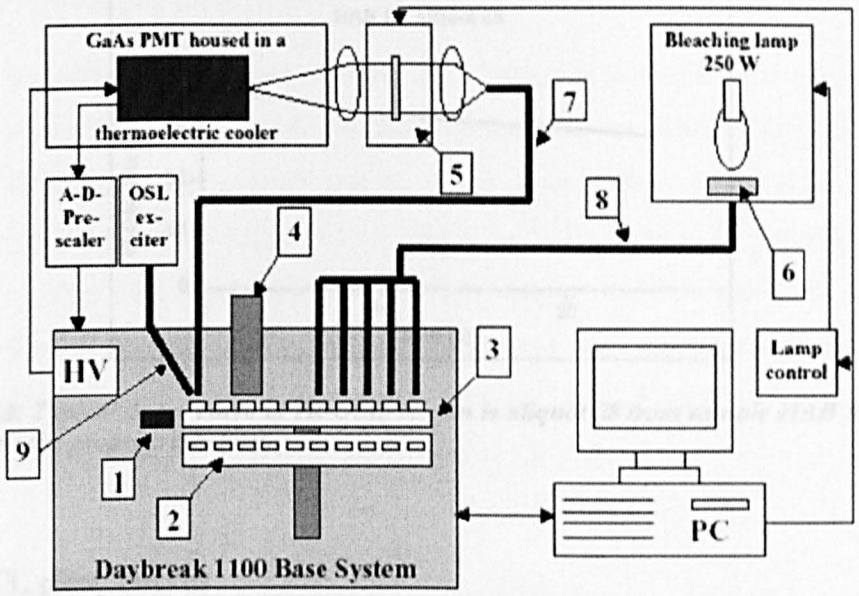

Figure 4.9.2: Schematic sketch of the radiofluorescence reader: 1-heating plate, 2-source platter, 3-sample platter, 4-inlet tube, 5-automated filter wheel, 6-IR absorbing filter, 7-signal optical fibre cable, 8-bleaching optical fibre cable, 9- optical fibre cable for optical excitation (from ERFURT et al. 2003).

4.10 Luminescence and radiofluorescence signals

Decay curves, glow curves and radiofluorescence signals vary with the amount of the luminescence/radiofluorescence flux and are characteristic in their shape for the individual emissions due to differences in trapping and recombination. Typical curves for the different stimulation methods are shown below.

4.10.1 IR-OSL decay curves

For the decay curve of the IR-OSL the luminescence intensity is plotted as a function of the IR stimulation time in seconds (Figure 4.10.1). The signal intensity decreases with the increase of the IR stimulation time and is the sum of the emissions in the chosen wavelengths band of the spectral detection window (cp. Chapter 5.3.3).

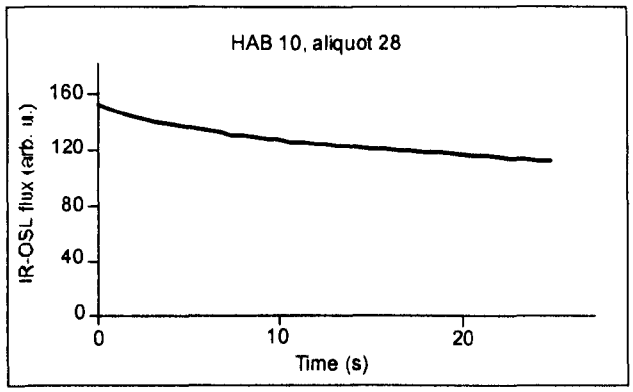

Figure 4.10.1: Typical decay curve of IR-OSL; shown is aliquot 28 from sample HAB 10 (redrawn from the program Analyst).

4.10.2 TL glow curves

For the TL glow curve the luminescence intensity is plotted as a function of the stimulation temperature (Figure 4.10.2). The signal increases and decreases forming a peak at higher temperatures and is similar to the IR-OSL dose characteristic the sum of the emissions in the chosen wavelengths band of the detection window (cp. Chapter 5.3.3).

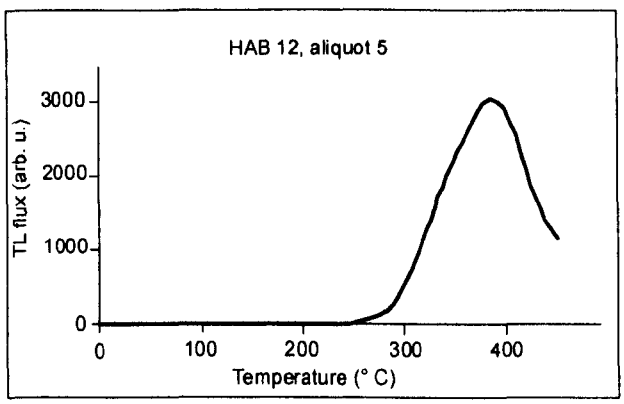

Figure 4.10.2: Typical glow curve of TL; shown is aliquot 5 from sample HAB 12 (redrawn from the program Analyst).

4.10.3 IR-RF characteristics

For the IR-RF characteristic the radiofluorescence intensity is plotted as a function of the stimulation dose (or radioactive stimulation time) (thick solid line in Figure 4.11.2). The signal decreases with an increase in dose. The signal measured is the sum of the bandwidth of the detection window (cp. Chapter 5.4.2).

4.11 Equivalent dose determination

Different mathematical approaches using the change in intensity of the luminescence response to varying doses were developed to determine the time of deposition. In IR-OSL and TL dating, this corresponds to a zero dose value or zero dose value plus residual, respectively, (cp. Chapter 4.11.1). While in IR-RF dating, the equivalent dose of deposition corresponds to a maximum dose (cp. Chapter 4.11.2). Below, the approaches used in this study are described. For other equivalent dose determination methods see for example WINTLE (1997), FOLZ and MERCIER (1999), KRBETSCHEK *et al.* (2000), MURRAY and WINTLE (2000) and WALLINGA *et al.* (2000a).

4.11.1 IR-OSL and TL multiple aliquot additive dose (MAAD) protocol

The response of the dosimeter to well defined laboratory doses is compared with the natural dose received by the dosimeter since deposition (e.g. AITKEN 1985, 1998, WINTLE 1997). In the multiple aliquot additive dose (MAAD) protocol successive increasing doses of laboratory irradiation are given on top of the natural dose. For each dose step a group of aliquots is used. One group of aliquots is not irradiated to obtain the natural dose. The measured luminescence intensities for the single groups are plotted as a function of irradiation dose or time (Figure 4.11.1a). The luminescence intensities for the natural dose with no irradiation plot above zero on the x-axis. The luminescence intensities for the irradiated dose groups should increase with higher irradiation doses. A mathematical function is iterated to fit the dose groups. To obtain the equivalent dose (or equivalent time of artificial irradiation) the fitted function is extrapolated backwards to the point of intersection with the x-axis. The absolute value between point of intersection and zero dose of the laboratory irradiation is the equivalent dose (or equivalent time of artificial irradiation). For practical purposes usually the equivalent time of the artificial irradiation is estimated in minutes (min) and the equivalent dose in Gray (Gy) is calculated with the dose rate in Gray per minute (Gy/min) of the source used for irradiation. The above described method ("additive dose", cp. WINTLE 1997) of equivalent dose determination is valuable for IR-OSL measurements as it requires a zero dose level at the time of deposition.

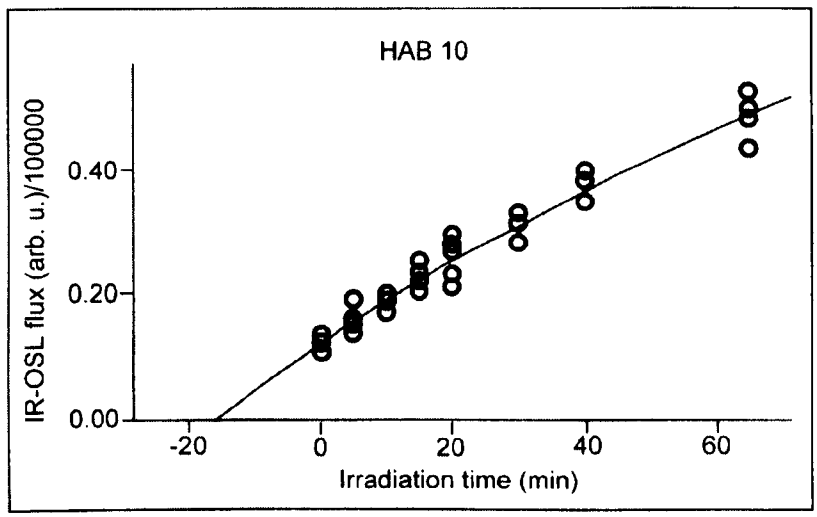

Figure 4.11.1a: IR-OSL dating with the MAAD protocol. Shown is the laboratory response for sample HAB 10 (redrawn from the program Analyst).

For TL measurements, where the luminescence signal can only be bleached to a residual level (cp. Chapter 4.5), the fitted mathematical function is extrapolated backwards to the point of intersection with that residual level (Figure 4.11.1b). The y-value of the residual signal is obtained by measuring an additional group of aliquots whose natural signal is removed through bleaching ("total bleach – additive dose", cp. WINTLE 1997).

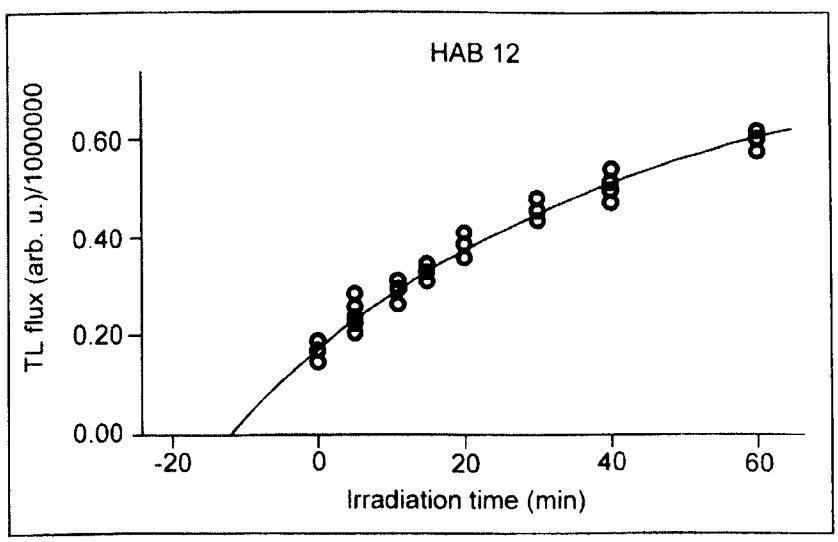

Figure4.11.1b: TL dating with the MAAD protocol. The unbleachable residual is already subtracted from the measured luminescence intensities by the program and the x-axis corresponds to the y-value of the residual signal. The laboratory response from sample HAB 12 is shown (redrawn from the program Analyst).

4.11.2 IR-RF single aliquot regenerative (IRSAR) dose protocol

The dose response curve matches the IR-RF characteristic (cp. Chapter 4.10.3). This is explained through the direct radiative transition of electrons during radioactive excitation from the conduction band into the 1.43 eV trap, which causes the IR-RF emission in potassium feldspars (e.g. TRAUTMANN 1999, ERFURT and KRBETSCHEK 2003b). In IR-RF dating the primary process of electron trapping is measured and not like in IR-OSL and TL dating the secondary process of recombination of electrons from traps with a luminescence centre.

The IR-RF signal is maximal after bleaching of the sample, because the 1.43 eV traps are empty and can be filled during the radioactive excitation with the maximum number of electrons and therewith fluorescence flux. The signal intensity decreases with higher doses as more and more traps are filled and fewer IR-RF radiative transitions from the conduction band can take place (e.g. TRAUTMANN 1999, ERFURT and KRBETSCHEK 2003b).

To obtain the equivalent dose the natural IR-RF is measured. After that the sample is bleached. It takes the phosphorescence after bleaching about an hour to settle. After that the sample is irradiated and the radiofluorescence detected to obtain the dose characteristic. Several hundred dose points are measured. A mathematical function to fit the dose points is fitted and the equivalent dose is obtained using the fit parameters and the IR-RF signal of the natural dose (cp. Chapter 5.4.4) (ERFURT and KRBETSCHEK 2003a) (Figure 4.11.2).

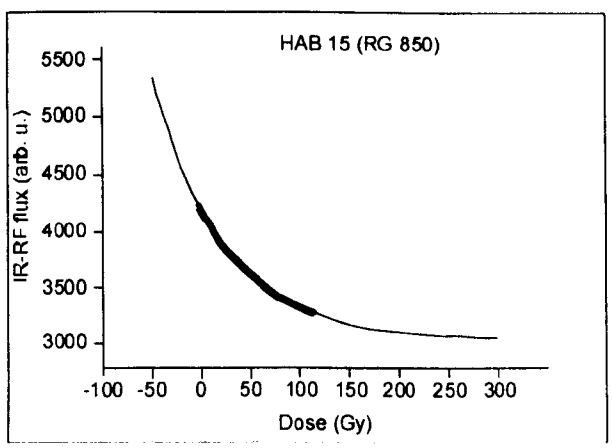

Figure 4.11.2: Dose response curve for IR-RF dating and the IRSAR protocol on the example of sample HAB 15.

4.12 Normalisation

In IR-OSL and TL coarse grain multiple aliquot dating a normalisation method is employed to equalise the disc to disc scattering of the aliquots (cp. Chapter 5.3.1). If discs are not normalised different orders of luminescence intensities can make it difficult to compare the signals in the individual dose groups to each other. The differences in signal are caused by varying numbers of grains on the discs or mineral grains with unequal luminescence intensities. In general three different normalisation methods are known as described below (cp. AITKEN 1998).

4.12.1 Geometrical normalisation

In this study the grains are brought onto the individual discs with the help of a geometrical device and fixed with a silicon oil aerosol (cp. Chapter 5.3.1). An unitised amount of grains is fixed in the centre of the disc area. Through a further preparation step the grains are brought into a monolayer. This preparation guarantees a relative disc to disc uniformity and helps to reduce scattering due to differences in grain numbers and volume. The effectiveness of such a geometrical normalisation depends strongly on the natural homogeneity of the sediment and the manual handling skills of the laboratory worker. For coastal dune sands which are generally a very well sorted sediment and in the hands of a precise working person with several years laboratory experience geometrical normalisation is an effective way of reducing disc to disc scatter caused by differences in volume and grain numbers.

4.12.2 Short shine normalisation

In short shine normalisation a very small IR stimulation is applied to all discs and the IR-OSL signal recorded. The luminescence intensity of the individual discs reflects not only differences in grain number or volume, but also varying luminescence intensities of the individual grains. Although this normalisation method is elegant in its usage and gives a good normalisation factor, it is rather inapplicable if the samples are irradiated externally and need to be transported over long distances. Because some grains might be lost or the grain geometry changed during transport, the measurement after irradiation is different and a previously obtained normalisation factor would be inadequate.

4.12.3 Second glow normalisation

In a second glow normalisation the sample is irradiated in the luminescence reader, preheated and the luminescence signal measured (second cycle) after the measurements to obtain the luminescence signals for dating (first cycle). This should result in a signal that is characteristic for the luminescence intensity of each disc. Unfortunately this approach is often hampered by luminescence sensitivity changes of the mineral grains due to the repeated cycle of dose accumulation, preheat and stimulation, which can result in an increase of scattering through second glow normalisation than without.

A geometrical normalisation does not require any mathematical procedure. Short shine or second glow normalisation can be applied by multiplying or dividing the original luminescence signal by the normalisation value.

4.13 Dosimetry

Any environmental radioactive ray with sufficient energy absorbed by the mineral grain since deposition causes the electron transition into excited states and the luminescence can be later measured in the laboratory. The environmental dose rate (cp. Chapter 4.1.2) is generally composed of the internal dose rate from radioisotopes built into the mineral lattice and the external dose rate from radioisotopes in the surrounding deposits and the cosmic ray dose rate which affects the upper parts of the sediment record.
The decays of the environmental radioisotopes give rise to alpha (α), beta (β) and gamma (γ) rays which affect the sediment. In the average sediment α-particles (helium nucleus: 2 protons, 2 neutrons) have a penetration range into material of about 25 μm, β-particles (electrons) of circa 3 mm and γ-rays (high energy electromagnetic radiation) reach as far as 0.3 m (AITKEN 1998). In addition to that contribute muons to the dose rate in the upper parts of the sediment record.

4.13.1 Internal dose rate

Because alkali-feldspars contain generally high quantities of potassium compared with other minerals, the grain internal contribution to the general dose rate needs to be considered. The main contribution to the internal dose rate derives from radioisotope ^{40}K although other radioisotopes like for example ^{87}Rb also contribute to the internal dose rate (HUNTLEY and CLAGUE 1996). In natural potassium the radioactive isotope

^{40}K shows an atomic abundance of about 0.01 % (AITKEN 1998). ^{40}K decays through electron capture to ^{40}Ar and through beta emission to ^{40}Ca which is stable. The latter decay is relevant for the internal dose rate contribution. In the luminescence age determination the contribution of the internal dose rate from ^{40}K to the total dose rate is taken into account by considering the general potassium content of the feldspar grains and with this the contribution that is made by the isotope ^{40}K.

BOTTER-JENSEN and MEJDAHL (1985) suggested the determination of the potassium content of potassium-feldspars *via* beta counting. This method is widely used in a number of laboratories, although an accurate determination of the potassium content depends on the success of the separation of the feldspar grains from quartz grains (cp. Chapter 7.1.5) and the general intergrowth of potassium-rich feldspars with sodium-rich feldspars, quartz or other mineral phases. This could result in the underestimation of the internal dose rate. HUNTLEY and BARIL (1997) theoretically calculated the bulk potassium content of 12.5 ± 0.5 % for potassium-rich feldspars, which is also consistent with data given for example by DÜTSCH and KRBETSCHEK (1997). As the total IR-OSL emission and in the main the TL emission comes from feldspars (potassium-rich through density separation) (cp. DÜTSCH and KRBETSCHEK 1997, KRBETSCHEK *et al.* 1997), the value of 12.5 ± 0.5 % is a good bulk estimate for the potassium content. DÜTSCH and KRBETSCHEK (1997) suggested further two other methods for the internal potassium dose determination. The first one is the determination of the potassium concentration of the pure feldspar fraction through detailed chemical analysis using atomic absorption spectro-photometry for element analysis. The second, more intriguing method, is based on the finding that the peak emission of the red afterglow after irradiation (radiophosphorescence) shifts in wavelength with the concentration of the potassium content from 700 nm to 750 nm for 14 % and less than 1 % of potassium respectively. This relationship between potassium content and emission wavelength can also be observed in plagioclases with a very low potassium content and is generally independent of the feldspar structure. The last method must be the most elegant because of its direct detection and also strict relation to the luminescence of feldspars (DÜTSCH and KRBETSCHEK 1997), though not every laboratory is equipped with the instrumentation (luminescence spectrometer or red sensitive photomultiplier) required for this approach.

4.13.2 External dose rate

The radioisotopes ^{232}Th, ^{235}U, ^{238}U, and their daughters, ^{40}K as well as cosmic rays form the primary contribution to the external dose rate in the sediment. The cosmic ray dose rate is considered below (cp. Chapter 4.13.3). The decay of ^{40}K is mentioned above (cp. Chapter 4.13.1). ^{232}Th decays over a series of other radioisotopes to the stable isotope ^{208}Pb (Figure 4.13.2a). The thorium concentration in sandstones is known to be low at around 1 ppm (cp. Chapter 6.3.1), given that the heavy mineral concentration is not increased (DURRANCE 1986). ^{235}U (actinium) decays through other radioisotopes to ^{207}Pb which is stable (Figure 4.13.2b). ^{238}U decays as a series to the stable isotope ^{206}Pb (Figure 4.13.2c). The uranium concentration in a sediment depends on factors like the uranium concentration in the source rock, the proximity to water, solubility of the chemical compounds and the absorption by organic matter, hydroxides and clays (DURRANCE 1986). Uranium, which is contained in minerals with soluble compositions (e.g. uranyl complexes) and in intergranular spaces, can be dissolved, transferred and precipitated elsewhere (cp. Chapter 4.13.5). Uranium built into the lattice of the minerals (e.g. zircon) will not be moved (DURRANCE 1986).

The concentration of the radioisotopes ^{40}K, ^{232}Th, ^{235}U and ^{238}U in sediment can be obtained by gamma spectrometry. This is possible directly in the field with a portable gamma spectrometer which measures the overall dose rate received by the sediment in a certain location, including the proportion of the cosmic ray dose rate. This has the advantage that variations in the contribution to the external dose rate from lithological horizons below and above the sampling point, with deviating dose rates compared to the sample material, can be better accounted for than by gamma spectrometry carried out in the laboratory, where the sample measured needs to be representative of the overall dose rate received at the sample point, except cosmic rays. In aeolian sediments, which are usually lithologically relatively homogenous, this is only of minor importance, while for example in a peat bog environment with intercalated detrital sand horizons the dose rate would be likely to vary significantly between layers next to each other and an accurate determination of the external dose rate over a representative sample taken in the field would be difficult to obtain. The disadvantage of portable gamma spectrometry is usually a limited measuring time provided by an built-in power supply and therefore reduced accuracy.

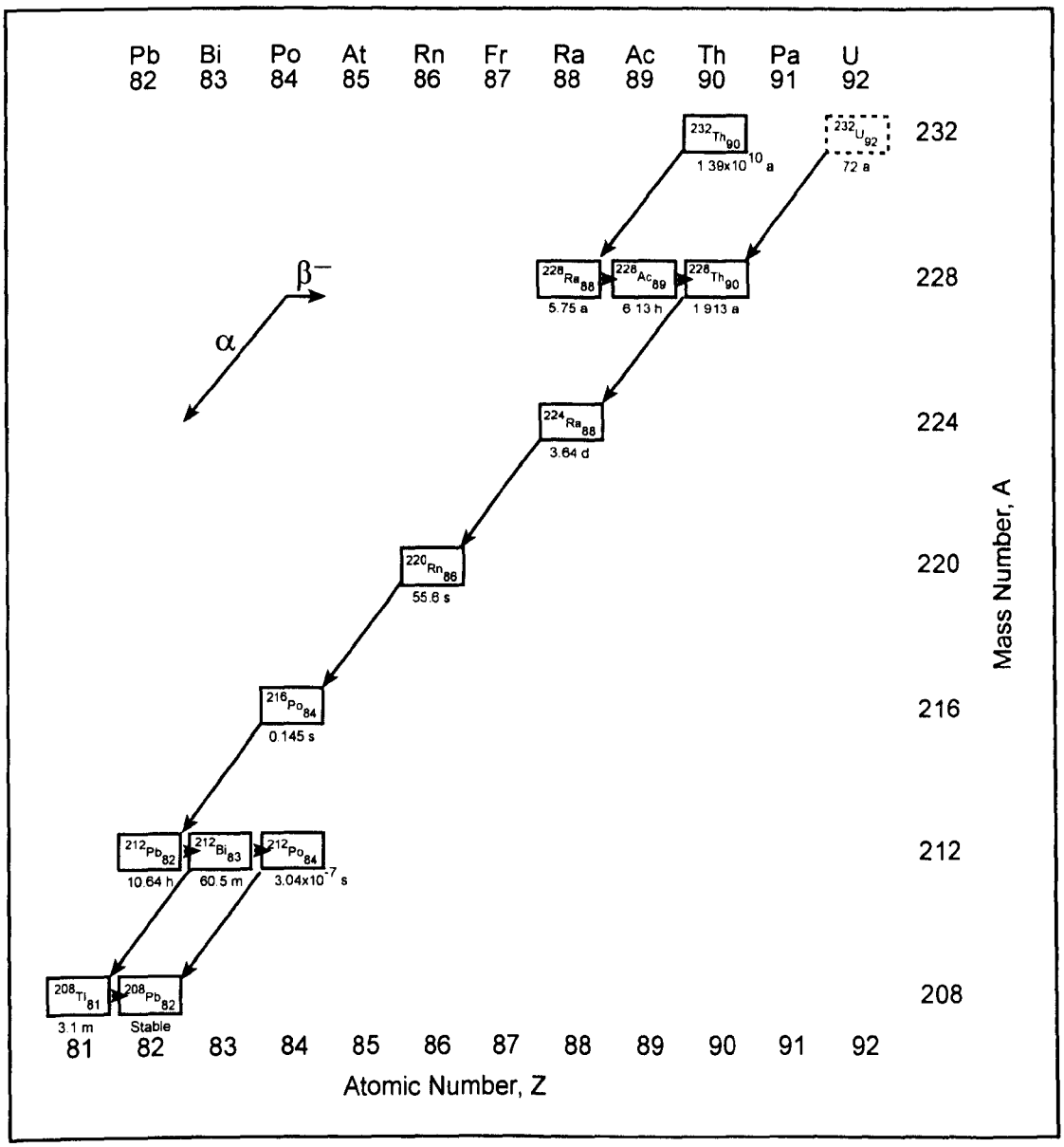

Figure 4.13.2a: Thorium decay series (redrawn from IVANOVICH 1992).

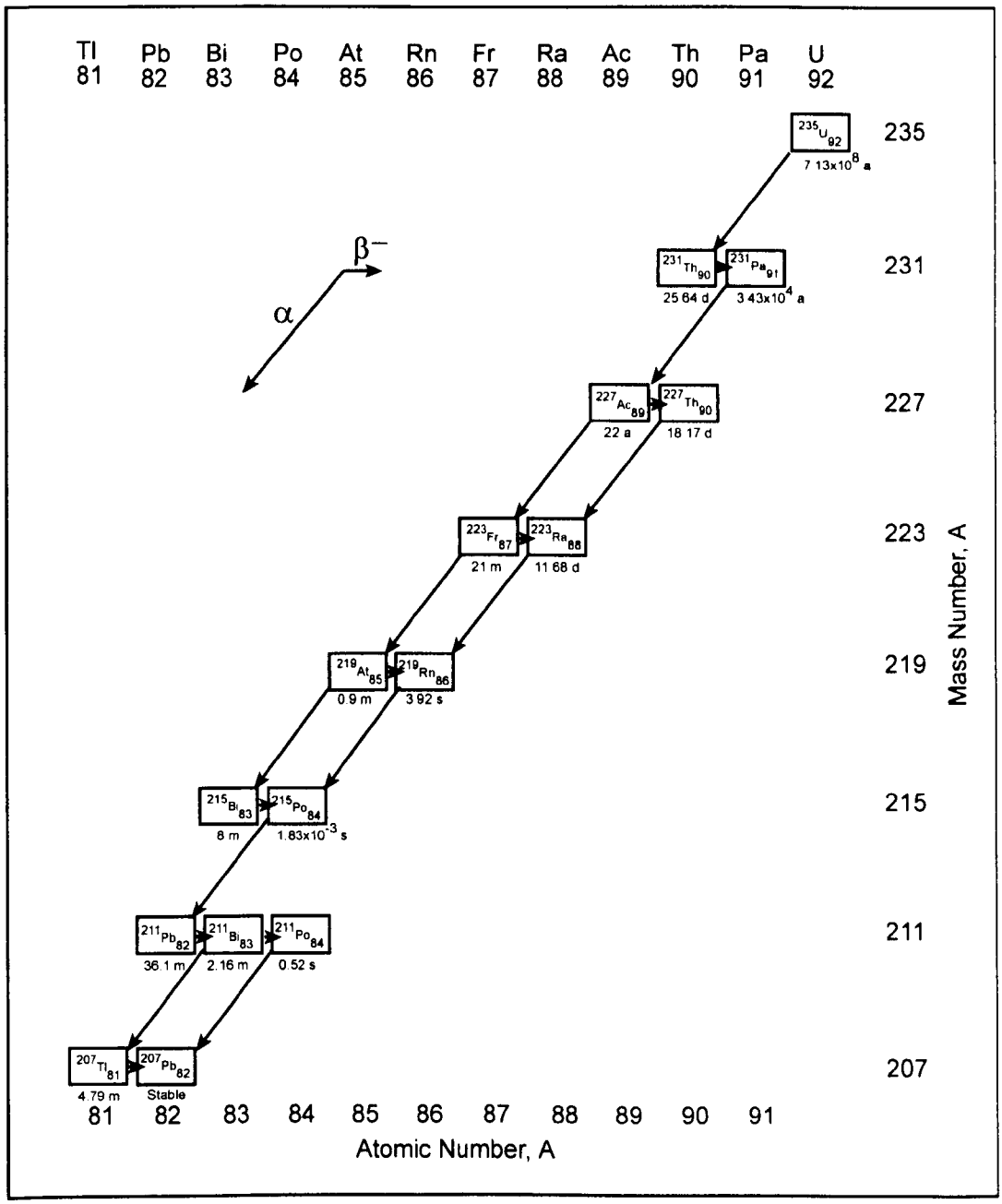

Figure 4.13.2b: Actinium decay series (redrawn from IVANOVICH 1992).

Generally in gamma spectrometry the energies of single decays of the radioisotopes in the decay series are measured. Because during the decay emitted energies are discrete for the individual radioisotopes they can be assigned to the individual daughters of a decay. Measurements of standards with known concentrations and comparison of the integration area underneath the peaks allow to calculated the concentration of ^{40}K, ^{232}Th and ^{238}U (cp. Chapter 5.5, Chapter 6.3).

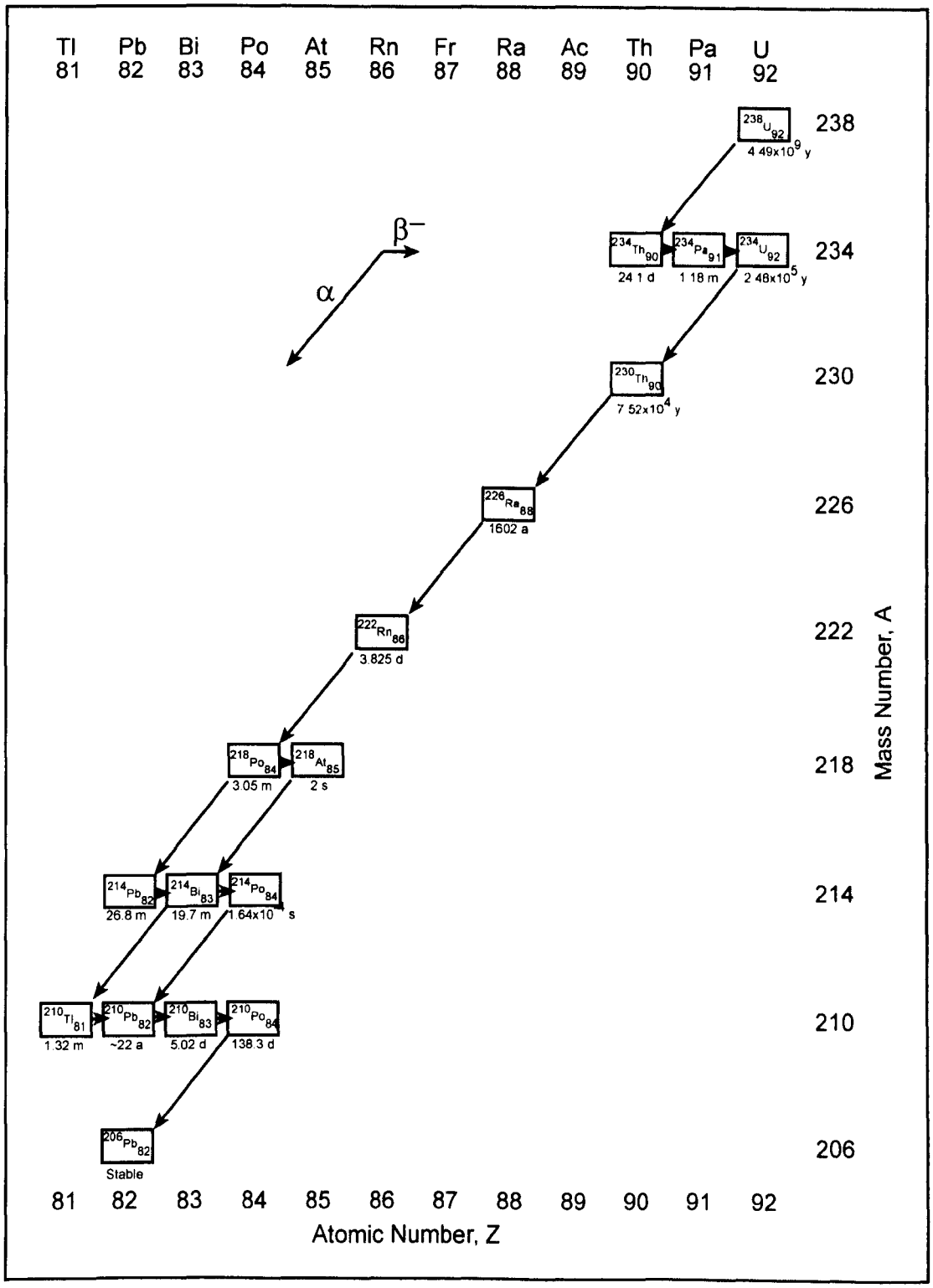

Figure 4.13.2c: Uranium decay series (redrawn from IVANOVICH 1992).

4.13.3 Cosmic ray dose rate

Cosmogenic radiation is high energy particle- and photon-radiation which penetrates from space into the Earth's atmosphere. The origins of this radiation are galactic and solar. The primary radiation consists of about 80 % protons, 19 % alpha-particles and the rest constitutes nuclei from lithium, beryllium, boron, carbon, nitrogen, oxygen and calcium. The frequency of these cores correspond – with exception of lithium, beryllium and boron – to the occurrence of these elements in the cosmos. The primary radiation penetrates the Earth's atmosphere down to 20 km altitude. Very energetic particles of the primary radiation lose their energy through the ionisation of the atoms of the air and the interaction with nuclei of the air molecules (N_2, O_2, Ar, Kr). The process is known as a cosmic ray shower (Figure 4.13.3). Partially nuclear spallation takes place: The hit atomic cores burst and the particles fly in all directions. This by the primary radiation produced particles and energy quanta are the so-called secondary radiation. Primary particles and secondary radiation cause further nuclear spallations, until the initial energy is used up. For the moment this causes an increase of the intensity of the cosmic radiation. But with further penetration of the primary and secondary radiation into the atmosphere the intensity decreases as a result of absorption. At the Earth's surface only secondary radiation can be observed. One distinguishes:

1) The nucleonic component, which is a slow energy component and the product of the disintegration of neutrons which degenerate to slow neutrons.

2) The hard component, which consists of muons. Their intensity decreases only half by passing through a 1 m thick lead plate and the component can still be measured on the bottom of deep seas.

3) The soft component, which exists of electrons and photons and is totally absorbed by passing for example through 15 cm of lead.

4) The neutrino current consists of elementary particles with no electric charge. Neutrinos originate through the decay of other particles. Owing to the weak interactions of neutrinos with matter the current passes through the whole Earth more or less unhindered and is therefore very difficult to observe.

Parts of cosmic radiation with lower energy originate from the Sun, while particles of higher energy are from the galaxy (BORUCKI *et al.* 1974, CE 2004).

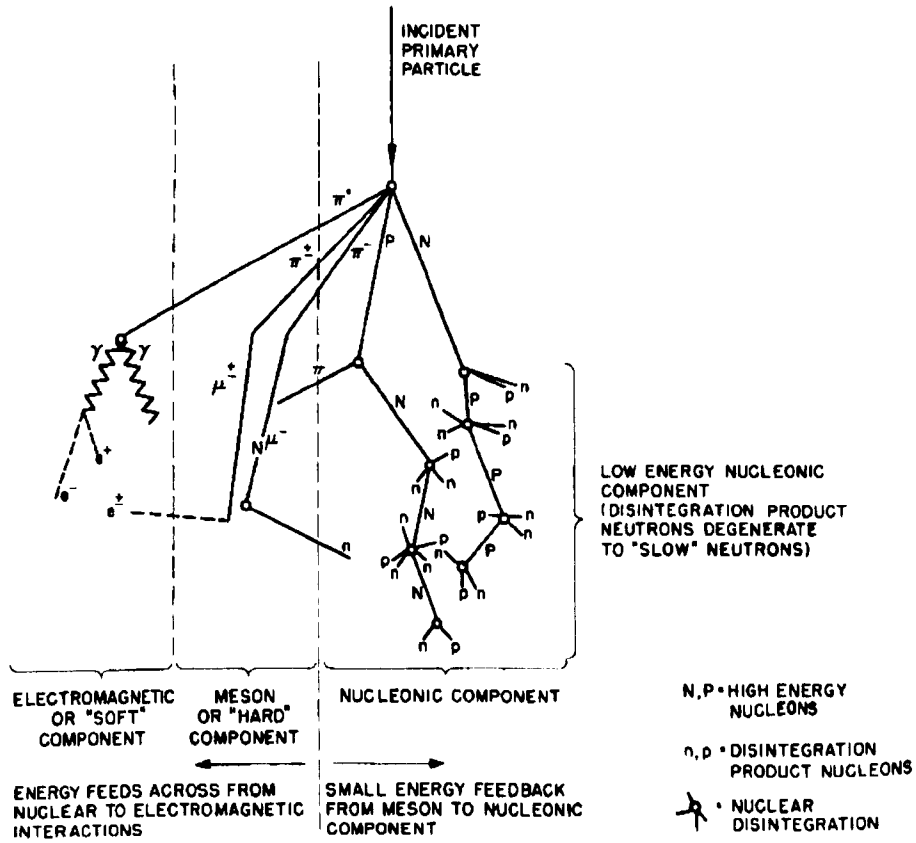

Figure 4.13.3: Schematic diagram of cosmic ray shower (NGDC 2004). Note that muons were re-classed from mesons to leptons (e.g. CE 2004).

Apart from that there are abundant gamma ray emissions through the interactions of cosmic ray with other matter, *a priori* the hard component (muons) of cosmic rays is contributing to the external dose rate (e.g. PRESCOTT and HUTTON 1994). Overall the cosmic rays interact with the elements of the sediment minerals and produce radioisotopes like ^{3}H, ^{10}Be, ^{14}C, ^{26}Al and ^{36}Cl which are also used for surface dating through neutron capture, muon capture and spallation (e.g. SINGHVI and KRBETSCHEK 1996, IVY-OCHS 1996). The radioisotope ^{3}H (tritium) is a pure beta emitter and decays to the stable isotope ^{3}He. The radioisotope ^{10}Be decays with a beta emission to ^{10}B. The radioisotope ^{14}C is also a pure beta emitter and decays to the stable isotope ^{14}N. ^{13}Al decays through electron capture to the stable ^{26}Mg and the radioisotope ^{36}Cl decays through beta emission to the stable isotope ^{36}Ar and through electron capture to ^{36}S (GAMMEL 1997).

The Earth's magnetic field acts as a shield for cosmic rays and deflects the cosmic particles. The amount of cosmic rays that arrives at the Earth's surface depends on the

magnetic field strength. As the Earth's magnetic field strength changes with the geomagnetic latitude it needs to be considered for a particular geographical point (e.g. MCNISH 1936). The shielding effect is the largest for low latitudes and decreases towards the poles. Spatial and temporal changes in magnetic field strength occurring during magnetic polarity excursions or changes in the primary cosmic ray flux cause also variations in the cosmic ray intensity (e.g. BEER *et al.* 2002).

The penetration depth of cosmic rays depends on the cosmic ray intensity, varying with location, altitude and density of the sediment and attenuating with depth (e.g. PRESCOTT and HUTTON 1994). In the case of the Israeli coastal dune sands and aeolianites, at an average penetration depth of 5.30 m 50 % of the cosmic dose rate surface intensity is attenuated (cp. Appedix 2).

The contribution of the cosmic ray dose to the total dose received by the sediment is generally low and does not exceed in most cases 10 % of the total dose (e.g. FRECHEN and DODONOV 1998, ~ 4.6 %). But this ratio is different for sediments with a generally low total dose rate, like for example dune sands with circa 1000 μGy/a (cp. Chapter 6.3). In near-surface samples from young Holocene dune sands the contribution of the cosmic dose rate towards the total dose rate is proportionally higher and in the case of the Israeli sediments in the Sharon coastal plain reaches up to 20 % of the total dose. Therefore the proportion of the cosmic dose rate towards the total dose needs to be considered carefully for young sediments.

Largely two methods have been used for the consideration of the cosmic ray dose rate (cp. MUNYIKWA 2000), the usage of an average bulk value for an average depth and the calculation of the cosmic dose rate for a certain geographical point and its attenuation (AITKEN 1985, 1998, PRESCOTT and HUTTON 1994). MUNYIKWA (2000) discusses temporal variations in cosmic dose rate intensities at certain depths due to variations in the overburden thickness of the sediment and suggests to allow mathematically for stagnation phases and accumulation phases in sediments. But the method does not account for erosional phases. As during stagnations of sediment accumulation it is very likely that erosion takes place, but erosion rates are usually uncertain, the approach by MUNYIKWA (2000) seems incomplete and suggests higher accuracy of the suggested cosmic dose rate calculation than the method probably yields.

4.13.4 Attenuation factors

Several factors can attenuate the accumulation of the total dose rate in the sediment. The evaluation of these attenuation factors for the calculation of the total dose rate aims to ensure more accurate age estimates.

Moisture content

The moisture in the sediment absorbs radiation and attenuates with this the total dose rate, that acts on the mineral grains. To correct for the moisture attenuation an estimated water content in weight percent is used in the age calculation. The moisture value is often deduced from the moisture content that prevailed in the sediment during sampling; also the filling of the open pore space with water gives an estimate for the possible maximum moisture (saturation value). Such approaches seem to be a good estimate for sediments that have always been under the same climate regime, always arid or near the saturation level (AITKEN 1998). In areas with varying climatic history and moisture regimes like Mediterranean-type climates an estimation of a representative mean palaeowatercontent since burial is difficult to obtain and causes uncertainty in the total dose rate calculation. Because clay minerals are known to absorb water into their lattice, a palaeowatercontent evaluation should also consider apart from the total pore space the average clay content of a sediment.

Alpha-efficiency

Because of the mass and size of alpha particles there is a high ionisation density along their fission tracks. The existing traps along these tracks are going to be filled and an excess of electrons will be removed over the conduction band. For this reason alpha particles are less luminescence-effective than beta particles or gamma rays. Only the outermost parts of the mineral grains are affected by this, as the alpha particles quickly lose their energy and only penetrate a few micrometers (cp. Chapter 4.13). Therefore the outer part of the mineral grain is removed by HF etching, or the attenuation of the total dose rate by alpha particles needs to be corrected by a factor regarding the alpha efficiency (cp. AITKEN 1985, 1998).

4.13.5 Radioactive disequilibria

Radioactive disequilibria relevant for luminescence sediment dating derive mainly from the removal of radionuclides from the geological system observed. Fractionation processes involved are solution and precipitation through percolating groundwater, diffusion of gaseous radioisotopes on gas-solid or gas-liquid phase boundaries, alpha recoil displacement especially on solid-liquid phase boundaries and recoil vulnerability (Szilard-Chalmers effect), which enhances the effect of leaching (OSMOND and IVANOVICH 1992). The first fractionation process is specially associated with carbonate solution and recrystallisation and can affect aeolianite dating. The daughters from isotopes removed or displaced from one system into another are missing in the decay series of the first and cause the radioactive disequilibrium between parent and later daughters. The detection of disequilibria with gamma spectrometry is only partly possible and depends also on the sensitivity range of the gamma spectrometer. KRBETSCHEK *et al.* (1994) suggested the use of both alpha and gamma spectrometry for the detection of disequilibria. But alpha spectrometry is usually not available for routine dating applications and the detection of disequilibria is therefore limited.

To overcome changes in the environmental dose rate, caused by disequilibria or varying moisture content (cp. Chapter 4.13.4), VOGEL *et al.* (1999, 2002) suggested to subtract the TL equivalent dose of quartz from the IR-OSL equivalent dose of potassium-rich feldspar from the same sample, leaving only the part of the equivalent dose which corresponds to the internal irradiation of the feldspar. As there is no change (~ 0.01 %) in the internal radiation over the time concerned for dating (Late Pleistocene) (^{40}K halflife $t_{1/2}$ = 1.277 x 10^9 a), the method is independent from all environmental effects that would cause a change in radiation, but the approach is strongly dependent on an accurate internal dose rate determination.

CHAPTER 5

Methods

The chapter describes the methods used in the study.

5.1 Field methods

5.1.1 Choice of sampling sites and sampling points

The sampling sites for the luminescence dating were chosen using the following criteria. The sites should cover sections in aeolianite ridges from the North to the South in the Carmel and Sharon coastal plains and also where possible, transects over the aeolianite ridges from East to West. Further it was attempted to cover a range of old to young samples from lithified dune sands, loose dune sands and palaeosols. The chosen sites were opted for using the above described criteria, but also for their detailed lithological and pedological composition (cp. Chapter 3.2). Each sampled section was described briefly sedimentologically and pedologically and the thickness of the horizons was measured with a surveyor's staff. At the coastal cliff at Netanya South it was also necessary to take the bearings of the thicknesses because of the steepness of the cliff and the upper part stands back compared to the lower part. The sampling points were chosen to cover all horizons from old to young and to cover all lithological types of strata in a section. Parallel to this study a detailed sedimentological study was carried out by NEBER (2002) partly on the same sections.

5.1.2 Sampling

At each sampling point a sample (hereafter called luminescence sample) for the determination of the equivalent dose and a sample for the gamma-spectrometry were taken. In soils or in loose sandy material the samples for the luminescence were taken with a metal (brass) cylinder in shady conditions and quickly transferred into light tight black photo bags. For the gamma spectrometry about 2 kg of material were taken using a garden shovel into sampling bags. From lithified dune sands the samples were taken in blocks with hammer and chisel, both for the luminescence and for gamma-spectrometry. The luminescence sample was wrapped for security in light tight black photo plastic and taped all around with parcel tape to prevent any breaking apart during transport. The gamma-spectrometry samples were also secured with tape.

5.1.3 Shipping of samples

For shipping the samples were packed in cardboard boxes and bolstered with newspaper. The boxes were secured with parcel tape and stored in wooden containers.

The containers were shipped from Haifa to Rotterdam and transported from Rotterdam to Cologne by a haulage contractor. The transfer of the luminescence samples to Cheltenham was carried out by private car. The samples for gamma-spectrometry remained in Cologne.

5.2 Choice of natural dosimeter and protocols

Potassium-rich feldspar was chosen as natural dosimeter for the luminescence measurements as it was expected that the aolianites in the northern coastal plain could possibly be considerably older than the Last Glacial/Integlacial and so quartz could be in saturation (cp. Chapter 4.3). Additionally, the luminescence emission of potassium-rich feldspar is known to be much brighter than that of quartz and is therefore suitable for dating of very young (Holocene) sediments, which generally show relatively weaker luminescence signal because of their young age. Use of potassium-rich feldspar enabled comparison of luminescence ages from different strata along the coastal plains on the same mineral.

For equivalent dose determination multiple aliquot additive dose (MAAD) protocols for IR-OSL and TL measuremtents were chosen. Additionally it was intended to date some samples with the IR-RF single aliquot regenerative (IRSAR) dose protocol (cp. Chapter 4.11) for comparison.

5.3 Laboratory methods for MAAD equivalent dose determination

5.3.1 Sample preparation

The blocks of aeolianite material taken for the luminescence measurements were cut with a rock-cutting machine in subdued light conditions. For the cutting the rock-cutting laboratory in the Geological Institute at the University of Cologne was converted into a luminescence dark laboratory. The windows were blackened with light-tight photo plastic and red light illumination was provided by portable strip lamps in which optical filter foils, types R10 and Melinex, from the company ENCAPSULITE were inserted, allowing wavelengths of transmitted light >600 nm (ENCAPSULITE

product information). The outer surface of the lithified samples which had seen light during sampling or in the field was carefully removed with a water cooled rock-cutting machine. To facilitate the cutting of irregular shaped rocks they were first cut into more or less rectangular shapes and then several centimetres from each side were removed, according to the degree of cementation of the rock. The rock-cutting machine was intensively cleaned of outer surface material before the remaining core material was cut into smaller pieces. The smaller pieces were stored into light tight photo bags and either as such transferred to the luminescence preparation laboratory in Cologne or in Cheltenham. In both laboratories preparation took place under subdued light conditions with visible light of the wavelengths >600 nm by ENCAPSULITE filters.

Very clayey samples from soils were first put into the air-circulated drying cabinet at 50 °C for one night, as the drying process cracks adhesive bonds in clay. All samples were watered and stirred with distilled water once or twice to decant most parts of the clay fraction after settling of the coarser sediment. Further the samples were treated with *circa* 17 % HCl to remove the carbonate and iron encrustations around the grains. The samples were stirred regularly and the sediment was allowed to settle, so that the acid could be decanted and renewed several times depending on the carbonate content of the sample and until all carbonate was dissolved and no reaction could be observed anymore. The procedure took up to several hours for the aeolianite samples. After the HCl treatment the samples were washed thoroughly several times with tap water and after that several times with distilled water using stirring and an ultrasonic bath for each wash. Usually the samples were dried in an oven at 50° C before the next step was commenced to remove adhesive bonds of fine particles. In the next step the samples were treated with 30 % H_2O_2 in order to remove organic matter. The solution was decanted and renewed until no reaction was observed. Afterwards the samples were washed with *aqua destillata* several times using stirring and an ultrasonic bath. To enhance the dispersal of grains the sediment was stirred and left to stand overnight or for at least eight hours in 0.1 N Na-Oxalate. Afterwards the liquid was decanted and the grains were repeatedly washed with distilled water using stirring and an ultrasonic bath until the decanted water was clear and the clay fraction was removed. After drying the sediment in an oven at 50° C the sediment was dry sieved with a sieving machine for 20 minutes. From all samples apart from the cliff section at Netanya South the fraction 100 – 200 µm was separated. The samples from the cliff at Netanya South were sieved into several grain size fractions between 100 – 125, 125 – 140, 140 – 160, 160 – 180 and 180

– 200 µm. Owing to aeolian sorting there was mostly a relatively large proportion of the sample in one of these grain size ranges. In the case of the samples from the coastal cliff at Netanya South the most frequent size fraction was selected for analysis (cp. Table 6.4c). From the selected subsamples potassium feldspar grains were enriched using sodium polytungstate solutions for heavy liquid separation of the grains with densities of 2.70, 2.62 and 2.58 g/cm^3. The separation was carried out with HERAEUS precession centrifuges in Cologne and Cheltenham and also with separating funnels in Cheltenham. After each separation the grains were thoroughly washed with distilled water to clean the grains from the remaining sodium polytungstate solution and to regain the substance. Further the grains were dried in an oven at 50° C. For the multiple aliquot measurements about 50 steel discs per sample were mounted with grains from the enriched potassium feldspar fractions using silicone spray and a geometrical normalisation method.

5.3.2 Irradiation of multiple aliquot luminescence samples

The multiple aliquot samples were irradiated with the gamma source of the Institute for Nuclear Chemistry, Catholic University of Louvain-la-Neuve, Belgium. The source consists of three rod-shaped ^{60}Co-sources (Photo 5.3.2a), which are situated in a panorama-chamber and can be remote-controlled by a computer device, as well as mechanically from the inside as a back-up. The aliquots were irradiated in a light-tight round aluminium irradiation box with a lid (Photo 5.3.2b). This box is placed on a rotating base a few centimetres distant from the source which is motor-driven over a bicycle chain. There are three different irradiation positions, the inner, middle and outer. The rotation ensures a homogenous irradiation of the aliquots. The three irradiation positions were regularly calibrated by the GSF – Forschungszentrum für Umwelt und Gesundheit, München (National Research Centre for Environment and Health, Munich) with alanin-dosimeters (Table 5.3.2). The results were converted for minerals (quartz) using a factor of 0.898 (A. Wieser pers.com. 1997, 2001). The relevant calibrations used in this study are given in Table 5.3.2. The dose rates for each sample irradiation were determined considering the halflife of ^{60}Co (5.3 a) and the natural decay of radioisotopes.

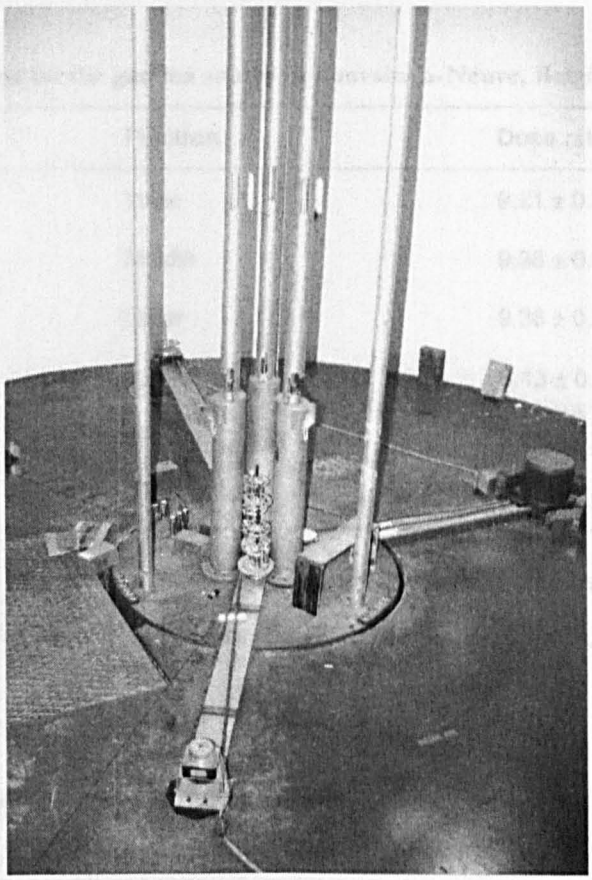

Photo 5.3.2a: Gamma source in the panorama chamber. The position for the irradiation of the luminescence samples is on the right.

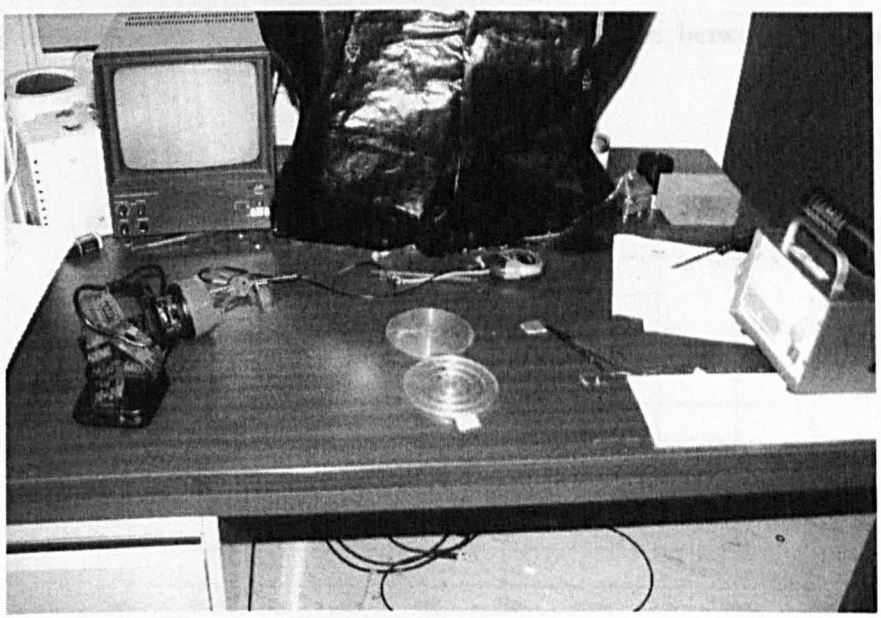

Photo 5.3.2b: The irradiation box for the luminescence samples is shown in the middle of the table with the lid open, so that the three irradiation positions - inner, middle, outer - are visible.

Table 5.3.2: Calibrations for the gamma source in Louvain-la-Neuve, Belgium.

Time of calibration	Position	Dose rate (Gy/min)
August 1997	Inner	9.21 ± 0.29
	Middle	9.38 ± 0.29
	Outer	9.38 ± 0.29
January 2001	Inner	6.13 ± 0.19
	Middle	6.07 ± 0.19
	Outer	6.16 ± 0.19

For the tests of the luminescence properties of the feldspar dosimeters beta irradiation with ^{90}Sr sources of the RISØ luminescence readers was carried out.

5.3.3 Detection window

For the multiple aliquot measurements of the potassium-rich feldspars SCHOTT BG39 and CORNING 7-59 filters were used and also a CHANCE PILKINGTON HA3 filter for heat protection of the photomultiplier. The SCHOTT BG39 filter allows transmission between 310 to 728 nm and the CORNING 7-59 between 284 to 506 nm as well as above 672 nm (Figures 5.3.3a, b). The heat protection filter HA3 allows transmission between 278 nm to >850 nm (Figure 5.3.3c). The photomultipliers used for signal detection show a typical spectral response curve between 150 to 625 nm (Figure 5.3.3d).

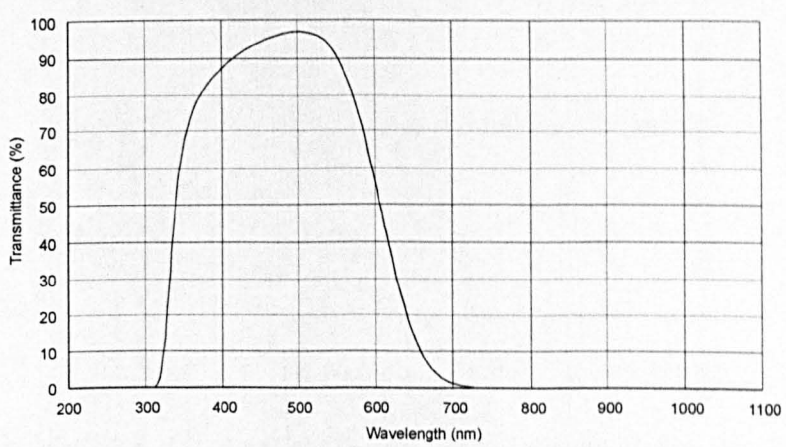

Figure 5.3.3a: Transmission of the SCHOTT BG39 filter (redrawn from SCHOTT product information).

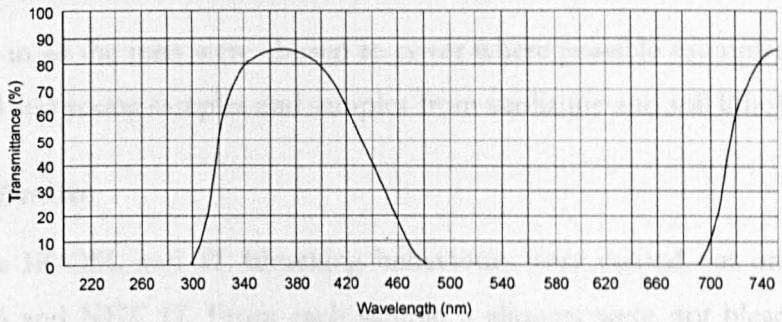

Figure 5.3.3b: Transmission of the CORNING 7-59 filter (redrawn from RISØ TL/OSL systems product information).

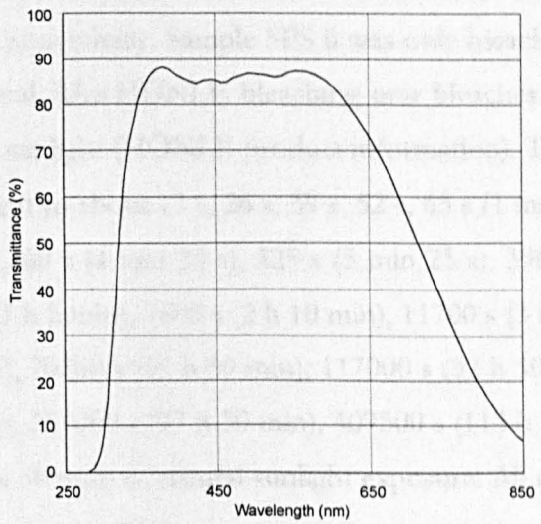

Figure 5.3.3c: Transmission of the CHANCE PILKINGTON HA3 filter (redrawn from RISØ TL/OSL systems product information).

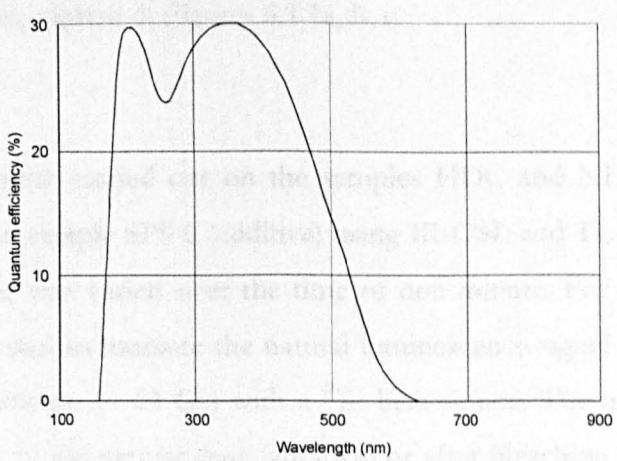

Figure 5.3.3d: Typical spectral response curve of the photomultipliers used (ELECTRON TUBES LIMITED product information).

5.3.4 Design of tests for bleaching behaviour, preheat, fading and combined measurements

The samples in all the tests were chosen to cover where possible examples from North to South, old and young samples and samples from aeolianite and soil lithologies.

Bleaching behaviour

Tests for the IR-OSL and TL bleaching behaviours were carried out on the samples HDC, SPS 6 and NET 17. From each sample 5 aliquots were not bleached at all to measure the natural luminescence signal. Further aliquots, 5 at a time from each sample, were bleached with a HÖNLE SOL 2 bleaching unit for 2 s, 4 s, 6 s, 8 s, 10 s, 20 s, 30 s, 40 s, 50 s, 1 min, 5 min, 10 min, 20 min, 30 min, 1 h, 2 h, 3 h, 5 h, 10 h, 12.5 h, 15 h, 17.5 h, 20 h and 23 h, respectively. Sample SPS 6 was only bleached up to 10 h because of a shortage of material. The HÖNLE bleaching unit bleaches the samples with *circa* factor 6.5 over natural sunlight (HÖNLE product information). Therefore the bleaching times used are equivalent to about 13 s, 26 s, 39 s, 52 s, 65 s (1 min 5 s), 130 s (2 min 10 s), 195 s (3 min 15 s), 260 s (4 min 20 s), 325 s (5 min 25 s), 390 s (6 min 30s), 1950 s (32 min 30 s), 3900 s (1 h 5 min), 7800 s (2 h 10 min), 11700 s (3 h 15 min), 23400 s (6 h 30 min), 46800 s (13 h), 70200 s (19 h 30 min), 117000 s (32 h 30 min), 234000 s (65 h), 292500 s (81 h 15 min), 351000 s (97 h 30 min), 409500 s (113 h 45 min), 468000 s (130 h) and 538200 s (149 h 30 min) of natural sunlight exposure. All aliquots were measured with 25 s IR-OSL stimulation followed by a TL measurement up to 450 °C. From the 5 aliquots of the same bleaching time the arithmetic mean was built from the signal intensities and expressed in per cent of the signal intensity of the natural luminescence signal. The results are plotted in Figures 6.1.1a, b, c.

Preheat

The preheat tests were carried out on the samples HDC and NET 17 (additive and regenerative) and on sample SPS 6 (additive) using IR-OSL and TL measurements. The preheat temperature was varied over the time of one minute. For each temperature 3 aliquots were untreated to measure the natural luminescence signal and 3 aliquots were irradiated for 10 minutes (~ 60 Gy) with a ^{90}Sr beta source. The irradiation was either applied additionally to the natural dose (additive) or after bleaching of the aliquots for 3 hours with the SOL 2 bleaching unit (regenerative) which simulates *circa* 19.5 hrs sunlight. The aliquots were preheated for one minute at temperatures of 160 °C, 180 °C,

200 °C, 220 °C, 240 °C, 260 °C, 280 °C and 300 °C before the IR-OSL was measured for 25 s followed by a TL measurement up to 450 °C. In Figures 6.1.1d - 6.1.1m the luminescence intensities (IR-OSL, TL) of the natural (NL) and the additive irradiated (NL + x min β) or the regenerative irradiated (SL + x min β) signals and the ratios (NL / (NL + x min β)) or (NL / (SL + x min β)) are plotted versus the preheat temperatures for one minute. For calculation the arithmetic means from 3 aliquots were used in each case.

Fading

Fading tests were carried out on samples HAB 3, HAB 5, HAB 16, SOP 1, SOP 3, SOP 5, NET 5, NET 10. From each sample 25 aliquots were left untreated to be able to measure the natural luminescence signal. A further 25 discs were irradiated for 10 min (~ 60 Gy) with a ^{90}Sr source additional to their natural dose. Five untreated and five irradiated aliquots were measured shortly after the irradiation and successively after storage times of up to 236 days. For the measurements the aliquots were preheated with 230 °C for one minute and IR-OSL was stimulated for 25 s, followed by a TL measurement up to 450 °C. In Figures 6.1.1n - 6.1.1v the storage time is plotted on the x-axis and the ratio from the additive luminescence signal (natural + irradiated) divided by the natural luminescence, in per cent of the initial measurement (arithmetic means out of 5 aliquots) on the y-axis.

Combined measurements

The influence of the IR stimulation on the TL signal in the combined measurements was tested on the samples HDC and WNS 15. The test was carried out twofold, (i) to check for the influence of the IR stimulations on the natural TL signal and (ii) to test the influence of the IR stimulations on the TL signal after varying doses of irradiation.

For case (i) 5 aliquots of both samples were preheated at 230 °C for one minute and after that a TL measurement to 450 °C was carried out. Further aliquots, 5 at a time, were preheated at 230 °C for one minute, IR-OSL stimulations for 5 s, 10 s, 15 s, 20 s, 25 s, 30 s, 40 s, 50 s and 60 s were carried out before measuring the TL to 450 °C. From each of the measurements the arithmetic mean of the signal intensities of the 5 aliquots was built. In Figures 6.1.1w and 6.1.1x the IR-OSL stimulation time is plotted on the x-axis and the IR-OSL intensity, the TL intensity after IR stimulation and the intensity of

the TL signal in per cent of the natural TL signal (0 s IR stimulation) after IR stimulation on the y-axis.

For case (ii) a set of 5 aliquots of each sample was preheated at 230 °C for one minute, the IR-OSL stimulated for 25 s before the TL was measured to 450 °C. Further aliquots, 5 at a time, were irradiated with a ^{90}Sr source on top of the natural luminescence signal (additive) for 2.5 min (~ 15 Gy), 5 min (~ 30 Gy), 10 min (~ 60 Gy), 15 min (~ 90), 20 min (~ 120 Gy), 30 min (~ 180 Gy), 40 min (~ 240 Gy) and 60 min (~ 360 Gy) with successive higher doses. The aliquots were then preheated at 230 °C for one minute before the IR-OSL was stimulated for 25 s and the TL was measured to 450 °C. From each of the measurements the arithmetic mean of the signal intensities of the 5 aliquots was built. In Figures 6.1.1y and 6.1.1z the irradiation times are plotted on the x-axis and the IR-OSL and TL signal intensities from the natural luminescence signal plus the added dose, the ratios TL intensity/IR-OSL intensity (cts) and the ratios TL intensity/IR-OSL intensity (%) of the first quotient are plotted on the y-axis.

5.3.5 MAAD protocol

After irradiation of the samples in Louvain-la-Neuve (Chapter 5.3.2) the following measuring sequence was employed. The aliquots were preheated at 230 °C for one minute with a heating ramp of 5 °C/1 s, IR-OSL was stimulated for 25 s at 30 °C, TL was measured to 450 °C with a heating ramp of 5 °C/1 s. For an initial second glow normalisation beta irradiation (^{90}Sr) was carried out for 300 s (~ 30 Gy); it followed a preheat of 230 °C for one minute with a heating ramp of 5 °C/1s, IR-OSL stimulation for 25 s at 30 °C, TL measurement to 450 °C with a heating ramp of 5 °C/1 s. The second glow normalisation was later not used in the equivalent dose determination as it resulted in increased scatter of the data. For background subtraction a further IR-OSL stimulation for 25 s at 30 °C was carried out. The background of the TL was subtracted automatically during the measurement. For the samples from the Netanya South Cliff section no IR-OSL run for a background subtraction was carried out.

5.3.6 Determination of equivalent doses and age calculation

The equivalent doses from the samples of the cliff at Netanya South were calculated with the program Analyse v. 6.37; all other samples were calculated with the program Analyst v. 3.05 both by G. A. T. Duller using an exponential fit. The samples from the

Netanya South Cliff section were second glow normalised. For the calculation of the equivalent doses of all other samples the second glow normalisation was omitted, as it resulted in an increased disc-to-disc scatter of several samples. However, because the feldspars were already volume-normalised on the discs during preparation process and the sediment is in geological terms homogeneous, the samples could be analysed without problems.

5.4 Laboratory methods for IRSAR equivalent dose determination

Two research visits to Freiberg/Germany took place to date the Israeli samples with IR-RF. During the first visit samples from the coastal cliff at Netanya South (NET, cp. Chapter 3.2.3) were investigated together with Toralf Trautmann using the original measuring instrumentation of his Ph.D. research (cp. TRAUTMANN 1999). The second visit concentrated on the measurements of samples from Habonim quarry (HAB, cp. Chapter 3.2.1) together with Gunter Erfurt on the newly built fully automated radiofluorescence reader (cp. ERFURT *et al.* 2003). In this thesis the measurements and results of the second research visit are reported.

5.4.1 Sample preparation

For the single aliquot IR-RF measurements in Freiberg (HAB samples) the enriched potassium feldspar fraction prepared for the multiple aliquot measurements was additionally etched for 40 minutes with 10 % HF and after neutralisation and washing, dried in a drying cabinet at 50° C. The grains were dry sieved to reduce the grain size further to 100 – 150 µm. Finally they were fixed on adhesive foil strips and the sample holder.

5.4.2 Detection windows

The IR-RF measurements on the HAB samples were carried out with SCHOTT RG830, SCHOTT RG850, ANDOVER 700FS10-25 and ANDOVER 200FC37-25/8650 optical filters. The SCHOTT RG830 transmits >785 nm and the SCHOTT RG850 >810 nm (Figure 5.4.2a, b). The ANDOVER 700FS10-25 transmits between 691 – 715 nm and the ANDOVER 200FC37-25/8650 between 845 – 890 nm (Figure 5.4.2c, d).

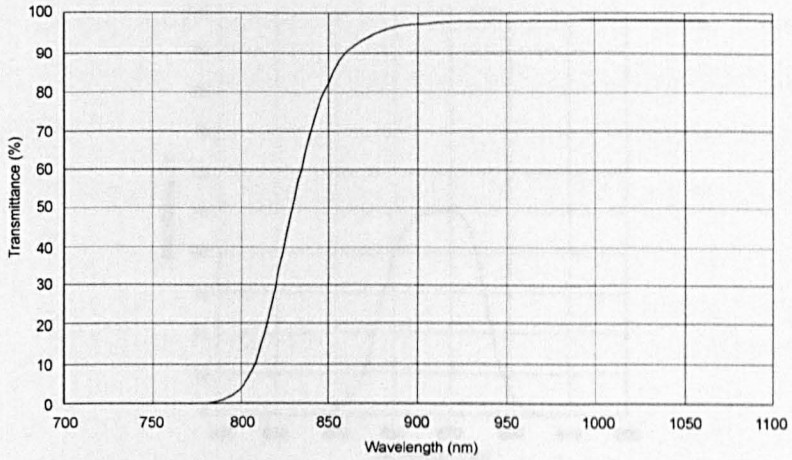

Figure 5.4.2a: Transmission from SCHOTT RG830 filter (redrawn from SCHOTT product information).

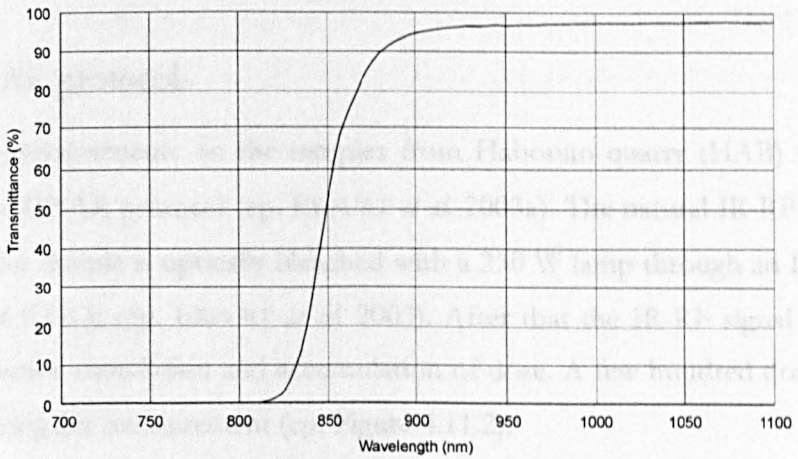

Figure 5.4.2b: Transmission from SCHOTT RG850 filter (redrawn from SCHOTT product information).

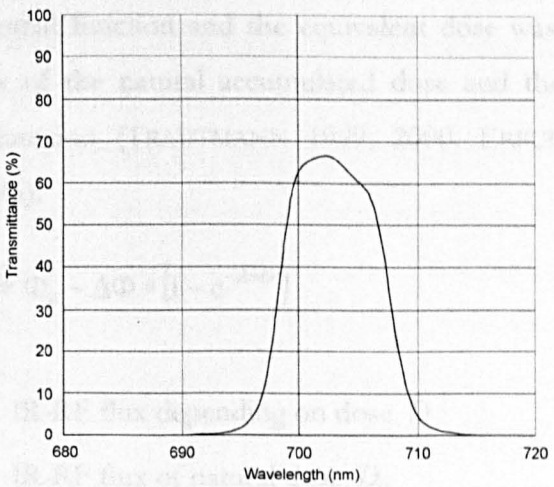

Figure 5.4.2c: Transmission from ANDOVER 700FS10-25 filter (redrawn from LOT-ORIEL product information).

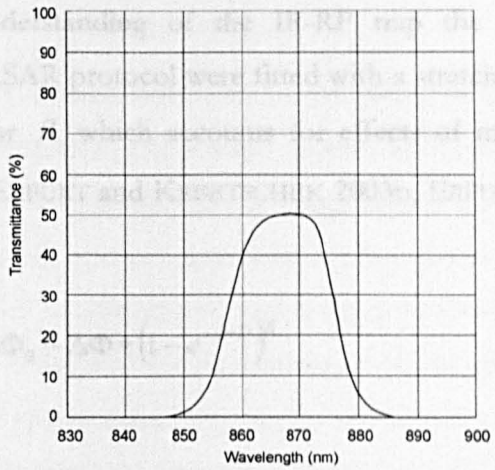

Figure 5.4.2d: Transmission from ANDOVER 200FC37-25/8650 filter (redrawn from LOT-ORIEL product information).

5.4.3 IRSAR protocol

The IR-RF measurements on the samples from Habonim quarry (HAB) were carried out using the IRSAR protocol (cp. ERFURT *et al.* 2003a). The natural IR-RF is measured first. Then the sample is optically bleached with a 250 W lamp through an IR absorbing filter (Schott KG 3) (cp. ERFURT *at al.* 2003). After that the IR-RF signal is measured during irradiative stimulation and accumulation of dose. A few hundred dose points are recorded during the measurement (cp. Figure 4.11.2).

5.4.4 Determination of equivalent doses and age calculation

In the case of the samples from Habonim quarry (HAB) the recorded dose points were fitted with an exponential function and the equivalent dose was determined over the radiofluorescence flux of the natural accumulated dose and the corresponding dose value of the fitted function (TRAUTMANN 1999, 2000, ERFURT and KRBETSCHEK 2003b) (Equation 5.4.4a).

$$\Phi(D) = \Phi_0 - \Delta\Phi * \left(1 - e^{-\lambda * D}\right) \qquad \text{(Equation 5.4.4a)}$$

$\Phi(D)$ IR-RF flux depending on dose D

Φ_0 IR-RF flux of natural dose D_0

$\Delta\Phi$ Change of IR-RF flux during irradiation

λ Exponential parameter

With an increased understanding of the IR-RF trap the dose points of IR-RF measurements in the IRSAR protocol were fitted with a stretched exponential function, using a stretching factor β which accounts for effects of multiple trapping and de-trapping mechanisms (ERFURT and KRBETSCHEK 2003b, ERFURT *et al.* 2003) (Equation 5.4.4b).

$$\Phi(D) = \Phi_0 - \Delta\Phi * \left(1 - e^{-\lambda * D}\right)^{\beta} \qquad \text{(Equation 5.4.4b)}$$

5.4.5 Radiofluorescence spectra

Radiofluorescence spectra were obtained from samples of the Netanya South Cliff section (NET) and the section in the East-wall at Habonim Quarry (HAB) during two visits to Freiberg/Germany (cp. Chapter 6.2.1). The spectrometer set-up is described elsewhere (RIESER *et al.* 1994, TRAUTMANN 1999).

5.5 Dosimetry

5.5.1 Gamma spectrometry

Sample preparation

All samples for gamma spectrometry measurements were prepared at the Geological Institute of the University of Cologne. The lithified samples, which were taken in blocks, were cut into small pieces with a rock cutting machine. After drying in a drying-cabinet at 50 °C for several days they were pulverised in a rock crusher, which was meticulously cleaned with a brush and pressurised air before each processing of a new sample. After this the material was further treated with a pestle and mortar until powdered and homogenised. Marinelli-beakers were filled with 1.6 kg of the material and sealed air-tight. The samples were stored for at least 4 weeks before measurement to allow for the restoration of equilibrium between the gaseous radioisotope radon and its daughters. Loose sample material was treated accordingly, but without the rock cutting and the crushing machines.

Gamma spectrometer

The measurements were carried out at the Geological Institute at the University of Cologne with a CANBERRA-PACKARD gamma-spectrometer, type (GC 2019-7935.2), with a connected CANBERRA multi-channel analyser. The semiconductor detector is made of p- and n-doped germanium. The gamma spectrometer measures peaks in a range of 186.0 to 2614.5 keV and is energy-calibrated using standards (cp. PREUSSER and KASPER 2001). For the measurements the Marinelli-beakers were placed over the detection-head of the detector tube in a cylindrical lead-chamber with 0.10 m thick walls. The Israeli samples were measured for 72,000 s (20 h).

Calculation of environmental dose rates

The data were mass-corrected for analysis and the respective background obtained for each peak was subtracted. For calculation a growth curve is used, which describes an increase of emitted gamma-radiation with increase of concentration of radioactive isotopes (PREUSSER 1999). Isotopes of the actinium decay series (^{235}U) are poor emitters of gamma-radiation. The strongest peak can be detected at an energy of 185.7 keV but is overlapped by the peak of the ^{226}radium decay of the uranium decay series (^{238}U). The calculation for this peak assumes a ^{238}uranium/^{235}uranium ratio of 137.88 (WILLEMS 1994, PREUSSER 1999). Peaks used for calculation of the annual external dose rate are given below (Table 5.5.1). The reproducibility of the Cologne gamma spectrometer for the calibrated peaks lies within an error of 5-10 % (WILLEMS 1994).

Table 5.5.1: Peaks used for the calculation of the annual external dose rate.

^{232}Thorium decays	^{238}Uranium decays	^{40}Potassium decay
^{212}Pb 238.6 keV	^{226}Ra 186.0 keV	^{40}K 1460.0 keV
^{212}Pb 300.1 keV	^{214}Pb 295.2 keV	
^{228}Ac 338.3 keV	^{214}Pb 351.9 keV	
^{208}Tl 538.2 keV	^{214}Bi 609.3 keV	
^{212}Bi 727.3 keV	^{214}Bi 1120.3 keV	
^{228}Ac 911.1 keV		
^{208}Tl 2614.5 keV		

5.5.2 Determination of cosmic ray dose rates

The cosmic dose rate in this study was determined after PRESCOTT and HUTTON (1994) for the northern coastal plains in Israel. For calculations an experimental estimation of the average bulk density of the Israeli samples was carried out. Two samples were chosen as examples. Sample HAB-II-9 was very strongly lithified. Sample HAB-II-4 was less lithified and showed several macroscopically visible mm-sized cavities. From both samples rectangular subsamples were cut with a rock-cutting machine. Their sizes were measured and their weight recorded in wet and dry conditions. From these sizes the volumes were also calculated. The 'wet' weight was determined after the subsamples were soaked overnight in water so that they were saturated. The 'dry' weight was determined after the subsamples were dried in a drying-cabinet for several days, so that the natural rock-moisture had vanished as well. From the measures of the sizes and the weights the densities were estimated (Table 5.5.2).

Table 5.5.2: Sizes, weights and densities of the subsamples as experimentally estimated.

	HAB-II-4	HAB-II-9
Sizes and volumes	4.4 cm * 6.8 cm * 2.4 cm = 71.81 cm^3	5.3 cm * 2.8 cm * 2.8 = 41.55 cm^3
Weight 'wet'	137.15 g	103.44 g
Weight 'dry'	123.63 g	100.08 g
Density 'wet'	ρ = 137.15 g / 71.81 cm^3 = 1.91 g/cm^3	ρ = 103.44 g / 41.55 cm^3 = 2.49 g/cm^3
Density 'dry'	ρ = 123.63 g / 71.81 cm^3 = 1.72 g/cm^3	ρ = 100.08 g / 41.55 cm^3 = 2.41 g/cm^3

Because loose sands, less lithified aeolianites and palaeosols are generally less compacted and are more frequent than very densely lithified aeolianites, an average bulk density of 2.0 g/cm^3, closer to the less compacted aeolianites, was used for all cosmic ray calculations. The calculations after PRESCOTT and HUTTON (1994) are given in Appendix 1. The results for a depth / are given in Appendix 2.

5.5.3 Beta counting

Beta counting was carried out test-wise on five samples to check whether the value given by HUNTLEY and BARIL (1997) for the internal potassium content used for age calculation is adequate. The counting could not be carried out on all samples because of shortages in potassium-rich feldspars.

Sample preparation

The enriched potassium feldspar fraction (Chapter 5.2.1) of the samples HAB-II-9, NET 18, NET 24, WNS 13 and WNS 17 was ground with a pestle and mortar until very fine and homogeneous. About 0.75 g of one sample were placed on top of a plastic sample holder with a diameter of 25 mm and covered with mylar foil.

Beta counter and determination of potassium-content

The measurements were carried out with a RISØ NATIONAL LABORATORY Low Level Beta Multicounter System (type GM-25-5) decribed by BØTTER-JENSEN and MEJDAHL (1988). The instrument consists of 5 Geiger-Müller counters which permit 5 samples to be measured simultaneously. For measurements 5 sample holders were placed on a specimen holder and slid into the counter. Each sample was measured on each of the positions. The external walls of the counter are built from 0.10 m thick lead bricks which shield against external radiation. During measurements the counter also detects, apart from the counts of the 5 sample positions, the background noise which is automatically subtracted. The equipment is controlled by the software GM-25-5 for Windows, version 1.0, from RISØ NATIONAL LABORATORY. The data obtained were exported to MS Excel and the potassium-content was calculated by comparing countrates to a standard.

5.6 Age calculation

The IR-OSL and TL ages were calculated with the program Age Calculation, revised version 2/10/1991, by R. GRÜN for RISØ NATIONAL LABORATORY. The equivalent doses were used as determined from the multiple aliquot measurements (Chapter 6.1.2). For the internal uranium and thorium contents zero values were used, as sedimentary potassium feldspars are not expected to have uranium or thorium built into their mineral grid. For the internal potassium content the theoretical value of 12.5

± 0.5 % was used, which covers at 95 % confidence the content range from 11.5 – 13.5 % after HUNTLEY and BARIL (1997). For alpha efficiency a maximum value of 0.08 ± 0.02 for IR-OSL and TL was assumed derived from the comparison of gamma and alpha irradiation of polymineral fine grain samples (e.g. ENGELMANN 1997). The attenuation of beta particles was accounted for. Grains of diameter 150 ± 50 µm were used for all samples apart from the samples from the Netanya South Cliff. These samples were sieved differently as given in Table 6.4c and the data were used accordingly. The enriched potassium-feldspar samples for the multiple aliquot measurements were not treated with hydrofluoric acid, and so the value for the layer removed was zero. For the density 2.55 ± 0.03 g/cm^3 was used as this covers the densities of potassium-rich feldspars best. As there is no internal uranium or thorium content expected, no internal alpha or beta dose rates were assigned and for these radionuclides an average alpha- or beta-self-irradiation was not accounted for. For the external uranium, thorium and potassium contents the values from the bulk samples as determined by gamma spectrometry were used. The water content of the sediments was considered to depend on the clay content of the sedimentary units since phyllosilicates are generally known to attach water molecules to their grid and to function also as water insulating layer. The water content was estimated with 5.0 ± 1.5 wt % for aeolianites and with 9 ± 3 wt % for soils. The water attenuation for the external doses was accounted for. The cosmic ray attenuation was calculated after PRESCOTT and HUTTON (1994) for a specific point in the central coastal plain (cp. Chapter 5.5.2). The cosmic attenuation values were read according to the sample depths.

CHAPTER 6

Results

The chapter presents the analytical results of the research.

6.1 IR-OSL and TL measurements

6.1.1 Properties of dosimeters

In the following the results for the tests on the luminescence properties of the used potassium-rich feldspar dosimeters are reported.

Bleaching behaviour

The optical bleaching behaviour of the samples HDC, SPS 6 and NET 17 towards artificial sunlight shows that the luminescence signal intensities decrease with increasing optical bleaching time. The IR-OSL signal from the tested samples is set to zero after about two minutes and the TL signal is reduced to an unbleachable rest after about five to eight hours light exposure to the HÖNLE SOL2 lamp. The IR-OSL signal is bleached significantly faster than the TL signal, and can be reduced to zero, while the TL signal can only be reduced to a finite value (Figures 6.1.1a, b, c).

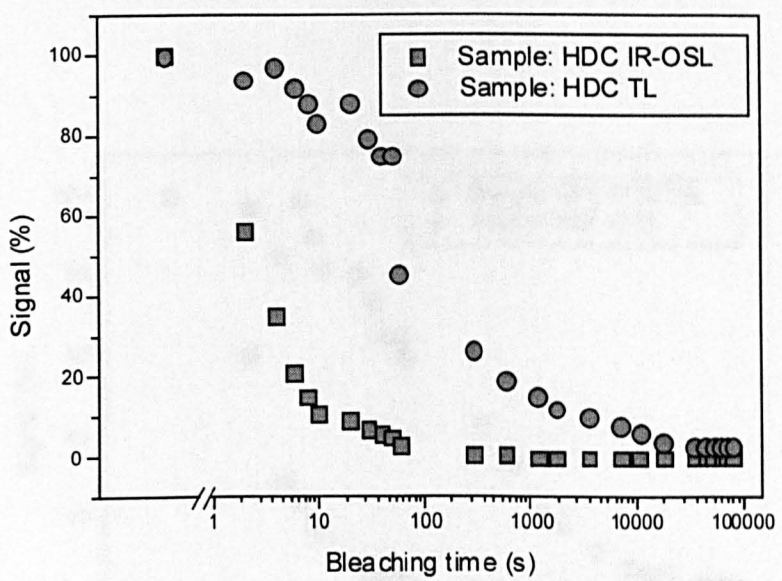

Figure 6.1.1a: Bleaching test for the IR-OSL and the TL signal on the sample HDC, carried out with an Hönle SOL2 bleaching unit.

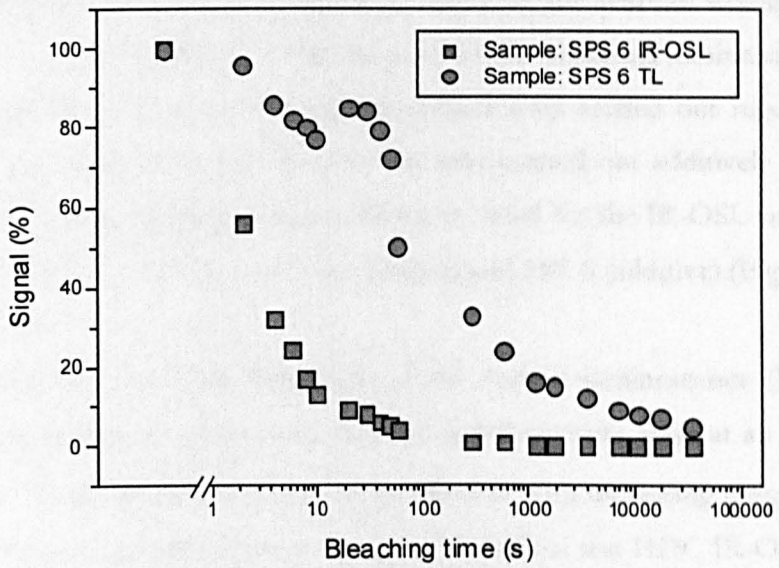

Figure 6.1.1b: Bleaching test for the IR-OSL and the TL signal on the sample SPS 6, carried out with an Hönle SOL2 bleaching unit.

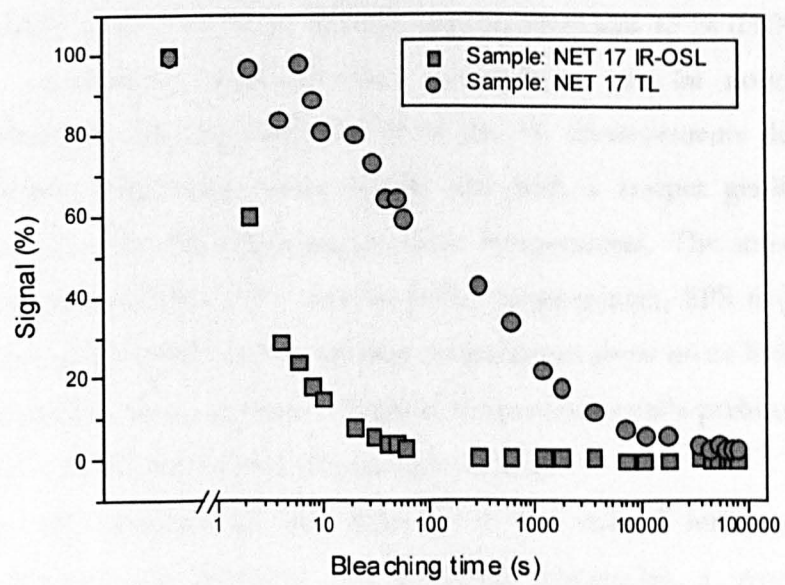

Figure 6.1.1c: Bleaching test for the IR-OSL and the TL signal on the sample NET 17, carried out with an Hönle SOL2 bleaching unit.

Preheat

The preheat tests showed that with a preheat duration of one minute the removal of the unstable luminescence component caused by the artificial irradiation is complete when the values of the ratio of the natural and the irradiated luminescence intensities reach a plateau at 240° C in case of the preheat tests carried out regeneratively or at earlier temperatures in case of the preheat tests carried out additively (cp. Chapter 4.7). The results of the preheat tests are shown in detail for the IR-OSL and TL of samples HDC and NET 17 (additive and regenerative) and SPS 6 (additive) (Figure 6.1.1d, e, f, g, h, i, j, k, l, m).

Observing the signal behaviour of the natural luminescence (NL) towards increased temperatures it can be seen that the signal intensity stays at an initial level until 220 - 240° C and decreases then very moderately with increasing temperatures. An exception is the natural luminescence signal in the preheat test HDC IR-OSL regenerative (Figure 6.1.1e) where the signal intensity increases around 20 % from an initial value towards 240° C and then decreases relatively rapidly with increasing temperatures compared to most of the other preheat tests.

The signal intensities of the irradiated subsamples decrease with increasing preheat temperatures to between *circa* 50 % (HDC IR-OSL additive, Figure 6.1.1d) and 16 % (NET 17 TL additive, Figure 6.1.1l) for the additive irradiated subsamples and to between *circa* 43 % (HDC IR-OSL regenerative) and 13 % (HDC TL regenerative) for the regenerative irradiated ones. Generally it can be noticed for the irradiated subsamples that the intensities from the TL measurements decrease with increasing preheat temperatures more rapidly and with a steeper gradient than the IR-OSL intensities do with increasing preheat temperatures. The intensities of the IR-OSL measurements from the samples HDC (regenerative), SPS 6 (additive) and NET 17 (regenerative) after varying preheat temperatures show no or little response (decrease of signal) towards an increase in preheat temperature until a preheat temperatures of about 220 – 260° C are reached (Figures 6.1.1e, h, k).

For the quotients of the intensity of the natural luminescence divided by the luminescence intensity of the irradiated subsamples, a general difference can be observed depending whether the irradiation dose of the irradiated subsamples was given on top of the natural luminescence (additive) or after bleaching of subsamples (regenerative). For the regenerative approach the value of the ratio increases with

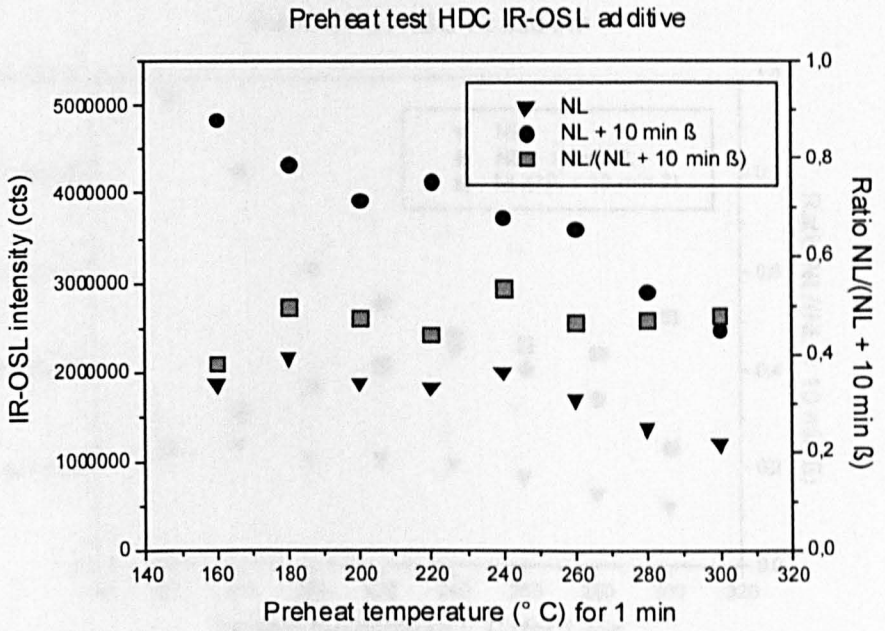

Figure 6.1.1d: Preheat test for the sample HDC IR-OSL additive.

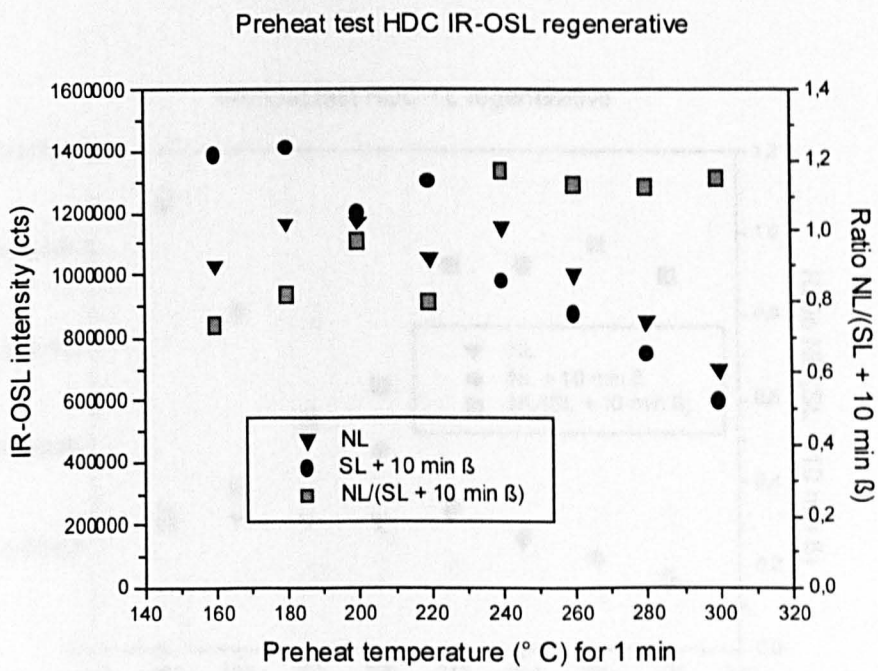

Figure 6.1.1e: Preheat test for the sample HDC IR-OSL regenerative.

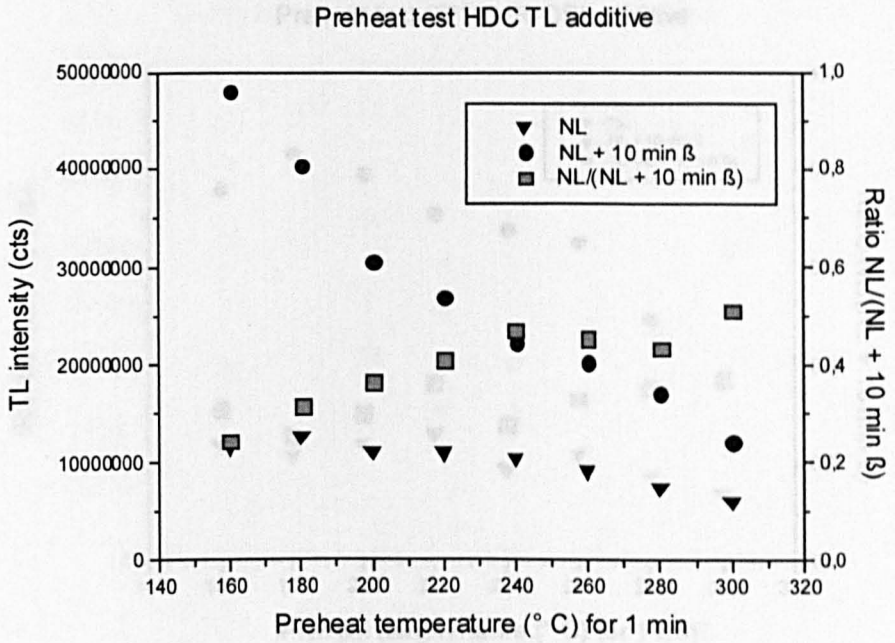

Figure 6.1.1f: Preheat test for the sample HDC TL additive.

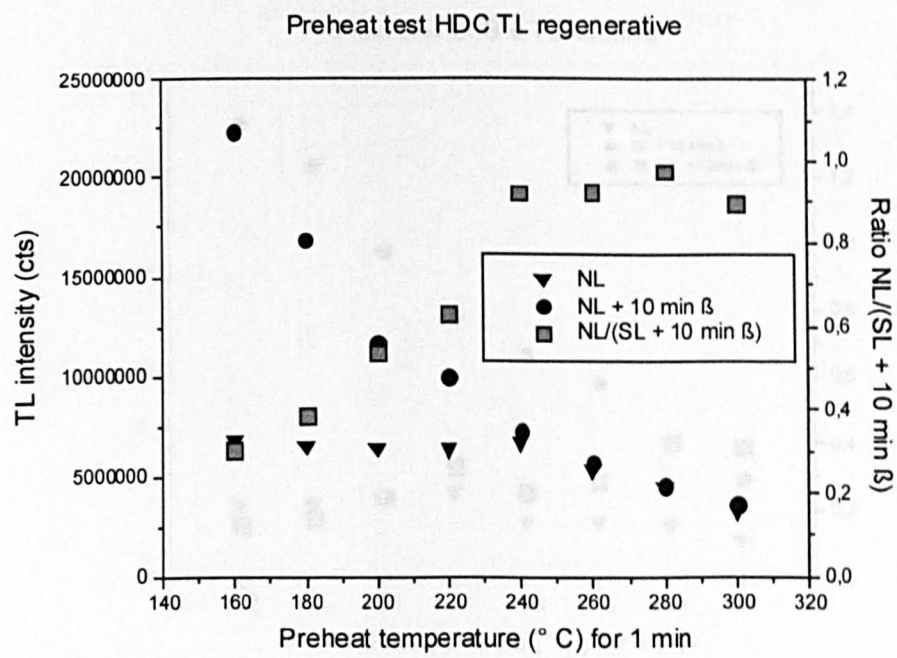

Figure 6.1.1g: Preheat test for the sample HDC TL regenerative.

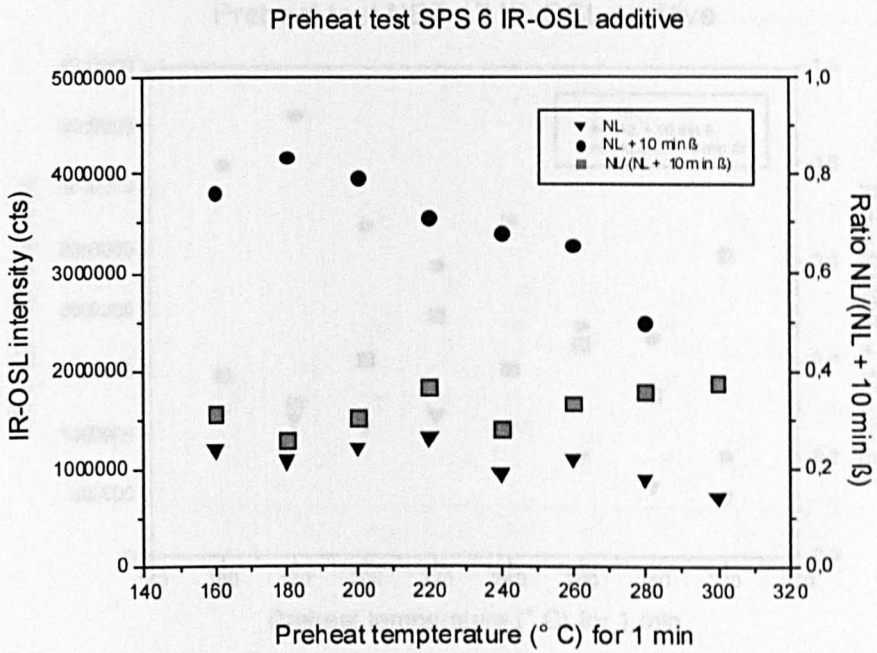

Figure 6.1.1h: Preheat test for the sample SPS 6 IR-OSL additive.

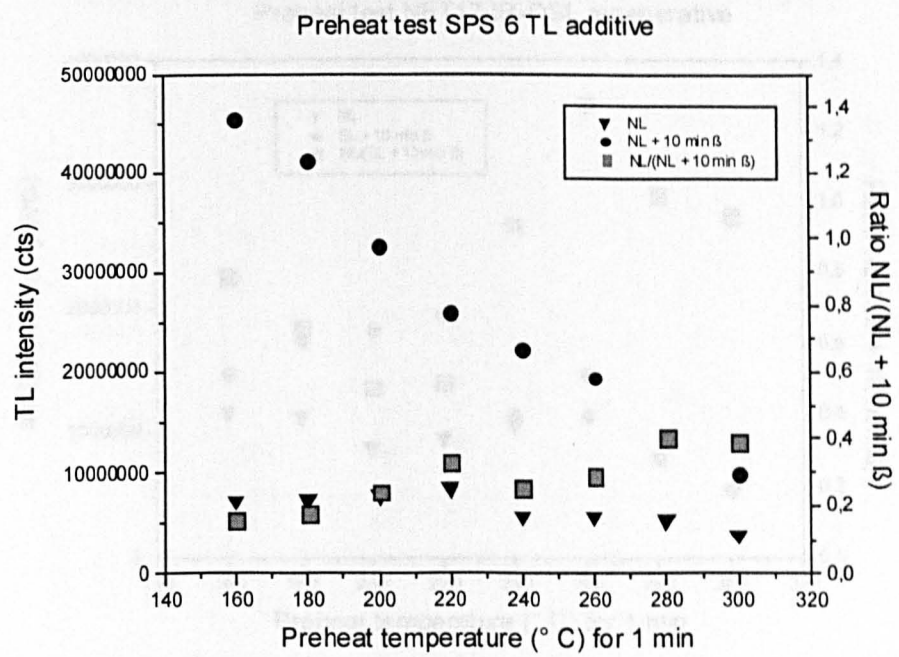

Figure 6.1.1i: Preheat test for the sample SPS 6 TL additive.

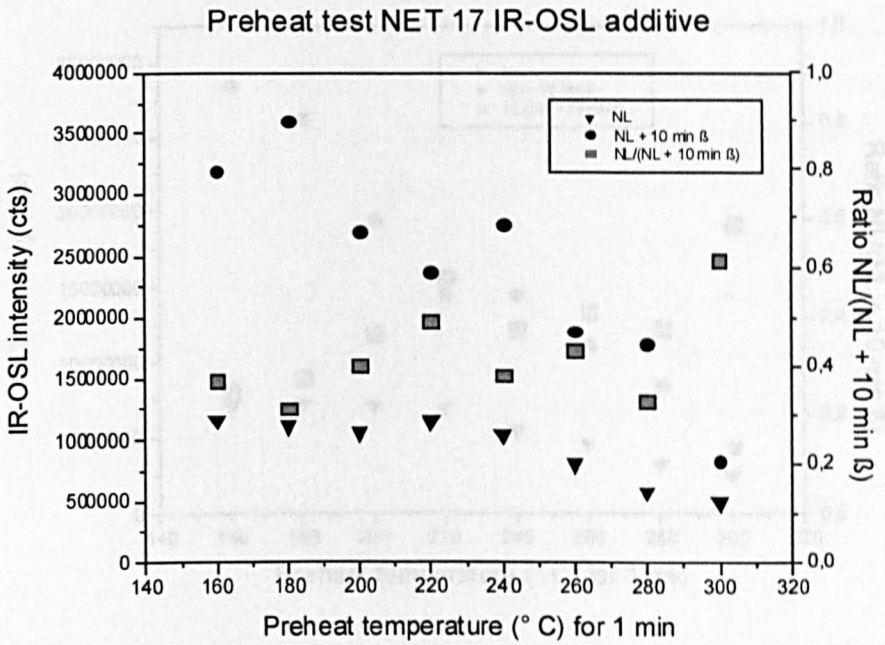

Figure 6.1.1j: Preheat test for the sample NET 17 IR-OSL additive.

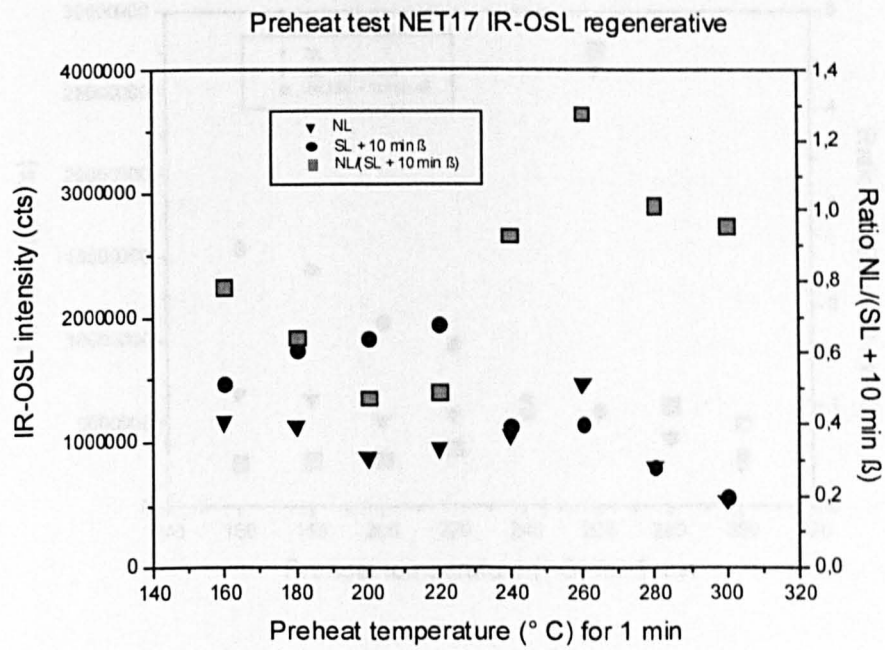

Figure 6.1.1k: Preheat test for the sample NET 17 IR-OSL regenerative.

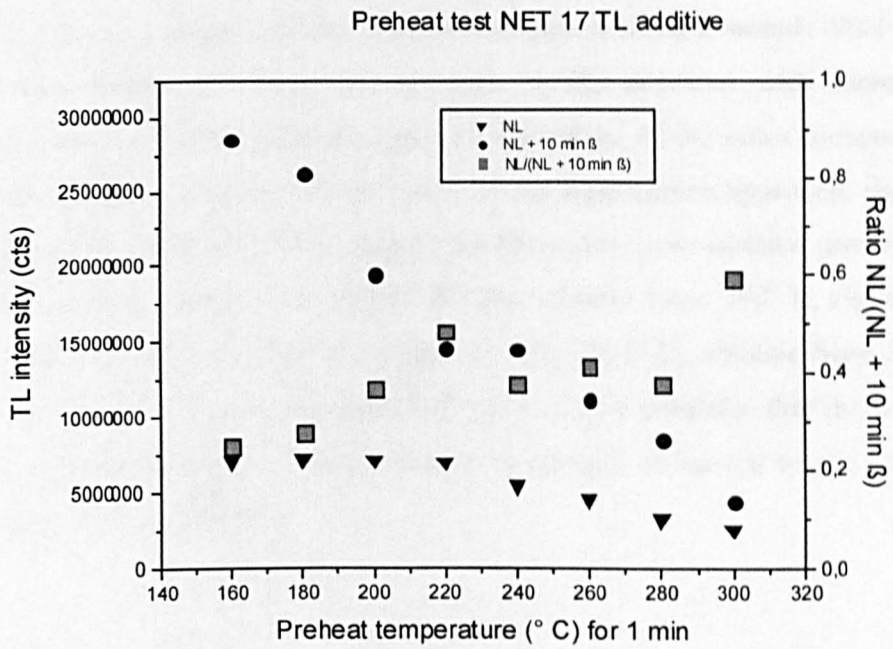

Figure 6.1.1l: Preheat test for the sample NET 17 TL additive.

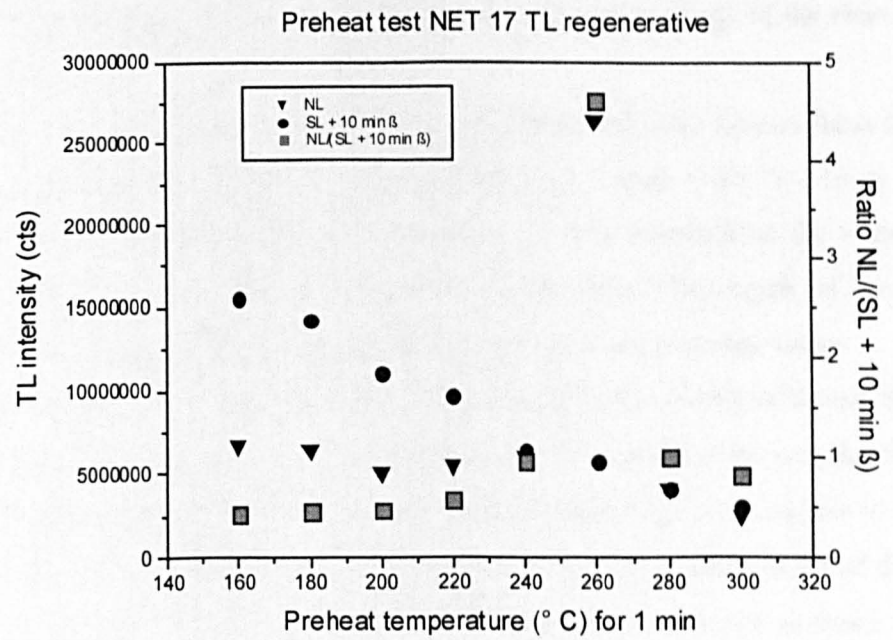

Figure 6.1.1m: Preheat test for the sample NET 17 TL regenerative.

increasing preheat temperature until it reaches a plateau at about 240° C (e.g. Figures 6.1.1e, g). An exception of the regenerative approach builds sample NET 17 TL (Figure 6.1.1m), where the value of the ratio hardly increases with increasing preheat temperatures. For the additive approach the values of the ratios increase over a more gentle gradient compared to the ratios of the regenerative approach, showing either a plateau from around 240° C (Figure 6.1.1f) or for most additive tested samples from earlier preheat temperatures (HDC IR-OSL additive from 180° C, Figure 6.1.1; SPS 6 IR-OSL additive from 160° C, Figure 6.1.1h; SPS 6 TL additive from 220° C, Figure 6.1.1i; NET 17 TL additive from 220° C). It is also noticable that the results from the tests on sample NET 17 scatter relatively strongly compared to the results from the samples HDC and SPS 6.

Fading

The fading tests were carried out on the samples HAB 3, HAB 5, HAB 16, SOP 1, SOP 3, SOP 5, NET 5 and NET 10 (Figures 6.1.1n, o, p, q, r, s, t, u, v). The results below are shown as the values of the ratios of the luminescence intensities of the additive irradiated subsamples divided by the luminescence intensities of the natural signals after varying storage times. The values are expressed in percentage of the ratio from the initial measurement.

The ratio values calculated for the samples from Habonim Quarry from IR-OSL and TL measurements lie within +/- 10 % (HAB 5) or within + 10 %/- 15 % (HAB 3, HAB 16) of the initial value (Figures 6.1.1n, o, p). The variation of the values within these percentages lies within the trend of the mean data. The signals of the tested samples from Habonim Quarry do not decrease with increasing storage times.

The results for the fading tests on the samples from South of Power Station are two-fold (Figures 6.1.1q, r, s). The fading values calculated for the samples SOP 1 and SOP 3 lie in general within +/- 10 % of the initial value (Figure 6.1.1q and r). Single scattered values outside this percentage do not indicate a trend and the ratios of the samples SOP 1 and SOP 3 from the site South of Power Station do not decrease with increasing storage times. Different from the above are the results obtained from sample SOP 5, where the fading values decrease with increasing storage times to about – 20 % from the initial measurements of the IR-OSL and the TL (Figure 6.1.1s).

The samples NET 5 and NET 10 tested from the Netanya South Cliff section show values of the fading ratios compared with the initial IR-OSL and TL measurements of + 10 % to ≥ - 25 % with a clear decrease towards increased storage times (Figures 6.1.1t and u). The values for the sample NET 20 scatter between + 75 %/- 5 % (Figure 6.1.1v). Dotted lines in the figures below represent ± 10 % deviation of the mean data from the initially measured IR-OSL and TL mean values.

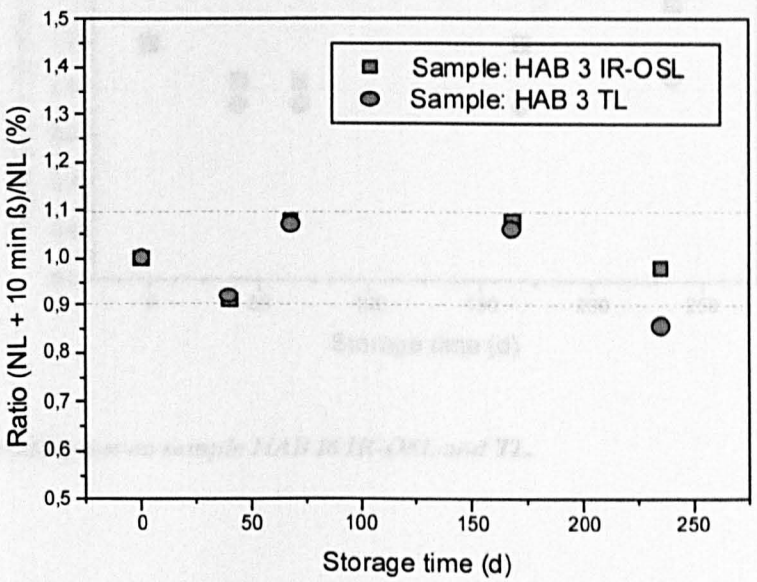

Figure 6.1.1n: Fading test on sample HAB 3 IR-OSL and TL.

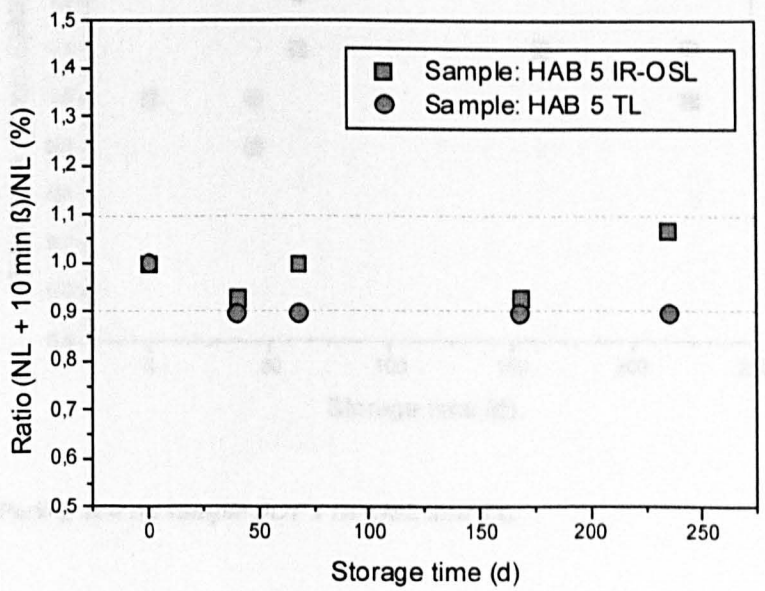

Figure 6.1.1o: Fading test on sample HAB 5 IR-OSL and TL.

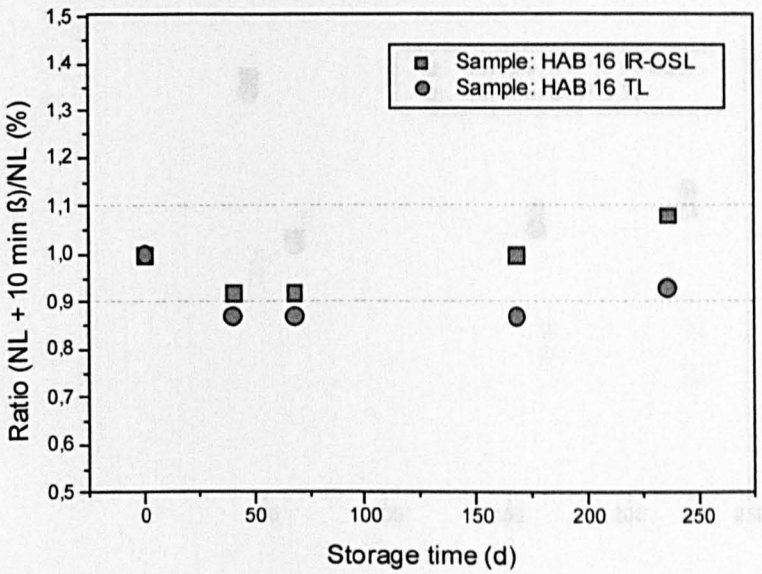

Figure 6.1.1p: Fading test on sample HAB 16 IR-OSL and TL.

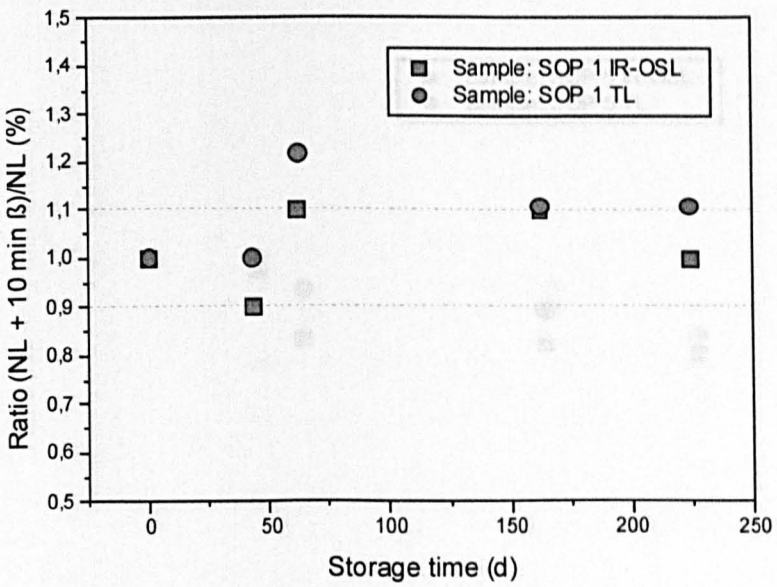

Figure 6.1.1q: Fading test on sample SOP 1 IR-OSL and TL.

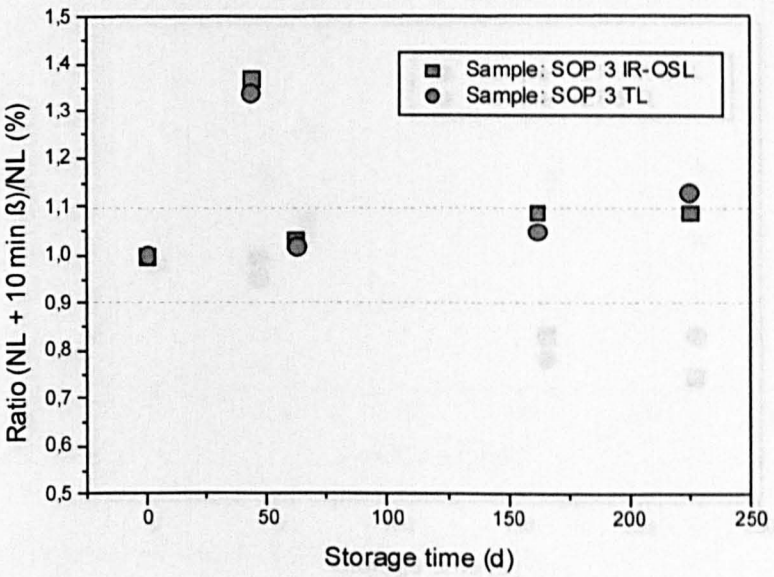

Figure 6.1.1r: Fading test on sample SOP 3 IR-OSL and TL.

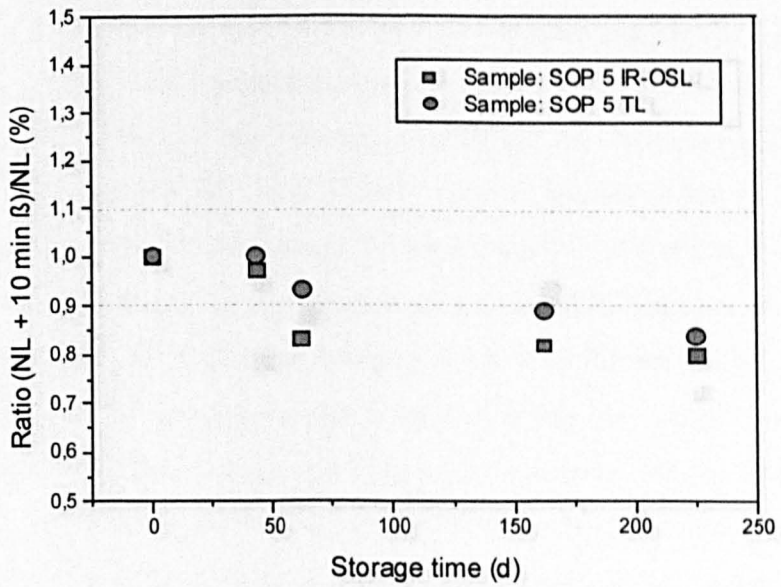

Figure 6.1.1s: Fading test on sample SOP 5 IR-OSL and TL.

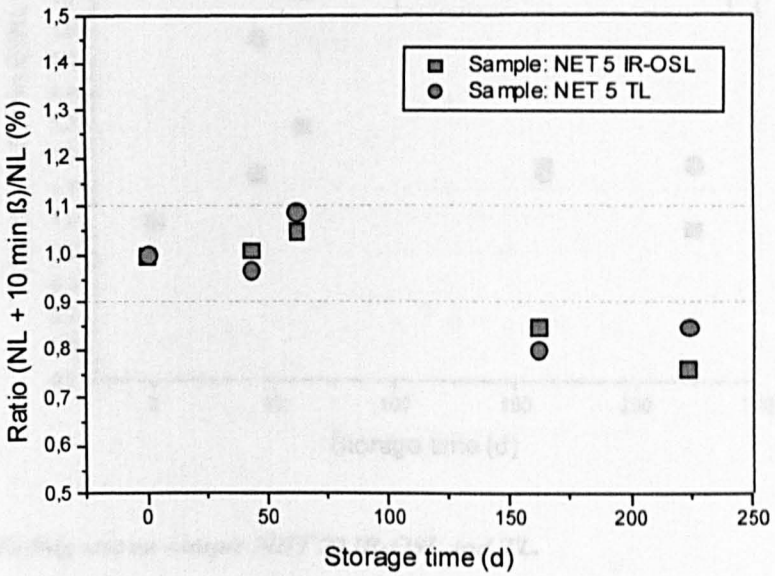

Figure 6.1.1t: Fading test on sample NET 5 IR-OSL and TL.

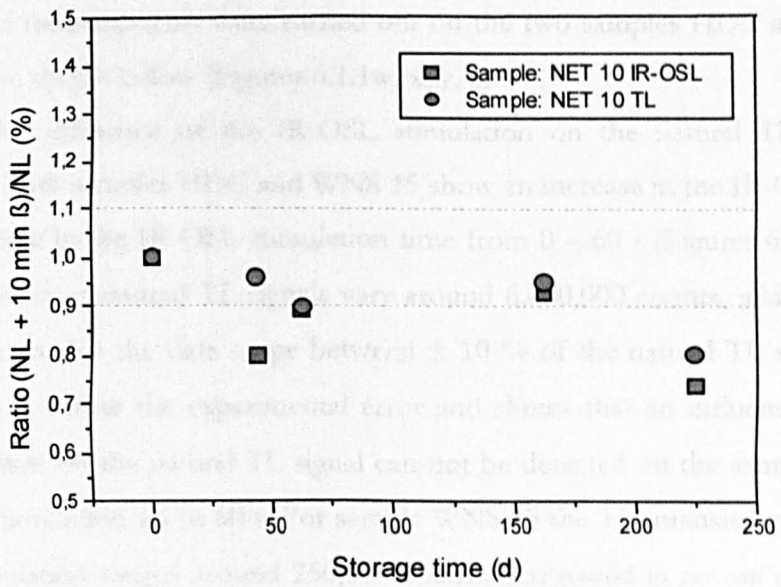

Figure 6.1.1u: Fading test on sample NET 10 IR-OSL and TL.

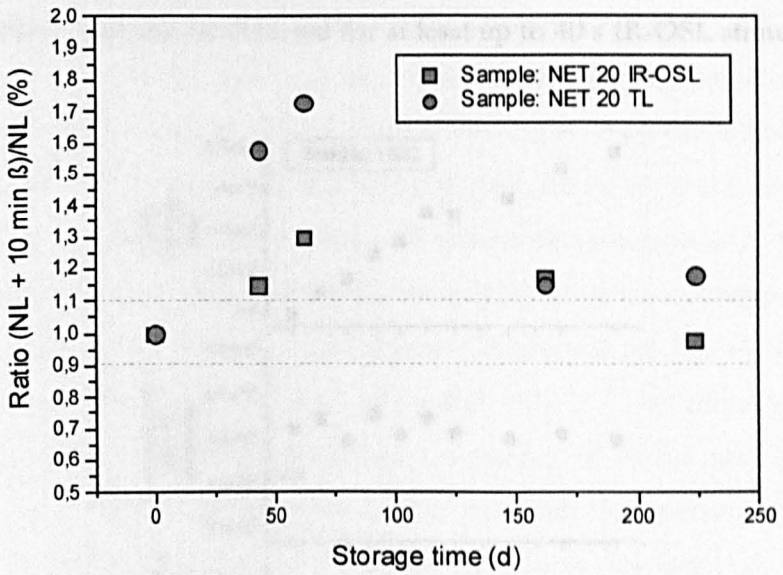

Figure 6.1.1v: Fading test on sample NET 20 IR-OSL and TL.

Combined measurements

The tests on the influence of the IR-OSL stimulation on the intensity of the TL signal in the combined measurements were carried out on the two samples HDC and WNS 15. The results are shown below (Figures 6.1.1w, x, y, z).

In case a) the influence of the IR-OSL stimulation on the natural TL signal was investigated. Both samples HDC and WNS 15 show an increase in the IR-OSL intensity with an increase in the IR-OSL stimulation time from 0 – 60 s (Figures 6.1.1w and x). The subsequently measured TL signals vary around 6,000,000 counts, which expressed in *per cent* shows that the data range between ± 10 % of the natural TL signal (Figure 6.1.1w). This is within the experimental error and shows that an influence of the IR-OSL stimulation on the natural TL signal can not be detected on the sample HDC for an IR-OSL stimulation up to 60 s. For sample WNS 15 the TL intensity measured after IR-OSL stimulation ranges around 250,000 counts. Expressed in *per cent* of the natural TL signal the data range between ± 10 % of the natural TL signal for an IR-OSL stimulation time of up to 40 s and between ± 20 % of the natural TL signal for IR-OSL stimulation times of 50 and 60 s (Figure 6.1.1x). With an assumed standard uncertainty

of 10 % this shows that an influence of the IR-OSL stimulation on the natural TL signal of sample WNS 15 can not be detected for at least up to 40 s IR-OSL stimulation time.

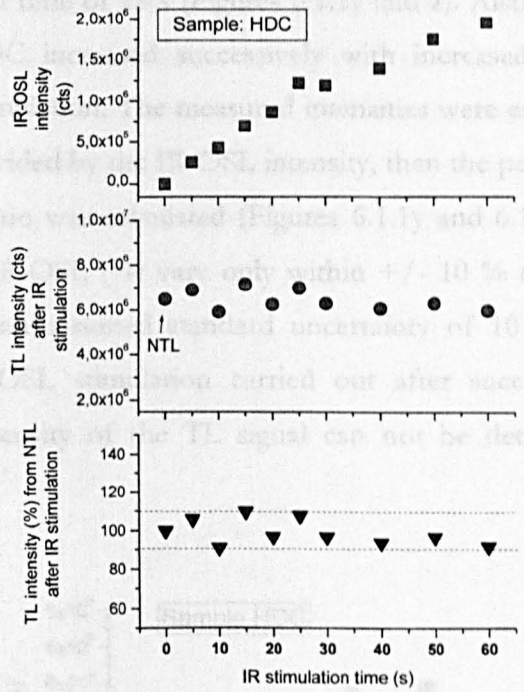

Figure 6.1.1w: Influence of the IR stimulation on the natural TL signal on sample HDC.

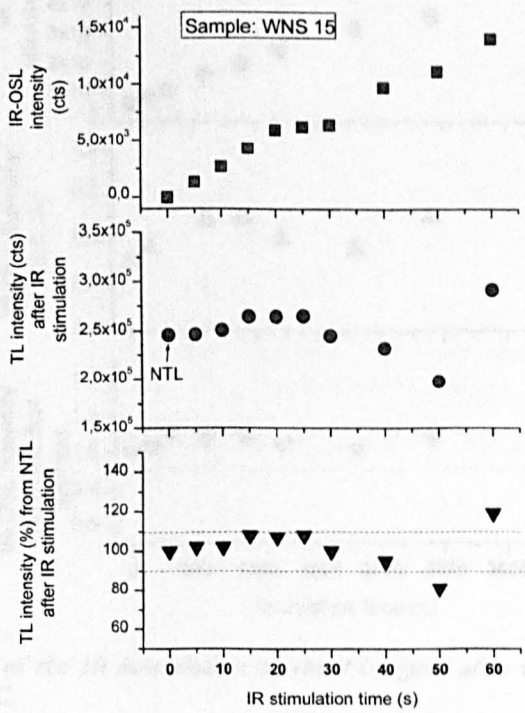

Figure 6.1.1x: Influence of the IR stimulation on the natural TL signal on sample WNS 15.

In case b) the influence of the IR-OSL stimulation on the intensity of the TL signal after varying doses of irradiation was investigated. Of the tested samples HDC and WNS 15 the intensity of the IR-OSL signal increased with increasing irradiation doses (time) and an IR-OSL stimulation time of 25 s (Figures 6.1.1y and z). Also the intensity of the TL signal of sample HDC increased successively with increased irradiation doses and preceding IR-OSL stimulation. The measured intensities were expressed in the quotient of the TL intensity devided by the IR-OSL intensity, then the percentage of the ratios in relation to the first ratio was calculated (Figures 6.1.1y and 6.1.1z). In case of sample HDC the ratios TL/IR-OSL (%) vary only within +/- 10 % of the value of the first ratio. This is within an assumed standard uncertainty of 10 % and shows that an influence of the IR-OSL stimulation carried out after successive higher doses of irradiation on the intensity of the TL signal can not be detected on sample HDC (Figure6.1.1y).

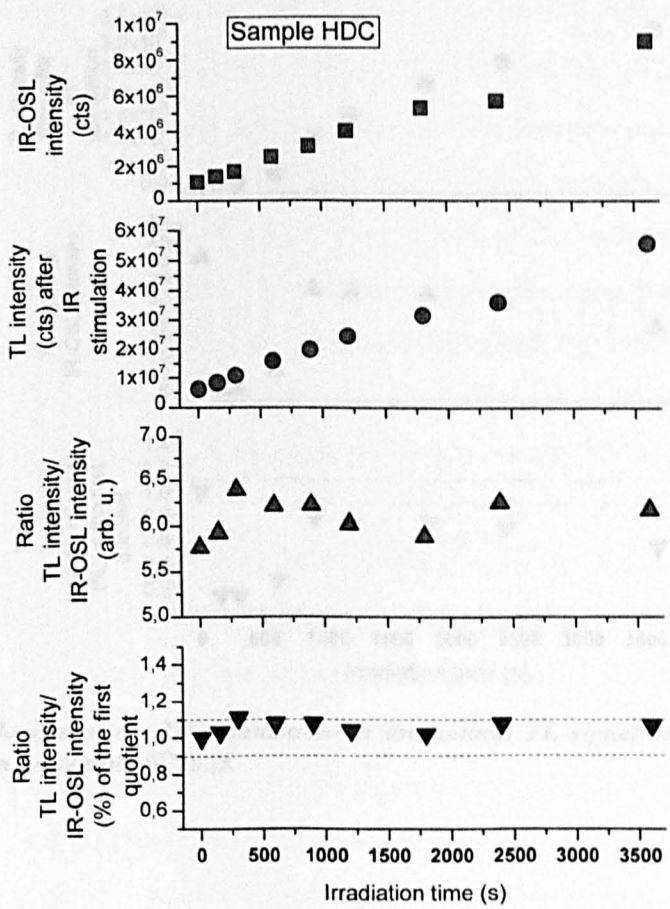

Figure 6.1.1y: Influence of the IR stimulation on the TL signal after varying doses of irradiation on sample HDC.

While the IR-OSL intensity of sample WNS 15 increases steadily with successive higher irradiation doses, this is not the case for the TL intensity of the lower irradiation doses (Figure 6.1.1z). This leads to an initial scatter of the TL/IR-OSL ratios (arb. u.) (%) and can have different reasons. The values of the ratios TL/IR-OSL (%) decrease systematically for the subsamples measured with higher irradiation doses to about – 40 % of the initial ratio. An influence of the IR-OSL measurements prior to the TL measurements on the intensity of the TL signal with successive higher irradiation doses cannot be excluded for the tested sample WNS 15 (cp. Chapter 7.1.1).

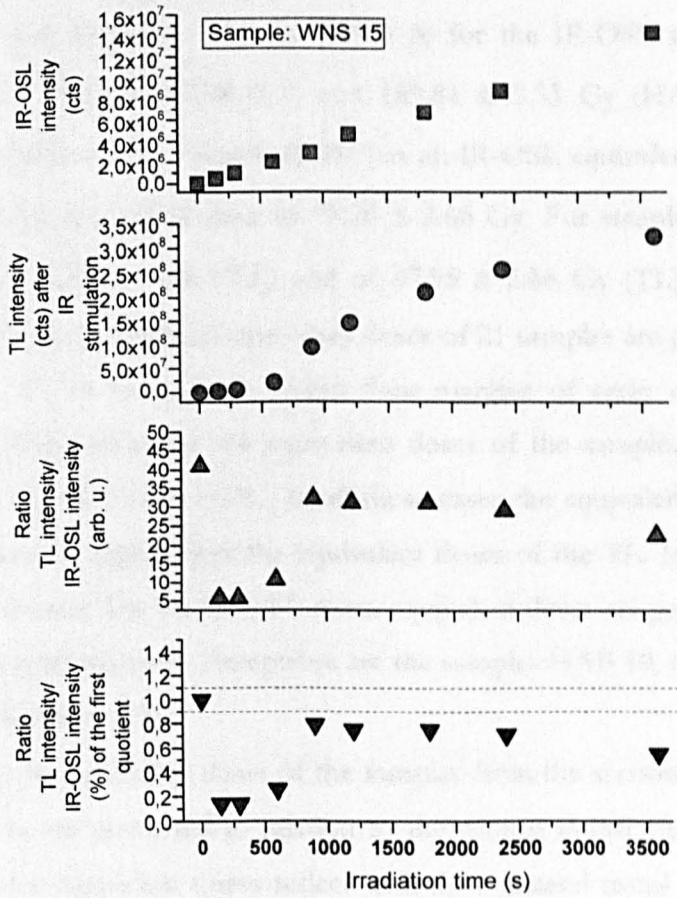

Figure 6.1.1z: Influence of the IR stimulation on the natural TL signal after varying doses of irradiation on sample WNS 15.

6.1.2 MAAD equivalent doses

The determination of equivalent doses brings into the age calculation information from the luminescence measurements (cp. Chapter 4). This information reflects the behaviour of the individual dosimeters measured and mirrors also their exposition to varying environmental dose rates.

Habonim Quarry, Dor-Habonim Nature Reserve Middle Ridge, Dor-Habonim Nature Reserve Coast

The equivalent doses for the samples of Habonim Quarry range between 53.33 ± 3.52 Gy (HAB-II-1) and 191.81 ± 7.33 Gy (HAB 8) for the IR-OSL measurements and between 51.57 ± 2.93 Gy (HAB-II-1) and 189.81 ± 5.33 Gy (HAB 8) for the TL measurements (Table 6.1.2a). Sample HDM has an IR-OSL equivalent dose of 96.57 ± 3.33 Gy and an TL equivalent dose of 71.26 ± 2.66 Gy. For sample HDC equivalent doses of 65.27 ± 5.33 Gy (IR-OSL) and of 47.95 ± 2.66 Gy (TL) were determined (Table 6.1.2a). From 42 obtained equivalent doses of 21 samples are paired data sets for 15 samples (71 %) in congruence within their margins of error or near agreement (Figure 6.1.2a). Exceptions are the equivalent doses of the samples HAB 6, HAB 7, HAB 15, HAB 16, HDM and HDC. In all these cases the equivalent doses of the IR-OSL are considerably higher than the equivalent doses of the TL. It is also prominent throughout the dataset that the IR-OSL mean equivalent doses are generally higher than the TL mean equivalent doses. Exceptions are the samples HAB 10, HAB 13, HAB-II-5 and HAB-II-9 (Figure 6.1.2a).

In Figure 6.1.2b the equivalent doses of the samples from the section in the East wall at Habonim Quarry are presented in relation to the sample depth and in stratigraphical order. Already the equivalent doses reflect with their general trend the stratigraphy of the section with lower equivalent doses at the top of the section and higher equivalent doses at the lower parts of the profile. Samples HAB 5, HAB 6, HAB 8 and HAB 9 show the highest equivalent doses of this section. As these samples are from well developed pedogenic horizons (Chapter 3.2.1) it can be expected that these higher equivalent doses are associated with respectively higher environmental dose rates of the soils. Considering well developed or weak pedogenic and non-pedogenic horizons, the equivalent doses reflect generally the stratigraphy of the section.

Table 6.1.2a: IR-OSL and TL equivalent doses (D_e) of the samples from Habonim Quarry, Dor-Habonim Nature Reserve Middle Ridge and Dor-Habonim Nature Reserve Coast. Samples are not in stratigraphical order.

Sample	Depth (m)	D_e IR-OSL (Gy)	D_e TL (Gy)	Ratio D_e IR-OSL/ D_e TL
HAB 1	9.00	59.27 ± 3.33	57.28 ± 2.66	1.03
HAB 2	7.20	64.60 ± 3.30	60.61 ± 2.66	1.07
HAB 3	6.10	67.93 ± 2.66	65.27 ± 2.66	1.04
HAB 4	8.90	151.85 ± 4.66	142.52 ± 4.00	1.07
HAB 5	7.75	155.18 ± 4.66	153.18 ± 5.99	1.01
HAB 6	7.45	165.17 ± 4.00	151.85 ± 3.33	1.09
HAB 7	6.75	149.18 ± 4.66	133.87 ± 3.33	1.11
HAB 8	6.25	191.81 ± 7.33	189.81 ± 5.33	1.01
HAB 9	6.05	171.35 ± 7.19	163.84 ± 5.89	1.05
HAB 10	5.55	105.95 ± 2.62	113.14 ± 3.27	0.94
HAB 11	5.25	107.23 ± 5.33	108.56 ± 5.33	0.99
HAB 12	4.50	79.25 ± 2.66	77.92 ± 2.66	1.02
HAB 13	4.20	75.92 ± 3.33	79.92 ± 6.66	0.95
HAB 14	3.60	---[1]	---[1]	---
HAB 15	4.45	77.26 ± 3.33	65.93 ± 2.66	1.17
HAB 16	10.45	158.51 ± 4.00	110.56 ± 2.00	1.43
HAB-II-1	1.40	53.33 ± 3.52	51.57 ± 2.93	1.03
HAB-II-4	2.50	79.70 ± 6.25	70.91 ± 5.86	1.12
HAB-II-5	3.20	141.23 ± 5.27	142.40 ± 4.69	0.99
HAB-II-9	2.60	150.54 ± 5.95	149.94 ± 5.95	1.00
HDM	0.50	96.57 ± 3.33	71.26 ± 2.66	1.36
HDC	0.50	65.27 ± 5.33	47.95 ± 2.66	1.36

[1]The equivalent doses for sample HAB14 could not be determined due to a technical failure and an additional shortage of sample material.

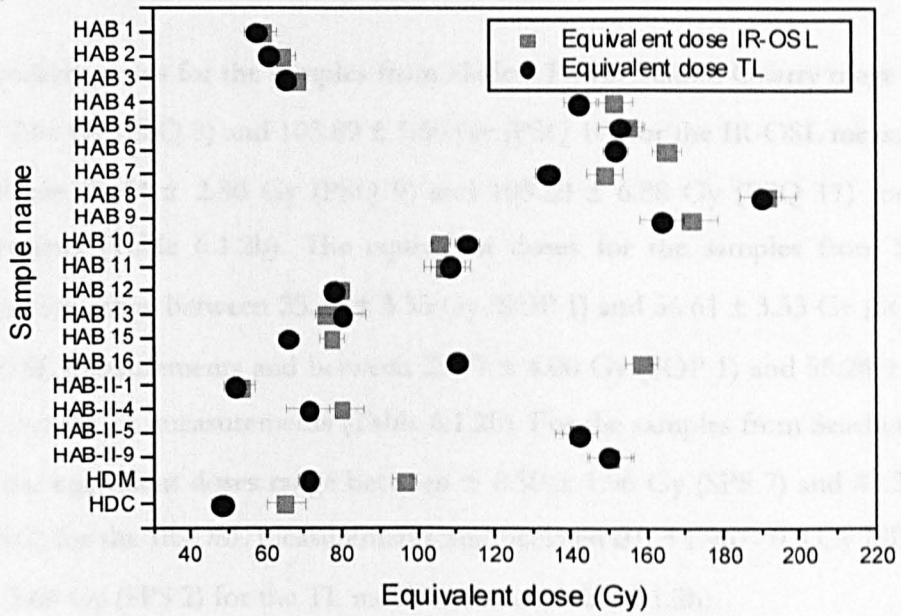

Figure 6.1.2a: Comparison of the IR-OSL and TL equivalent doses of the samples from the sections at Habonim Quarry, Dor-Habonim Nature Reserve Middle Ridge and Dor-Habonim Nature Reserve Coast. The samples and the equivalent doses shown are not in stratigraphical order.

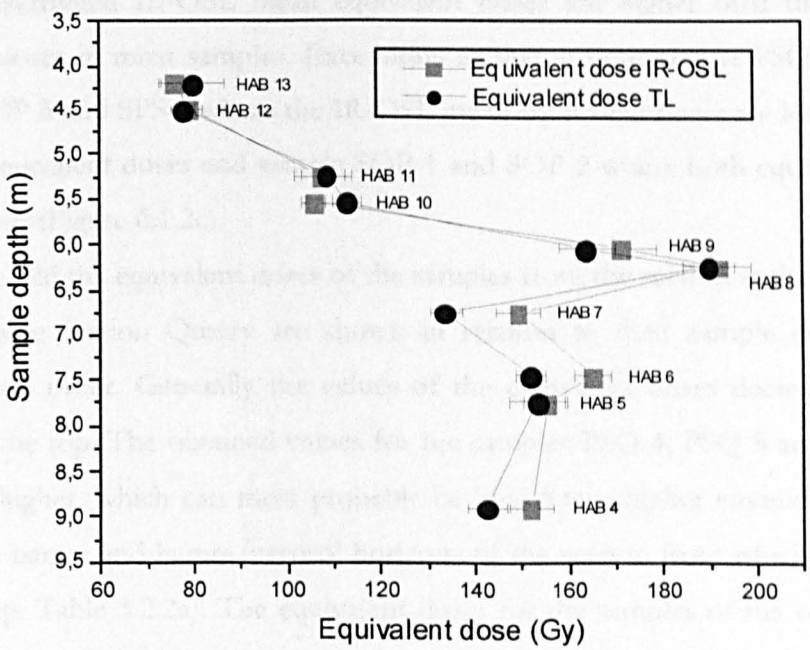

Figure 6.1.2b: Equivalent doses of the samples from the section at the East-wall at Habonim Quarry in relation to their sample depth.

The equivalent doses for the samples from Hadera Power Station Quarry range between 17.53 ± 7.01 Gy (PSQ 8) and 103.89 ± 5.50 Gy (PSQ 10) for the IR-OSL measurements and between 29.44 ± 2.80 Gy (PSQ 9) and 103.20 ± 6.88 Gy (PSQ 11) for the TL measurements (Table 6.1.2b). The equivalent doses for the samples from South of Power Station range between 25.31 ± 3.33 Gy (SOP 1) and 56.61 ± 3.33 Gy (SOP 3) for the IR-OSL measurements and between 25.97 ± 4.00 Gy (SOP 1) and 55.28 ± 3.33 Gy (SOP 3) for the TL measurements (Table 6.1.2b). For the samples from Seashore Power Station the equivalent doses range between ≤ 8.50 ± 1.96 Gy (SPS 7) and 43.29 ± 2.00 Gy (SPS 2) for the IR-OSL measurements and between 0.0 +1.96/- 0.0 Gy (SPS 8) and 32.63 ± 2.66 Gy (SPS 2) for the TL measurements (Table 6.1.2b).

From 44 obtained IR-OSL and TL equivalent doses of 24 samples are 30 equivalent doses in congruence with their margin of error or near agreement (Figure 6.1.2 c). This equals 75 % if one disregards the samples PSQ 2, PSQ 5, PSQ 7 and PSQ 8 from which only one equivalent dose could be obtained. Samples with IR-OSL and TL doses are not in agreement within their margins of error are PSQ 12, SPS 2, SPS 3, SPS 7 and SPS 8 (Figure 6.1.2c). Disregarding the samples with only one equivalent dose it is distinctive, that the determined IR-OSL mean equivalent doses are higher than the TL mean equivalent doses in most samples. Exceptions to that are the sample PSQ 6, PSQ 11, PSQ 12, SOP 5 and SPS 6 where the IR-OSL mean equivalent doses are lower than the TL mean equivalent doses and sample SOP 1 and SOP 2 where both equivalent doses are congruent (Figure 6.1.2c).

In Figure 6.1.2d the equivalent doses of the samples from the section at the East-wall at Hadera Power Station Quarry are shown in relation to their sample depth and in stratigraphical order. Generally the values of the equivalent doses decrease from the bottom to the top. The obtained values for the samples PSQ 4, PSQ 5 and PSQ 6 are somewhat higher, which can most probably be linked to a higher environmental dose rates in the hamra and hamra/vertisol horizons of the section from which the samples originate (cp. Table 3.2.2a). The equivalent doses for the samples of the section at the West-wall at Hadera Power Station Quarry increase with depth (Figure 6.1.2e). Figure 6.1.2f shows the equivalent doses of the samples from the section at the North-wall at South of Power Station in relation to their sample depth. Generally the equivalent doses

from the top of the sequence are lower than from the bottom of the section. Only that the equivalent doses of the samples SOP 2, SOP 3 and SOP 4 are somewhat higher compared to the top or bottom ones. This possibly reflects high environmental dose rates in the weakly developed soils (SOP 3, SOP 4) and adjacent aeolianite (SOP 2). Similarily, the equivalent doses shown in relation to their sample depth from a part of the section Seashore Power Station increase with depth (Figure 6.1.2g).

Table 6.1.2b: IR-OSL and TL equivalent doses (D_e) of the samples from Hadera Power Station Quarry, South of Power Station, Seashore Power Station. Samples are not in stratigraphical order.

Sample	Depth (m)	D_e IR-OSL (Gy)	D_e TL (Gy)	Ratio D_e IR-OSL/ D_e TL
PSQ 1	0.50	58.18 ± 4.21	54.68 ± 3.51	1.06
PSQ 2	0.75	≤[1] 25.24 ± 5.61	---[2]	---
PSQ 3	3.05	35.75 ± 7.01	30.14 ± 6.31	1.19
PSQ 4	2.50	44.86 ± 4.91	39.26 ± 3.51	1.14
PSQ 5	2.10	---[2]	39.26 ± 4.21	---
PSQ 6	1.55	35.75 ± 7.71	38.56 ± 7.71	0.93
PSQ 7	1.00	18.93 ± 8.41	---[2]	---
PSQ 8	0.50	17.53 ± 7.01	---[2]	---
PSQ 9	0.25	33.65 ± 2.80	29.44 ± 2.80	1.14
PSQ 10	0.55	103.89 ± 5.50	93.57 ± 6.19	1.11
PSQ 11	0.85	101.14 ± 6.19	103.20 ± 6.88	0.98
PSQ 12	5.50	(34.35 ± 11.22)[3]	60.29 ± 4.21	---
SOP 1	0.25	25.31 ± 3.33	25.97 ± 4.00	0.97
SOP 2	2.40	37.96 ± 2.66	37.96 ± 2.00	1.00
SOP 3	2.60	56.61 ± 3.33	55.28 ± 3.33	1.02
SOP 4	3.60	52.61 ± 4.00	46.62 ± 2.66	1.13
SOP 5	5.30	32.63 ± 4.00	35.30 ± 2.66	0.92
SPS 1	0.50	37.30 ± 2.00	34.63 ± 1.33	1.08
SPS 2	1.60	43.29 ± 2.00	32.63 ± 2.66	1.33
SPS 3	0.20	≤[1] 9.32 ± 1.33	2.66 ± 2.0	---
SPS 5	1.20	36.62 ± 3.27	32.05 ± 2.62	1.14
SPS 6	0.80	20.93 ± 2.62	23.54 ± 3.27	0.89
SPS 7	0.60	≤[1] 8.50 ± 1.96	0.65 + 2.62/- 0.65	---
SPS 8	0.25	≤[1] 10.46 ± 1.96	0.0 + 1.96/- 0.0	---

Sample SPS 4 is missing because it is a pumice sample, not a luminescence sample.
[1]Background not subtracted, because natural luminescence/background ratio too low.
[2]D_e calculation not possible. Natural luminescence signal is not detectable against the background noise.
[3]Eventually partially bleached during sampling process. Difficult to sample through alternating hard and loose layers.

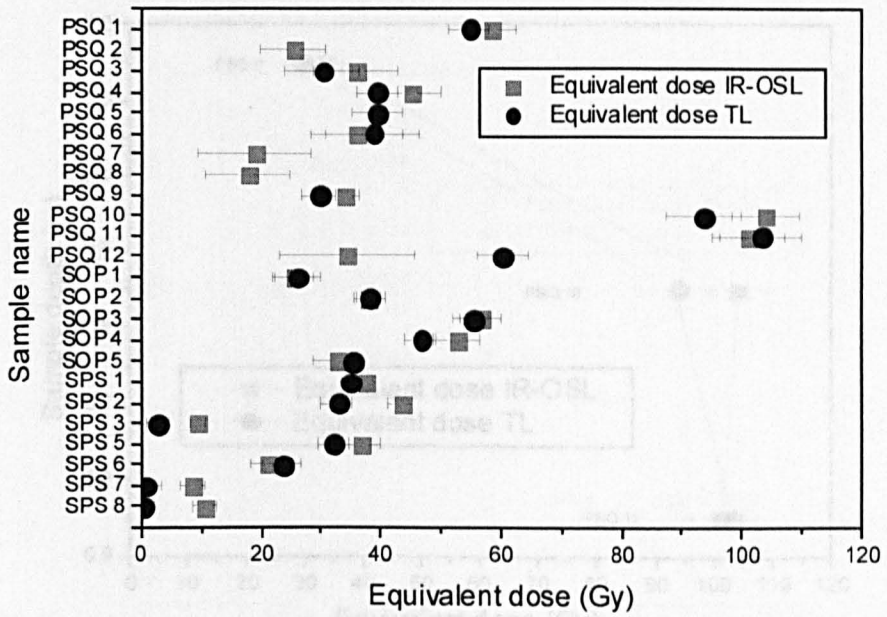

Figure 6.1.2c: Comparison of the IR-OSL and TL equivalent doses of the samples from the sections at Hadera Power Station Quarry, South of Power Station and Seashore Power Station. The samples and the equivalent doses shown are not in stratigraphical order.

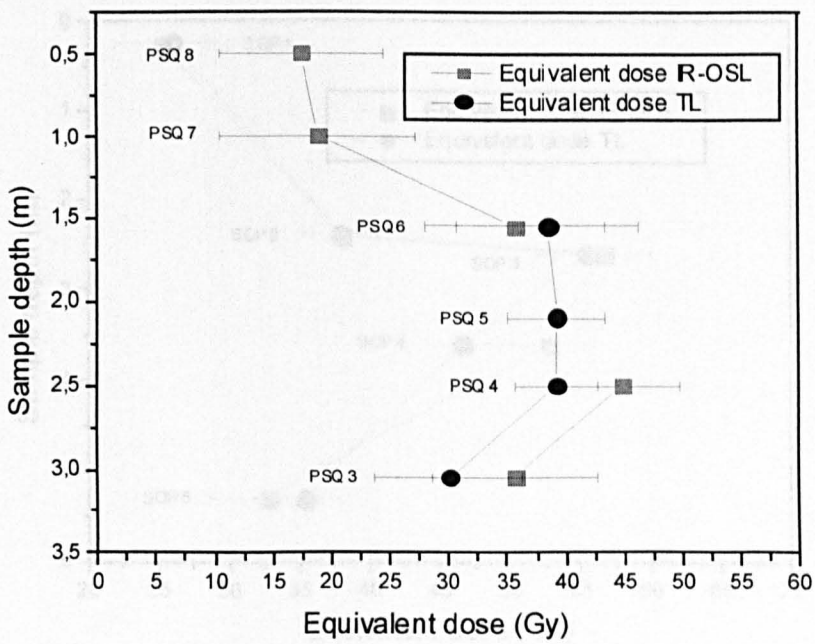

Figure 6.1.2d: Equivalent doses of the samples from the section at the East-wall at Hadera Power Station Quarry in relation to their sample depth.

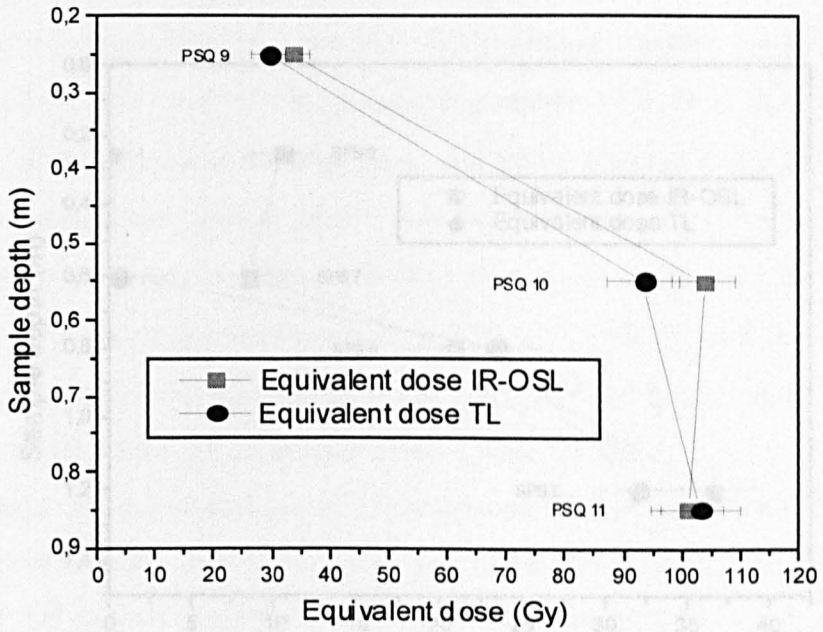

Figure 6.1.2e: Equivalent doses of the samples from the section at the West-wall at Hadera Power Station Quarry in relation to their sample depth.

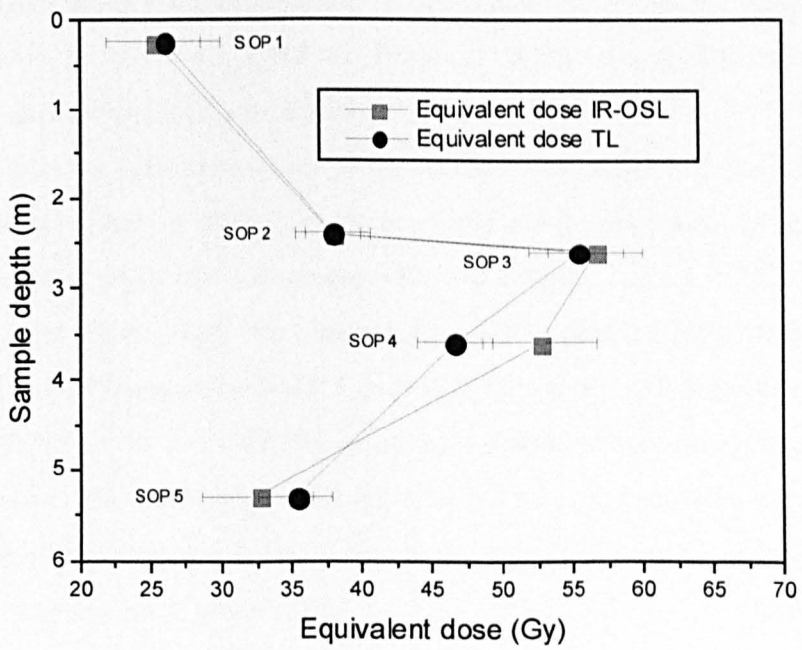

Figure 6.1.2f: Equivalent doses of the samples from the section at the North-wall at South of Power Station in relation to their sample depth.

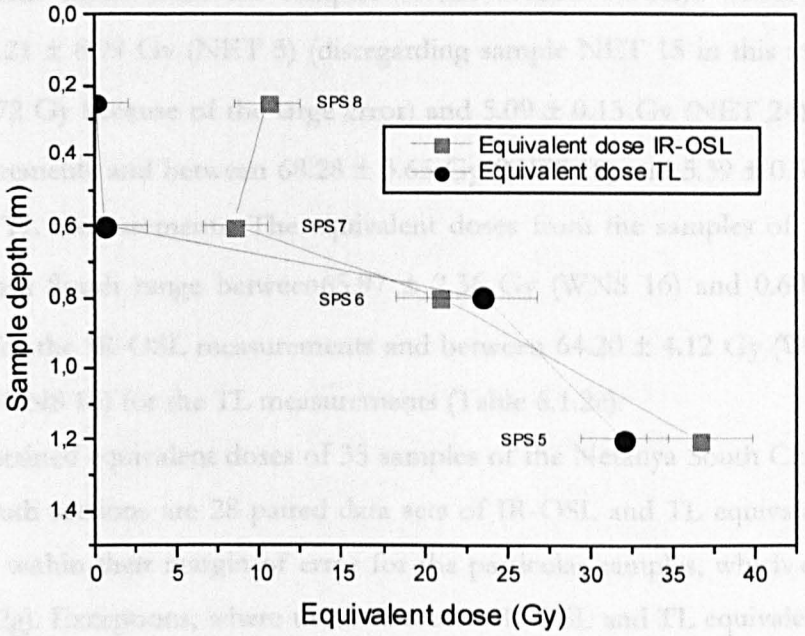

Figure 6.1.2g: Equivalent doses of the samples from a part of the section Seashore Power Station in relation to their sample depth.

Netanya South Cliff, Wadi Netanya South

The equivalent doses from the samples of the section Netanya South Cliff range between 74.21 ± 8.99 Gy (NET 5) (disregarding sample NET 15 in this instance with 82.26 ± 21.72 Gy because of the large error) and 5.09 ± 0.15 Gy (NET 24) for the IR-OSL measurements and between 68.28 ± 3.65 Gy (NET 18) and 5.39 ± 0.30 Gy (NET 22) for the TL measurements. The equivalent doses from the samples of the sections Wadi Netanya South range between65.97 ± 2.36 Gy (WNS 16) and 0.60 ± 0.60 Gy (WNS 14) for the IR-OSL measurements and between 64.20 ± 4.12 Gy (WNS 16) and 0.0 + 0.59 (WNS 15) for the TL measurements (Table 6.1.2c).

From 66 obtained equivalent doses of 35 samples of the Netanya South Cliff and Wadi Netanya South sections are 28 paired data sets of IR-OSL and TL equivalent doses in congruence within their margin of error for the particular samples, which equals 80 % (Figure 6.1.2g). Exceptions, where the determined IR-OSL and TL equivalent doses for any one sample are not in agreement within the margins of errors, are the samples NET 3, NET 15, NET 19, NET 20, NET 21 and NET 23. The IR-OSL mean equivalent doses are tendentially higher than the TL mean equivalent doses for a number of samples. Exceptions are the samples NET 4, NET 12, NET 13 where the IR-OSL mean equivalent doses are lower than the TL equivalent doses and the samples NET 11, NET 24, WNS 10, WNS 11, WNS 12, WNS 13, WNS 14 and WNS 15 where both equivalent doses are equal (Figure 6.1.2h).

In Figure 6.1.2h the equivalent doses obtained from the samples of the Netanya South Cliff section are shown in relation to their sample depth. The values of the equivalent doses are clearly devided into two clusters. For the samples NET 1 to NET 4 and NET 7 to NET 18 the values range *circa* between 40 – 70 Gy, that is disregarding the IR-OSL equivalent doses of the samples NET 3 and NET 15 which seem overestimated. For the samples NET 19 to NET 24 the values of the equivalent doses range between 5 – 20 Gy and increase with depth (Figure 6.1.2h). The values of the equivalent doses from the samples of the Wadi Netanya South increase clearly from the top towards the bottom of the sections (Figures 6.1.2j and 6.1.2k).

Table 6.1.2c: IR-OSL and TL equivalent doses (D_e) of the samples from Netanya South Cliff and Wadi Netanya South. Samples are not in stratigraphical order.

Sample	Depth (m)	D_e IR-OSL (Gy)	D_e TL (Gy)	Ratio D_e IR-OSL/ D_e TL
NET 1	35.10	66.15 ± 8.13	56.74 ± 5.39	1.17
NET 2	34.30	61.98 ± 4.18	57.50 ± 1.75	1.08
NET 3	33.30	84.08 ± 13.75	55.29 ± 6.08	1.52
NET 4	32.70	62.89 ± 4.48	67.29 ± 5.54	0.93
NET 5	14.50	74.21 ± 8.66	61.07 ± 4.48	1.22
NET 6	12.00	60.23 ± 7.37	57.65 ± 5.39	1.04
NET 7	31.80	49.29 ± 6.38	39.19 ± 5.09	1.26
NET 8	29.40	62.51 ± 5.77	53.01 ± 5.77	1.18
NET 9	27.10	63.91 ± 10.89	53.92 ± 9.55	1.19
NET 10	25.70	66.22 ± 6.12	64.43 ± 5.97	1.03
NET 11	24.30	45.04 ± 3.95	45.57 ± 4.03	0.99
NET 12	22.80	47.39 ± 7.44	48.38 ± 4.63	0.98
NET 13	22.30	54.38 ± 6.08	63.50 ± 8.73	0.86
NET 14	21.60	55.29 ± 7.37	49.90 ± 6.00	1.10
NET 15	20.50	82.26 ± 21.72	54.69 ± 3.19	1.50
NET 16	16.00	53.62 ± 9.19	45.04 ± 7.14	1.19
NET 17	11.00	54.91 ± 6.23	51.88 ± 7.60	1.06
NET 18	7.80	68.66 ± 6.08	68.28 ± 3.65	1.01
NET 19	6.60	18.94 ± 1.72	13.20 ± 1.27	1.43
NET 20	4.60	18.20 ± 3.88	11.71 ± 1.64	1.57
NET 21	4.10	15.34 ± 1.14	8.51 ± 0.53	1.80
NET 22	1.30	6.81 ± 0.30	5.39 ± 0.30	1.26
NET 23	0.90	12.08 ± 0.53	6.84 ± 0.23	1.77
NET 24	0.10	5.09 ± 0.15	5.85 ± 0.38	0.87
WNS 10	3.20	5.98 ± 1.79	5.38 ± 1.20	1.11
WNS 11	2.55	3.59 ± 1.20	3.59 ± 1.20	1.00
WNS 12	2.00	---[1]	4.19 ± 1.20	---
WNS 13	1.60	1.79 ± 0.60	2.39 ± 0.60	0.75
WNS 14	1.15	0.60 ± 0.60	1.20 ± 1.20	0.50
WNS 15	0.70	---[2]	0.0 ± 0.59	---
WNS 16	6.00	65.97 ± 2.36	64.20 ± 4.12	1.03
WNS 17	4.75	50.07 ± 1.77	45.94 ± 2.36	1.09
WNS 18	4.25	33.32 ± 1.19	32.13 ± 1.19	1.04
WNS 19	3.65	19.04 ± 1.19	17.85 ± 1.79	1.06
WNS 20	3.00	---[3]	---[3]	---

[1] D_e calculation not possible. Signal intensity too low which resulted in scatter.
[2] D_e calculation not possible. Natural luminescence/background ratio too small.
[3] D_e calculation not possible. No signal increase responding to dose (saturation?).

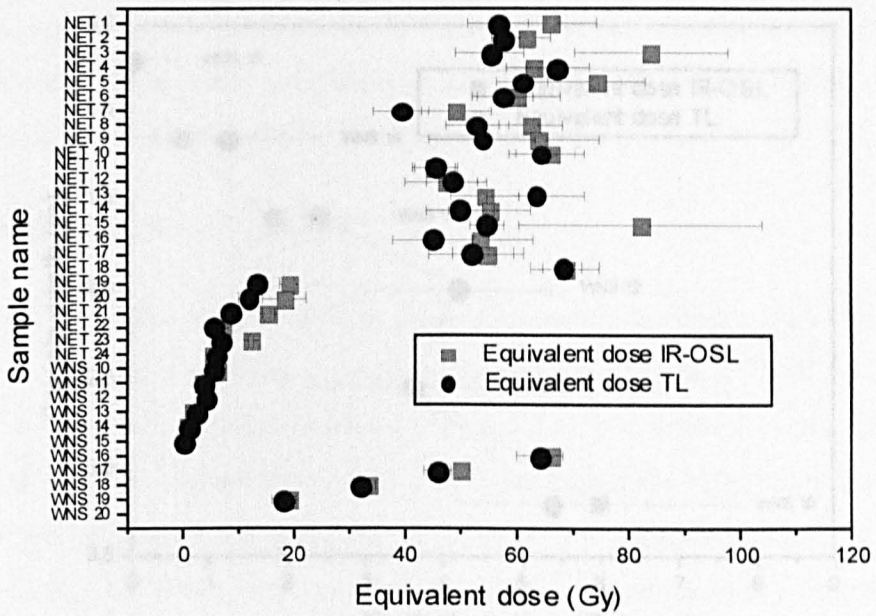

Figure 6.1.2g: Comparison of the IR-OSL and TL equivalent doses of the samples from the sections at Netanya South Cliff and at Wadi Netanya South. The samples and equivalent doses shown are not in stratigraphical order.

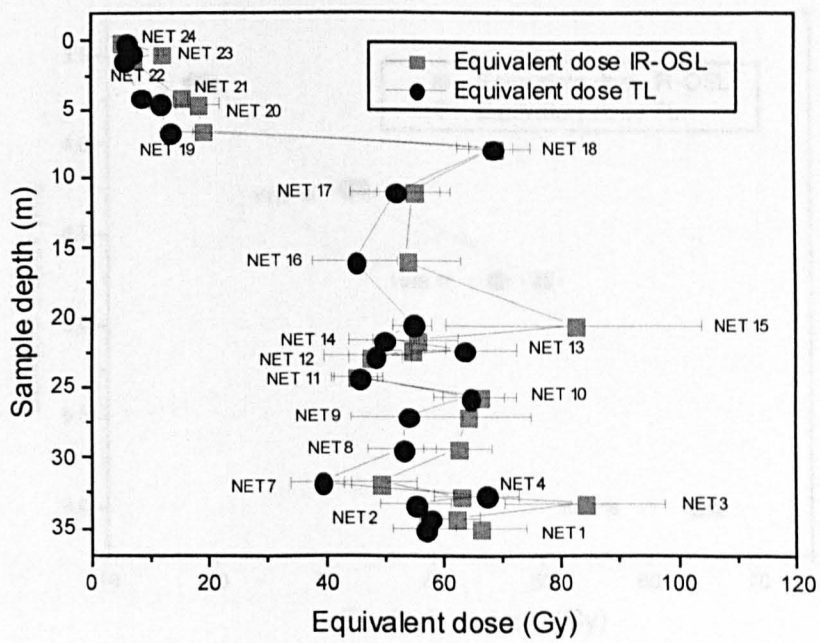

Figure 6.1.2h: Equivalent doses of the samples from the section at the Netanya South Cliff in relation to their sample depth.

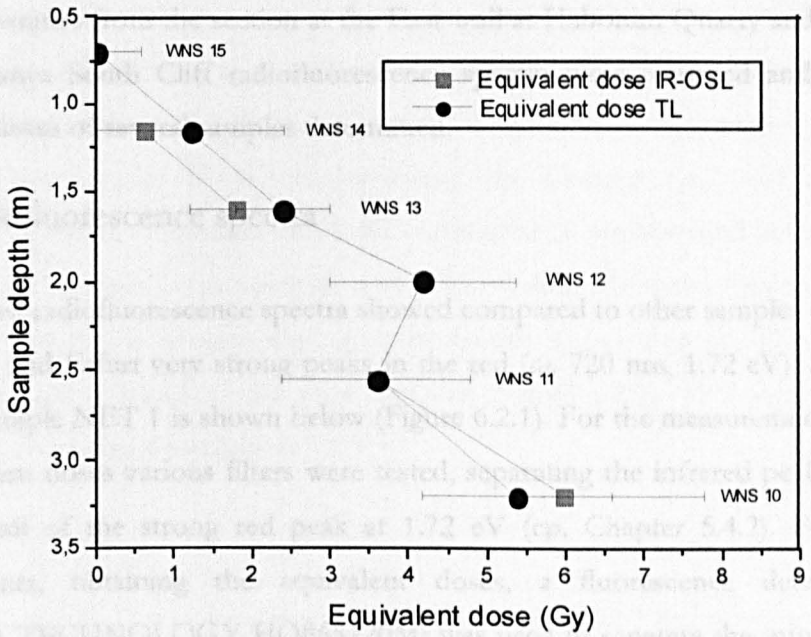

Figure 6.1.2i: Equivalent doses of the samples from the western section at the Wadi Netanya South in relation to their sample depth.

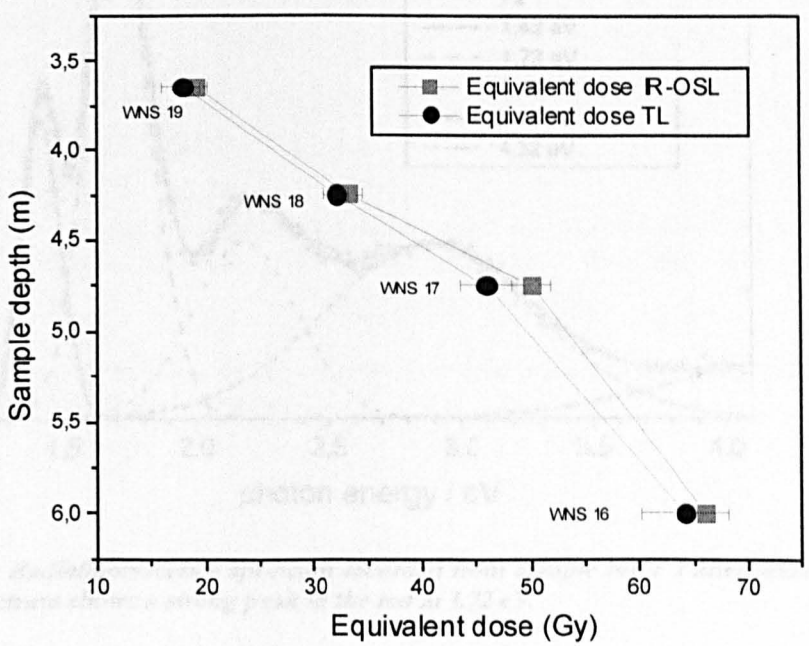

Figure 6.1.2j: Equivalent doses of the samples from the eastern section at the Wadi Netanya South in relation to their sample depth.

6.2 RF measurements

From the samples from the section at the East-wall at Habonim Quarry and the section at the Netanya South Cliff radiofluorescence spectra were recorded and the IR-RF equivalent doses of several samples determined.

6.2.1 Radiofluorescence spectra

The recorded radiofluorescence spectra showed compared to other samples observed by Trautmann and Erfurt very strong peaks in the red (*ca.* 720 nm, 1.72 eV). An example from the sample NET 1 is shown below (Figure 6.2.1). For the measurement of the IR-RF equivalent doses various filters were tested, separating the infrared peak at 1.42 eV from the tail of the strong red peak at 1.72 eV (cp. Chapter 5.4.2). For the final measurements, obtaining the equivalent doses, a fluorescence detection filter (CHROMA TECHNOLOGY HQ865/20M) was used to separate the infrared peak at 1.42 eV (cp. ERFURT *et al.* 2003).

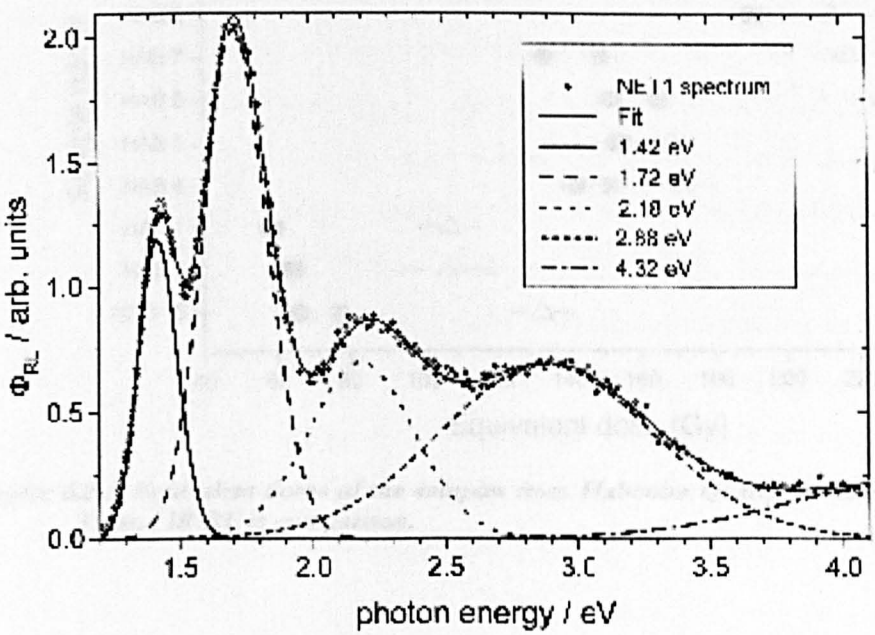

Figure 6.2.1: Radiofluorescence spectrum recorded from sample NET 1 after several hours. The spectrum shows a strong peak in the red at 1.72 eV.

6.2.2 IR-RF equivalent doses

The IR-RF equivalent doses obtained from samples of the Netanya South Cliff and the samples from the section at the East-wall at Habonim Quarry differed from the equivalent doses obtained with IR-OSL and TL from the same samples. The use of different filters for the IR-RF measurements (cp. Chapter 5.4.2) did not made a significant difference. Examples of IR-RF equivalent doses obtained with the IRSAR protocol from samples of the section at the East-wall at Habonim Quarry (HAB 4 to HAB 13) show that in general they are considerably higher than the IR-OSL and TL equivalent doses obtained of the same samples (Figure 6.2.2). This can have various reasons and is discussed in Chapter 7.1.3.

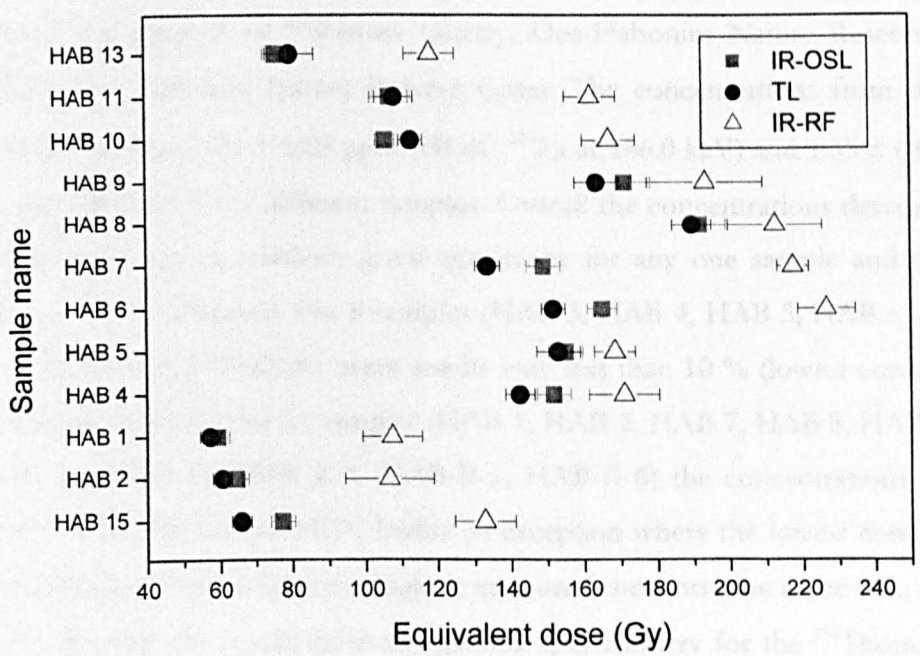

Figure 6.2.2: Equivalent doses of the samples from Habonim Quarry determined with IR-OSL, TL and IR-RF in comparison.

6.3 Dosimetry

The internal and external environmental dose received and the potential energy stored during burial by the dosimeter used for dating determines the relative intensity measured of the natural luminescence signal for each sample. The subchapter presents the dosimetric results of the study.

6.3.1 Gamma spectrometry

Habonim Quarry, Dor-Habonim Nature Reserve Middle Ridge, Dor-Habonim Nature Reserve Coast

In Table 6.3.1a the results from the gamma spectrometry for the ^{238}Uranium decay chain with the peaks measured at different energies from the isotopes ^{226}Ra, ^{214}Pb and ^{214}Bi are shown for the samples of Habonim Quarry, Dor-Habonim Nature Reserve Middle Ridge and Dor-Habonim Nature Reserve Coast. The concentrations from the single peaks range between 0.51 ± 0.08 ppm (HDK, ^{226}Ra at 186.0 keV) and 1.35 ± 0.05 (HAB 3, ^{214}Bi at 1120.3 keV) for different samples. Overall the concentrations determined for the single peaks are in relatively good agreement for any one sample and no major differences can be observed. For 8 samples (HAB 3, HAB 4, HAB 5, HAB 6, HAB 11, HAB 14, HAB-II-4, HDM) the mean results vary less than 10 % (lowest concentration in % from the highest). For 11 samples (HAB 1, HAB 2, HAB 7, HAB 8, HAB 9, HAB 10, HAB 12, HAB 16, HAB-II-1, HAB-II-5, HAB-II-6) the concentrations vary less than 20 %. Only the sample HDC builds an exception where the lowest concentration (^{226}Ra at 186.0 keV) varies from the highest measured concentration more than 20 %.
Table 6.3.1b gives the results from the gamma spectrometry for the ^{232}Thorium decay chain with the peaks measured at different energies from the isotopes ^{228}Ac, ^{212}Pb, ^{212}Bi and ^{208}Tl. The concentrations range between 0.14 ± 0.07 ppm (HAB 1, ^{212}Bi at 727.3 keV) and 6.42 ± 0.34 ppm (HAB 10, ^{212}Pb at 300.1 keV) for different samples. The variations in the concentrations of the ^{232}Thorium decay chain for the individual samples is significantly higher compared to the ^{238}Uranium decay chain. For 6 samples (HAB 6, HAB 7, HAB 8, HAB 9, HAB 10, HAB 11) the concentrations of the measured isotopes of the ^{232}Thorium decay chain vary less than 10 % and from 4 samples (HAB 5, HAB 12, HAB-II-5, HDM) less than 20 % for the individual samples. The measured

concentrations from 8 samples (HAB 2, HAB 3, HAB 4, HAB 14, HAB 16, HAB-II-4, HAB-II-9, HDC) vary up to 40 % for the individual sample. Exceptions from the above are the samples HAB 1 and HAB-II-1 whose concentrations for the single peaks vary so strongly that differences of up to 80 % (HAB 1) from the highest measured concentration can be observed.

In Table 6.3.1c are the Potassium concentrations measured with the gamma spectrometry presented. The concentrations range between 0.09 ± 0.01 % (HAB-II-1) and 0.98 ± 0.01 % (HAB 9).

From the ^{238}Uranium and ^{232}Thorium concentrations measured of the single peaks the arithmetic mean was calculated and for all concentrations (Uranium, Thorium and Potassium) an error of 7 % was assumed. The results are given in Table 6.3.1d.

The uranium content of the samples ranges between 0.54 ± 0.04 ppm (HAB-II-9) and 1.28 ± 0.09 ppm (HAB 11). A dependence, whether the sample is from an aeolianite or a soil can not be observed.

The thorium contents of the samples range between 0.43 ± 0.03 ppm (HAB 1) and 1.16 ± 0.08 ppm (HAB 4) for the aeolianites and between 3.22 ± 0.23 ppm (HAB 5) and 6.13 ± 0.43 ppm (HAB 10) for the soils. The soils contain clearly higher thorium contents than the aeolianites and at Habonim Quarry East-wall it can be observed that the thorium concentrations decrease towards the bottom of the section (Figure 6.3.1a).

The potassium contents range between 0.09 ± 0.01 % (HAB-II-1) and 0.45 ± 0.03 % (HAB 16) for the aeolianites and between 0.64 ± 0.04 % (HAB 5) and 0.98 ± 0.07 % (HAB 9) for the soil horizons. The potassium contents of the soils are somewhat higher than those of the aeolianites.

Table 6.3.1a: Equivalent ^{238}Uranium contents from isotope concentrations of the ^{238}Uranium decay chain for samples of the sections Habonim Quarry, Dor-Habonim Nature Reserve Middle Ridge and Dor-Habonim Nature Reserve Coast determined with gamma spectrometry.

Sample	Equivalent ^{238}Uranium (ppm) from ^{226}Ra at 186.0 keV	Equivalent ^{238}Uranium (ppm) from ^{214}Pb at 295.2 keV	Equivalent ^{238}Uranium (ppm) from ^{214}Pb at 351.9 keV	Equivalent ^{238}Uranium (ppm) from ^{214}Bi at 609.3 keV	Equivalent ^{238}Uranium (ppm) from ^{214}Bi at 1120.3 keV
HAB 1	1.10 ± 0.05	1.23 ± 0.04	1.30 ± 0.02	1.33 ± 0.02	1.28 ± 0.05
HAB 2	1.03 ± 0.05	1.14 ± 0.04	1.17 ± 0.02	1.18 ± 0.02	1.24 ± 0.05
HAB 3	1.26 ± 0.05	1.28 ± 0.04	1.35 ± 0.02	1.33 ± 0.02	1.35 ± 0.05
HAB 4	0.57 ± 0.04	0.54 ± 0.03	0.55 ± 0.01	0.57 ± 0.01	0.59 ± 0.06
HAB 5	0.80 ± 0.08	0.76 ± 0.03	0.74 ± 0.03	0.76 ± 0.02	0.80 ± 0.05
HAB 6	0.94 ± 0.06	0.87 ± 0.05	0.92 ± 0.02	0.94 ± 0.02	0.96 ± 0.05
HAB 7	1.02 ± 0.05	0.89 ± 0.04	0.84 ± 0.02	0.87 ± 0.02	0.88 ± 0.06
HAB 8	1.27 ± 0.07	1.04 ± 0.04	1.04 ± 0.03	1.12 ± 0.02	1.09 ± 0.06
HAB 9	1.24 ± 0.07	1.07 ± 0.03	1.06 ± 0.02	1.02 ± 0.02	1.10 ± 0.06
HAB 10	1.26 ± 0.06	1.04 ± 0.04	1.06 ± 0.03	1.07 ± 0.03	1.03 ± 0.06
HAB 11	1.31 ± 0.07	1.21 ± 0.04	1.25 ± 0.02	1.30 ± 0.02	1.31 ± 0.06
HAB 12	1.32 ± 0.06	1.14 ± 0.04	1.14 ± 0.02	1.10 ± 0.03	1.30 ± 0.06
HAB 13	---[1]	---[1]	---[1]	---[1]	---[1]
HAB 14	1.27 ± 0.10	1.18 ± 0.04	1.29 ± 0.04	1.23 ± 0.02	1.22 ± 0.05
HAB 15	---[1]	---[1]	---[1]	---[1]	---[1]
HAB 16	0.68 ± 0.04	0.80 ± 0.03	0.84 ± 0.02	0.81 ± 0.02	0.83 ± 0.05
HAB-II-1	0.91 ± 0.05	1.07 ± 0.03	1.00 ± 0.02	1.08 ± 0.02	1.10 ± 0.05
HAB-II-4	1.00 ± 0.09	1.01 ± 0.03	1.00 ± 0.01	1.05 ± 0.02	1.05 ± 0.05
HAB-II-5	0.96 ± 0.07	0.78 ± 0.04	0.86 ± 0.02	0.85 ± 0.03	0.93 ± 0.06
HAB-II-6	0.56 ± 0.04	0.52 ± 0.03	0.50 ± 0.01	0.52 ± 0.01	0.58 ± 0.05
HDM	0.74 ± 0.07	0.71 ± 0.04	0.77 ± 0.01	0.73 ± 0.01	0.74 ± 0.04
HDC	0.51 ± 0.08	0.64 ± 0.03	0.69 ± 0.02	0.72 ± 0.02	0.74 ± 0.04

[1]The values of the samples HAB 13 and HAB 15 could not be determined as the samples went missing during shipping. The ages of these samples were calculated using the values of sample HAB 12.

Table 6.3.1b: Equivalent ^{232}Thorium contents from isotope concentrations of the ^{232}Thorium decay chain for samples of the sections Habonim Quarry, Dor-Habonim Nature Reserve Middle Ridge and Dor-Habonim Nature Reserve Coast determined with gamma spectrometry.

Sample	Equivalent ^{232}Thorium (ppm) from ^{212}Pb at 238.6 keV	Equivalent ^{232}Thorium (ppm) from ^{212}Pb at 300.1 keV	Equivalent ^{232}Thorium (ppm) from ^{228}Ac at 338.3 keV	Equivalent ^{232}Thorium (ppm) from ^{208}Tl at 583.2 keV	Equivalent ^{232}Thorium (ppm) from ^{212}Bi at 727.3 keV	Equivalent ^{232}Thorium (ppm) from ^{228}Ac at 911.1 keV	Equivalent ^{232}Thorium (ppm) from ^{208}Tl at 2614.5 keV
HAB 1	0.41 ± 0.02	0.30 ± 0.18	0.50 ± 0.10	0.48 ± 0.03	0.14 ± 0.07	0.67 ± 0.05	0.54 ± 0.02
HAB 2	0.62 ± 0.03	1.01 ± 0.17	0.71 ± 0.11	0.66 ± 0.07	0.79 ± 0.16	0.78 ± 0.05	0.71 ± 0.03
HAB 3	0.46 ± 0.02	0.42 ± 0.20	0.49 ± 0.10	0.47 ± 0.04	0.69 ± 0.20	0.51 ± 0.04	0.54 ± 0.02
HAB 4	1.13 ± 0.04	1.21 ± 0.12	1.16 ± 0.10	1.18 ± 0.05	0.95 ± 0.12	1.19 ± 0.06	1.28 ± 0.05
HAB 5	3.08 ± 0.07	3.22 ± 0.19	3.20 ± 0.22	3.02 ± 0.07	3.25 ± 0.23	3.31 ± 0.09	3.45 ± 0.09
HAB 6	4.04 ± 0.08	4.08 ± 0.31	4.21 ± 0.24	4.18 ± 0.08	4.67 ± 0.26	4.03 ± 0.14	4.06 ± 0.10
HAB 7	4.47 ± 0.09	4.79 ± 0.32	4.60 ± 0.15	4.48 ± 0.08	4.22 ± 0.25	4.60 ± 0.14	4.34 ± 0.10
HAB 8	5.61 ± 0.13	5.58 ± 0.32	5.70 ± 0.25	5.69 ± 0.09	5.70 ± 0.29	5.64 ± 0.11	5.67 ± 0.12
HAB 9	6.01 ± 0.11	6.26 ± 0.28	6.08 ± 0.26	6.09 ± 0.10	6.14 ± 0.29	6.14 ± 0.12	6.13 ± 0.13
HAB 10	5.85 ± 0.13	6.42 ± 0.34	6.35 ± 0.33	6.02 ± 0.10	6.05 ± 0.38	6.11 ± 0.16	6.12 ± 0.13
HAB 11	5.90 ± 0.12	6.06 ± 0.38	6.22 ± 0.16	6.03 ± 0.10	5.91 ± 0.28	5.81 ± 0.16	6.13 ± 0.13
HAB 12	5.31 ± 0.11	4.89 ± 0.27	5.32 ± 0.27	5.28 ± 0.09	5.02 ± 0.26	5.68 ± 0.19	5.64 ± 0.12
HAB 13	---[1]	---[1]	---[1]	---[1]	---[1]	---[1]	---[1]
HAB 14	0.55 ± 0.03	0.62 ± 0.14	0.80 ± 0.09	0.63 ± 0.04	0.73 ± 0.14	0.53 ± 0.05	0.69 ± 0.03
HAB 15	---[1]	---[1]	---[1]	---[1]	---[1]	---[1]	---[1]
HAB 16	0.94 ± 0.03	1.29 ± 0.18	1.12 ± 0.15	1.01 ± 0.05	1.03 ± 0.15	1.02 ± 0.06	1.12 ± 0.04
HAB-II-1	0.37 ± 0.02	0.85 ± 0.19	0.38 ± 0.10	0.33 ± 0.03	0.53 ± 0.13	0.52 ± 0.04	0.51 ± 0.02
HAB-II-4	0.44 ± 0.02	0.57 ± 0.14	0.57 ± 0.12	0.56 ± 0.04	0.65 ± 0.13	0.59 ± 0.04	0.61 ± 0.03
HAB-II-5	4.63 ± 0.11	4.13 ± 0.34	4.94 ± 0.17	4.56 ± 0.10	4.79 ± 0.31	4.62 ± 0.12	5.01 ± 0.13
HAB-II-9	0.43 ± 0.02	0.52 ± 0.12	0.46 ± 0.08	0.44 ± 0.03	0.52 ± 0.11	0.68 ± 0.05	0.51 ± 0.02
HDM	0.69 ± 0.03	0.81 ± 0.14	0.82 ± 0.10	0.75 ± 0.04	0.78 ± 0.13	0.74 ± 0.05	0.80 ± 0.03
HDC	0.70 ± 0.03	1.05 ± 0.15	0.64 ± 0.14	0.79 ± 0.04	0.70 ± 0.13	0.81 ± 0.06	0.73 ± 0.03

[1]The values of the samples HAB 13 and HAB 15 could not be determined as the samples went missing during shipping. The ages of these samples were calculated using the values of sample HAB 12.

Table 6.3.1c: Potassium concentrations of the samples of the sections Habonim Quarry, Dor-Habonim Nature Reserve Middle Ridge and Dor-Habonim Nature Reserve Coast determined with gamma spectrometry.

Sample	K (%) determined over the concentration of ^{40}K at 1460 keV
HAB 1	0.14 ± 0.01
HAB 2	0.14 ± 0.01
HAB 3	0.14 ± 0.01
HAB 4	0.34 ± 0.01
HAB 5	0.64 ± 0.01
HAB 6	0.77 ± 0.01
HAB 7	0.84 ± 0.01
HAB 8	0.94 ± 0.01
HAB 9	0.98 ± 0.01
HAB 10	0.94 ± 0.01
HAB 11	0.89 ± 0.01
HAB 12	0.81 ± 0.01
HAB 13	---[1]
HAB 14	0.18 ± 0.01
HAB 15	---[1]
HAB 16	0.45 ± 0.01
HAB-II-1	0.09 ± 0.01
HAB-II-4	0.11 ± 0.01
HAB-II-5	0.73 ± 0.01
HAB-II-9	0.23 ± 0.01
HDM	0.16 ± 0.01
HDC	0.30 ± 0.01

[1]The values of the samples HAB 13 and HAB 15 could not be determined as the samples went missing during shipping. The ages of these samples were calculated using the values of sample HAB 12.

Table 6.3.1d: Concentrations Uranium, Thorium and Potassium of the samples of the sections Habonim Quarry, Dor-Habonim Nature Reserve Middle Ridge and Dor-Habonim Nature Reserve Coast determined with gamma spectrometry.

Sample	Uranium (ppm)	Thorium (ppm)	Potassium (%)
HAB 1	1.25 ± 0.09	0.43 ± 0.03	0.14 ± 0.01
HAB 2	1.15 ± 0.08	0.75 ± 0.05	0.14 ± 0.01
HAB 3	1.31 ± 0.09	0.51 ± 0.04	0.14 ± 0.01
HAB 4	0.56 ± 0.04	1.16 ± 0.08	0.34 ± 0.02
HAB 5	0.77 ± 0.05	3.22 ± 0.23	0.64 ± 0.04
HAB 6	0.93 ± 0.06	4.18 ± 0.29	0.77 ± 0.05
HAB 7	0.90 ± 0.06	4.50 ± 0.32	0.84 ± 0.06
HAB 8	1.11 ± 0.08	5.66 ± 0.40	0.94 ± 0.07
HAB 9	1.10 ± 0.08	6.12 ± 0.43	0.98 ± 0.07
HAB 10	1.09 ± 0.08	6.13 ± 0.43	0.94 ± 0.07
HAB 11	1.28 ± 0.09	6.01 ± 0.42	0.89 ± 0.06
HAB 12	1.20 ± 0.08	5.31 ± 0.37	0.81 ± 0.06
HAB 13	---[1]	---[1]	---[1]
HAB 14	1.24 ± 0.09	0.65 ± 0.46	0.18 ± 0.01
HAB 15	---[1]	---[1]	---[1]
HAB 16	0.79 ± 0.06	1.08 ± 0.08	0.45 ± 0.03
HAB-II-1	1.03 ± 0.07	0.50 ± 0.03	0.09 ± 0.01
HAB-II-4	1.02 ± 0.07	0.57 ± 0.04	0.11 ± 0.01
HAB-II-5	0.88 ± 0.06	4.67 ± 0.33	0.73 ± 0.05
HAB-II-9	0.54 ± 0.04	0.51 ± 0.04	0.23 ± 0.02
HDM	0.74 ± 0.05	0.77 ± 0.05	0.16 ± 0.01
HDC	0.66 ± 0.05	0.77 ± 0.05	0.30 ± 0.02

[1]The values of the samples HAB 13 and HAB 15 could not be determined as the samples went missing during shipping. The ages of these samples were calculated using the values of sample HAB 12.

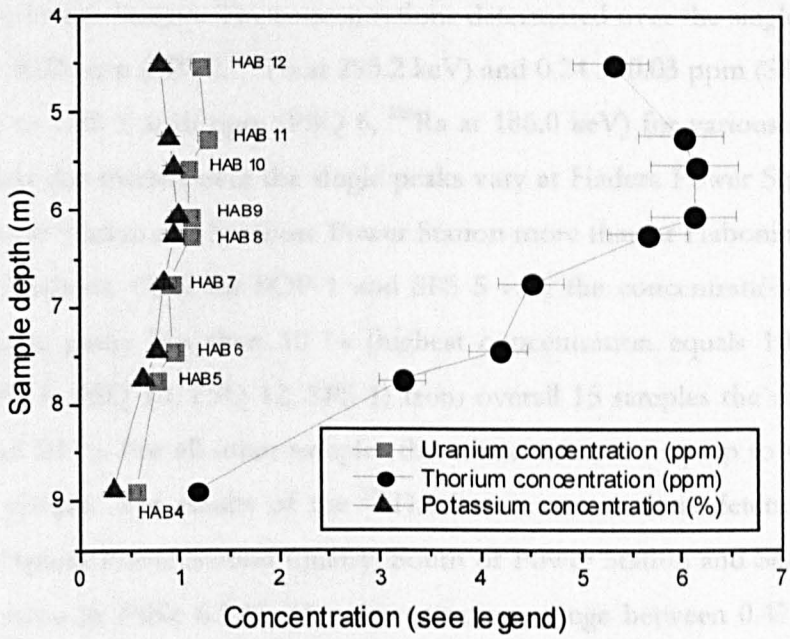

Figure 6.3.1a: Uranium, Thorium and Potassium concentrations of the samples from the section at Habonim Quarry East-wall.

Hadera Power Station Quarry, South of Power Station and Seashore Power Station

Table 6.3.1e presents the results from the gamma spectrometry for the ^{238}Uranium decay chain for the samples taken from Hadera Power Station Quarry, South of Power Station and Seashore Power Station. The concentrations determined over the single peaks range from 0.24 ± 0.02 ppm (SPS 7, ^{214}Pb at 295.2 keV) and 0.24 ± 0.03 ppm (SPS 7, 214Bi at 1120.3 keV) to 1.26 ± 0.10 ppm (PSQ 6, ^{226}Ra at 186.0 keV) for various samples. The concentrations determined over the single peaks vary at Hadera Power Station Quarry, South of Power Station and Seashore Power Station more than at Habonim Quarry and the western sections. Only for SOP 1 and SPS 5 vary the concentrations determined over the single peaks less than 10 % (highest concentration equals 100 %). For 4 samples (PSQ 6, PSQ 10, PSQ 12, SPS 1) from overall 15 samples the concentrations vary less than 20 %. For all other samples the concentrations vary up to 41 % (SPS 7) for anyone sample. The results of the ^{232}Thorium concentrations determined for the samples of Hadera Power Station Quarry, South of Power Station and Seashore Power Station are given in Table 6.3.1f. The concentrations range between 0.47 ± 0.02 ppm (SPS 7, ^{212}Pb at 238.6 keV) and 5.18 ± 0.13 ppm (PSQ 7, ^{208}Tl at 2614.5 keV). For 2 samples (PSQ 5, PSQ 6) the concentrations of the single peaks vary less than 10 % and for further 2 samples (PSQ 4, PSQ 7) the concentrations vary less than 20 %. For all other samples the concentrations vary more than 20 % and up to 50 % for sample SPS 7. The results for the Potassium concentrations determined with the gamma spectrometry are given in Table 6.3.1g. The concentrations range between 0.27 ± 0.01 % (PSQ 2) and 0.53 ± 0.01 % (PSQ 4).

The results of the arithmetic means of the single Uranium and Thorium concentrations for any one sample and the Potassium concentrations are given in Table 6.3.1h. From the samples of Hadera Power Station Quarry, South of Power Station and the section Seashore Power Station the Uranium concentrations range between 0.29 ± 0.02 ppm (PSQ 2, SPS 7) and 1.11 ± 0.08 ppm (PSQ 6). The Thorium concentrations range between 0.69 ± 0.05 ppm (SPS 7, SPS 8) and 4.79 ± 0.34 ppm (PSQ 7) and the Potassium concentrations between 0.27 ± 0.02 % (PSQ 2) and 0.53 ± 0.04 % (PSQ 4). For the section at the East-wall of Hadera Power Station Quarry it can be observed that the Uranium and Potassium concentrations are relatively uniform while the Thorium concentrations decrease with sample depth (Figure 6.3.1b).

Table 6.3.1e: Equivalent ^{238}Uranium content from isotope concentrations of the ^{238}Uranium decay chain for samples of the sections Hadera Power Station Quarry, South of Power Station and Seashore Power Station determined with gamma spectrometry.

Sample	Equivalent ^{238}Uranium (ppm) from ^{226}Ra at 186.0 keV	Equivalent ^{238}Uranium (ppm) from ^{214}Pb at 295.2 keV	Equivalent ^{238}Uranium (ppm) from ^{214}Pb at 351.9 keV	Equivalent ^{238}Uranium (ppm) from ^{214}Bi at 609.3 keV	Equivalent ^{238}Uranium (ppm) from ^{214}Bi at 1120.3 keV
PSQ 1	---	---	---	---	---
PSQ 2	0.34 ± 0.03	0.26 ± 0.02	0.28 ± 0.02	0.29 ± 0.01	0.29 ± 0.03
PSQ 3	0.79 ± 0.05	0.52 ± 0.03	0.55 ± 0.01	0.57 ± 0.01	0.55 ± 0.04
PSQ 4	0.88 ± 0.05	0.71 ± 0.03	0.74 ± 0.01	0.74 ± 0.02	0.65 ± 0.04
PSQ 5	1.02 ± 0.06	0.78 ± 0.03	0.84 ± 0.02	0.79 ± 0.02	0.85 ± 0.05
PSQ 6	1.26 ± 0.10	1.07 ± 0.04	1.08 ± 0.02	1.08 ± 0.02	1.07 ± 0.05
PSQ 7	1.33 ± 0.12	1.03 ± 0.04	1.03 ± 0.02	1.05 ± 0.02	1.07 ± 0.06
PSQ 8	---	---	---	---	---
PSQ 9	---	---	---	---	---
PSQ 10	0.47 ± 0.04	0.42 ± 0.03	0.48 ± 0.01	0.46 ± 0.02	0.45 ± 0.05
PSQ 11	---	---	---	---	---
PSQ 12	0.61 ± 0.04	0.50 ± 0.03	0.51 ± 0.01	0.51 ± 0.01	0.58 ± 0.04
SOP 1	0.37 ± 0.03	0.37 ± 0.02	0.36 ± 0.01	0.38 ± 0.01	0.36 ± 0.03
SOP 2	---	---	---	---	---
SOP 3	0.39 ± 0.04	0.28 ± 0.02	0.34 ± 0.01	0.36 ± 0.01	0.27 ± 0.03
SOP 4	0.38 ± 0.05	0.28 ± 0.02	0.30 ± 0.01	0.31 ± 0.01	0.34 ± 0.04
SOP 5	---	---	---	---	---
SPS 1	0.37 ± 0.05	0.34 ± 0.03	0.35 ± 0.01	0.36 ± 0.01	0.30 ± 0.04
SPS 2	---	---	---	---	---
SPS 3	---	---	---	---	---
SPS 5	0.73 ± 0.05	0.69 ± 0.03	0.71 ± 0.01	0.72 ± 0.02	0.69 ± 0.04
SPS 6	---	---	---	---	---
SPS 7	0.41 ± 0.03	0.24 ± 0.02	0.27 ± 0.01	0.27 ± 0.01	0.24 ± 0.03
SPS 8	0.39 ± 0.05	0.26 ± 0.02	0.27 ± 0.01	0.30 ± 0.01	0.34 ± 0.03

Table 6.3.1f: Equivalent ^{232}Thorium contents from isotope concentrations of the ^{232}Thorium decay chain for samples of the sections Hadera Power Station Quarry, South of Power Station and Seashore Power Station determined with gamma spectrometry.

Sample	Equivalent ^{232}Thorium (ppm) from ^{212}Pb at 238.6 keV	Equivalent ^{232}Thorium (ppm) from ^{212}Pb at 300.1 keV	Equivalent ^{232}Thorium (ppm) from ^{228}Ac at 338.3 keV	Equivalent ^{232}Thorium (ppm) from ^{208}Tl at 583.2 keV	Equivalent ^{232}Thorium (ppm) from ^{212}Bi at 727.3 keV	Equivalent ^{232}Thorium (ppm) from ^{228}Ac at 911.1 keV	Equivalent ^{232}Thorium (ppm) from ^{208}Tl at 2614.5 keV
PSQ 1	---	---	---	---	---	---	---
PSQ 2	0.59 ± 0.03	0.97 ± 0.17	0.62 ± 0.06	0.66 ± 0.04	0.73 ± 0.13	0.64 ± 0.07	0.76 ± 0.03
PSQ 3	2.29 ± 0.05	2.08 ± 0.29	2.31 ± 0.12	2.31 ± 0.06	2.64 ± 0.21	2.30 ± 0.08	2.29 ± 0.07
PSQ 4	3.07 ± 0.07	2.82 ± 0.19	2.82 ± 0.22	3.23 ± 0.07	3.48 ± 0.23	3.20 ± 0.09	3.03 ± 0.08
PSQ 5	3.77 ± 0.08	3.80 ± 0.29	3.77 ± 0.24	3.87 ± 0.07	4.10 ± 0.24	3.84 ± 0.10	3.77 ± 0.09
PSQ 6	4.55 ± 0.11	4.39 ± 0.26	4.57 ± 0.24	4.54 ± 0.11	4.57 ± 0.23	4.68 ± 0.10	4.64 ± 0.11
PSQ 7	4.70 ± 0.10	4.73 ± 0.24	4.70 ± 0.17	4.51 ± 0.09	4.85 ± 0.30	4.84 ± 0.18	5.18 ± 0.13
PSQ 8	---	---	---	---	---	---	---
PSQ 9	---	---	---	---	---	---	---
PSQ 10	0.78 ± 0.03	0.71 ± 0.23	0.80 ± 0.16	0.71 ± 0.04	0.79 ± 0.14	0.84 ± 0.05	0.92 ± 0.04
PSQ 11	---	---	---	---	---	---	---
PSQ 12	0.74 ± 0.03	0.91 ± 0.14	0.83 ± 0.10	0.74 ± 0.04	0.71 ± 0.13	0.83 ± 0.05	0.87 ± 0.04
SOP 1	0.85 ± 0.02	1.39 ± 0.16	0.82 ± 0.08	0.97 ± 0.04	0.74 ± 0.13	0.96 ± 0.05	1.01 ± 0.04
SOP 2	---	---	---	---	---	---	---
SOP 3	0.73 ± 0.03	0.93 ± 0.14	0.83 ± 0.09	0.89 ± 0.06	0.78 ± 0.14	0.77 ± 0.05	0.85 ± 0.04
SOP 4	0.54 ± 0.02	0.91 ± 0.12	0.84 ± 0.08	0.77 ± 0.04	0.75 ± 0.14	0.90 ± 0.05	0.79 ± 0.03
SOP 5	---	---	---	---	---	---	---
SPS 1	0.82 ± 0.03	1.12 ± 0.14	1.10 ± 0.10	0.84 ± 0.04	0.95 ± 0.15	0.94 ± 0.05	0.98 ± 0.04
SPS 2	---	---	---	---	---	---	---
SPS 3	---	---	---	---	---	---	---
SPS 5	2.35 ± 0.06	2.26 ± 0.19	3.09 ± 0.25	2.46 ± 0.06	2.57 ± 0.20	2.40 ± 0.08	2.43 ± 0.07
SPS 6	---	---	---	---	---	---	---
SPS 7	0.47 ± 0.02	0.71 ± 0.12	0.72 ± 0.09	0.62 ± 0.04	0.94 ± 0.13	0.68 ± 0.05	0.72 ± 0.03
SPS 8	0.58 ± 0.02	0.82 ± 0.20	0.51 ± 0.09	0.65 ± 0.03	0.81 ± 0.13	0.85 ± 0.05	0.63 ± 0.03

Table 6.3.1g: Potassium concentrations of the samples of the sections Hadera Power Station Quarry, South of Power Station and Seashore Power Station determined with gamma spectrometry.

Sample	K (%) determined over the concentration of ^{40}K at 1460 keV
PSQ 1	---
PSQ 2	0.27 ± 0.01
PSQ 3	0.45 ± 0.01
PSQ 4	0.53 ± 0.01
PSQ 5	0.49 ± 0.01
PSQ 6	0.50 ± 0.01
PSQ 7	0.51 ± 0.01
PSQ 8	---
PSQ 9	---
PSQ 10	0.30 ± 0.01
PSQ 11	---
PSQ 12	0.30 ± 0.01
SOP 1	0.31 ± 0.01
SOP 2	---
SOP 3	0.36 ± 0.01
SOP 4	0.35 ± 0.01
SOP 5	---
SPS 1	0.35 ± 0.01
SPS 2	---
SPS 3	---
SPS 5	0.51 ± 0.01
SPS 6	---
SPS 7	0.33 ± 0.01
SPS 8	0.31 ± 0.01

Table 6.3.1h: Concentrations Uranium, Thorium and Potassium of the samples of the sections Hadera Power Station Quarry, South of Power Station and Seashore Power Station determined with gamma spectrometry.

Sample	Uranium (ppm)	Thorium (ppm)	Potassium (%)
PSQ 1	---	---	---
PSQ 2	0.29 ± 0.02	0.71 ± 0.05	0.27 ± 0.02
PSQ 3	0.60 ± 0.04	2.32 ± 0.16	0.45 ± 0.03
PSQ 4	0.74 ± 0.05	3.09 ± 0.22	0.53 ± 0.04
PSQ 5	0.86 ± 0.06	3.85 ± 0.27	0.49 ± 0.03
PSQ 6	1.11 ± 0.08	4.56 ± 0.32	0.50 ± 0.04
PSQ 7	1.10 ± 0.08	4.79 ± 0.34	0.51 ± 0.04
PSQ 8	---	---	---
PSQ 9	---	---	---
PSQ 10	0.46 ± 0.03	0.79 ± 0.06	0.30 ± 0.02
PSQ 11	---	---	---
PSQ 12	0.54 ± 0.04	0.80 ± 0.06	0.30 ± 0.02
SOP 1	0.37 ± 0.03	0.96 ± 0.07	0.31 ± 0.02
SOP 2	---	---	---
SOP 3	0.33 ± 0.02	0.83 ± 0.06	0.36 ± 0.03
SOP 4	0.32 ± 0.02	0.79 ± 0.06	0.35 ± 0.03
SOP 5	---	---	---
SPS 1	0.34 ± 0.02	0.96 ± 0.07	0.35 ± 0.03
SPS 2	---	---	---
SPS 3	---	---	---
SPS 5	0.71 ± 0.05	2.51 ± 0.18	0.51 ± 0.04
SPS 6	---	---	---
SPS 7	0.29 ± 0.02	0.69 ± 0.05	0.33 ± 0.02
SPS 8	0.31 ± 0.02	0.69 ± 0.05	0.31 ± 0.02

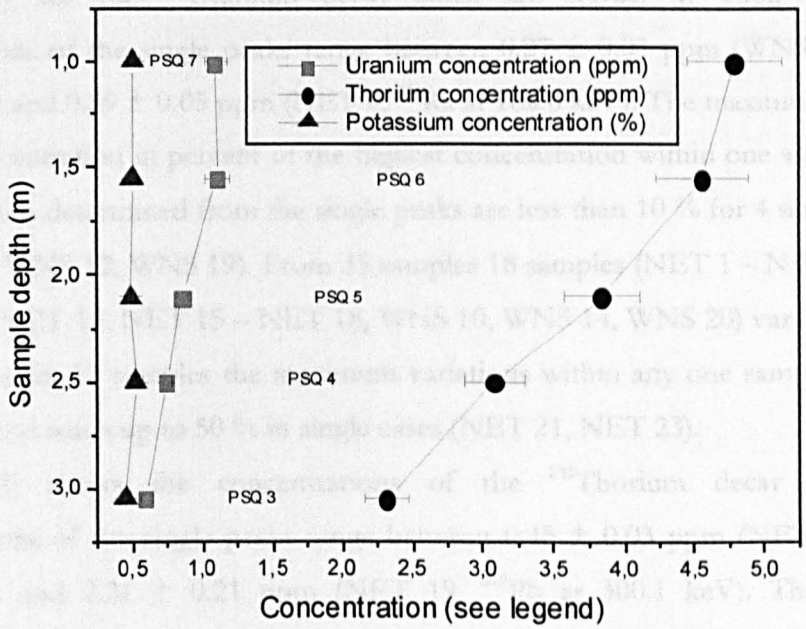

Figure 6.3.1b: Uranium, Thorium and Potassium concentration of the samples from the section at Hadera Power Station Quarry East-wall.

Netanya South Cliff and Wadi Netanya South

The results for the sections Netanya South Cliff and Wadi Netanya South of the gamma spectrometry for the ^{238}Uranium decay chain are shown in Table 6.3.1i. The concentrations of the single peaks range between 0.27 ± 0.03 ppm (WNS 20, ^{214}Bi at 1120.3 keV) and 0.89 ± 0.05 ppm (NET 4, ^{226}Ra at 186.0 keV). The maximum variations (lowest concentration in percent of the highest concentration within one sample) in the concentrations determined from the single peaks are less than 10 % for 4 samples (NET 8, NET 12, WNS 12, WNS 19). From 35 samples 18 samples (NET 1 – NET 7, NET 9 – NET 11, NET 13, NET 15 – NET 18, WNS 10, WNS 14, WNS 20) vary less than 20 %. For all other 13 samples the maximum variations within any one sample are larger than 20 % and reach up to 50 % in single cases (NET 21, NET 23).

Table 6.3.1j shows the concentrations of the ^{232}Thorium decay chain. The concentrations of the single peaks range between 0.45 ± 0.03 ppm (NET 21, ^{208}Tl at 583.2 keV) and 2.21 ± 0.21 ppm (NET 19, ^{212}Pb at 300.1 keV). The maximum variations within any one sample in the Thorium concentrations determined over the singles peaks are much more varied compared to the maximum variations of the Uranium concentrations. For none of the 35 samples the single Thorium concentrations vary less than 10 %. For 10 samples (NET 4, NET 8, NET 14, NET 20, NET 24, WNS 11, WNS 14, WNS 16, WNS 17, WNS 19) the concentrations vary less than 20 %. For a further 14 samples (NET 1, NET 5 – NET 7, NET 10 – NET 13, NET 17, NET 18, WNS 10, WNS 13, WNS 18, WNS 20) the concentrations within any one sample vary less than 30 %. For all other samples from the sections Netanya South Cliff and Wadi Netanya South the single Thorium concentrations within one sample vary more than that. The samples NET 9, NET 15 and NET 23 show maximum variations in the concentrations larger than 50 %.

Table 6.3.1k presents the concentrations of the Potassium content determined over gamma spectrometry. The concentrations range between 0.13 ± 0.01 % (NET 21) and 0.63 ± 0.01 % (NET 5, NET 6).

The above information is summarised in Table 6.3.1l. The Uranium and Thorium concentrations are given as the arithmetic mean of the concentrations determined over the single peaks and for all concentrations (Uranium, Thorium and Potassium) an estimated error of 7 % was assumed. The Uranium concentration ranges between 0.30 ± 0.02 ppm (WNS 20) and 0.82 ± 0.06 ppm (NET 4). The Thorium concentrations

range between 0.62 ± 0.04 ppm (NET 21) and 1.92 ± 0.13 ppm (NET 4). The Potassium concentrations range between 0.13 ± 0.01 % (NET 21) and 0.63 ± 0.04 % (NET 5, NET 6). At the Netanya South Cliff section it can be seen that the Uranium and the Thorium concentrations are somewhat higher in well developed soils (NET 4, NET 19, NET 20, NET 24) (Figure 6.3.1c). A similar trend is observed for the Thorium concentrations of the sections at the Wadi Netanya South (Figures 6.3.1d and 6.3.1e).

Table 6.3.1i: Equivalent ^{238}Uranium contents from isotope concentrations of the ^{238}Uranium decay chain for samples of the sections Netanya South Cliff and Wadi Netanya South determined by gamma spectrometry.

Sample	Equivalent ^{238} Uranium (ppm) from ^{226}Ra at 186.0 keV	Equivalent ^{238} Uranium (ppm) from ^{214}Pb at 295.2 keV	Equivalent ^{238} Uranium (ppm) from ^{214}Pb at 351.9 keV	Equivalent ^{238} Uranium (ppm) from ^{214}Bi at 609.3 keV	Equivalent ^{238} Uranium (ppm) from ^{214}Bi at 1120.3 keV
NET 1	0.66 ± 0.05	0.58 ± 0.03	0.59 ± 0.02	0.57 ± 0.01	0.61 ± 0.04
NET 2	0.75 ± 0.05	0.62 ± 0.03	0.62 ± 0.01	0.62 ± 0.01	0.63 ± 0.04
NET 3	0.83 ± 0.05	0.66 ± 0.03	0.69 ± 0.01	0.73 ± 0.02	0.75 ± 0.04
NET 4	0.89 ± 0.05	0.81 ± 0.04	0.82 ± 0.01	0.78 ± 0.02	0.80 ± 0.05
NET 5	0.72 ± 0.05	0.71 ± 0.03	0.70 ± 0.03	0.71 ± 0.02	0.60 ± 0.05
NET 6	0.62 ± 0.04	0.59 ± 0.03	0.58 ± 0.01	0.63 ± 0.02	0.67 ± 0.05
NET 7	0.40 ± 0.03	0.35 ± 0.03	0.40 ± 0.01	0.44 ± 0.01	0.42 ± 0.04
NET 8	0.51 ± 0.04	0.46 ± 0.03	0.51 ± 0.01	0.49 ± 0.01	0.46 ± 0.04
NET 9	0.33 ± 0.03	0.40 ± 0.03	0.39 ± 0.01	0.40 ± 0.01	0.36 ± 0.03
NET 10	0.49 ± 0.04	0.41 ± 0.03	0.44 ± 0.01	0.45 ± 0.01	0.41 ± 0.04
NET 11	0.34 ± 0.03	0.32 ± 0.02	0.32 ± 0.01	0.36 ± 0.02	0.39 ± 0.04
NET 12	0.44 ± 0.04	0.43 ± 0.03	0.45 ± 0.01	0.46 ± 0.01	0.44 ± 0.04
NET 13	0.37 ± 0.03	0.35 ± 0.03	0.32 ± 0.01	0.30 ± 0.02	0.32 ± 0.03
NET 14	0.49 ± 0.03	0.38 ± 0.03	0.40 ± 0.01	0.41 ± 0.01	0.35 ± 0.04
NET 15	0.32 ± 0.03	0.36 ± 0.03	0.30 ± 0.02	0.33 ± 0.01	0.36 ± 0.03
NET 16	0.36 ± 0.04	0.34 ± 0.03	0.31 ± 0.01	0.33 ± 0.01	0.34 ± 0.04
NET 17	0.36 ± 0.04	0.33 ± 0.03	0.33 ± 0.01	0.36 ± 0.01	0.29 ± 0.03
NET 18	0.45 ± 0.04	0.39 ± 0.03	0.38 ± 0.01	0.42 ± 0.02	0.47 ± 0.05
NET 19	0.57 ± 0.04	0.50 ± 0.03	0.47 ± 0.01	0.47 ± 0.01	0.41 ± 0.04
NET 20	0.79 ± 0.04	0.52 ± 0.03	0.56 ± 0.02	0.57 ± 0.01	0.63 ± 0.04
NET 21	0.78 ± 0.06	0.40 ± 0.02	0.42 ± 0.01	0.41 ± 0.02	0.41 ± 0.03
NET 22	0.54 ± 0.06	0.40 ± 0.02	0.39 ± 0.01	0.38 ± 0.01	0.33 ± 0.03
NET 23	0.89 ± 0.04	0.44 ± 0.03	0.45 ± 0.01	0.46 ± 0.01	0.45 ± 0.03
NET 24	0.87 ± 0.07	0.59 ± 0.03	0.61 ± 0.01	0.62 ± 0.01	0.68 ± 0.04

Table 6.3.1i: Continued.

Sample	Equivalent ^{238}Uranium (ppm) from ^{226}Ra at 186.0 keV	Equivalent ^{238}Uranium (ppm) from ^{214}Pb at 295.2 keV	Equivalent ^{238}Uranium (ppm) from ^{214}Pb at 351.9 keV	Equivalent ^{238}Uranium (ppm) from ^{214}Bi at 609.3 keV	Equivalent ^{238}Uranium (ppm) from ^{214}Bi at 1120.3 keV
WNS 10	0.40 ± 0.03	0.33 ± 0.02	0.37 ± 0.01	0.38 ± 0.01	0.37 ± 0.03
WNS 11	0.52 ± 0.04	0.37 ± 0.02	0.44 ± 0.01	0.42 ± 0.01	0.46 ± 0.04
WNS 12	0.45 ± 0.06	0.45 ± 0.03	0.47 ± 0.01	0.47 ± 0.01	0.44 ± 0.04
WNS 13	0.42 ± 0.03	0.36 ± 0.02	0.39 ± 0.02	0.40 ± 0.02	0.50 ± 0.04
WNS 14	0.50 ± 0.04	0.44 ± 0.03	0.46 ± 0.01	0.48 ± 0.02	0.46 ± 0.03
WNS 15	0.39 ± 0.04	0.30 ± 0.02	0.34 ± 0.01	0.34 ± 0.02	0.38 ± 0.04
WNS 16	0.41 ± 0.03	0.33 ± 0.02	0.35 ± 0.01	0.34 ± 0.02	0.32 ± 0.03
WNS 17	0.55 ± 0.07	0.42 ± 0.03	0.41 ± 0.01	0.41 ± 0.01	0.43 ± 0.04
WNS 18	0.58 ± 0.04	0.43 ± 0.03	0.40 ± 0.01	0.43 ± 0.02	0.38 ± 0.05
WNS 19	0.47 ± 0.06	0.46 ± 0.03	0.47 ± 0.02	0.46 ± 0.01	0.43 ± 0.06
WNS 20	0.32 ± 0.03	0.29 ± 0.02	0.30 ± 0.01	0.32 ± 0.01	0.27 ± 0.03

Table 6.3.1j: Equivalent ^{232}Thorium contents from isotope concentrations of the ^{232}Thorium decay chain for samples of the sections Netanya South Cliff and Wadi Netanya South determined by gamma spectrometry.

Sample	Equivalent ^{232}Thorium (ppm) from ^{212}Pb at 238.6 keV	Equivalent ^{232}Thorium (ppm) from ^{212}Pb at 300.1 keV	Equivalent ^{232}Thorium (ppm) from ^{228}Ac at 338.3 keV	Equivalent ^{232}Thorium (ppm) from ^{208}Tl at 583.2 keV	Equivalent ^{232}Thorium (ppm) from ^{212}Bi at 727.3 keV	Equivalent ^{232}Thorium (ppm) from ^{228}Ac at 911.1 keV	Equivalent ^{232}Thorium (ppm) from ^{208}Tl at 2614.5 keV
NET 1	0.85 ± 0.03	1.02 ± 0.13	0.89 ± 0.09	0.90 ± 0.05	0.84 ± 0.14	1.03 ± 0.06	1.09 ± 0.04
NET 2	0.85 ± 0.03	0.78 ± 0.23	0.90 ± 0.10	0.86 ± 0.04	0.75 ± 0.14	0.94 ± 0.06	1.13 ± 0.04
NET 3	1.18 ± 0.04	1.23 ± 0.19	0.99 ± 0.20	1.22 ± 0.05	1.47 ± 0.18	1.42 ± 0.07	1.38 ± 0.05
NET 4	1.83 ± 0.05	1.96 ± 0.24	1.83 ± 0.12	1.83 ± 0.05	2.13 ± 0.21	1.92 ± 0.08	1.96 ± 0.06
NET 5	0.84 ± 0.04	1.18 ± 0.17	0.87 ± 0.05	0.93 ± 0.04	1.03 ± 0.13	0.91 ± 0.06	1.03 ± 0.04
NET 6	0.87 ± 0.03	0.93 ± 0.11	0.92 ± 0.18	0.91 ± 0.05	1.09 ± 0.17	0.92 ± 0.06	1.23 ± 0.04
NET 7	0.85 ± 0.04	0.88 ± 0.15	1.08 ± 0.16	0.95 ± 0.05	1.20 ± 0.16	1.05 ± 0.06	1.12 ± 0.04
NET 8	1.10 ± 0.04	1.08 ± 0.17	1.15 ± 0.09	1.10 ± 0.05	0.99 ± 0.15	1.12 ± 0.06	0.00 ± 0.00
NET 9	0.93 ± 0.03	1.11 ± 0.18	0.88 ± 0.10	0.98 ± 0.04	0.70 ± 0.14	0.91 ± 0.06	0.53 ± 0.02
NET 10	1.18 ± 0.04	1.15 ± 0.18	1.38 ± 0.10	1.22 ± 0.05	1.22 ± 0.16	1.39 ± 0.07	1.50 ± 0.05
NET 11	0.87 ± 0.03	0.88 ± 0.07	0.85 ± 0.10	0.77 ± 0.06	1.03 ± 0.14	0.89 ± 0.06	0.94 ± 0.04
NET 12	1.13 ± 0.04	1.01 ± 0.14	1.18 ± 0.10	1.13 ± 0.05	1.13 ± 0.15	1.18 ± 0.06	1.36 ± 0.05
NET 13	0.76 ± 0.03	1.07 ± 0.17	0.83 ± 0.09	0.80 ± 0.04	0.94 ± 0.14	0.85 ± 0.05	0.98 ± 0.04
NET 14	1.09 ± 0.04	1.02 ± 0.21	1.09 ± 0.15	1.20 ± 0.05	1.19 ± 0.17	1.23 ± 0.07	1.27 ± 0.05
NET 15	0.57 ± 0.02	1.16 ± 0.22	0.90 ± 0.09	0.80 ± 0.04	0.91 ± 0.13	1.03 ± 0.06	0.92 ± 0.04
NET 16	0.74 ± 0.03	1.03 ± 0.12	0.81 ± 0.09	0.84 ± 0.04	0.67 ± 0.14	0.82 ± 0.05	0.85 ± 0.03
NET 17	0.85 ± 0.03	0.89 ± 0.19	1.11 ± 0.10	1.00 ± 0.04	1.14 ± 0.16	0.92 ± 0.06	1.15 ± 0.04
NET 18	1.06 ± 0.04	1.26 ± 0.18	0.99 ± 0.10	1.10 ± 0.07	0.97 ± 0.16	1.03 ± 0.05	1.02 ± 0.04
NET 19	1.47 ± 0.04	2.21 ± 0.21	1.60 ± 0.10	1.53 ± 0.09	1.47 ± 0.18	1.66 ± 0.06	1.39 ± 0.05
NET 20	1.48 ± 0.05	1.49 ± 0.23	1.45 ± 0.11	1.55 ± 0.05	1.81 ± 0.19	1.55 ± 0.07	1.65 ± 0.06
NET 21	0.48 ± 0.02	0.64 ± 0.09	0.79 ± 0.09	0.45 ± 0.03	0.64 ± 0.13	0.61 ± 0.04	0.76 ± 0.03
NET 22	0.52 ± 0.03	0.90 ± 0.14	0.72 ± 0.09	0.52 ± 0.03	0.81 ± 0.12	0.59 ± 0.04	0.51 ± 0.03
NET 23	0.62 ± 0.02	1.12 ± 0.11	0.81 ± 0.09	0.68 ± 0.04	0.49 ± 0.11	0.67 ± 0.05	0.81 ± 0.03
NET 24	1.55 ± 0.04	1.52 ± 0.18	1.77 ± 0.11	1.46 ± 0.07	1.49 ± 0.16	1.53 ± 0.07	1.55 ± 0.05

Table 6.3.1j: Continued.

Sample	Equivalent ^{232}Thorium (ppm) from ^{212}Pb at 238.6 keV	Equivalent ^{232}Thorium (ppm) from ^{212}Pb at 300.1 keV	Equivalent ^{232}Thorium (ppm) from ^{228}Ac at 338.3 keV	Equivalent ^{232}Thorium (ppm) from ^{208}Tl at 583.2 keV	Equivalent ^{232}Thorium (ppm) from ^{212}Bi at 727.3 keV	Equivalent ^{232}Thorium (ppm) from ^{228}Ac at 911.1 keV	Equivalent ^{232}Thorium (ppm) from ^{208}Tl at 2614.5 keV
WNS 10	0.88 ± 0.03	1.05 ± 0.16	0.85 ± 0.08	0.93 ± 0.04	1.17 ± 0.14	0.93 ± 0.05	0.87 ± 0.03
WNS 11	1.16 ± 0.04	1.28 ± 0.13	1.21 ± 0.10	1.22 ± 0.05	1.18 ± 0.16	1.40 ± 0.06	1.18 ± 0.04
WNS 12	1.30 ± 0.04	1.42 ± 0.16	1.52 ± 0.10	1.34 ± 0.07	0.84 ± 0.22	1.33 ± 0.06	1.47 ± 0.05
WNS 13	1.20 ± 0.04	1.46 ± 0.15	1.37 ± 0.09	1.23 ± 0.04	1.06 ± 0.15	1.35 ± 0.06	1.18 ± 0.05
WNS 14	1.49 ± 0.05	1.40 ± 0.21	1.46 ± 0.11	1.39 ± 0.05	1.48 ± 0.16	1.64 ± 0.07	1.46 ± 0.05
WNS 15	0.80 ± 0.30	1.05 ± 0.14	1.01 ± 0.09	0.73 ± 0.05	0.70 ± 0.13	0.83 ± 0.07	0.94 ± 0.04
WNS 16	1.09 ± 0.04	1.22 ± 0.12	1.15 ± 0.17	1.05 ± 0.07	1.02 ± 0.16	1.13 ± 0.06	1.12 ± 0.04
WNS 17	1.37 ± 0.04	1.43 ± 0.18	1.54 ± 0.10	1.32 ± 0.05	1.30 ± 0.23	1.46 ± 0.09	1.30 ± 0.05
WNS 18	1.36 ± 0.05	1.46 ± 0.13	1.69 ± 0.10	1.43 ± 0.05	1.24 ± 0.17	1.45 ± 0.09	1.47 ± 0.05
WNS 19	1.57 ± 0.05	1.90 ± 0.18	1.65 ± 0.10	1.75 ± 0.06	1.70 ± 0.18	1.70 ± 0.07	1.64 ± 0.06
WNS 20	0.69 ± 0.03	0.76 ± 0.12	0.84 ± 0.09	0.71 ± 0.04	0.63 ± 0.12	0.74 ± 0.05	0.78 ± 0.03

Table 6.3.1k: Potassium concentrations of the samples of the sections Netaya South Cliff and Wadi Netanya South determined by gamma spectrometry.

Sample	K (%) determined over the concentration of ^{40}K at 1460 keV
NET 1	0.52 ± 0.01
NET 2	0.55 ± 0.01
NET 3	0.58 ± 0.01
NET 4	0.59 ± 0.01
NET 5	0.63 ± 0.01
NET 6	0.63 ± 0.01
NET 7	0.44 ± 0.01
NET 8	0.41 ± 0.01
NET 9	0.55 ± 0.01
NET 10	0.58 ± 0.01
NET 11	0.51 ± 0.01
NET 12	0.55 ± 0.01
NET 13	0.46 ± 0.01
NET 14	0.53 ± 0.01
NET 15	0.45 ± 0.01
NET 16	0.42 ± 0.01
NET 17	0.45 ± 0.01
NET 18	0.38 ± 0.01
NET 19	0.42 ± 0.01
NET 20	0.40 ± 0.01
NET 21	0.13 ± 0.01
NET 22	0.14 ± 0.01
NET 23	0.17 ± 0.01
NET 24	0.37 ± 0.01

Table 6.3.1k: Continued.

Sample	K (%) determined over the concentration of ^{40}K at 1460 keV
WNS 10	0.23 ± 0.01
WNS 11	0.29 ± 0.01
WNS 12	0.32 ± 0.01
WNS 13	0.31 ± 0.01
WNS 14	0.36 ± 0.01
WNS 15	0.29 ± 0.01
WNS 16	0.40 ± 0.01
WNS 17	0.43 ± 0.01
WNS 18	0.42 ± 0.01
WNS 19	0.40 ± 0.01
WNS 20	0.21 ± 0.01

Table 6.3.1l: Uranium, Thorium and Potassium concentrations of the samples of the sections Netanya South Cliff and Wadi Netanya South determined by gamma spectrometry.

Sample	Uranium (ppm)	Thorium (ppm)	Potassium (%)
NET 1	0.60 ± 0.04	0.95 ± 0.07	0.52 ± 0.04
NET 2	0.65 ± 0.05	0.89 ± 0.06	0.55 ± 0.04
NET 3	0.73 ± 0.05	1.27 ± 0.09	0.58 ± 0.04
NET 4	0.82 ± 0.06	1.92 ± 0.13	0.59 ± 0.04
NET 5	0.69 ± 0.05	0.97 ± 0.07	0.63 ± 0.04
NET 6	0.62 ± 0.04	0.98 ± 0.07	0.63 ± 0.04
NET 7	0.40 ± 0.03	1.02 ± 0.07	0.44 ± 0.03
NET 8	0.49 ± 0.03	1.09 ± 0.08	0.41 ± 0.03
NET 9	0.38 ± 0.03	0.86 ± 0.06	0.55 ± 0.04
NET 10	0.44 ± 0.03	1.29± 0.09	0.58 ± 0.04
NET 11	0.35 ± 0.02	0.89 ± 0.06	0.51 ± 0.04
NET 12	0.44 ± 0.03	1.16 ± 0.08	0.55 ± 0.04
NET 13	0.33 ± 0.02	0.89 ± 0.06	0.46 ± 0.03
NET 14	0.41 ± 0.03	1.16 ± 0.08	0.53 ± 0.04
NET 15	0.33 ± 0.02	0.90 ± 0.06	0.45 ± 0.03
NET 16	0.34 ± 0.02	0.82 ± 0.06	0.42 ± 0.03
NET 17	0.33 ± 0.02	1.01 ± 0.07	0.45 ± 0.03
NET 18	0.42 ± 0.03	1.06 ± 0.07	0.38 ± 0.03
NET 19	0.48 ± 0.03	1.62 ± 0.11	0.42 ± 0.03
NET 20	0.61 ± 0.04	1.57 ± 0.11	0.40 ± 0.03
NET 21	0.48 ± 0.03	0.62 ± 0.04	0.13 ± 0.01
NET 22	0.41 ± 0.03	0.65 ± 0.05	0.14 ± 0.01
NET 23	0.54 ± 0.04	0.74 ± 0.05	0.17 ± 0.01
NET 24	0.67 ± 0.05	1.55 ± 0.11	0.37 ± 0.03

Table 6.3.1l: Continued.

Sample	Uranium (ppm)	Thorium (ppm)	Potassium (%)
WNS 10	0.37 ± 0.03	0.95 ± 0.07	0.23 ± 0.02
WNS 11	0.44 ± 0.03	1.23 ± 0.09	0.29 ± 0.02
WNS 12	0.46 ± 0.03	1.32 ± 0.09	0.32 ± 0.02
WNS 13	0.41 ± 0.03	1.26 ± 0.09	0.31 ± 0.02
WNS 14	0.47 ± 0.03	1.47 ± 0.10	0.36 ± 0.03
WNS 15	0.35 ± 0.03	0.87 ± 0.06	0.29 ± 0.02
WNS 16	0.35 ± 0.03	1.11 ± 0.08	0.40 ± 0.03
WNS 17	0.44 ± 0.03	1.39 ± 0.10	0.43 ± 0.03
WNS 18	0.44 ± 0.03	1.44 ± 0.10	0.42 ± 0.03
WNS 19	0.46 ± 0.03	1.70 ± 0.12	0.40 ± 0.03
WNS 20	0.30 ± 0.02	0.74 ± 0.05	0.21 ± 0.01

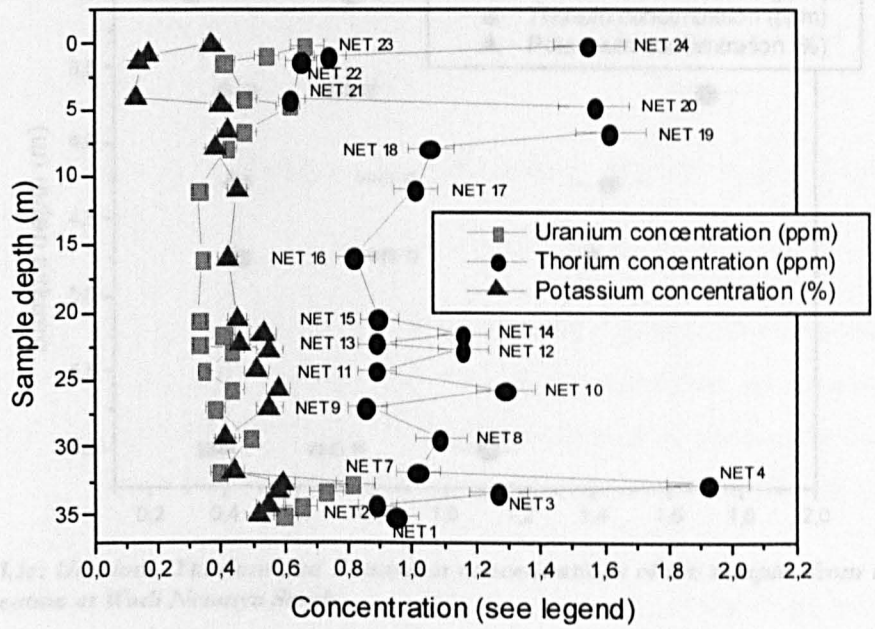

Figure 6.3.1c: Uranium, Thorium and Potassium concentrations of the samples of the southern section at Netanya South Cliff.

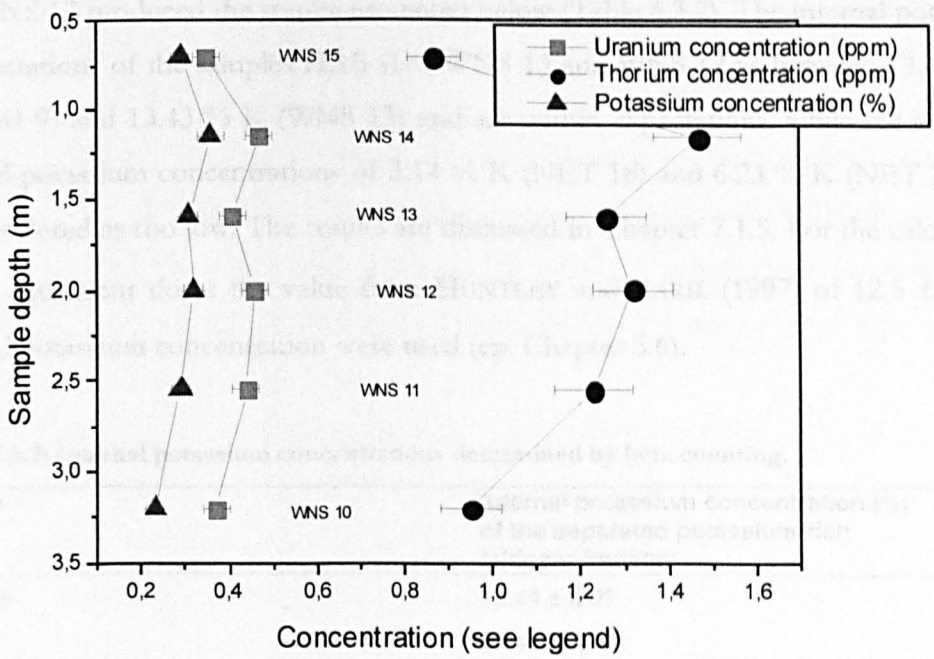

Figure 6.3.1d: Uranium, Thorium and Potassium concentrations of the samples from the western section at Wadi Netanya South.

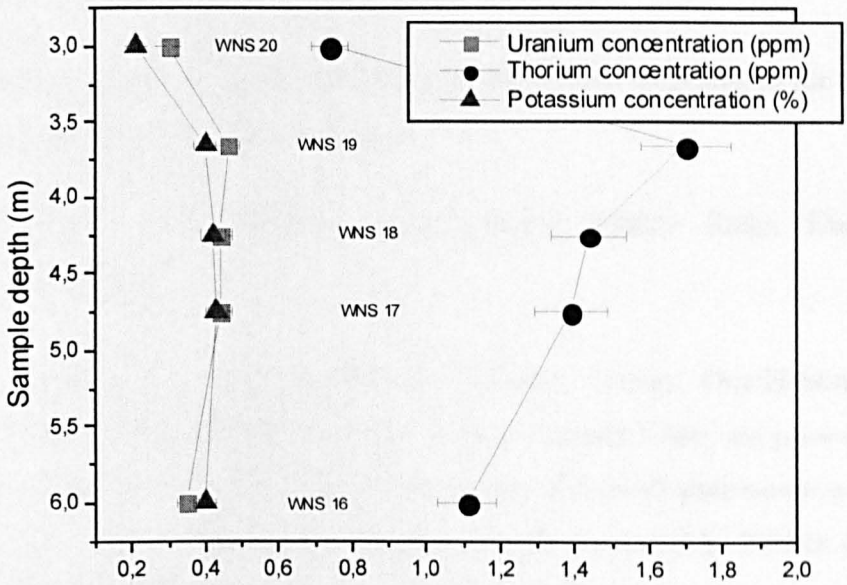

Figure 6.3.1e: Uranium, Thorium and Potassium concentrations of the samples from the eastern section at Wadi Netanya South.

6.3.2 Beta counting

The determination of the internal potassium concentration *via* beta counting on the potassium-rich feldspar fraction of the samples HAB-II-9, NET 18, NET 24, WNS 13 and WNS 17 produced the results presented below (Table 6.3.2). The internal potassium concentrations of the samples HAB-II-9, WNS 13 and WNS 17 lie between 12.44 % K (HAB-II-9) and 13.43 % K (WNS 13) and are within expectations, while the obtained internal potassium concentrations of 3.14 % K (NET 18) and 6.23 % K (NET 24) can be considered as too low. The results are discussed in Chapter 7.1.5. For the calculation of the equivalent doses the value from HUNTLEY and BARIL (1997) of 12.5 ± 0.5 % internal potassium concentration were used (cp. Chapter 5.6).

Table 6.3.2: Internal potassium concentrations determined by beta counting.

Sample	Internal potassium concentration (%) of the separated potassium-rich feldspar fraction
HAB-II-9	12.44 ± 0.01
NET 18	3.14 ± 0.01
NET 24	6.23 ± 0.01
WNS 13	13.43 ± 0.01
WNS 17	12.90 ± 0.01

6.4 Luminescence ages

The luminescence ages obtained from the various samples collected at the Sharon and Carmel coastal plains are presented below.

Habonim Quarry, Dor-Habonim Nature Reserve Middle Ridge, Dor-Habonim Nature Reserve Coast

Here the luminescence dating results for Habonim Quarry, Dor-Habonim Nature Reserve Middle Ridge and Dor-Habonim Nature Reserve Coast are presented (Table 6.4a). Preliminary data for Habonim Quarry, with individual parameters not adjusted exactly for the Israeli coastal plain, were prematurely presented by NEBER (2002). The data given here are the final results of the study (Table 6.4a).

The ages obtained from the different horizons at Habonim Quarry range between 32 ± 3 ka (HAB 15 TL) and 132 ± 18 ka (HAB 4 IR-OSL) (Table 6.4a). For the section at the East-wall at Habonim Quarry an IR-OSL age of 132 ± 18 ka and an TL age of 124 ± 17 ka was determined for the aeolianite samples from underneath the pedocomplex (HAB 4) (Figure 6.4a). Ages obtained for an additional sample (HAB 16) taken from the same aeolianite north of the particular sampled section at the East-wall were estimated at 122 ± 15 ka for the IR-OSL and at 85 ± 10 ka for the TL (Figure 6.4b). The samples from the soil sequence above the aeolianite show ages of 96 ± 10 ka (HAB 5 IR-OSL) to 73 ± 6 ka (HAB 9 TL) and of 51 ± 4 ka (HAB 10 TL) to 37 ± 3 (HAB 13 IR-OSL), decreasing in age from the bottom to the top. The ages suggest a hiatus between the samples HAB 9 and HAB 10 of about 25 ka. Ages from the sample (HAB 14) of the aeolianite above the pedocomplex could not be obtained. Sample HAB 15 taken further south than the particular sampled section shows an IR-OSL age of 37 ± 3 ka and a TL age of 32 ± 3 ka (Figure 6.4b).

For the samples of the aeolianites of the North-wall (Figure 3.2.1b) ages of 60 ± 9 ka (HAB 3) to 53 ± 8 ka (HAB 1) were obtained (Figure 6.4c).

Supplementary samples came from the North-wall of the quarry after successive quarrying activities (Figure 3.2.1c). The lower sampled aeolianite (HAB-II-9) shows an IR-OSL age of 142± 7 ka and a TL age of 141 ± 7 ka (Figure 6.4d). For the sample (HAB-II-5) from the soil on top of the aeolianite ages of 75 ± 7 ka were determined for both IR-OSL and TL. The overlying aeolianite shows ages of 74 ± 12 ka (HAB-II-4 IR-

OSL) and 66 ± 11 ka (HAB-II-4 TL). The section displays a hiatus of maximum 65 ka between the lower sampled aeolianite (HAB-II-9) and the soil (HAB-II-5). For an adjacent aeolianite directly to the West, ages of 49 ± 8 ka (HAB-II-1 IR-OSL) and 48 ± 7 ka (HAB-II-1 TL) were determined (Figure 6.4d).

The aeolianite from Dor-Habonim Nature Reserve Middle Ridge (HDM) showed ages of 87 ± 13 ka (IR-OSL) and 64 ± 9 ka (TL) (Figure 6.4c).

For the aeolianite from the coast at Dor-Habonim Nature Reserve (HDC) ages of 53 ± 8 ka (IR-OSL) and 39 ± 6 ka (TL) were obtained (Figure 6.4c).

Table 6.4a: Luminescence dating results for the sections at Habonim Quarry, Dor-Habonim Nature Reserve Middle Ridge, Dor-Habonim Nature Reserve Coast.

Sample	Depth (m)	D_e IR-OSL (Gy)	D_e TL (Gy)	Grain size (µm)	Water (%)	Uranium (ppm)	Thorium (ppm)	Potassium (%)	Cosmic dose (µGy/a)	Total dose (µGy/a)	Age IR-OSL (ka)	Age TL (ka)	Ratio IR-OSL age/ TL age
HAB 1	9.00	59.27 ± 3.33	57.28 ± 2.66	150 ± 50	5.00 ± 1.50	1.25 ± 0.09	0.43 ± 0.03	0.14 ± 0.01	68	1080 ± 155	55 ± 8	53 ± 8	1.03
HAB 2	7.20	64.60 ± 3.30	60.61 ± 2.66	150 ± 50	5.00 ± 1.50	1.15 ± 0.08	0.75 ± 0.05	0.14 ± 0.01	82	1094 ± 155	59 ± 9	55 ± 8	1.07
HAB 3	6.10	67.93 ± 2.66	65.27 ± 2.66	150 ± 50	5.00 ± 1.50	1.31 ± 0.09	0.51 ± 0.04	0.14 ± 0.01	93	1127 ± 155	60 ± 9	58 ± 8	1.04
HAB 4	8.90	151.85 ± 4.66	142.52 ± 4.00	150 ± 50	5.00 ± 1.50	0.56 ± 0.04	1.16 ± 0.08	0.34 ± 0.02	69	1151 ± 157	132 ± 18	124 ± 17	1.07
HAB 5	7.75	155.18 ± 4.66	153.18 ± 5.99	150 ± 50	9.00 ± 3.00	0.77 ± 0.05	3.22 ± 0.23	0.64 ± 0.04	77	1613 ± 156	96 ± 10	95 ± 10	1.01
HAB 6	7.45	165.17 ± 4.00	151.85 ± 3.33	150 ± 50	9.00 ± 3.00	0.93 ± 0.06	4.18 ± 0.29	0.77 ± 0.05	80	1847 ± 157	89 ± 8	82 ± 7	1.09
HAB 7	6.75	149.18 ± 4.66	133.87 ± 3.33	150 ± 50	9.00 ± 3.00	0.90 ± 0.06	4.50 ± 0.32	0.84 ± 0.06	87	1935 ± 160	77 ± 7	69 ± 6	1.11
HAB 8	6.25	191.81 ± 7.33	189.81 ± 5.33	150 ± 50	9.00 ± 3.00	1.11 ± 0.08	5.66 ± 0.40	0.94 ± 0.07	91	2170 ± 163	88 ± 7	87 ± 7	1.01
HAB 9	6.05	171.35 ± 7.19	163.84 ± 5.89	150 ± 50	9.00 ± 3.00	1.10 ± 0.08	6.12 ± 0.43	0.98 ± 0.07	94	2242 ± 163	76 ± 6	73 ± 6	1.05
HAB 10	5.55	105.95 ± 2.62	113.14 ± 3.27	150 ± 50	9.00 ± 3.00	1.09 ± 0.08	6.13 ± 0.43	0.94 ± 0.07	99	2210 ± 163	48 ± 4	51 ± 4	0.94
HAB 11	5.25	107.23 ± 5.33	108.56 ± 5.33	150 ± 50	9.00 ± 3.00	1.28 ± 0.09	6.01 ± 0.42	0.89 ± 0.06	103	2206 ± 158	49 ± 4	49 ± 4	0.99
HAB 12	4.50	79.25 ± 2.66	77.92 ± 2.66	150 ± 50	9.00 ± 3.00	1.20 ± 0.08	5.31 ± 0.37	0.81 ± 0.06	112	2069 ± 159	38 ± 3	38 ± 3	1.02
HAB 13	4.20	75.92 ± 3.33	79.92 ± 6.66	150 ± 50	9.00 ± 3.00	(HAB 12)[1]	(HAB 12)[1]	(HAB 12)[1]	116	2073 ± 159	37 ± 3	39 ± 4	0.95
HAB 14	3.60	---[2]	---[2]	150 ± 50	---[2]	1.24 ± 0.09	0.65 ± 0.46	0.18 ± 0.01	126	---[2]	---[2]	---[2]	---
HAB 15	4.45	77.26 ± 3.33	65.93 ± 2.66	150 ± 50	9.00 ± 3.00	(HAB 12)[1]	(HAB 12)[1]	(HAB 12)[1]	113	2070 ± 159	37 ± 3	32 ± 3	1.17
HAB 16	10.45	158.51 ± 4.00	110.56 ± 2.00	150 ± 50	5.00 ± 1.50	0.79 ± 0.06	1.08 ± 0.08	0.45 ± 0.03	59	1299 ± 156	122 ± 15	85 ± 10	1.43
HAB-II-1	1.40	53.33 ± 3.52	51.57 ± 2.93	150 ± 50	5.00 ± 1.50	1.03 ± 0.07	0.50 ± 0.03	0.09 ± 0.01	168	1081 ± 158	49 ± 8	48 ± 7	1.03
HAB-II-4	2.50	79.70 ± 6.25	70.91 ± 5.86	150 ± 50	5.00 ± 1.50	1.02 ± 0.07	0.57 ± 0.04	0.11 ± 0.01	145	1080 ± 157	74 ± 12	66 ± 11	1.12
HAB-II-5	3.20	141.23 ± 5.27	142.40 ± 4.69	150 ± 50	9.00 ± 3.00	0.88 ± 0.06	4.67 ± 0.33	0.73 ± 0.05	132	1888 ± 157	75 ± 7	75 ± 7	0.99
HAB-II-9	2.60	150.54 ± 5.95	149.94 ± 5.95	150 ± 50	5.00 ± 1.50	0.54 ± 0.04	0.51 ± 0.04	0.23 ± 0.02	143	1062 ± 35	142 ± 7	141 ± 7	1.00
HDM	0.50	96.57 ± 3.33	71.26 ± 2.66	150 ± 50	5.00 ± 1.50	0.74 ± 0.05	0.77 ± 0.05	0.16 ± 0.01	190	1116 ± 159	87 ± 13	64 ± 9	1.36
HDC	0.50	65.27 ± 5.33	47.95 ± 2.66	150 ± 50	5.00 ± 1.50	0.66 ± 0.05	0.77 ± 0.05	0.30 ± 0.02	190	1228 ± 159	53 ± 8	39 ± 6	1.36

[1]Uranium, Thorium and Potassium values for the samples HAB13 and HAB15 could not be determined as the samples went missing during shipping. The ages of these samples were calculated using the values of sample HAB12.
[2]The equivalent doses for sample HAB14 could not be determined due to a technical failure and an additional shortage of sample material

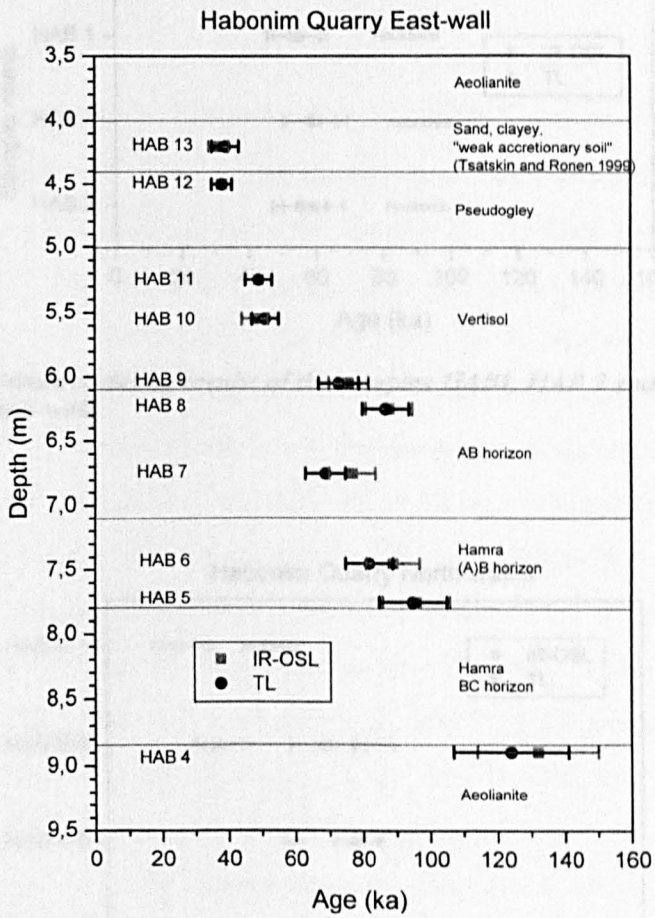

Figure 6.4a: Luminescence dating results of the section at Habonim Quarry East-wall.

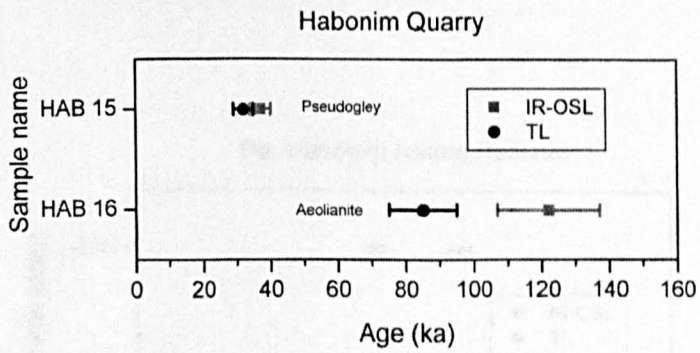

Figure 6.4b: Luminescence dating results of the samples HAB 15 and HAB 16 at Habonim Quarry East-wall.

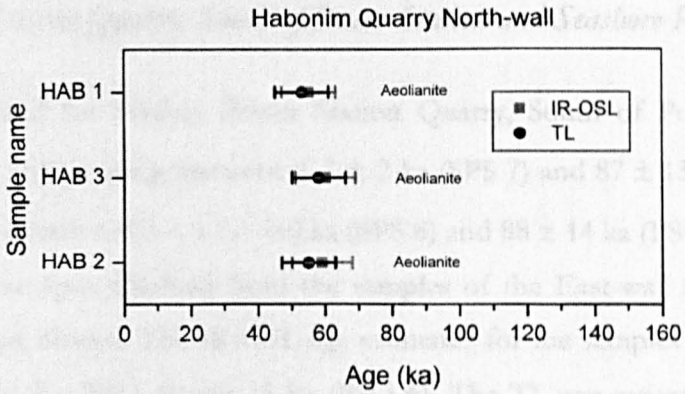

Figure 6.4c: Luminescence dating results of the samples HAB1, HAB 2 and HAB 3 at Habonim Quarry North-wall.

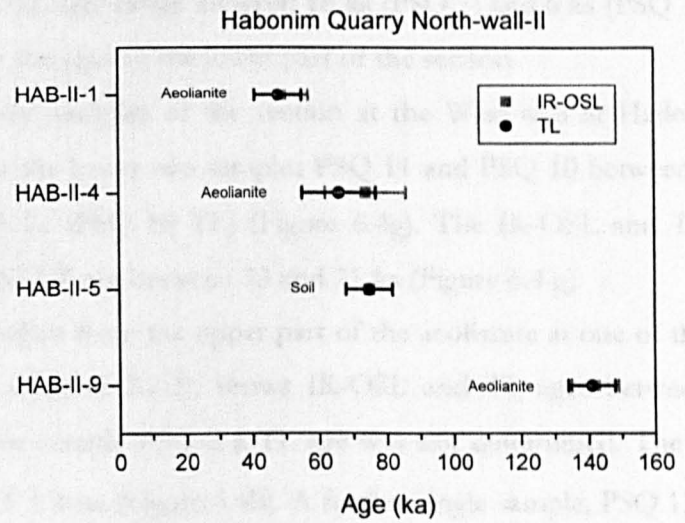

Figure 6.4d: Luminescence dating results of the samples HAB-II-1, HAB-II-4, HAB-II-5 and HAB-II-9 from Habonim Quarry North-wall-II.

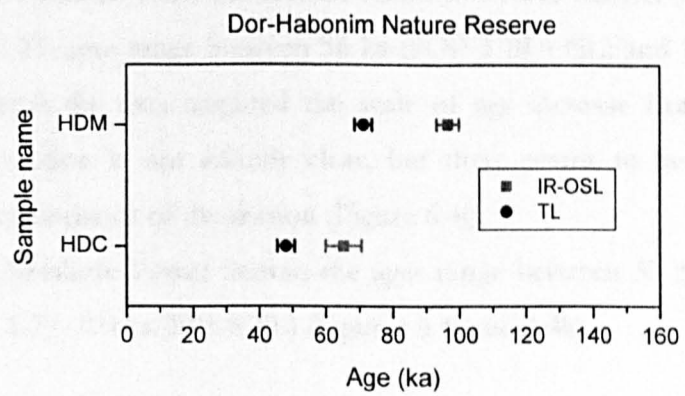

Figure 6.4e: Luminescence dating results of the samples from Dor-Habonim Nature Reserve Middle Ridge (HDM) and Coast (HDC).

Hadera Power Station Quarry, South of Power Station and Seashore Power Station

The ages estimated for Hadera Power Station Quarry, South of Power Station and Seashore Power Station range between ≤ 7 ± 2 ka (SPS 7) and 87 ± 13 ka (PSQ 11) for the IR-OSL and between 0.0 + 1.7/- 0.0 ka (SPS 8) and 88 ± 14 ka (PSQ 11) for the TL. In Figure 6.4f the ages obtained from the samples of the East-wall at Hadera Power Station Quarry are shown. The IR-OSL age estimates for the samples PSQ 3 to PSQ 6 range between 33 ka (PSQ 4) and 15 ka (PSQ 6). The TL age estimates for the same samples range from 28 ka (PSQ 4) to 17 ka (PSQ 3 and PSQ 6). A general age increase with depth cannot be observed clearly for the lower part of the section. For the upper part of the pedocomplex (PSQ 7 and PSQ 8) no TL age estimates were obtained. The determined IR-OSL ages range between 16 ka (PSQ 7) and 6 ka (PSQ 7 and PSQ 8) and are younger than the ages of the lower part of the section.

The ages from the samples of the section at the West-wall at Hadera Power Station Quarry range for the lower two samples PSQ 11 and PSQ 10 between 101 ka (PSQ 10 IR-OSL) and 68 ka (PSQ 10 TL) (Figure 6.4g). The IR-OSL and TL ages from the sample above (PSQ 9) are between 33 and 21 ka (Figure 6.4 g).

Sample PSQ 1, taken from the upper part of the aeolianite at one of the North-walls of the quarry (cp. Chapter 3.2.2), shows IR-OSL and TL ages between 57 and 39 ka (Figure 6.4h). For sample PSQ 2 a TL age was not determined. The IR-OSL age was estimated as ≤ 23 ± 6 ka (Figure 6.4h). A further single sample, PSQ 12, was taken from the lower part of the aeolianite underneath the pedocomplex and just above the quarry surface. For the sample an IR-OSL age of 31 ± 11 ka and a TL age of 54 ± 9 ka was determined (Figure 6.4h).

For the samples obtained from the section South of Power Station (SOP 1 to SOP 5) the IR-OSL and TL ages range between 56 ka (SOP 3 IR-OSL) and 17 ka (SOP 1 TL) (Figure 6.4i). From the data acquired the scale of age increase from the top to the bottom of the section is not entirely clear, but there seems to be no major hiatus between different horizons of the section (Figure 6.4i).

For the section Seashore Power Station the ages range between 37 ± 5 ka (SPS 2 IR-OSL) and 0.0 + 1.7/- 0.0 ka (SPS 8 TL) (Figures 6.4j and 6.4k).

Table 6.4b: Luminescence dating results for the sections at Hadera Power Station Quarry and South of Power Station.

Sample	Depth (m)	D_e IR-OSL (Gy)	D_e TL (Gy)	Grain size (μm)	Water (%)	Uranium (ppm)	Thorium (ppm)	Potassium (%)	Cosmic dose (μGy/a)	Total dose (μGy/a)	Age IR-OSL (ka)	Age TL (ka)	Ratio IR-OSL age/ TL age
PSQ 1	0.50	58.18 ± 4.21	54.68 ± 3.51	150 ± 50	5.00 ± 1.50	(PSQ 10)[1]	(PSQ 10)[1]	(PSQ 10)[1]	190	1178 ± 161	49 ± 8	46 ± 7	1.06
PSQ 2	0.75	≤ 25.24 ± 5.61	---	150 ± 50	5.00 ± 1.50	0.29 ± 0.02	0.71 ± 0.05	0.27 ± 0.02	183	1092 ± 163	≤ 23 ± 6	---	---
PSQ 3	3.05	35.75 ± 7.01	30.14 ± 6.31	150 ± 50	9.00 ± 3.00	0.60 ± 0.04	2.32 ± 0.16	0.45 ± 0.03	135	1388 ± 158	26 ± 6	22 ± 5	1.19
PSQ 4	2.50	44.86 ± 4.91	39.26 ± 3.51	150 ± 50	9.00 ± 3.00	0.74 ± 0.05	3.09 ± 0.22	0.53 ± 0.04	145	1564 ± 157	29 ± 4	25 ± 3	1.14
PSQ 5	2.10	---	39.26 ± 4.21	150 ± 50	9.00 ± 3.00	0.86 ± 0.06	3.85 ± 0.27	0.49 ± 0.03	153	1624 ± 154	---	24 ± 3	---
PSQ 6	1.55	35.75 ± 7.71	38.56 ± 7.71	150 ± 50	9.00 ± 3.00	1.11 ± 0.08	4.56 ± 0.32	0.50 ± 0.04	164	1760 ± 155	20 ± 5	22 ± 5	0.93
PSQ 7	1.00	18.93 ± 8.41	---	150 ± 50	9.00 ± 3.00	1.10 ± 0.08	4.79 ± 0.34	0.51 ± 0.04	177	1798 ± 155	11 ± 5	---	---
PSQ 8	0.50	17.53 ± 7.01	---	150 ± 50	9.00 ± 3.00	(PSQ 7)[2]	(PSQ 7)[2]	(PSQ 7)[2]	190	1811 ± 155	10 ± 4	---	---
PSQ 9	0.25	33.65 ± 2.80	29.44 ± 2.80	150 ± 50	5.00 ± 1.50	(PSQ 10)[1]	(PSQ 10)[1]	(PSQ 10)[1]	197	1185 ± 162	28 ± 5	25 ± 4	1.14
PSQ 10	0.55	103.89 ± 5.50	93.57 ± 6.19	150 ± 50	5.00 ± 1.50	0.46 ± 0.03	0.79 ± 0.06	0.30 ± 0.02	189	1177 ± 161	88 ± 13	80 ± 12	1.11
PSQ 11	0.85	101.14 ± 6.19	103.20 ± 6.88	150 ± 50	5.00 ± 1.50	(PSQ 10)[1]	(PSQ 10)[1]	(PSQ 10)[1]	181	1169 ± 161	87 ± 13	88 ± 14	0.98
PSQ 12	5.50	34.35 ± 11.22	60.29 ± 4.21	150 ± 50	5.00 ± 1.50	0.54 ± 0.04	0.80 ± 0.06	0.30 ± 0.02	100	1110 ± 159	31 ± 11	54 ± 9	0.57
SOP 1	0.25	25.31 ± 3.33	25.97 ± 4.00	150 ± 50	9.00 ± 3.00	0.37 ± 0.03	0.96 ± 0.07	0.31 ± 0.02	197	1161 ± 162	22 ± 4	22 ± 5	0.97
SOP 2	2.40	37.96 ± 2.66	37.96 ± 2.00	150 ± 50	5.00 ± 1.50	(SOP 3)[3]	(SOP 3)[3]	(SOP 3)[3]	147	1162 ± 162	33 ± 5	33 ± 5	1.00
SOP 3	2.60	56.61 ± 3.33	55.28 ± 3.33	150 ± 50	5.00 ± 1.50	0.33 ± 0.02	0.83 ± 0.06	0.36 ± 0.03	143	1158 ± 162	49 ± 7	48 ± 7	1.02
SOP 4	3.60	52.61 ± 4.00	46.62 ± 2.66	150 ± 50	5.00 ± 1.50	0.32 ± 0.02	0.79 ± 0.06	0.35 ± 0.03	126	1125 ± 162	47 ± 8	41 ± 6	1.13
SOP 5	5.30	32.63 ± 4.00	35.30 ± 2.66	150 ± 50	5.00 ± 1.50	(SOP 4)[4]	(SOP 4)[4]	(SOP 4)[4]	102	1101 ± 162	30 ± 6	32 ± 5	0.92

Table 6.4b: Continued.

Sample	Depth (m)	D_e IR-OSL (Gy)	D_e TL (Gy)	Grain size (µm)	Water (%)	Uranium (ppm)	Thorium (ppm)	Potassium (%)	Cosmic dose (µGy/a)	Total dose (µGy/a)	Age IR-OSL (ka)	Age TL (ka)	Ratio IR-OSL age/ TL age
SPS 1	0.50	37.30 ± 2.00	34.63 ± 1.33	150 ± 50	5.00 ± 1.50	0.34 ± 0.02	0.96 ± 0.07	0.35 ± 0.03	190	1208 ± 162	31 ± 5	29 ± 4	1.08
SPS 2	1.60	43.29 ± 2.00	32.63 ± 2.66	150 ± 50	5.00 ± 1.50	(SPS 1)[5]	(SPS 1)[5]	(SPS 1)[5]	163	1181 ± 162	37 ± 5	28 ± 4	1.33
SPS 5	1.20	36.62 ± 3.27	32.05 ± 2.62	150 ± 50	9.00 ± 3.00	0.71 ± 0.05	2.51 ± 0.18	0.51 ± 0.04	172	1521 ± 159	24 ± 3	21 ± 3	1.14
SPS 6	0.80	20.93 ± 2.62	23.54 ± 3.27	150 ± 50	9.00 ± 3.00	(SPS 5)[6]	(SPS 5)[6]	(SPS 5)[6]	182	1531 ± 159	14 ± 2	15 ± 3	0.89
SPS 7	0.60	≤ 8.50 ± 1.96	0.65 + 2.62/- 0.65	150 ± 50	5.00 ± 1.50	0.29 ± 0.02	0.69 ± 0.05	0.33 ± 0.02	187	1151 ± 162	≤ 7 ± 2	0.6 + 2/- 0.6	---
SPS 8	0.25	≤ 10.46 ± 1.96	0.0 + 1.96/- 0.0	150 ± 50	5.00 ± 1.50	0.31 ± 0.02	0.69 ± 0.05	0.31 ± 0.02	197	1147 ± 162	≤ 9 ± 2	0.0 + 1.7/- 0.0	---

[1]Uranium, Thorium and Potassium values were not available for the samples PSQ 1, PSQ 9 and PSQ 11. The ages of these samples were calculated using the values of sample PSQ 10.
[2]Uranium, Thorium and Potassium values were not available for sample PSQ 8. The IR-OSL age was calculated with the values of sample PSQ 7 which is from the same horizon than PSQ 8.
[3]Uranium, Thorium and Potassium values were not available for sample SOP 2. The ages of the sample were calculated using the values of sample SOP 3 which was taken from the horizon directly underneath.
[4]Uranium, Thorium and Potassium values were not available for sample SOP 5. The ages of the sample were calculated using the values of sample SOP 4 which was taken from the horizon directly above.
[5]Uranium, Thorium and Potassium values were not available for sample SPS 1. The ages of the sample were calculated using the values of sample SPS 1 which was taken from the horizon directly above.
[6]Uranium, Thorium and Potassium values were not available for sample SPS 6. The ages of the sample were calculated using the values of sample SPS 5 which was taken from the same horizon.

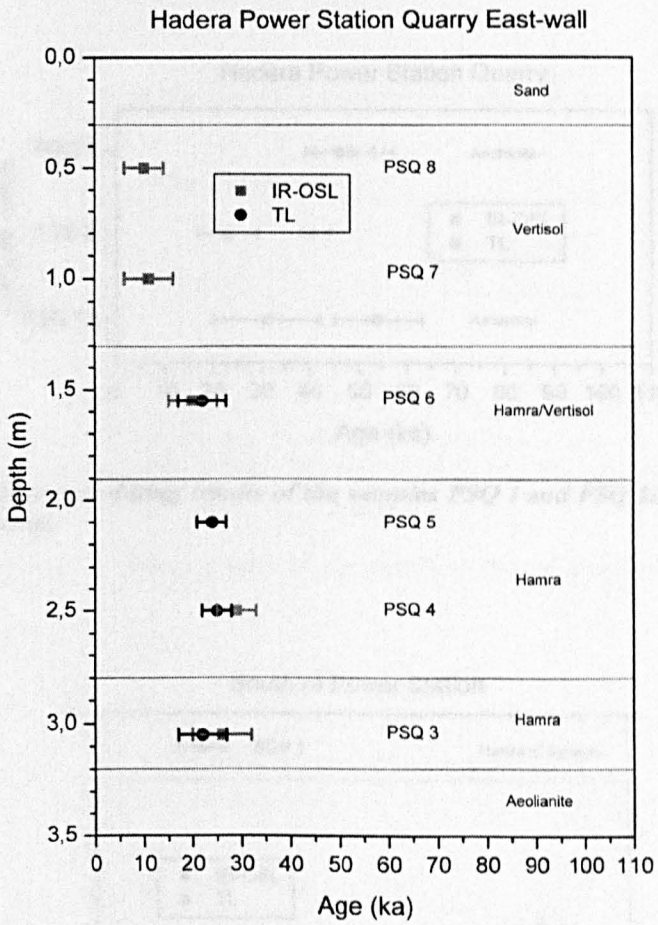

Figure 6.4f: Luminescence dating results of the section at Hadera Power Station Quarry East-wall.

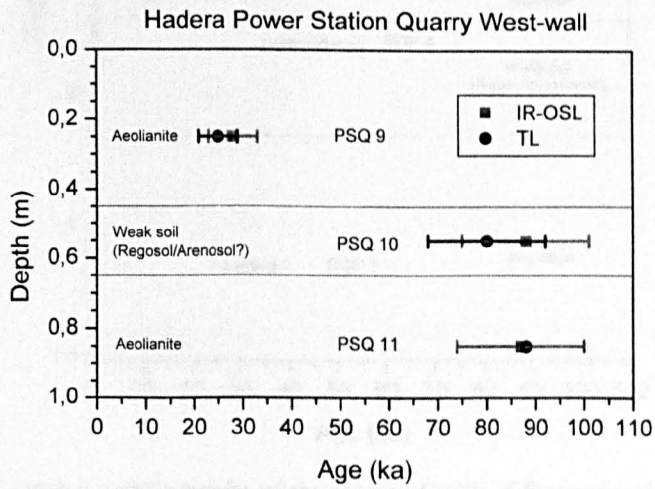

Figure 6.4g: Luminescence dating results of the section at Hadera Power Station Quarry West-wall.

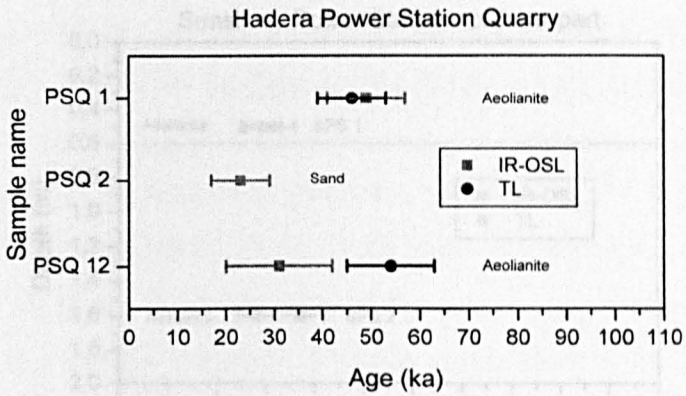

Figure 6.4h: Luminescence dating results of the samples PSQ 1 and PSQ 12 from Hadera Power Station Quarry.

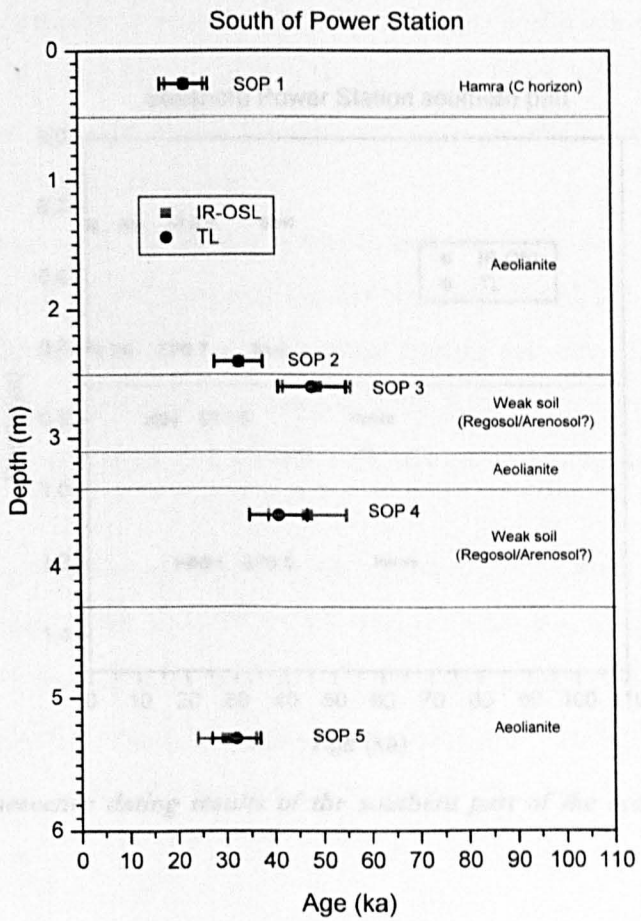

Figure 6.4i: Luminescence dating results of the section South of Power Station.

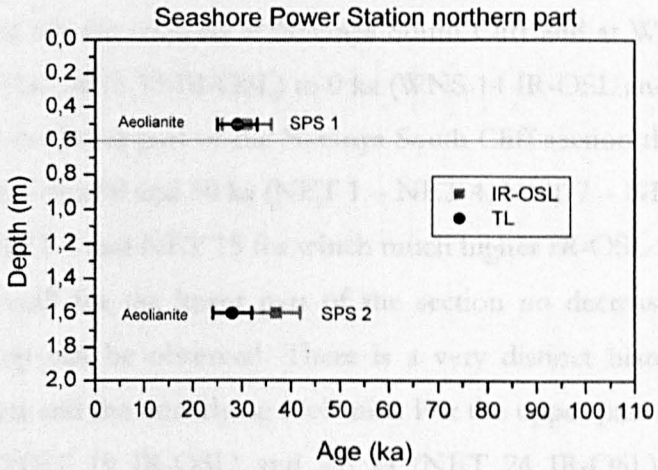

Figure 6.4j: Luminescence dating results of the northern part of the section Seashore Power Station.

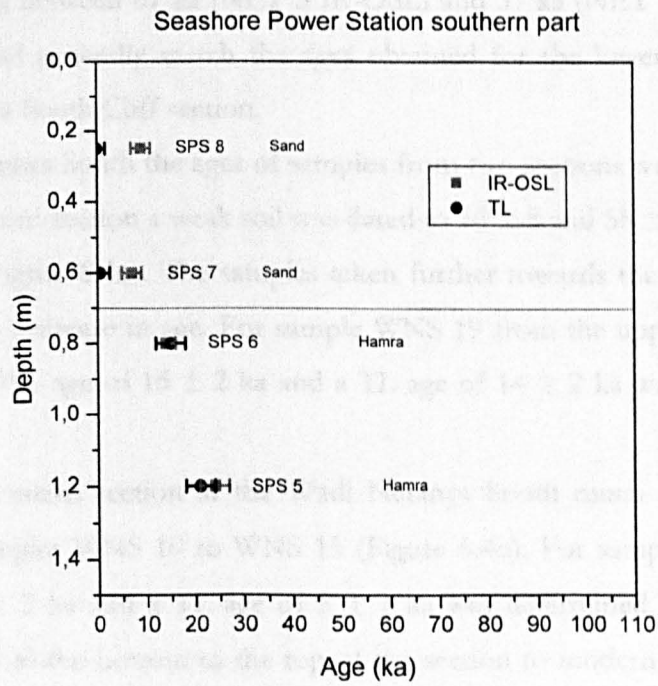

Figure 6.4k: Luminescence dating results of the southern part of the section Seashore Power Station.

Netanya South Cliff and Wadi Netanya South

The ages obtained for the sections at Netanya South Cliff and at Wadi Netanya South range between 87 ka (NET 15 IR-OSL) to 0 ka (WNS 14 IR-OSL and TL, WNS 15 TL) (Table 6.4c). For the lower part of the Netanya South Cliff section the IR-OSL and TL ages range between *circa* 60 and 30 ka (NET 1 – NET 4, NET 7 – NET 18). Exceptions are the samples NET 4 and NET 15 for which much higher IR-OSL ages were obtained (Figure 6.4l). Overall for the lower part of the section no decrease of age from the bottom to the top can be observed. There is a very distinct hiatus of about 30 ka between the hamra and the underlying aeolianite. For the upper part of the section, ages between 15 ka (NET 19 IR-OSL) and 2.8 ka (NET 24 IR-OSL) were determined. Generally the ages of the younger part of the section decrease towards the top (Figure 6.4l). Two additional samples (NET 5 and NET 6) taken from an aeolianite further North, which can laterally be traced to belong stratigraphically below the section in the South, show ages between 61 ka (NET 5 IR-OSL) and 37 ka (NET 6 IR-OSL and TL) (Figure 6.4m) and generally match the ages obtained for the lower part of the more southern Netanya South Cliff section.

In the Wadi Netanya South the ages of samples from two sections were obtained (Table 6.4c). At the eastern section a weak soil was dated to 56 ± 8 and 55 ± 8 ka (WNS 16 IR-OSL and TL) (Figure 6.4n). The samples taken further towards the top of the section show a dramatic decrease in age. For sample WNS 19 from the upper part of a hamra horizon an IR-OSL age of 15 ± 2 ka and a TL age of 14 ± 2 ka was obtained (Figure 6.4n).

For the more western section at the Wadi Netanya South much younger ages were obtained for samples WNS 10 to WNS 15 (Figure 6.4o). For sample WNS 10 an IR-OSL age of 6 ± 2 ka and a TL age of 5 ± 1 ka was determined. The ages decrease systematically from the bottom to the top of the section to modern/recent ages (WNS 14, WNS 15) (Figure 6.4o). The luminescence ages are discussed in Chapter 7.2.1.

Table 6.4c: Luminescence dating results for the sections at Netanya South Cliff and Wadi Netanya South.

Sample	Depth (m)	D_e IR-OSL (Gy)	D_e TL (Gy)	Grain size (µm)	Water (%)	Uranium (ppm)	Thorium (ppm)	Potassium (%)	Cosmic dose (µGy/a)	Total dose (µGy/a)	Age IR-OSL (ka)	Age TL (ka)	Ratio IR-OSL ages/ TL ages
NET 1	35.10	66.15 ± 8.13	56.74 ± 5.39	132.5 ± 7.5	5 ± 1.5	0.60 ± 0.04	0.95 ± 0.07	0.52 ± 0.04	12	1207 ± 52	55 ± 7	47 ± 5	1.17
NET 2	34.30	61.98 ± 4.18	57.50 ± 1.75	112.5 ± 12.5	5 ± 1.5	0.65 ± 0.05	0.89 ± 0.06	0.55 ± 0.04	12	1185 ± 60	52 ± 4	49 ± 3	1.08
NET 3	33.30	84.08 ± 13.75	55.29 ± 6.08	132.5 ± 7.5	5 ± 1.5	0.73 ± 0.05	1.27 ± 0.09	0.58 ± 0.04	13	1326 ± 54	63 ± 11	42 ± 5	1.52
NET 4	32.70	62.89 ± 4.48	67.29 ± 5.54	112.5 ± 12.5	5 ± 1.5	0.82 ± 0.06	1.92 ± 0.13	0.59 ± 0.04	13	1358 ± 62	46 ± 4	50 ± 5	0.93
NET 5	14.50	74.21 ± 8.66	61.07 ± 4.48	132.5 ± 7.5	5 ± 1.5	0.69 ± 0.05	0.97 ± 0.07	0.63 ± 0.04	42	1368 ± 54	54 ± 7	45 ± 4	1.22
NET 6	12.00	60.23 ± 7.37	57.65 ± 5.39	150.0 ± 10.0	5 ± 1.5	0.62 ± 0.04	0.98 ± 0.07	0.63 ± 0.04	51	1411 ± 57	43 ± 6	41 ± 4	1.04
NET 7	31.80	49.29 ± 6.38	39.19 ± 5.09	150.0 ± 10.0	5 ± 1.5	0.40 ± 0.03	1.02 ± 0.07	0.44 ± 0.03	14	1138 ± 50	43 ± 6	34 ± 5	1.26
NET 8	29.40	62.51 ± 5.77	53.01 ± 5.77	150.0 ± 10.0	5 ± 1.5	0.49 ± 0.03	1.09 ± 0.08	0.41 ± 0.03	16	1141 ± 50	55 ± 6	46 ± 5	1.18
NET 9	27.10	63.91 ± 10.89	53.92 ± 9.55	150.0 ± 10.0	5 ± 1.5	0.38 ± 0.03	0.86 ± 0.06	0.55 ± 0.04	18	1229 ± 56	52 ± 9	44 ± 8	1.19
NET 10	25.70	66.22 ± 6.12	64.43 ± 5.97	150.0 ± 10.0	5 ± 1.5	0.44 ± 0.03	1.29± 0.09	0.58 ± 0.04	19	1309 ± 57	51 ± 5	49 ± 5	1.03
NET 11	24.30	45.04 ± 3.95	45.57 ± 4.03	150.0 ± 10.0	5 ± 1.5	0.35 ± 0.02	0.89 ± 0.06	0.51 ± 0.04	21	1189 ± 56	38 ± 4	38 ± 4	0.99
NET 12	22.80	47.39 ± 7.44	48.38 ± 4.63	150.0 ± 10.0	5 ± 1.5	0.44 ± 0.03	1.16 ± 0.08	0.55 ± 0.04	23	1274 ± 56	37 ± 6	38 ± 4	0.98
NET 13	22.30	54.38 ± 6.08	63.50 ± 8.73	150.0 ± 10.0	5 ± 1.5	0.33 ± 0.02	0.89 ± 0.06	0.46 ± 0.03	24	1139 ± 50	48 ± 6	56 ± 8	0.86
NET 14	21.60	55.29 ± 7.37	49.90 ± 6.00	150.0 ± 10.0	5 ± 1.5	0.41 ± 0.03	1.16 ± 0.08	0.53 ± 0.04	25	1246 ± 56	44 ± 6	40 ± 5	1.11
NET 15	20.50	82.26 ± 21.72	54.69 ± 3.19	170.0 ± 10.0	5 ± 1.5	0.33 ± 0.02	0.90 ± 0.06	0.45 ± 0.03	27	1195 ± 51	69 ± 18	46 ± 3	1.50
NET 16	16.00	53.62 ± 9.19	45.04 ± 7.14	170.0 ± 10.0	5 ± 1.5	0.34 ± 0.02	0.82 ± 0.06	0.42 ± 0.03	37	1173 ± 51	46 ± 8	38 ± 6	1.19
NET 17	11.00	54.91 ± 6.23	51.88 ± 7.60	150.0 ± 10.0	5 ± 1.5	0.33 ± 0.02	1.01 ± 0.07	0.45 ± 0.03	56	1171 ± 50	47 ± 6	44 ± 7	1.06
NET 18	7.80	68.66 ± 6.08	68.28 ± 3.65	170.0 ± 10.0	5 ± 1.5	0.42 ± 0.03	1.06 ± 0.07	0.38 ± 0.03	77	1215 ± 51	57 ± 6	56 ± 4	1.01
NET 19	6.60	18.94 ± 1.72	13.20 ± 1.27	190.0 ± 10.0	9 ± 3	0.48 ± 0.03	1.62 ± 0.11	0.42 ± 0.03	88	1352 ± 56	14 ± 1	10 ± 1	1.43
NET 20	4.60	18.20 ± 3.88	11.71 ± 1.64	190.0 ± 10.0	9 ± 3	0.61 ± 0.04	1.57 ± 0.11	0.40 ± 0.03	111	1384 ± 57	13 ± 3	8 ± 1	1.55
NET 21	4.10	15.34 ± 1.14	8.51 ± 0.53	250 ± 25.0	5 ± 1.5	0.48 ± 0.03	0.62 ± 0.04	0.13 ± 0.01	118	1176 ± 93	13 ± 1	7 ± 0.7	1.80
NET 22	1.30	6.81 ± 0.30	5.39 ± 0.30	190.0 ± 10.0	5 ± 1.5	0.41 ± 0.03	0.65 ± 0.05	0.14 ± 0.01	170	1109 ± 47	6 ± 0.4	5 ± 0.3	1.26
NET 23	0.90	12.08 ± 0.53	6.84 ± 0.23	190.0 ± 10.0	5 ± 1.5	0.54 ± 0.04	0.74 ± 0.05	0.17 ± 0.01	180	1187 ± 48	10 ± 0.6	6 ± 0.3	1.77
NET 24	0.10	5.09 ± 0.15	5.85 ± 0.38	190.0 ± 10.0	5 ± 1.5	0.67 ± 0.05	1.55 ± 0.11	0.37 ± 0.03	201	1493 ± 57	3 ± 0.2	4 ± 0.3	0.87

Table 6.4c: Continued.

Sample	Depth (m)	D_e IR-OSL (Gy)	D_e TL (Gy)	Grain size (μm)	Water (%)	Uranium (ppm)	Thorium (ppm)	Potassium (%)	Cosmic dose (μGy/a)	Total dose (μGy/a)	Age IR-OSL (ka)	Age TL (ka)	Ratio IR-OSL ages/ TL ages
WNS 10	3.20	5.98 ± 1.79	5.38 ± 1.20	150 ± 50	5 ± 1.5	0.37 ± 0.03	0.95 ± 0.07	0.23 ± 0.02	132	1043 ± 161	6 ± 2	5 ± 1	1.11
WNS 11	2.55	3.59 ± 1.20	3.59 ± 1.20	150 ± 50	5 ± 1.5	0.44 ± 0.03	1.23 ± 0.09	0.29 ± 0.02	144	1153 ± 159	3 ± 1	3 ± 1	1.00
WNS 12	2.00	---	4.19 ± 1.20	150 ± 50	5 ± 1.5	0.46 ± 0.03	1.32 ± 0.09	0.32 ± 0.02	155	1205 ± 159	---	3 ± 1	---
WNS 13	1.60	1.79 ± 0.60	2.39 ± 0.60	150 ± 50	5 ± 1.5	0.41 ± 0.03	1.26 ± 0.09	0.31 ± 0.02	163	1186 ± 160	2 ± 1	2 ± 1	0.75
WNS 14	1.15	0.60 ± 0.60	1.20 ± 1.20	150 ± 50	5 ± 1.5	0.47 ± 0.03	1.47 ± 0.10	0.36 ± 0.03	173	1276 ± 159	0.5 ± 0.5	1 ± 1	0.50
WNS 15	0.70	---	0.0 ± 0.59	150 ± 50	5 ± 1.5	0.35 ± 0.03	0.87 ± 0.06	0.29 ± 0.02	185	1141 ± 162	---	0 + 0.5	---
WNS 16	6.00	65.97 ± 2.36	64.20 ± 4.12	150 ± 50	5 ± 1.5	0.35 ± 0.03	1.11 ± 0.08	0.40 ± 0.03	94	1175 ± 160	56 ± 8	55 ± 8	1.03
WNS 17	4.75	50.07 ± 1.77	45.94 ± 2.36	150 ± 50	9 ± 3	0.44 ± 0.03	1.39 ± 0.10	0.43 ± 0.03	109	1232 ± 160	41 ± 5	37 ± 5	1.09
WNS 18	4.25	33.32 ± 1.19	32.13 ± 1.19	150 ± 50	9 ± 3	0.44 ± 0.03	1.44 ± 0.10	0.42 ± 0.03	116	1234 ± 160	27 ± 4	26 ± 4	1.04
WNS 19	3.65	19.04 ± 1.19	17.85 ± 1.79	150 ± 50	9 ± 3	0.46 ± 0.03	1.70 ± 0.12	0.40 ± 0.03	125	1250 ± 160	15 ± 2	14 ± 2	1.07
WNS 20	3.00	---	---	150 ± 50	9 ± 3	0.30 ± 0.02	0.74 ± 0.05	0.21 ± 0.01	136	---	---	---	---

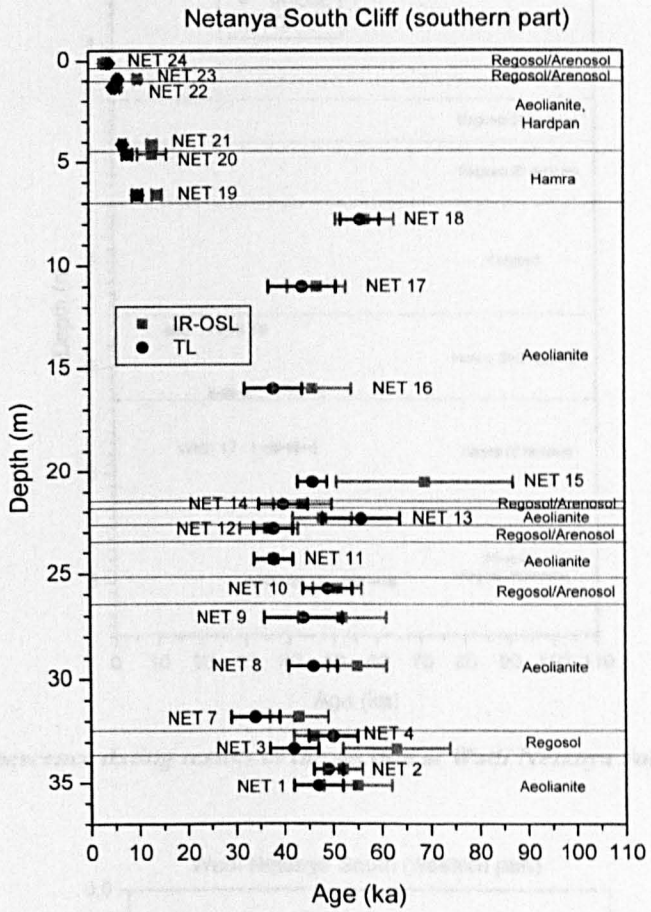

Figure 6.4l: Luminescence dating results of the section at Netanya South Cliff (southern part).

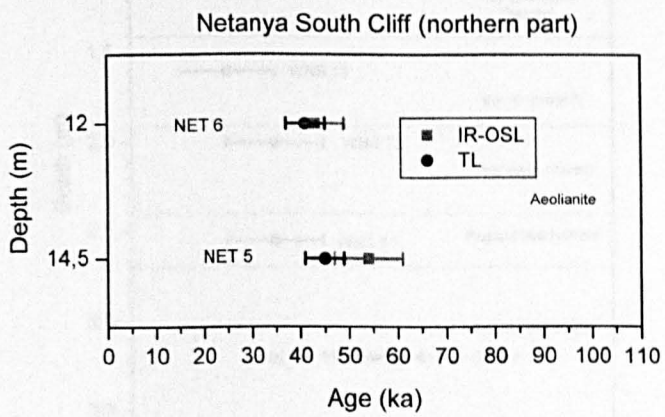

Figure 6.4m: Luminescence dating results of the section at Netanya South Cliff (northern part).

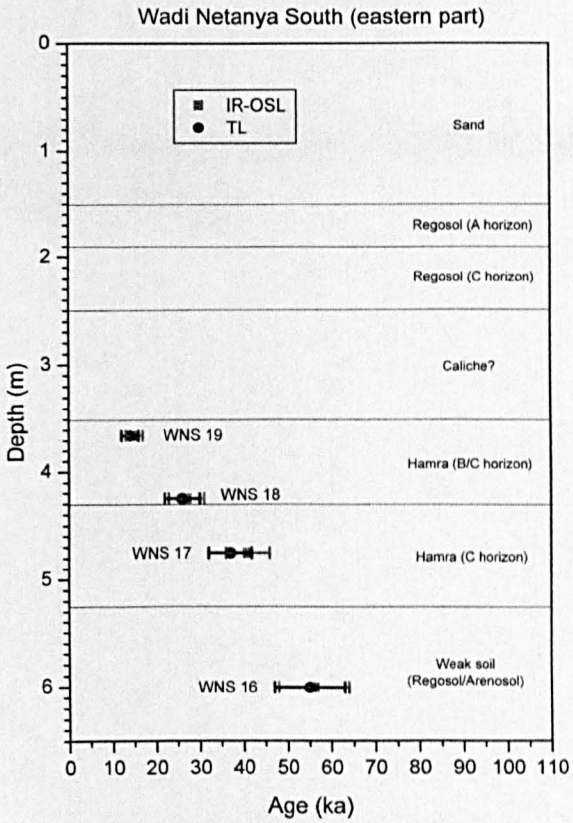

Figure 6.4n: Luminescence dating results of the section at Wadi Netanya South (eastern part).

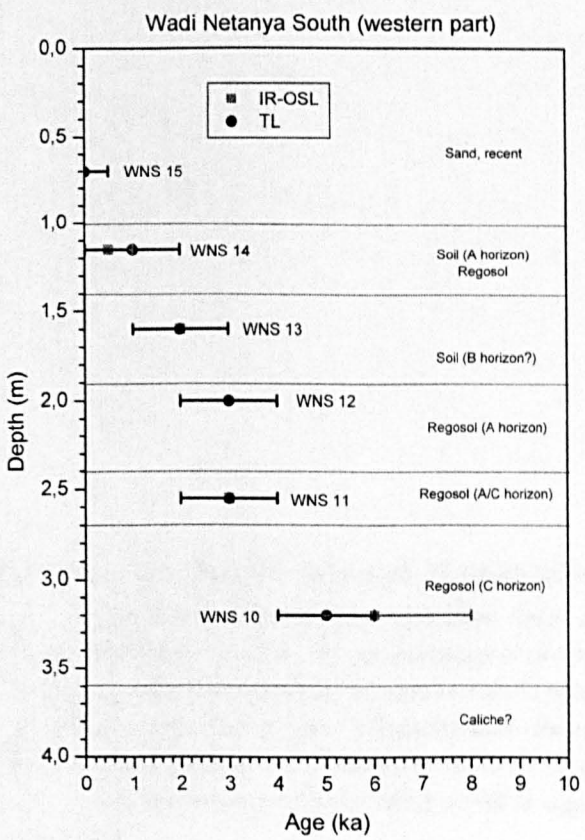

Figure 6.4o: Luminescence dating results of the section at Wadi Netanya South (western part).

CHAPTER 7

Discussion and Interpretation: Significance for climatic and environmental change

In the first part the methodical results from the study of the bleaching behaviour, preheat tests, fading tests, signal influences of the combined measurements, equivalent doses and dosimetry results are discussed. The second part of the chapter contains the geochronological discussion and interpretation of the data. The dating results of the single sites are discussed and correlated according to their luminescence ages to the marine oxygen isotope stages and Eastern Mediterranean climate events; correlations with luminescence data obtained from other aeolianite and palaeosol sequences along the Carmel and Sharon coastal plains are discussed. A new climate-event-stratigraphical model is suggested for the deposits in the Carmel and Sharon coastal plains.

7.1 Methodological discussion and interpretation

7.1.1 Discussion of the results on the luminescence properties of the used dosimeters

The results on the properties of the used dosimeters presented in Chapter 6.1.1 are discussed below.

Bleaching behaviour

The results on the bleaching behaviour of the dosimeters which were tested on three samples representing sites from the North to the South of the investigated area lie within expectations. The IR-OSL signal is bleached faster than the TL signal and can in contrast to the TL signal be reduced to a zero value, which is important for the later discussion (Chapter 7.1.2). The results of the bleaching tests on the three different samples are relatively uniform and no particular differences caused by geographical position or different mineral compositions can be observed. The results show that the basic requirement of bleachability of the used dosimeter is fulfilled and that the used potassium-rich feldspar dosimeters regarding their bleaching behaviour are fit for dating.

Preheat

The preheat tests showed a general difference between an additive or regenerative approach. The additively carried out preheat tests showed that a preheat temperature of 230° C for one minute is an adequate preheat for an additive approach of equivalent dose determination and for most of the tested samples. Would the determination of the equivalent doses have been carried out regeneratively a preheat temperature of 240° C or somewhat higher would have been more suitable to use regarding preheat plateau temperatures.

Fading

The fading tests showed different results for different sites. Tests on samples from the North, from Habonim Quarry, showed no fading for IR-OSL or TL measurements and observed deviations from the initial values by 10 – 15 % can be considered as trend of mean data. The results of the fading tests on the samples from the site South of Power Station are split. For two samples no fading could be detected and the scatter of the obtained values lies within the trend of the mean data. But for one sample from the site

the obtained values decreased with increasing storage times to about 80 % of the initial value. In this case fading of the signal for the particular sample cannot be excluded. The IR-OSL and TL signals from two samples from further South from the Netanya South Cliff section also decreased with increased storage times and showed fading of the signals of about 25 % during the time of storage. While in the North on the tested samples of Habonim Quarry no fading could be detected, further South a 20 – 25 % of observed signal loss on the samples (SOP 5, NET 5, NET 10) points towards some fading over the observed storage time. If the data show a general North-South trend in fading rates is uncertain as only a small number of samples were tested. The findings are congruent with some minor fading observed on samples of the section Givat Olga which is located like the section Netanya South Cliff at the Sharon coast escarpment (FRECHEN *et al.* 2001). FRECHEN *et al.* (2004) also observed some minor fading on samples from exposures along the Tel-Aviv – Haifa motorway in the Carmel coastal plain. For all the fading tests carried out in this study it was also noticeable that the values obtained after varying times of storage (cp. Chapter 5.3.4) with IR-OSL and TL measurements were generally comparable and that there was no distinction between the two luminescence methods.

The luminescence signal for equivalent dose determination of the samples measured in this study was detected between 30 and 120 days after the artificial irradiation. A fading of up to about 25 % over a storage time of up to 235 days obtained for some of the tested samples from the more southern sections can therefore be considered as minor. However, the influence of fading on the natural signal could be significant. The rate of fading on the natural signal would be more progressed than the fading rate after laboratory irradiation. The signal measured in the laboratory could therefore be higher per dose unit in relation to the natural signal, which would result in age underestimation.

Combined measurements

To determine the equivalent dose from the TL signal after a preceding IR stimulation requires that the natural thermoluminescence signal is not altered by the foregoing IR-OSL stimulation; further, could the effect of a preceding IR stimulation be different at varying doses. Both aspects have been investigated on the samples HDC and WNS 15.

The influence of the IR stimulation on the natural TL signal was tested in case a) (cp. Chapter 6.1.1). Compared with the natural TL signal, with no preceding IR measurement, the TL signal intensities measured after varying times of IR-OSL

stimulation showed no influence on the TL signal for up to 60 s IR stimulation of sample HDC and for up to 40 s IR stimulation of sample WNS 15. Differing values of ± 10 % of the TL intensity/IR-OSL intensity ratios lie within the trend of the mean data. For the determination of the equivalent doses the IR-OSL was only stimulated for up to 25 s prior to the TL measurements so an influence of the IR-OSL stimulation on the natural TL signals is unlikely.

In case b) the influence of a preceding IR-OSL stimulation on the TL signal by varying doses was investigated. The values of the quotient TL intensity divided by the IR-OSL intensity expressed in *per cent* of the value of the first quotient showed no influence of the IR on the TL signal for different doses and 25 s of IR stimulation for sample HDC. This is different from the data obtained for sample WNS 15, where the TL intensity/IR-OSL intensity ratios (%) after an initial scatter decrease systematically to about 60 % of the initial value. Therefore influence of the IR-OSL signal measured prior to the TL signal cannot be excluded for sample WNS 15 and successive higher doses. The corresponding doses covered the range up to about 360 Gy (source ~ 6 Gy/1 min). In contrast to most of the dated samples and HDC, is sample WNS 15 very young (recent) (cp. Table 6.4c). The dose groups used for the equivalent dose determination of sample WNS 15 and also the natural signal lie in the lower dose region compared to the administered doses of the test. Considering the general trend of the mean data and disregarding the scatter of the second to fourth ratio, a possible TL signal loss would only have a minor affect on the TL intensity/IR-OSL intensity ratio. Therefore the TL measurement of such young samples should not be significantly affected by a preceeding IR stimulation of up to 25 s.

The sample shows that the decreasing TL intensity/IR-OSL intensity ratio may be due to a sub-linear increase of the TL signal with higher doses in contrast to the linear increase of the IR-OSL signal. Anomalous fading, which could be one possibility for a decreasing TL signal after artificial irradiation, seems in this case unlikely to be the reason for the observed data because the aforegoing fading tests showed that if there would be anomalous fading of the TL signal intensities it is likely that they would change proportionally in the same order as the IR-OSL intensities, in which case the values of the ratios would not decrease but would be constant. Another argument should also exclude sensitivity changes with higher irradiation doses, as they are likely to affect both IR-OSL and TL intensities and a strongly linear decreasing effect on the TL

intensity/IR-OSL intensity ratios (%) would be unlikely as the signals derive from different luminescence centres.

7.1.2 Discussion of the obtained IR-OSL and TL equivalent doses

For most cases the equivalent doses could generally be obtained in a straightforward way. Where this was not the case it is indicated in the Tables 6.1.2a, 6.1.2b and 6.1.2c and the reason is given below the tables. One observation which is prominent throughout the datasets of the equivalent doses of the different sites is that for a considerable number of samples the IR-OSL equivalent doses are systematically higher than the TL equivalent doses yet statistically insignificant (cp. Chapter 6.1.2). However, for a proportion of data the systematic difference is statistically significant, e.g. for the samples HDM, HDC, HAB 4, HAB 6, HAB 7 (Figures 6.1.2a and 6.1.2b). Methodologically the background was subtracted from both the IR-OSL and TL measurements and the equivalent doses were determined by the intersections of the growth curves with the y-value of the finite remainder in the case of TL and with y = 0 for IR-OSL (cp. Chapter 4.11.1). As all three bleaching experiments above have shown (cp. Chapter 6.1.1), the IR-OSL signal of each of the tested samples can optically be bleached to a zero value and an optical bleaching problem is unlikely to be the reason for the higher IR-OSL equivalent doses. This can be demonstrated on the samples HDC and NET 17 whose IR-OSL equivalent doses are higher than the TL equivalent doses (Figures 6.1.2a and 6.1.2i) and the IR-OSL signals are also optically bleachable to zero (Figures 6.1.1a and 6.1.1c). Additionally, no geographical trend North-South or East-West can be observed. Systematically higher IR-OSL than TL equivalent doses are seen in younger and older samples as well as in samples from soil horizons or aeolianites alike (cp. Chapter 6.1.2). Fading of the TL signal intensities can be excluded as a reason for the observed data as shown before, it would be unlikely that the TL intensities fade and the IR-OSL intensities would not (cp. Chapter 6.1.1). That leaves open at present the reason for the systematically higher IR-OSL equivalent doses and the discrepancy towards the TL equivalent doses.

7.1.3 Discussion of the IR-RF equivalent doses

The obtained IR-RF equivalent doses are systematically higher than the IR-OSL and TL equivalent doses (cp. Chapter 6.2.2). The calculation of the IR-RF age estimates shows that they are also systematically higher than the IR-OSL and TL ages, with the exception of the samples HAB 4, HAB 5, HAB 8 and HAB 9 whose IR-RF, IR-OSL and TL ages are in good agreement within the error margins (Figure 7.1.3).

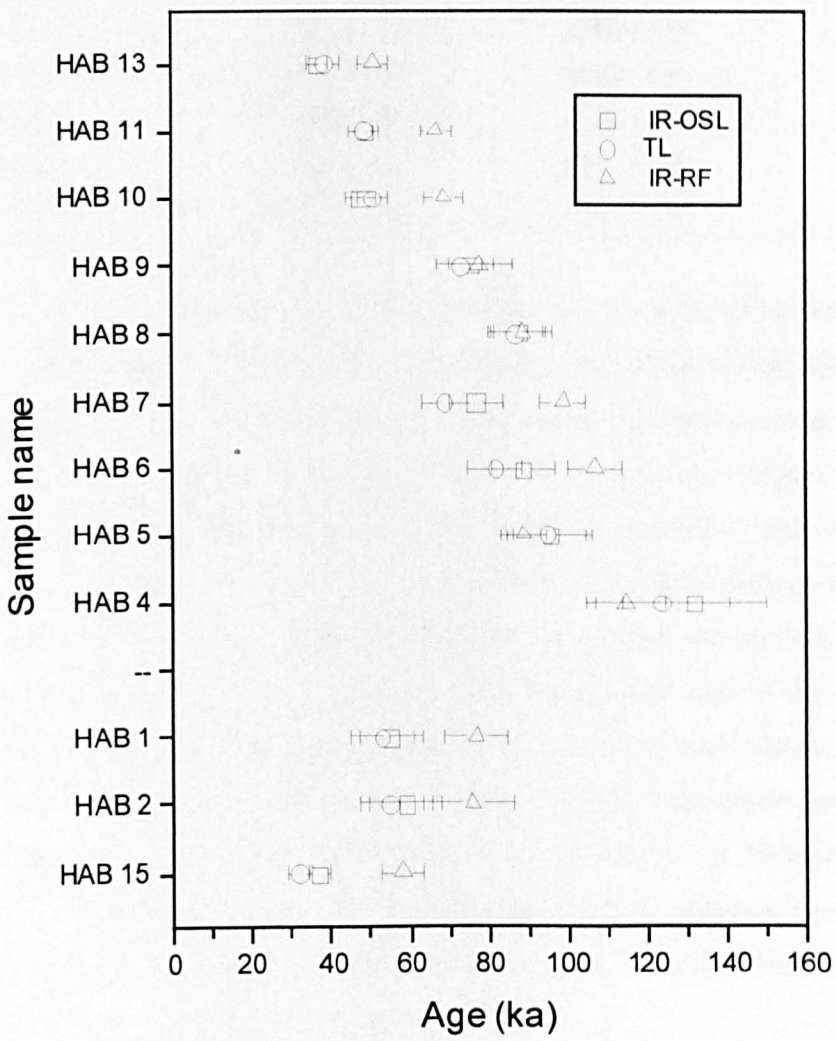

Figure 7.1.3: IR-RF age estimates in comparison with the IR-OSL and TL ages.

The comparison of the doses rates of the IR-RF age estimates and the IR-OSL and TL ages shows that the doses rates of the IR-RF age estimates are systematically higher between 219 and 335 μGy/a (Table 7.1.3a).

Table 7.1.3a: Total dose rates for IR-OSL/TL and IR-RF age estimates.

Sample	IR-OSL/TL dose rates (µGy/a)	IR-RF total rates (µGy/a)	Difference in dose rates (µGy/a)
HAB 1	1080 ± 155	1397 ± 104	317
HAB 2	1094 ± 155	1411 ± 104	317
HAB 4	1151 ± 157	1486 ± 105	335
HAB 5	1613 ± 156	1903 ± 111	290
HAB 6	1847 ± 157	2112 ± 116	265
HAB 7	1935 ± 160	2195 ± 120	260
HAB 8	2170 ± 163	2401 ± 127	231
HAB 9	2242 ± 163	2466 ± 128	224
HAB 10	2210 ± 163	2435 ± 128	225
HAB 11	2206 ± 159	2425 ± 124	219
HAB 13	2073 ± 159	2305 ± 122	232
HAB 15	2070 ± 159	2305 ± 122	235

For the calculation of the IR-RF age estimates, no alpha-efficiency factor was assumed as the grains were treated with hydrofluoric acid which should result in the removal of the alpha particle affected portion. The mean penetration range of alpha particles in sediments is usually considered to be about 25 µm (cp. Chapter 4.13), which is taken into account in the calculation of the IR-RF age estimates. Tests on quartz grains have shown that an even removal of the outer rim of the grain through etching is not the case and that the grains are affected differently along their surface (e.g. ZANDER 2000). This results on the one hand in large cavities in the grains and on the other hand in surface areas hardly affected by the etching. This effect is probably larger on feldspar grains as because of their cleavage they are easier to etch than quartz grains. Also, weathered feldspars from a semiarid to arid environments like in the Mediterranean coast in Israel should be more strongly affected than for example feldspars from a moderate climate zone. It is therefore likely that the investigated feldspars were not evenly etched and remained partly with alpha-affected parts.

Higher total doses of the IR-RF age estimates can in general be explained in this way and also with the smaller grain size of 100 to 150 µm used. However, an inhomogeneous etching of the outer surface layer and left over alpha-particle affected portions of the grains cannot account for the age differences observed between some of the IR-RF and IR-OSL/TL age estimates. Left over grain portions affected by alpha particles would require an alpha-efficiency factor to be considered despite the etching.

Although this would increase the total dose rate and therefore reduce the age, the maximum effect would not exceed *circa* 8 % based on an a-value from polymineral fine grains. This is considerably less than the difference between the age estimates, so that most of the age difference seems to be caused by higher equivalent doses.

The IR-RF ages of some of the samples (HAB 4, HAB 5, HAB 8 HAB 9) show good agreement with other luminescence ages of this study and also, the obtained ratios of the natural IR-RF intensity divided by the bleached IR-RF intensity from all Habonim samples fit excellently to the exponential distribution curve of ratios from samples of other studies (cp. ERFURT 2003a). Problems with the IR-RF equivalent dose determination can therefore be excluded as the reason for the differences observed between some of the IR-RF ages and the conventional luminescence ages on samples of this study.

ERFURT (2003b) and ERFURT and KRBETSCHEK (2003b) discuss Pb^{+} in the lattice of potassium-rich feldspar as a possible centre for infrared luminescence (radiofluorescence and photoluminescence). They showed by comparing potassium-chloride (KCl:Pb) and lead-rich potassium-feldspar ($KAlSi_3O_8$) (amazonite) that the emissions from the investigated centre are relatively independent from the structure of the crystal lattice (monoclinic, triclinic).

BODET and SCHÄRER (2001) investigated Pb isotope systematics on K-feldspar grains derived from large rivers in SE-Asia. They found that many lead ratios ($^{206}Pb/^{204}Pb$ (α), $^{207}Pb/^{204}Pb$ (β), $^{208}Pb/^{204}Pb$ (γ)) were significantly more radiogenic than ratios known from any type of Phanerozoic crust, from what they concluded that recycling of Precambrian crust into the source material of the potassium-feldspars must have taken place in connection with orogenies. The high radiogenic Pb ratios indicate high Th/U source material BODET and SCHÄRER (2001). As the Nile river, from which the Israeli K-feldspars derive, cuts through about 6,000 km of African crust and the geological situation is similar to that in SE-Asia, in that parts of the old Precambrian material would have been recycled in later orogenies, higher radiogenic lead ratios can also be expected for the potassium-rich Israeli feldspars. However, a possibly higher concentration of Pb^{+} centres in the Israeli feldspars is not connected with the dosimetric properties of the IR-RF (cp. ERFURT 2003b). Therefore the reason for the higher IR-RF ages is still uncertain.

7.1.4 Discussion of the results of the gamma spectrometry

The gamma spectrometry results of the uranium and thorium contents in the aeolianites of the Israeli Mediterranean coastal plains show variations from the average Th/U ratio of the Earth's crust of 3.5. In the observed samples Th/U ratios range from 0.39 (HAB 3) in aeolianites to 5.62 (HAB 10) in soils (cp. Chapter 3.2.1 and Table 7.1.4a). These ratios are not untypical for dune sand or aeolianites where the thorium content is usually lower compared to the average crust ratio. It can be seen from the distinction of aeolianite and soil horizons in the obtained data that the thorium concentration raises with the fraction of fines in the soils. This can particularly be observed in the samples from the pedocomplex section in the East-wall at Habonim Quarry, where the vertisol shows the highest thorium contents from all measured samples of this study (cp. Chapter 3.2, Tables 6.3.1d, h, l). Vertisols are soils with very high amounts of fines (cp. Chapter 3.1.2). Overall it can be seen that the samples from the Netanya South Cliff sections and the Wadi Netanya South sections show relatively uniform Th/U ratios for the aeolianites and the soils between 1.29 (NET 21, aeolianite) and 3.70 (WNS 19, hamra) (Table 7.1.4a). Usually the soils show higher thorium contents than the aeolianites, but comparatively high thorium concentrations are not limited to soils only and can be also observed in aeolianites (3.06 NET 17) and *vice versa* regosols/arenosols can show comparatively low thorium contents (1.37 NET 23).

Considering that the sediment sources of the Israeli dune sands should not have changed dramatically over the observed time span, higher thorium concentrations in relation to uranium concentrations are most likely reflecting the accumulation of fines in sand and soils through dust storms in the area. This might also indicate phases of sand stabilisation.

The sections further North, South of Power Station and Seashore Power Station, show similar Th/U ratios to the sections at Netanya South. For the section in the East-wall at Power Station Quarry the Th/U ratios show a considerably higher thorium concentration for the pedocomplex compared with sections further south. Highest Th/U ratios can be observed in the vertisol (4.35 PSQ 7) and in the hamra (4.48 PSQ 5) (Table 7.1.4a). Similar results were obtained for the samples from the pedocomplex at the East-wall at Habonim Quarry. The higher thorium concentrations are clearly connected with the higher concentrations of fines in the palaeosols, particularly in the vertisols of the pedocomplexes at Habonim Quarry and at Power Station Quarry.

While the obtained U/Th ratios for well developed soils and aeolianites are relatively uniform in the South (Netanya South Cliff, Wadi Netanya South) they vary considerably in the North (Habonim Quarry) (Table 7.1.4a). This might also reflect the influence of a lessening amount of precipitation towards the South (cp. Chapter 1.3.3) and possible connected variations of radioactive disequilibria. Although the formation of aeolianites involves the solution of carbonates and their precipitation (cp. Chapter 1.1), the carbonate transport in the solution is limited to a few centimetres before precipitation takes place, so that possible radioactive disequilibria are thought to be initially limited to a relatively small area of a few centimetres. With increasing carbonate consolidation of aeolianites, increasing radioactive disequilibria can be expected.

The measured isotope concentrations for the uranium decay series do not distinguish whether there are radioactive disequilibria at the beginning or the end of the decay chain. However, possible disequilibria caused by the gaseous radioisotope ^{222}Rn can be detected. The first isotope measured is ^{226}Ra, followed by peaks for ^{214}Pb and ^{214}Bi (cp. Figure 4.13.2c). If the concentrations determined for the peaks of ^{214}Pb and ^{214}Bi are much lower than the concentration of ^{226}Ra it is likely that a disequilibrium is caused for example by the loss of ^{222}Rn. For most of the samples the concentrations obtained from measured peaks are relatively consistent with each other so that disequilibria do not show in the obtained results (Tables 6.3.1a, e, i). However, examples for a possible radon loss can be observed in the results for the samples NET 20, NET 21 and NET 23, where the concentration of ^{226}Ra is considerably higher than the concentrations determined for ^{214}Pb and ^{214}Bi (Table 6.3.1i).

Disequilibria at the beginning of the thorium decay series cannot be detected with gamma spectrometry. The first isotope to be measured is ^{228}Ac whose concentrations can be compared to those of ^{212}Pb, ^{212}Bi and ^{208}Tl. The loss of ^{228}Ac daughters should result in lower concentrations of ^{212}Pb, ^{212}Bi and ^{208}Tl. The obtained concentrations for the isotopes of the thorium decay series are not so uniform for any one sample than the concentrations of the isotopes of the Uranium decay series but disequilibria cannot generally be detected from the obtained data (Tables 6.3.1b, f, j).

Similar to the thorium concentrations the obtained potassium concentrations also show higher values for soil horizons compared to aeolianites (Tables 6.3.1d, h, l).

Table 7.1.4a: Thorium/Uranium ratios for the samples HAB, HAB-II, HDM, HDC, PSQ, SOP, SPS, NET and WNS.

Sample	Th/U ratio
HAB 1	0.34
HAB 2	0.86
HAB 3	0.39
HAB 4	2.07
HAB 5	4.18
HAB 6	4.49
HAB 7	5.00
HAB 8	5.10
HAB 9	5.56
HAB 10	5.62
HAB 11	4.70
HAB 12	4.43
HAB 14	0.52
HAB 16	1.37
HAB-II-1	0.49
HAB-II-4	0.56
HAB-II-5	5.31
HAB-II-9	0.94
HDM	1.04
HDC	1.17

Sample	Th/U ratio
PSQ 2	2.45
PSQ 3	3.87
PSQ 4	4.18
PSQ 5	4.48
PSQ 6	4.11
PSQ 7	4.35
PSQ 10	1.72
PSQ 12	1.48
SOP 1	2.59
SOP 3	2.52
SOP 4	2.47
SPS 1	2.82
SPS 5	3.54
SPS 7	2.38
SPS 8	2.23

Sample	Th/U ratio
NET 1	1.58
NET 2	1.37
NET 3	1.74
NET 4	2.34
NET 5	1.41
NET 6	1.58
NET 7	2.55
NET 8	2.22
NET 9	2.26
NET 10	2.93
NET 11	2.54
NET 12	2.64
NET 13	2.70
NET 14	2.83
NET 15	2.73
NET 16	2.41
NET 17	3.06
NET 18	2.52
NET 19	3.38
NET 20	2.57
NET 21	1.29
NET 22	1.59
NET 23	1.37
NET 24	2.31
WNS 10	2.57
WNS 11	2.80
WNS 12	2.87
WNS 13	3.07
WNS 14	3.13
WNS 15	2.49
WNS 16	3.17
WNS 17	3.16
WNS 18	3.27
WNS 19	3.70
WNS 20	2.47

7.1.5 Discussion of the beta counting results

The results of the beta counting of five samples (cp. Chapter 6.3.2) show a clear difference between the preparation methods used (cp. Chapter 5.3.1). The potassium-rich feldspars from samples NET 18 and NET 24 of the Netanya South Cliff section were separated in Cologne with a centrifuge. The obtained results from the beta counting on these samples show concentrations for the internal potassium content, which are stoichiometrically too low. This points towards a poor separation between potassium-rich feldspar grains and quartz grains. In contrast to that good results for the internal potassium content were obtained for the samples that were separated with separating funnels in Cheltenham. This shows that a separation in funnels can be very successful and also that values by HUNTLEY and BARIL (1997) given for the internal potassium content on theoretical grounds are a good estimate for the internal potassium content of potassium-rich feldspars.

7.2 Geochronological discussion and interpretation

7.2.1 Habonim Quarry, Dor-Habonim Nature Reserve Middle Ridge and Dor-Habonim Nature Reserve Coast

The luminescence ages obtained for the aeolianite underneath the pedocomplex at the East-wall in Habonim Quarry range from 150 – 107 ka (cp. Figure 6.4a and Table 6.4a) and indicate deposition during the transition from late oxygen isotope stage (MIS) 6 to MIS 5 (cp. Figure 7.2.1a). The TL value of HAB 16 is not included in the interpretation of the age of the aeolianite as it seems to be underestimated. The sedimentation of the parent material of the hamra soil follows. Ages obtained for the upper part of the hamra soil are in the range of 105 – 85 ka (HAB 5) and indicate a deposition during MISs 5c – 5a. Ages obtained for the deposition of the parent material of the soil horizons decrease further towards the top and are separated by a hiatus. The early phase of soil formation continued until 82 – 67 ka (HAB 9) showing parent material sedimentation during MISs 5a – 4. The initiation of a later depositional phase followed between 55 – 44 ka (HAB 10, HAB 11) during the early MIS 3. Another deposition followed at 43 – 34 ka (HAB 12, HAB 13) being equivalent with the time of the upper MIS 3. Considering the medial distribution values of the age determinations, the hiatus seen between the two accumulation phases (between samples HAB 9 and HAB 10), is in the order of just less than 30 ka and indicates either erosion processes or a pause in accumulation or both. The pedogenesis of the vertisol is superimposed over the hiatus and indicates a transition to wetter environmental conditions. Increased precipitation most likely caused the interdune depression to function as catchment for water during the late MIS 4 and the very early MIS 3. This view is also aided by the pedological investigations made by TSATSKIN and RONEN (1999) who confirmed moister environmental conditions. For the aeolianite above the sampled pedocomplex, the age of sample HAB 14 could not be obtained (cp. Table 6.4a).

The section at Habonim East-wall was also dated with radio-thermoluminescence (RTL) after VLASOV and KULIKOV (1989) by LAUKHIN, Radiochemistry Laboratory of Moscow State University (RONEN *et al.* 1999). Radio-thermoluminescence (RTL) is thermoluminescence (TL), only, that the excitation energy is stated first. The RTL date obtained for the aeolianite above the pedocomplex is 30 ± 7 ka (RONEN *et al.* 1999), which is in congruence with the data obtained in this study for horizons below the

aeolianite and places the sedimentation of the aeolianite in the late MIS3. The RTL date of 160 ± 40 ka determined for the aeolianite underneath the pedocomplex ranges from 200 – 120 ka (RONEN *et al.* 1999).

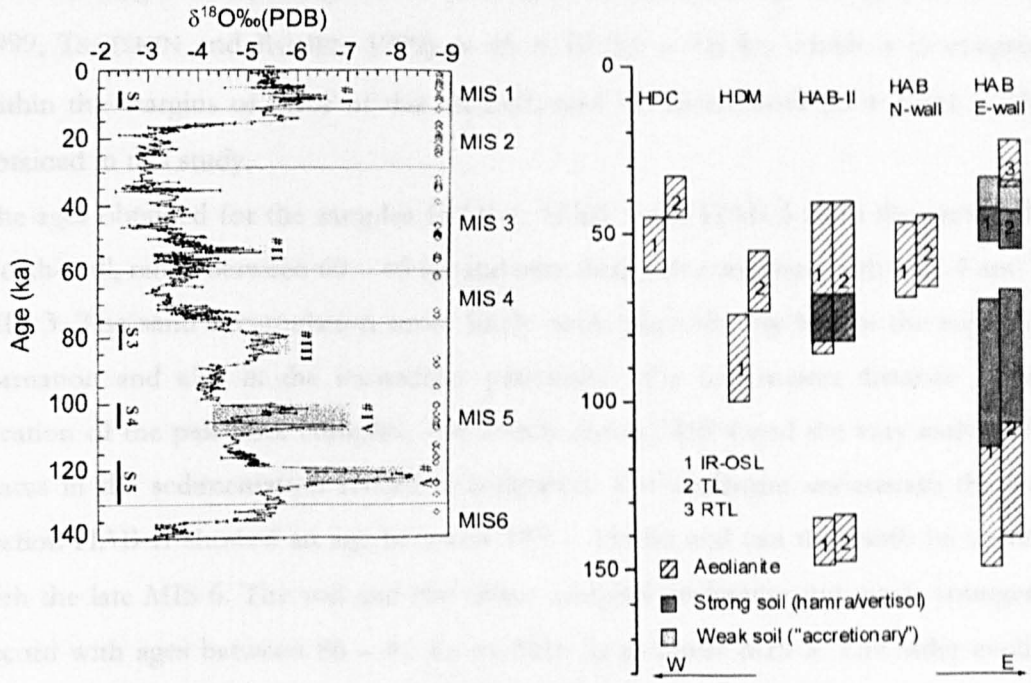

Figure 7.2.1a: Correlation of the dated deposits (sedimentation ages) of Habonim Quarry (HAB), Dor-Habonim Nature Reserve Middle Ridge (HDM) and Dor-Habonim Nature Reserve Coast (HDC) with the speleothem oxygen isotope record, marine isotope stages (MIS), sapropels (S1, S3-S5) and periods of enhanced rainfall (#I-#V) in the eastern Mediterranean (BAR-MATTHEWS et al. 2000).

which would place the sedimentation of the aeolianite in the latest part of MIS 7 to early MIS 5 (MIS 5e) covering the whole MIS 6. The margin of error of this RTL date is too large to allow a more definate correlation with the oxygen isotope stages. Within the margins of error the RTL date does not contradict the ages obtained for the aeolianite in this study. An RTL date obtained from the lower part of the hamra horizon just above the underlying aeolianite showed an age of 107 ± 27 ka (RONEN *et al.* 1999) allowing for the deposition of the parent material of the hamra soil to have taken place between 154 – 80 ka . A further RTL age in the upper part of the hamra horizon was determined at 130 ± 33 (163 – 97) ka (RONEN *et al.* 1999). Again, within the margins of error, these RTL ages are in congruence with the IR-OSL and TL ages obtained in this study. The RTL age obtained from the vertisol 90 ± 20 (110 – 70) ka (RONEN *et al.* 1999) seems because of its age to be obtained from the parent material of the soil from underneath the above described hiatus. Overall, the medial values of the RTL dates (RONEN *et al.*

1999) for the lower parts of the section are generally somewhat higher than the values obtained in this study. The RTL ages (RONEN *et al.* 1999) show also for the lower and older parts of the section large margins of error which prevent a meaningful correlation with the oxygen isotope stages. The RTL age obtained for the pseudogley (RONEN *et al.* 1999, TSATSKIN and RONEN 1999) is 45 ± 10 (55 – 35) ka, which is in congruence within the margins of error of the IR-OSL and TL dates, both 38 ± 3 (41 – 35) ka, obtained in this study.

The ages obtained for the samples HAB 1, HAB 2 and HAB 3 from the section HAB North-wall, range between 69 – 45 ka and can clearly be correlated with MIS 4 and early MIS 3. The sand accumulation most likely took place shortly before the sapropel S2 formation and also in the immediate proximity of a few metres distance from the location of the palaeosol complex, for which during MIS 4 and the very early MIS 3 a hiatus in the sedimentation record is indicated. The aeolianite underneath the soil of section HAB-II showed an age between 149 – 134 ka and can therewith be correlated with the late MIS 6. The soil and the other sampled aeolianites are much younger and accord with ages between 86 – 41 ka to MIS 5a to lower MIS 3. The older aeolianite deposited during MIS 6 can be correlated with a part of the aeolianite underneath the pedocomplex. The parent material of the soil in the section HAB-II was synchronously deposited with the sediment of the upper part of the hamra soil in the pedocomplex around MIS 5a to the early MIS 4. The hiatus between the older aeolianite and the deposition of the parent material of the soil in section HAB-II is very large and of the order of around 50 - 60 ka, for which no record has prevailed.

The ages obtained for the aeolianites at the Dor-Habonim Nature Reserve Middle Ridge (HDM) and at Dor-Habonim Nature Reserve Coast (HDC) are difficult to correlate, as there is a strong discrepancy between the IR-OSL and the TL results. Considering the overall higher IRSL results as mentioned before (cp. Chapter 7.1.2), it seems likely that the TL ages of these two samples are more reliable than the IR-OSL ones. A correlation of the two samples according to their TL age estimates shows that the sampled aeolianite from the middle ridge would have been deposited during MIS 4 to the early MIS 3 and would be contemporaneous to the aeolianite above the soil horizon in section HAB-II and to the aeolianites of HAB North-wall (Figure 7.2.1a), while the sampled aeolianite at the coast would be younger and deposited during MIS 3, corresponding to the upper aeolianite formation above the pedocomplex.

7.2.2 Hadera Power Station Quarry, South of Power Station and Seashore Power Station

The pedocomplex at the East-wall at Hadera Power Station shows, like the pedocomplex at Habonim Quarry, a succession from hamra horizons to a vertisol and is also placed in an interdune depression. The sedimentation ages for the parent material of the pedocomplex range from 33 ka to 6 ka and were deposited in late MIS 3, MIS 2 and early MIS 1 to the time of sapropel S1 formation, considering the IR-OSL ages. For the upper two samples of the pedocomplex no TL ages could be determined (cp. Table 6.4b), but the obtained TL ages indicate also a sedimentation during MIS 2. Most likely the depression acted as a catchment for excess water so that fines like clay could accumulate which allowed the vertisol to form and to superimpose the underlying hamra. The underlying aeolianite of the pedocomplex was sampled elsewhere (cp. Figure 3.2.2b) and showed ages between 57 to 39 ka (PSQ 1), which places its sedimentation into MIS 3 (cp. Figure 7.2.2a).

The section in the West-wall of the quarry showed a lower aeolianite and a lens-like intercalated weak soil followed by an upper aeolianite. The sedimentation ages of the parent material of the lower aeolianite and the weak soil range between 102 – 68 ka which correlates with MIS 5c to the early MIS 4. The weak soil cannot be distinguished by the luminescence ages from the aeolianite below, but it is likely that the weak soil formed during moister and perhaps somewhat warmer conditions for example during MIS 5a. For the upper aeolianite, ages between 33 – 21 ka were determined which places its sedimentation in late MIS 3 (Figure 7.2.2a).

In the section South of Power Station further West (cp. Figure 3.2.2a) two weak soils (regosol/arenosol) are intercalated between aeolianites followed by a hamra above. The weak soils cannot be distinguished from the aeolianites through the luminescence ages. Overall the weak show soils somewhat older ages than the lower aeolianite, which for stratigraphical reasons is not credible (cp. Figure 7.2.2a). The obtained ages of the aeolianites and the weak soils range between 56 – 28 ka and correlate with MIS 3. The weak soils (regosols/arenosols) are likely to have been developed during slightly moister phases of early MIS 3, perhaps connected with the sapropel S2 formation. The above developed hamra marks with deposition ages between 27 – 17 ka the transition from the end of MIS 3 to the Last Glacial Maximum (LGM) of MIS 2. The parent material of the hamra at the section South of Power Station was according to the luminescence ages sedimentated contemporaneously with the parent material of the hamra of the Power

Station Quarry East-wall section. The upper aeolianite at the section South of Power Station correlates according to the ages with the aeolianite underneath the pedocomplex at Power Station Quarry (PSQ 1) (cp. Figure 7.2.2a).

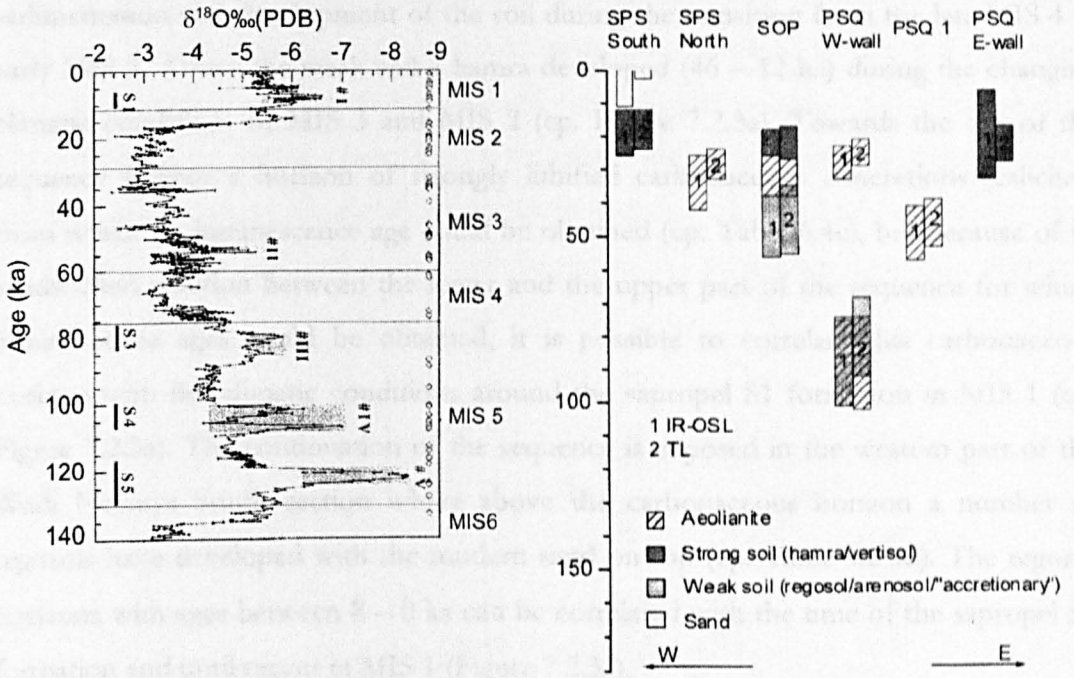

Figure 7.2.2a: Correlation of the dated deposits (sedimentation ages) of Hadera Power Station Quarry (PSQ), South of Power Station (SOP) and Seashore Power Station (SPS) with the speleothem oxygen isotope record, marine isotope stages (MIS), sapropels (S1, S3-S5) and periods of enhanced rainfall (#I-#V) in the eastern Mediterranean (BAR-MATTHEWS et al. 2000).

At the northern section Seashore Power Station (cp. Chapter 3.2.2) aeolianites are exposed with ages between 42 – 26 ka, which correlates to late MIS 3. The aeolianites of the section Seashore Power Station are seen to be contemporaneous with the upper aeolianite at the section South of Power Station, also partly with the upper aeolianite at Power Station Quarry West-wall and perhaps with the lower part of the pedocomplex at Power Station Quarry East-wall (cp. Figure 7.2.2a). Above the aeolianites at the Seashore Power Station sequence follows a hamra in the southern part of the section with sedimentation ages of the parent material between 26 – 12 ka. The hamra developed most likely contemporaneously with the hamra horizons in the sections South of Power Station and Power Station Quarry East-wall with similar sedimentation ages of the parent materials. Towards the top of the southern part of the section Seashore Power Station, loose sand was deposited between 11 and 0 ka, which correlates to MIS 1 (cp. Figure 7.2.2a).

7.2.3 Netanya South Cliff and Wadi Netanya South

At the eastern part of the section of Wadi Netanya South a weak soil (regosol/arenosol) is exposed at the basement of the Wadi with ages between 64 – 47 ka. This shows sedimentation and development of the soil during the transition from the late MIS 4 to early MIS 3. Above the weak soil a hamra developed (46 – 12 ka) during the changing climatic conditions of MIS 3 and MIS 2 (cp. Figure 7.2.3a). Towards the top of the sequence follows a horizon of strongly lithified carbonaceous concretions (caliche?) from which no luminescence age could be obtained (cp. Table 6.4c), but because of its sandwiched position between the lower and the upper part of the sequence for which luminescence ages could be obtained, it is possible to correlate this carbonaceous horizon with the climatic conditions around the sapropel S1 formation in MIS 1 (cp. Figure 7.2.3a). The continuation of the sequence is exposed in the western part of the Wadi Netanya South section where above the carbonaceous horizon a number of regosols have developed with the modern sand on top (cp. Table 3.2.3d). The regosol horizons with ages between 8 – 0 ka can be correlated with the time of the sapropel S1 formation and until recent in MIS 1 (Figure 7.2.3a).

The aeolianite of the northern part of the Netanya South Cliff section is stratigraphically positioned below the deposits in the southern part of the section, but the obtained ages between 63 – 37 ka are not distinguishable from the ages obtained for the lower part of the southern section at Netanya South Cliff. The aeolianite in the northern section at Netanya South Cliff can be correlated with late MIS 4 and into MIS 3.

At the southern section various aeolianites alternate with a thicker regosol and thinner regosols/arenosols (cp. Table 3.2.3a). Age-wise the weak soils cannot be distinguished from the adjacent aeolianites and the whole sequence of the deposits in the lower part of the section shows ages between 74 – 29 ka, disregarding the IR-OSL age of sample NET 15 because compared to the TL age of the same sample and the ages of the other samples it is considerably overestimated. The aeolianites and weak soils were deposited and developed during MIS 4 and MIS 3 (cp. Figure 7.2.3a). The weak soils indicated perhaps somewhat moister phases during that time.

The upper part of the Netanya South Cliff section was deposited after a large hiatus which coincides with the end of MIS 3 and MIS 2. The luminescence ages for the hamra horizons range between 16 – 7 ka covering the end of MIS 2 and the beginning of MIS 1 towards the Holocene climatic optimum and the formation of sapropel S1. Above the

hamra horizons towards the top a strongly lithified whitish aeolianite was deposited for which ages between 14 – 4.7 ka were determined and a weak soil (regosol/arenosol) with ages between 6.3 – 2.8 ka (disregarding for the latter the IR-OSL age of sample NET 23 which seems overestimated). Although the ages of the aeolianite partly overlap with their margins of error with the hamra below and the weak soil above it seems clear that the hamra developed during the increasingly moister and also warmer environmental conditions towards the Holocene climatic optimum compared to the extreme arid and cool conditions of the LGM and the formation of sapropel S1, while the sedimentation and pedogenesis of the weak soil took place after the Holocene climate optimum.

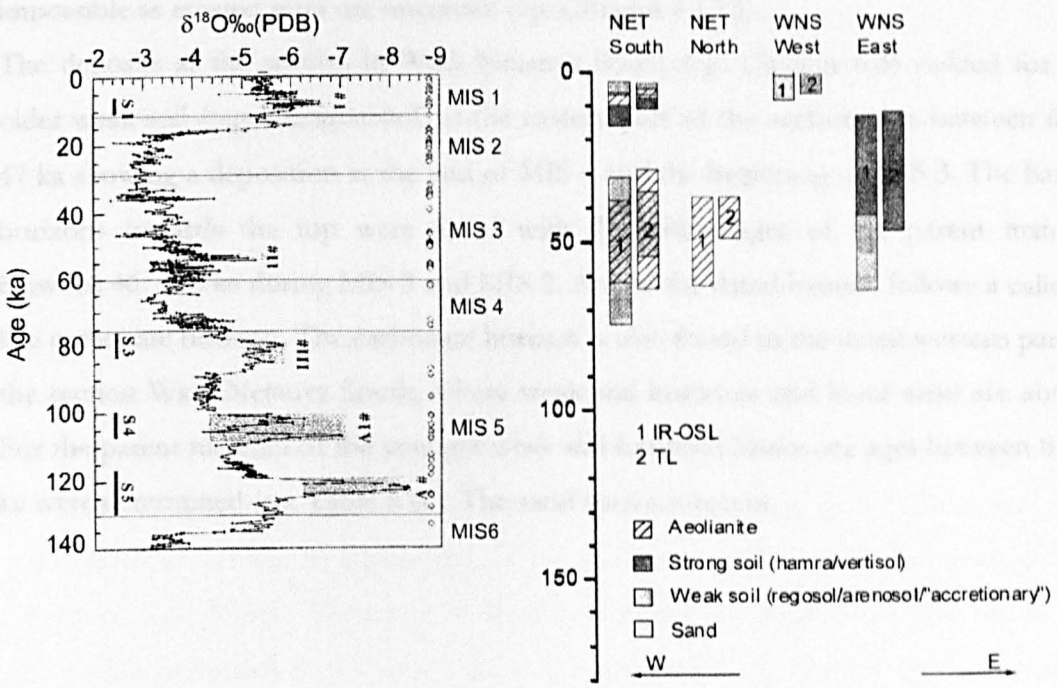

Figure 7.2.3a: Correlation of the dated deposits (sedimentation ages) of Netanya South Cliff (NET) and Wadi Netanya South (WNS) with the speleothem oxygen isotope record, marine isotope stages (MIS), sapropels (S1, S3-S5) and periods of enhanced rainfall (#I-#V) in the eastern Mediterranean (BAR-MATTHEWS et al. 2000).

Early data for the Netanya South Cliff section which were obtained with an alternative token value of the cosmic dose rate of 150 μGy/a for an average sediment depth and different water contents (cp. ENGELMANN *et al.* 2001) vary from the above data only slightly and do not lead to a different interpretation of the deposits (cp. Table 7.2.4g). The above published data for the Netanya South Cliff section were later recalculated by

FRECHEN *et al.* (2002) to accommodate attenuation of the cosmic dose rate with sediment depth. FRECHEN *et al.* (2002) attenuated the cosmic dose rate from a surface value (1 m) for the cosmic dose of 150 μGy/a given by AITKEN (1985, 1998) for more northern latitudes. The use of a token value of an average sediment depth for the cosmic dose rate like in ENGELMANN *et al.* (2001) has the physical advantage that a relatively difficult to determine factor is held constant in order to observe the effect of the other parameters on the age calculation more clearly. On the other hand, the method of PRESCOTT and HUTTON (1994) used in this study allows one, to determine the attenuation of the cosmic dose rate with depth for locations at different latitudes (cp. Chapter 5.5.2). However, the large hiatus between the lower and the upper part of the Netanya South Cliff section makes the determination of the correct cosmic dose rate impossible as erosion rates are uncertain (cp. Chapter 4.13.3).

The deposits at the section in Wadi Netanya South (cp. Chapter 6.4) yielded for the older weak soil (regosol/arenosol) at the eastern part of the section ages between 64 – 47 ka showing a deposition at the end of MIS 4 and the beginning of MIS 3. The hamra horizons towards the top were dated with deposition ages of the parent material between 46 – 12 ka during MIS 3 and MIS 2. Above the dated hamras follows a caliche-like carbonate horizon. The carbonate horizon is also found in the dated western part of the section Wadi Netanya South, where weak soil horizons and loose sand are above. For the parent material of the younger weak soil horizons Holocene ages between 8 – 0 ka were determined (cp. Table 6.4c). The sand above is recent.

7.2.4 Synopsis of the luminescence dating results of aeolianites and palaeosols along the Carmel and Sharon coastal plains

In the Carmel and Sharon coastal plains various sites have been investigated using luminescence dating techniques. The sites differ considerably in their stratigraphical sequences with alternating lithological units of aeolianites, strong soils (hamras/ vertisols), weak soils (regosols/arenosols) and sand. For the synopsis, the stratigraphy and the obtained luminescence ages from the sites that are not subject of this study are briefly summarised below and compared with the data of this study.

Carmel coastal plain

Several sites were dated using exposures at the road cut or in the near vicinity of the Tel Aviv – Haifa motorway in the Carmel coastal plain (cp. Figure . Luminescence datings and extensive sedimentological studies are reported in NIEBER (2002) and FRECHEN *et al.* (2004).

Motorway km 93

The northernmost dated site is located at the motorway km 93 where a beach rock on the one side and an aeolianite on the other side are exposed underneath a hamra, above which another aeolianite was deposited. NIEBER (2002) characterised the lower aeolianite as Kurkar-A-type, well-cemented with a massive appearance, cross-bedded and with well preserved structures, representing former barchanoid-like transgressive dunes (cp. FRECHEN *et al.* 2004). The hamra is described as strongly cemented in the upper part and weakly cemented in the lower part. The lower part could be identified as *in situ* while the upper part shows signs of reworking. The upper aeolianite above the hamra is characterised as Kurkar-C1-type with a nodular appearance being the result of an intensive vegetation cover with vertical sand accretion (NIEBER 2002, cp. FRECHEN *et al.* 2004). The luminescence datings obtained for the deposits at the site show sedimentation ages for the lower aeolianite of 57 ± 11 ka and 51 ± 10 ka. A sample from the lower part of the hamra yielded an age of 65 ± 9 ka that is seen as possibly overestimated owing to insufficient bleaching of that part of the hamra because of reworking of the horizon and close transport of pellets after heavy rainfalls. This is contradictionary to the above where the lower part of the hamra was described as being *in situ* while the upper part was reworked (cp. FRECHEN *et al.* 2004). For the covering

aeolianite ages of 59 ± 14 and 47 ± 9 ka were determined (cp. FRECHEN *et al.* 2004). With the obtained luminescence ages the two aeolianites cannot be distinguished from each other nor can the sedimentation phase of the parent material of the hamra (cp. Figure 7.2.4a). According to the obtained luminescence ages the sediments were deposited during MIS 4 and MIS 3. Time succession and luminescence ages of the deposits are summarised in Table 7.2.4a.

Table 7.2.4a: Time succession of deposits at Motorway km 93.

IR-OSL ages (ka) (FRECHEN *et al.* 2004)	Time succession (cp. Neber 2002)	Interpretation in this study
47 ± 9 59 ± 14	Aeolianite C1	MIS 4 to first half MIS 3
65 ± 9	Hamra upper part reworked Lower part *in situ*	
51 ± 10 57 ± 11	Aeolianite A	
---	Beach rock	Marine transgression MIS 5e

Atlit Railroad Bridge

At Atlit Railroad Bridge, motorway km 90, was a large section including a palaeocliff investigated on the seaside of the ridge (cp. NEBER 2002). The samples for the luminescence datings were taken from the southern part of that section. For the stratigraphically lower aeolianite, which is identified by NEBER (2002) as Kurkar-A-type, an IR-OSL age of 153 ± 31 ka was obtained placing the deposition in MIS 6 (cp. FRECHEN *et al.* 2004). The development of a hamra *in situ* followed, for which no luminescence age could be obtained. Above the hamra a Kurkar-B-type aeolianite was deposited, showing a nodular appearance and abundant rizolithes giving evidence for an extended cover of vegetation, which caused the vertical build-up of the dune system (NEBER 2002). FRECHEN *et al.* (2004) determined for this aeolianite an IR-OSL age of 143 ± 27 ka placing its deposition in the second half of MIS 6 to the transition to MIS 5. Marine transgression led to some erosion of the lower aeolianite forming a palaeocliff and the deposition of a beach rock described in NEBER (2002). A second hamra developed in the southern part of the section and a further aeolianite, Kurkar-C1-type filled the abrasion platform further North at the palaeocliff. The sedimentation ceased forming a caliche-like hardpan on top of the aeolianite (NEBER 2002). From the

luminescence datings obtained for the section the exact timing of the sedimentation and development of the hamra above the Kurkar-B-type aeolianite and the deposition of the Kurkar-C1-type aeolianite as well as the caliche-like hardpan is not entirely clear. Above the second hamra in the southern part of the section and the caliche-like hardpan further North a further aeolianite Kurkar-C2-type, similar to Kurkar-C1-types, was deposited (cp NEBER 2002). IR-OSL ages of 60 ± 14 ka and 74 ± 17 ka were obtained for this lithological unit (cp. FRECHEN *et al.* 2004) establishing the sedimentation of the aeolianite during the end of MIS 5 to the beginning of MIS 3. An upper hamra developed and eroded above the aeolianite. The remains were sampled in a solution pocket of the aeolianite underneath and an IR-OSL age of 12 ± 2 ka was obtained (FRECHEN *et al.* 2004) which places the accumulation of the parent material of the soil at the beginning of the Holocene (MIS 1).

With the help of geological events, the comparison of petrographical data with other sections and available luminescence data (cp. FRECHEN *et al.* 2004), NEBER (2002) established a time succession for the deposits at the section Atlit Railroad Bridge (Table 7.2.4b).

Table 7.2.4b: Time succession of deposits at Atlit Railroad Bridge.

IR-OSL ages (ka) (FRECHEN *et al.* 2004)	Time succession (cp. NEBER 2002)	Interpretation in this study
12 ± 2	Hamra	Beginning MIS 1
74 ± 17 60 ± 14	Aeolianite C2	End MIS 5 to beginning MIS 3
---	Hamra	
---	Beach rock	Marine transgression MIS 5e
143 ± 27	Aeolianite B	Second half of MIS 6 to the transition to MIS 5
---	Hamra in situ	
153 ± 31	Aeolianite A	MIS 6

Atlit Junction

At motorway km 90, section Atlit Junction (AJU), a lower aeolianite Kurkar A-type was dated with IR-OSL to 93 ± 15 ka (FRECHEN *et al.* 2004). Above this aeolianite a hamra developed which showed carbonate concretions in the lower part, prismatic structures in the sandy loam above and an upper part consisting of sand. For the hamra IR-OSL

ages of 57 ± 7 ka and 46 ± 8 ka were determined (FRECHEN *et al.* 2004). The hamra is covered with a further aeolianite Kurkar-C2-type (cp. NEBER 2002). This aeolianite shows a weak cementation in some parts and irregular carbonate precipitation in others. Acidic waters from a former hamra above, which is now eroded, resulted in solution pockets in the upper part of the aeolianite. Such a lense-like cavity is filled with remains of soil material. For the aeolianite itself no luminescence age was given in FRECHEN *et al.* (2004). NEBER (2002) stated age estimates for the aeolianite of 48 ± 7 ka and 35 ± 7 ka. A sample from the remains of the hamra had an IR-OSL age of 20 ± 3 ka (FRECHEN *et al.* 2004). The succession of units for this site is given in Table 7.2.4c.

Table 7.2.4c: Time succession of deposits at Atlit Junction.

IR-OSL ages (ka) (FRECHEN *et al.* 2004, cp. Neber 2002)	**Time succession (cp. NEBER 2002)**	**Interpretation in this study**
20 ± 3	Hamra	Sedimentation MIS 2, Pedogenesis MIS 1
35 ± 7 48 ± 7	Aeolianite C2	MIS 3
46 ± 8 57 ± 7	Hamra	MIS 4 to MIS 3
93 ± 15	Aeolianite A	MIS 5 (5c to 5.0)

Motorway km 85

The section at motorway km 85 consists of an alternation of three aeolianites and three hamras and is stratigraphically equivalent to the section at Atlit Railroad Bridge (FRECHEN *et al.* 2004). The lower aeolianite is identified as Kurkar-A-type and bears an IR-OSL age of 126 ± 20 ka (FRECHEN *et al.* 2004). For the hamra above no luminescence age was obtained. An IR-OSL age of 120 ± 23 ka was determined for the succeeding Kurkar-B-type aeolianite. The hamra towards the top yielded for the upper part of the soil an age of 67 ± 10 ka and the Kurkar-C2-type aeolianite an age of 65 ± 12 ka (FRECHEN *et al.* 2004). Above the aeolianite was another hamra deposited for which no age was obtained (FRECHEN *et al.* 2004). The horizons and their ages are summarised in Table 7.2.4d.

Table 7.2.4d: Time succession of deposits at Motorway km 85.

IR-OSL ages (ka) (FRECHEN *et al.* 2004)	Time succession (cp. NEBER 2002)	Interpretation in this study
---	Hamra	
65 ± 12 ka	Aeolianite C2	End of MIS 5 to beginning of MIS 3
67 ± 10 ka for uppermost part	Hamra	Deposition MIS 4
120 ± 23	Aeolianite B	End of MIS 6 to MIS 5 (5c)
---	Hamra	
126 ± 20	Aeolianite A	End of MIS 6 to MIS 5 (5c)

Habonim Quarry

The sections at Habonim Quarry that are investigated with luminescence dating in this study are located towards the sea at motorway km 82.

En Ayyala

At the section of En Ayyala, motorway km 80, a hamra is sandwiched between two aeolianites. The lower aeolianite is characterised as Kurkar-A-type (cp. NEBER 2002) and an IR-OSL age of 134 ± 30 ka was determined for this horizon (FRECHEN *et al.* 2004). The hamra shows similar features as the hamra at the section Atlit Junction and IR-OSL dates for the sedimentation of the parent material of 95 ± 18 ka and 80 ± 12 ka were obtained. The aeolianite on top of the hamra, a Kurkar-C2-type, showed an IR-OSL age of 64 ± 11 ka (FRECHEN *et al.* 2004). The time succession of the horizons is summarised in Table 7.2.4e.

Table 7.2.4e: Time succession of deposits at En Ayyala.

IR-OSL ages (ka) (FRECHEN *et al.* 2004)	Time succession (cp. NEBER 2002)	Interpretation in this study
64 ± 11	Aeolianite C2	MIS 4 (beginning of MIS 3)
80 ± 12 95 ± 18	Hamra	MIS 5 to beginning of MIS 4
134 ± 30	Aeolianite A	MIS 6 to MIS 5

NEBER (2002) and FRECHEN *et al.* (2004) correlated the deposits along the exposures at the motorway and nearby and distinguished five phases of aeolianite formation corresponding to an increased sand accumulation and different phases of soil development and also beach rock deposition for the Carmel coastal plain (cp. Figure 7.2.4a).

The oldest accumulation phase NEBER (2002) and FRECHEN *et al.* (2004) describe, resulted in the formation of Kurkar-A-type aeolianites which are exposed at the sections Atlit Railroad Bridge, Motorway km 85, Habonim Quarry and at En Ayyala (cp. Figure 7.2.4a). It followed the development of hamras at the sections Atlit Railroad Bridge and Motorway km 85. Whether these two hamras are contemporaneous belonging to the same pedogenic phase or not was not established as no luminescence age was reported. Above the hamras at the sections Atlit Railroad Bridge and Motorway km 85 an aeolianite Kurkar-B-type was deposited. The same aeolianite according to NEBER (2002) was also deposited at Habonim Quarry succeeding the lower aeolianite Kurkar-A-type.

The deposition of beach rocks at the sections Motorway km 93 and Atlit Railroad Bridge can because of similar elevations of about 10 m asl be assigned to the same marine transgression during the Last Interglacial, most likely during MIS 5e (cp. NEBER 2002 and FRECHEN *et al.* 2004).

The Kurkar-B-type aeolianite at Atlit Railroad Bridge was assigned as stratigraphically older than the marine transgression although from the geological information in the field this is not necessarily evident (cp. NEBER 2002 Figure 21).

Post-transgressional Kurkar-A-type aeolianites were deposited at the sections Motorway km 93 and at Atlit Junction and seen as one sedimentational phase with IR OSL ages of 57 ± 11 ka and 51 ± 10 ka (km 93) and 93 ± 15 ka (AJU) (cp. FRECHEN *et al.* 2004).

A phase of hamra development following the deposition of the Kurkar-A-type aeolianite is documented at the section Motorway km 93 and correlated by NEBER (2002) and FRECHEN *et al.* (2004) with hamras at Atlit Railroad Bridge following the marine transgression, at Atlit Junction following the Kurkar-A-type aeolianite, at Motorway km 85 following the Kurkar-B-type aeolianite and also at En Ayyala over a Kurkar-B-type aeolianite but also covering parts of the stratigraphically lower Kurkar-A-type aeolianite (cp. Figure 7.2.4a and NEBER 2002, Figures 58 and 60). The luminescence date given for the aeolianite underneath the hamra at the section En Ayyala is by FRECHEN *et al.* (2004) assigned to the Kurkar-A-type aeolianite while in NEBER (2002, Figure 119) this is not clear (cp. Figure 7.2.4a). The start of the pedo-

development documented at the pedocomplex at Habonim Quarry East-wall is seen to be earlier than the lower pedogenic phase of the sandwiched hamra between the aeolianites Kurkar-B-type and Kurkar-C2-type at the section Motorway km 85 and the sandwiched hamra at En Ayyala (NEBER 2002 Figure 119) (cp. Figure 7.2.4a).

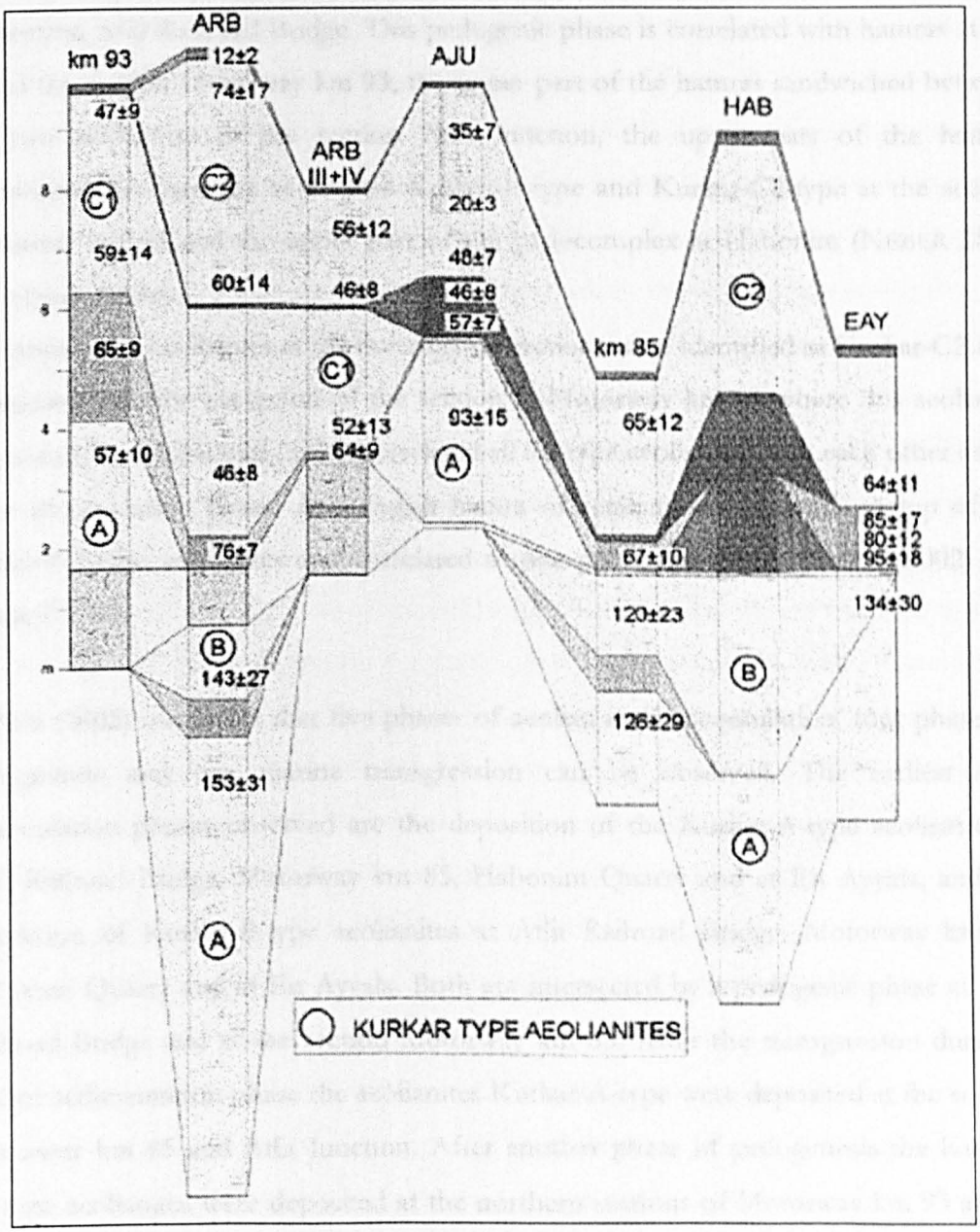

Figure 7.2.4a: "Chronostratigraphical cross correlation" of the sections at the motorway and in its near vicinity in the Carmel coastal plain. "Luminescence age estimates in ka after FRECHEN et al. (in prep.) and NEBER et al. (in prep.)." Changed from NEBER (2002, p. 154). km 93 = Motorway km 93, ARB = Atlit Railroad Bridge, AJU = Atlit Junction, km 85 = Motorway km 85, HAB = Habonim Quarry, EAY = En Ayyala.

At the section Atlit Railroad Bridge the morphological negative form, eroded through the transgression, is filled with the deposition of a Kurkar-C1-type aeolianite which is correlated with the same accumulation phase as the Kurkar-C1-type aeolianite in section Motorway km 93 (NEBER 2002).

Above the Kurkar-C1-type aeolianites at the sections Motorway km 93 and Atlit Railroad Bridge a further pedogenic phase with hamra development was documented at the section Atlit Railroad Bridge. This pedogenic phase is correlated with hamras at the top of the section Motorway km 93, the upper part of the hamras sandwiched between the two aeolianites at the section Atlit Junction, the upper part of the hamras sandwiched between the aeolianites Kurkar-B-type and Kurkar-C2-type at the section Motorway km 85 and the upper part of the pedocomplex at Habonim (NEBER 2002) (cp. Figure 7.2.4a).

The uppermost aeolianites at the investigated sections were identified as Kurkar-C2-type aeolianites with the exception of the section at Motorway km 93 where this aeolianite was not observed. NEBER (2002) correlated all C2 type aeolianites with each other as the same accumulation phase. A youngish hamra or remains are exposed on top of the Kurkar-C2-type aeolianites and correlated as one pedogenic phase (NEBER 2002) (cp. Figure 7.2.4a).

NEBER (2002) concludes that five phases of aeolian sand accumulation, four phases of pedogenesis and one marine transgression can be observed. The earliest sand accumulation phases observed are the deposition of the Kurkar-A-type aeolianites at Atlit Railroad Bridge, Motorway km 85, Habonim Quarry and at En Ayyala, and the deposition of Kurkar-B-type aeolianites at Atlit Railroad Bridge, Motorway km 85, Habonim Quarry and at En Ayyala. Both are intersected by a pedogenic phase at Atlit Railroad Bridge and at the section Motorway km 85. After the transgression during a further sedimentation phase the aeolianites Kurkar-A-type were deposited at the section Motorway km 85 and Atlit Junction. After another phase of pedogenesis the Kurkar-C1-type aeolianites were deposited at the northern sections of Motorway km 93 and at Atlit Railroad Bridge. A next phase of pedogenesis is correlated along the sections with the exception of the section at En Ayyala before the uppermost aeolianites Kurkar C2-type indicate a last sand accumulation phase after which the youngest soil formation took place (cp. NEBER 2002).

FRECHEN *et al.* (2004) gave the following chronological framework for sand accumulation phases and pedogenesis. For the lower Kurkar-A-type aeolianite deposition ages between 153 and 126 ka are given. For the following Kurkar-B-type aeolianites a range of age estimates of 143 to 120 ka was determined. As for the accumulation of the parent material of the pedogenic phases between the two aeolianites no ages were determined. FRECHEN *et al.* (2004) could not distinguish between the sedimentation ages for the two aeolianites or the parent materials of the soils. For the Kurkar-C1-type aeolianites ages between 59 and 46 ka are indicated. For the Kurkar-C2-type aeolianites a correlation with MIS 3 is suggested, with a given age range of 74 to 35 ka (FRECHEN *et al.* 2004). The hamra horizons between the lower Kurkar-A-type aeolianites and the Kurkar-B-type aeolianites and the aeolianites are correlated with MIS 6, as the exposed beach rock is most likely deposited during a transgressional phase of MIS 5e (FRECHEN *et al.* 2004). At the pedocomplex at Habonim Quarry the lowermost part is interpreted with the help of the RTL data by RONEN *et al.* (1999) (cp. Chapter 7.2.1) to have formed between 130 and 100 ka (FRECHEN *et al.* 2004). Other formation periods of hamra at En Ayyala, motorway km 85, Atlit Railroad Bridge and Atlit Junction are correlated with 95 to 67 ka. A younger pedogenic phase is interpreted to range from 57 to 46 ka and also to be present at the pedocomplex at Habonim Quarry (FRECHEN *et al.* 2004). Also, the dated hamras of this last pedogenic phase are correlated with the brownish palaeosol horizon at Givat Olga at the coastal cliff in the Sharon coastal plain (cp. FRECHEN *et al.* 2001, 2002). The remnants of hamras dated from cavities near the surface of the uppermost aeolianites in the coastal plain could both be identified as reworked and were interpreted with luminescence ages of *circa* 12 and 20 ka to be equivalent with the upper red palaeosol at the section Givat Olga at the Sharon coastal cliff (cp. FRECHEN *et al.* 2004).

The stratigraphical model suggested by NEBER (2002) and FRECHEN *et al.* (2004) seems to accommodate well the different types of deposits along the Carmel coastal plain and also their time succession suggested through the geological evidence, as for example the beach rock at the sections Atlit Railroad Bridge and Motorway km 93. However, there are problems associated with this model.

The chronological framework that NEBER (2002) and FRECHEN *et al.* (2004) assign to the deposits does not consider in the interpretation of the luminescence data the margins of error, which are large, and the small number of data available for any one

horizon. This is problematic as it is questionable that a correlation of the deposits like in the suggested model would have been possible, considering the large errors, without the help of the sedimentological characterisation of the Kurkar-types by NEBER (2002). This is already cautioned by FRECHEN *et al.* (2004) themselves.

On the other hand it is also uncertain whether NEBER (2002) and FRECHEN *et al.* (2004) could correlate the deposits on sedimentological or lithological information only, which is also remarked in NEBER (2002, p. 155) who calls for luminescence dating to correlate the deposits of the coastal plains.

NEBER (2002) correlated the deposits of the section at Habonim using premature data which should not be used for any correlation and interpretation (cp. Chapter 6.4). FRECHEN *et al.* (2004) correlated the deposits of the pedocomplex at Habonim Quarry with the ages obtained by LAUKHIN (RONEN *et al.* 1999) for which no accompanying datasets are available. Depending on the data for the pedocomplex at Habonim the correlation of the different pedogenic phases documented in the pedological record at Habonim Quarry and the adjacent sites of the section Motorway km 85 and En Ayyala could vary.

Despite the Kurkar-type characterisation by NEBER (2002), if a correlation between the Kurkar-A-type aeolianite at Atlit Junction, 108 – 78 ka, and the Kurkar-A-type aeolianite at the section Motorway km 93 with age estimate of 57 ± 11 (68 – 46) ka and 51 ± 10 (61 – 41) ka like in NEBER (2002) and FRECHEN *et al.* (2004) is possible, then the obtained luminescence ages (cp. NEBER 2002 and FRECHEN *et al.* 2004) would allow, for example, also a correlation of the Kurkar-A-type aeolianite at the section motorway km 85 that has an age estimate of 126 ± 20 (146 – 106) ka with the Kurkar-A-type aeolianite at the section Atlit Junction that has an age estimate of 93 ± 15 (108 – 78) ka.

Habonim Quarry

The data obtained for the section at Habonim Quarry East-wall in this study (cp. Chapter 6.4) compare to the adjacent sections along the motorway and the suggested stratigraphical model as follows. For the aeolianite underneath the pedocomplex luminescence ages of 132 ± 18 ka (IR-OSL HAB 4) and 124 ± 17 ka (TL HAB 4) were determined (cp. Figure 6.4a, Table 6.4a, Chapter 7.2.1), which would fit well with the ages obtained for the Kurkar-B-type aeolianites at the sections Motorway km 85 and En Ayyala, also correlated by NEBER (2002) with the aeolianite, Kurkar B-type, underneath

the pedocomplex at Habonim Quarry. The pedocomplex itself displays at least four pedogenic phases (lower hamra horizon, upper hamra horizon, AB horizon, vertisol, pseudogley, weak accretionary soil) (cp. TSATSKIN and RONEN 1999) (cp. Table 3.2.1a). The lower hamra horizon was not sampled. The upper hamra horizon was dated with IR-OSL to 96 ± 10 ka (HAB 5) and 89 ± 8 ka (HAB 6) and with TL to 95 ± 10 ka (HAB 5) and 82 ± 7 ka (HAB 6) and cannot be distinguished according to the luminescence ages from the AB horizon towards the top. For the AB horizon IR-OSL ages of 77 ± 7 ka (HAB 7) and 88 ± 7 ka (HAB 8) as well as TL ages of 69 ± 6 ka (HAB 7) and 87 ± 7 ka (HAB 8) were determined. The lowest part of the vertisol shows also ages of 76 ± 6 ka (IR-OSL HAB 9) and 73 ± 6 ka (TL HAB 9). The ages obtained for the lower part of the pedocomplex decrease from the bottom to the top, but the individual sedimentation phases of the parent material cannot be separated with the obtained luminescence data for the individual horizons. Nevertheless, the lower part of the pedocomplex can be correlated to the palaeosol at the section En Ayyala according to the luminescence ages. This is different from the correlation by NEBER (2002) (cp. FRECHEN *et al.* 2004). Age-wise the lower part of the vertisol can also be correlated with the hamra horizon, deposited and developed after the marine transgression, at the section Atlit Railraod Bridge, where an age of this horizon of 76 ± 7 ka is stated (cp. NEBER 2002), but which is not discussed in FRECHEN *et al.* (2004), yet is correlated differently.

The upper part of the vertisol is much younger and shows sedimentation ages of the parent material around 50 ka (cp. Table 6.4a, Figure 6.4a) and can probably be time correlated with a part of the hamra sandwiched between the two aeolianites at the section Atlit Junction, similar to NEBER (2002) and FRECHEN *et al.* (2004). The sedimentation ages of the parent material of the pseudogley and the weak accretionary soil at the Habonim Quarry pedocomplex cannot be distinguished with luminescence dating. The ages of around 38 ka coincide with the upper aeolianite formation at the section Atlit Junction (cp. Figure 7.2.4a) and also the TL age with the aeolianite formation sampled at the site Dor-Habonim Nature Reserve coast (cp. Figure 7.2.5a).

Sharon coastal plain

Cliff at Netanya South, North of Gaash and Gaash-Shefayim

At the Sharon coastal plain the coastal cliff between the area of Netanya and Gaash is exposed through marine erosion (cp. Figure 1.1a). Several sites were dated with luminescence along the escarpment. The sections at the cliff at Gaash-Shefayim (PORAT and WINTLE 1994), North of Gaash (RITTE *et al.* 1997) and Netanya South (ENGELMANN *et al.* 2001) all show a similar stratigraphy (cp. Chapter 3.2.3). At the base, at beach level, a thick aeolianite is exposed which was given the stratigraphical name Ramat Gan Kurkar (cp. GVIRTZMAN *et al.* 1984, 1998). Above this aeolianite a thick bed of sands is deposited with the stratigraphical name Nasholim Sands (GVIRTZMAN *et al.* 1984, 1998) and partly superimposed by a regosol. Towards the top follows the so called Dor Kurkar (cp. HOROWITZ 1979, GVIRTZMAN *et al.* 1984, 1998), a number of aeolianites with interposed weak sandy soils (regosols/arenosols) (cp. ENGELMANN *et al.* 2001). NEBER (2002) describes up to six weak soils in aeolianites at the coastal cliff. The alternation of aeolianites with intercalated weak soils is followed by the deposition of the parent material of well developed hamra horizons, the so-called Netanya Hamra (cp. HOROWITZ 1979, GVIRTZMAN *et al.* 1984, 1998). Above the hamra horizons a whitish very strongly cemented aeolianite, the Tel Aviv Kurkar after HOROWITZ (1979) and GVIRTZMAN *et al.* (1984, 1998), was deposited. Upon the strongly cemented aeolianite are deposited loose pedogenised sands named Taarukha Sands (cp. HOROWITZ 1979, GVIRTZMAN *et al.* 1984, 1998).

The luminescence ages obtained for the deposits at the southern part of the Sharon coastal cliff are summarised below (Table 7.2.4f).

The data for the section at the coastal cliff at Netanya South obtained in this study show few differences from the data for the same section published in ENGELMANN *et al.* (2001) and would not lead to a different interpretation. This shows that the differently used cosmic dose rates (attenuated in this study after PRESCOTT and HUTTON (1994) and token value for an average depth of 150 µGy/a in ENGELMANN *et al.* (2001)) make little difference for most of the samples. FRECHEN *et al.* (2002) recalculated the cosmic dose rates for the section of Netanya South (ENGELMANN *et al.* 2001) with values attenuated from a surface value of 150 µGy/a for more northern latitudes than Israel (cp. Table 7.2.4f). The data obtained in this study are used for the correlation and interpretation of the section Netanya South (cp. Chapter 7.2.3).

Table 7.2.4f: Summary of luminescence ages obtained for the southern part of the Sharon coastal cliff at the sections Netanya South from this study, ENGELMANN *et al.* (2001) and FRECHEN *et al.* (2002), North of Gaash (RITTE *et al.* 1997) and Gaash-Shefayim (PORAT and WINTLE 1994) (from North to South). "s" indicates weak soils.

Deposit (stratigraphical names after HOROWITZ 1979, GVIRTZMAN *et al.* 1984, 1998)	Netanya South ENGELMANN (this study) (ka)		Netanya South ENGELMANN *et al.* (2001) (ka)		Netanya South FRECHEN *et al.* (2002) (ka)	North of Gaash RITTE *et al.* (1997) (ka)	Gaash-Shefayim PORAT and WINTLE (1994) (ka)
	IR-OSL	TL	IR-OSL	TL	IR-OSL	IR-OSL	IR-OSL
Pedogenised sands (Taarukha Sands)	3 ± 0.2 10 ± 0.6	4 ± 0.3 6 ± 0.3	4 ± 0.5 10 ± 1	4 ± 0.5 6 ± 0.5	3.5 ± 0.3 10.4 ± 1.1	0.16 ± 0.02 2 ± 0.2	
Aeolianite (Tel Aviv Kurkar)	6 ± 0.4 13 ± 1	5 ± 0.3 7 ± 0.7	6 ± 0.5 13 ± 1	5 ± 0.5 7 ± 1	6.2 ± 0.7 13.0 ± 1.9	5.3 ± 0.3	5 ± 0.5
Hamra (Netanya Hamra)	13 ± 3 14 ± 1	8 ± 1 10 ± 1	13 ± 3 13 ± 1	8 ± 1 9 ± 1	13.1 ± 3.0 14.0 ± 1.8	12.9 ± 1.3 39.5 ± 1.9 56 ± 5	4 ± 1
Aeolianite with intercalated weak soils (s) (Dor Kurkar)	57 ± 6 47 ± 6 46 ± 6 69 ± 18 44 ± 6 s 48 ± 6 37 ± 6 s 38 ± 4 51 ± 5 s 52 ± 9 55 ± 6 43 ± 6	56 ± 4 44 ± 7 38 ± 6 46 ± 3 40 ± 5 s 56 ± 8 38 ± 4 s 38 ± 4 49 ± 5 s 44 ± 8 46 ± 5 34 ± 5	53 ± 5 43 ± 5 41 ± 7 62 ± 17 41 ± 6 s 43 ± 5 35 ± 6 s 34 ± 3 47 ± 5 s 47 ± 8 49 ± 5 38 ± 5	53 ± 4 41 ± 6 35 ± 6 41 ± 3 37 ± 5 s 50 ± 7 35 ± 4 s 34 ± 3 46 ± 5 s 39 ± 7 41 ± 5 31 ± 4	57.4 ± 7.2 47.6 ± 6.7 46.2 ± 9.0 69.2 ± 19.3 44.5 ± 6.9 48.0 ± 6.7 37.3 ± 6.5 38.0 ± 4.6 50.8 ± 6.1 52.3 ± 9.9 54.9 ± 6.9 43.3 ± 6.7	48.5 ± 4 51.8 ± 3.2	51 ± 3 53 ± 4
Pedogenised sands (Nasholim Sands)	46 ± 4 63 ± 11	50 ± 5 42 ± 5	43 ± 4 59 ± 10	46 ± 4 39 ± 5	46.4 ± 4.5 63.4 ± 11.4	49.7 ± 2.5 53.1 ± 3.8 57.4 ± 2.8	48 ± 4
Aeolianite (Ramat Gan Kurkar)	52 ± 4 55 ± 7 43 ± 6 54 ± 7	49 ± 3 47 ± 5 41 ± 4 45 ± 4	47 ± 4 49 ± 6 40 ± 5 50 ± 6	43 ± 2 42 ± 4 38 ± 4 41 ± 3	52.3 ± 5.2 54.8 ± 8.0	57.1 ± 2.9 57.8 ± 2.6	59 ± 5 64 ± 8

The data from the sections at Netanya South, North of Gaash and Gaash-Shefayim suggest that the lower parts of the sections were deposited during MIS 3 (cp. Table 7.2.4f). The pedogenised sands known as Nasholim Sands cannot be distinguished by the data from the aeolianites below and above. Also the weak intercalated soils between the aeolianites above cannot be separated (cp. ENGELMANN *et al.* 2001). The ages of the hamra deposits above differ in the studies considerably. In this study at Netanya ages between 15 – 7 ka were obtained for the horizon, while North of Gaash RITTE *et al.* (1997) obtained ages from 12.9 ± 1.3 ka to 56 ± 5 ka. The data by RITTE *et al.* (1997) are in agreement with the ages given by GVIRTZMAN *et al.* (1998) for the hamra. Either at the section North of Gaash older hamra deposits are exposed or pedogenesis

superimposed older deposits underneath a hiatus, similar to the vertisol development of the pedocomplex at Habonim Quarry East-wall. The pedogenesis of the upper part of the hamra at the section North of Gaash and also the section at Netanya South can only have taken place after the parent material was deposited, according to the luminescence ages not before the end of MIS 2 and the beginning of the Holocene (cp. Table 7.2.4f). For the following whitish and well cemented aeolianite Holocene ages between 7.7 – 4.5 ka were estimated, disregarding the IR-OSL date of sample NET 20 (cp. Table 6.4c and Table 7.2.4f). The ages for the pedogenised sand above the well cemented aeolianite vary considerably between 6.3 – 0.14 ka, not including the IR-OSL age of sample NET 23 as it seemed overestimated. Overall the ages obtained for the deposits of the sections at Netanya South, North of Gaash and Gaash-Shefayim are in good agreement with each other.

Wadi Netanya South

Samples taken not far from the coastal cliff, from deposits at the section Wadi Netanya South, placed the deposition of the parent material of a weak soil (regosol/arenosol) (cp. Table 3.2.3c) at the transition of MIS 4 to MIS 3. According to the luminescence ages the deposit could most likely be correlated with the timing of the weak soils in the so-called Dor Kurkar or the Nasholim Sands of the sections North of Gaash and Gaash-Shefayim, and also the section at the cliff at Netanya South. For the hamra horizons at the Wadi Netanya South the deposition of the parent material took place during the time of MIS 3 and MIS 2. The dated hamra horizons seem to be an equivalent to the so-called Netanya Hamra, which is exposed in the sections of the coastal cliff (cp. GVIRTZMAN *et al.* 1998, PORAT and WINTLE 1994, RITTE *et al.* 1997, ENGELMANN *et al.* 2001). The young, Holocene, weak soils at the section Wadi Netanya South might be correlated with the Taarukha Sands of GVIRTZMAN *et al.* (1998). The section at the Wadi does not expose an aeolianite (Tel Aviv Kurkar) above the hamra though a carbonaceous caliche-like horizon can be described. Whether this caliche like carbonaceous horizon could be correlated with the formation of the so-called Tel Aviv Kurkar exposed at the coastal cliff is unclear (cp. GVIRTZMAN *et al.* 1998, PORAT and WINTLE 1994, RITTE *et al.* 1997, ENGELMANN *et al.* 2001).

Givat Olga

FRECHEN *et al.* (2001) dated the coastal section of Givat Olga. Stratigraphically a well cemented and layered aeolianite is exposed on the base at sea level, over which a pedocomplex with two different soil units follows. The lower one of these soils is a red-brown palaeosol and the upper one a reddish hamra followed by a reworked horizon. Above the soils a further well cemented aeolianite and thick sands are deposited. The sands show two pedogenic horizons (FRECHEN *et al.* 2001, 2002). For the lower aeolianite ages between 74 – 46 ka were indicated, disregarding the IR-OSL age of the sample OLG 2 (cp. Table 7.2.4g). For the lower red-brown soil, ages range between 81 – 28 ka. The upper soil was dated to 26 – 10 ka (FRECHEN *et al.* 2001). The reworked horizon above yielded ages between 5 – 7 ka (cp. Table 7.2.4g). The ages for the upper strongly calcareous aeolianite ranged between 11 – 3 ka followed by the sand deposits with weak pedogenesis ranging between 6 – 2 ka (FRECHEN *et al.* 2001). The exact data are given below (Table 7.2.4g).

The lower aeolianite at the section Givat Olga is correlated with the Ramat Gan Kurkar, the Nasholim Sands and the Dor Kurkar (cp. GVIRTZMAN *et al.* 1998, FRECHEN *et al.* 2001). FRECHEN *et al.* (2001) also correlate the lower part of the hamra at the section Givat Olga with the lower part of the hamra at the section North of Gaash, which yielded similar luminescence ages for the lower part of the soil (cp. RITTE *et al.* 1997).

Table 7.2.4g: Luminescence dating results for the section Givat Olga (FRECHEN *et al.* 2001).

Deposits	Sample name	IR-OSL (ka)	TL (ka)
Sand pedogenised	OLG 16	3.3 ± 0.5	2.9 ± 0.5
	OLG 15	4.8 ± 0.5	3.8 ± 0.5
	OLG 14	5.3 ± 0.7	3.8 ± 0.5
Aeolianite	OLG 13	4.1 ± 0.3	9.7 ± 1.1
	OLG 12	5.5 ± 0.7	3.8 ± 0.7
Reworked material	OLG 11	5.7 ± 0.8	6.1 ± 0.6
Hamra reddish	OLG 10	12.3 ± 1.4	11.2 ± 1.4
	OLG 9	14.2 ± 1.6	20.3 ± 5.2
	OLG 8	19.4 ± 2.0	23.0 ± 2.7
Hamra red-brown	OLG 7	33.0 ± 2.8	29.9 ± 2.1
	OLG 6	41.9 ± 8.2	---
	OLG 5	50.5 ± 9.0	66.5 ± 5.8
	OLG 4	55.7 ± 5.0	74.5 ± 6.4
Aeolianite	OLG 3	54.7 ± 9.1	52.9 ± 4.8
	OLG 2	100.6 ± 20.5	61.5 ± 7.4
	OLG 1	66.9 ± 7.0	52.2 ± 5.1

The upper part of the pedocomplex was correlated with the Epi-Palaeolithic hamra *sensu* RONEN (1983), containing Epi-Palaeolithic industries (20 – 10 ka), which is exposed further south along the coastal cliff (cp. FRECHEN *et al.* 2001). The aeolianite above the pedocomplex is correlated with the Tel Aviv Kurkar exposed at the cliff further south (cp. FRECHEN *et al.* 2001, GVIRTZMAN *et al.* 1998). FRECHEN *et al.* (2002) summarise the correlation of the deposits of the section Givat Olga with the stratigraphy by GVIRTZMAN *et al.* (1998) (Table 7.2.4h).

Table 7.2.4h: Correlation of the deposits of the section Givat Olga and the coastal cliff further south with the stratigraphy by GVIRTZMAN *et al.* (1998) (cp. FRECHEN *et al.* 2002).

FRECHEN *et al.* (2002)	GVIRTZMAN *et al.* (1998)
Aeolian sand	Taarukha and Hadera Sands
Aeolianite (calcareous sandstone)	Tel Aviv Kurkar
Red palaeosol (hamra)	Netanya Hamra
Red-brown palaeosol	Not defined
Aeolianite (intercalated by several regosols)	Dor Kurkar

FRECHEN *et al.* (2002) assigned mean IR-OSL age estimates to the discussed lithological units of the Sharon coastal plain and distinguished three sand accumulation periods (Table 7.2.4i).

Table 7.2.4i: Lithological units and mean IR-OSL age estimates according to FRECHEN *et al.* (2002) for the deposits of sand accumulation periods of the Sharon coastal plain.

Lithological unit	Mean IR-OSL age estimate
Aeolian sand	5 – 2 ka and modern
Aeolianite (calcareous sandstone)	7 – 5 ka
Aeolianite	65 – 50 ka

The oldest sand accumulation period is reported to have occurred between 65 – 50 ka, correlating with the time of formation of sapropel S2 in the eastern Mediterranean. The next period of sand formation is described between 7 – 5 ka and correlates with the time of formation of sapropel S1 (cp. FRECHEN *et al.* 2002). The third sand accumulation period is described between 5 – 2 ka and also during modern times, not in phase with sapropel formation (FRECHEN *et al.* 2002). Two main periods of soil development are distinguished. For the brown palaeosol, ages between 35 – 25 ka are

estimated and for the reddish hamra, ages between 15 – 12 ka. The brown palaeosol developed under conditions of increased precipitation and the red hamra under reduced precipitation (cp. FRECHEN *et al.* 2002). Neither the weak soils in the lower aeolianites, nor the Holocene and modern sands, could be correlated with periods of increased precipitation (FRECHEN *et al.* 2002).

Power Station Quarry, South of Power Station and Seashore Power Station

The last sections compared here and dated in this study, are at Power Station Quarry near Hadera and westward from there (cp. Chapter 3.2.2).

The pedocomplex in the interdune depression at the East-wall at Power Station Quarry consists of several hamra horizons superimposed by a vertisol with a similar succession to the pedocomplex at the Habonim Quarry East-wall, most likely also indicating moister conditions towards the top of the complex. The ages of the pedocomplex at Power Station Quarry range between 33 – 17 ka for the lower hamra horizons. For the vertisol above, which is also superimposed on the upper hamra horizon, ages between 16 – 6 ka were determined. The pedo-horizons seem to be in phase with parts of the hamra horizons further south (cp. PORAT and WINTLE 1994, RITTE *et al.* 1997, GVIRTZMAN *et al.* 1998, ENGELMANN *et al.* 2001, FRECHEN *et al.* 2001, 2002). In particular the vertisol development at Hadera Power Station Quarry can be time correlated with the upper parts of the hamra exposed at the coastal cliff further South, whereas the lower part of the pedocomplex, the hamra horizons, would correlate to a certain extent with the lower part of the hamra dated at the section North of Gaash (RITTE *et al.* 1997).

The stratigraphically oldest aeolianite formation of the dated sites in the area took place according to the luminescence ages between 102 – 74 ka at the section Hadera Power Station West-wall. This aeolianite formation would be in phase with luminescence ages obtained for the lower aeolianite at the section Atlit Junction. Another aeolianite dated at Power Station Quarry (PSQ 1) yields ages of 57 – 39 ka, being in phase with the lower aeolianites (Dor Kurkar) at the cliff sections further South, but also with aeolianite formation at the section Habonim Quarry and more western sites and sections at the motorway. The stratigraphically youngest aeolianites at the sections Power Station Quarry West-wall, South of Power Station and also at Seashore Power Station seem to be with ages between 42 – 21 ka in phase with the upper aeolianite observed at the

Habonim Quarry East-wall section and also with the upper aeolianite at the section Atlit Junction.

Young Holocene to modern sands above the hamra at Seashore Power Station most likely correlate with Holocene and modern sands further South (Givat Olga, Netanya South Cliff, Wadi Netanya South).

The intercalated weak soils at Power Station Quarry West-wall and the section South of Power Station cannot be distinguished with the obtained luminescence ages from the surrounding aeolianites. The weak soils at the West-wall from Power Station Quarry represent the oldest weak soil at the Carmel and Sharon coastal plains discussed in this study. Interestingly, the timing correlates with the lower part of the soil formation at the pedocomplex at Habonim Quarry and also with the timing of the hamra formation at the section En Ayyala. The intercalated weak soils at the section South of Power Station correlate perhaps with the weak accretionary soil on top of the pedocomplex at Habonim Quarry East-wall and also with the timing of weak soils described further South (cp. ENGELMANN *et al.* 2001, NEBER 2002, FRECHEN *et al.* 2002, this study).

7.2.5 Significance for climate change (Interpretation)

The sedimentation and formation phases of aeolianites and soils as suggested by NEBER (2002) and FRECHEN *et al.* (2004) for the Carmel coastal plain and also by FRECHEN *et al.* (2002) for the Sharon coastal plain suppose an alternation of aeolianite formation phases and periods of soil development (cp. Chapter 7.2.4). The formation of aeolianites is seen as short sharp events compared to the geological time scale. This is inferred mainly from the high sedimentation rates and the marginal increase in age which can be observed at aeolianites (Dor Kurkar) at the coastal cliff in the Sharon coastal plain, for example at the dated section at Netanya South (cp. ENGELMANN *et al.* 2001). FRECHEN *et al.* (2002) and FRECHEN *et al.* (2004) state 15 ka to 5 ka, respectively, for such sedimentation events of aeolianites at the Sharon coastal plain. For the aeolianites of the Carmel coastal plain similar rapid accumulation rates are expected (FRECHEN *et al.* 2004).

The stratigraphical models of NEBER (2002), FRECHEN *et al.* (2002) and FRECHEN *et al.* (2004) suggested for the Carmel and the Sharon coastal plains are summarised below (Table 7.2.5a). The luminescence ages for the pedocomplex at the section Habonim Quarry East-wall obtained in this study are not contradictory to the stratigraphic interpretation of NEBER (2002) and FRECHEN *et al.* (2004). The results obtained in this study for the section at the coastal cliff at Netanya South are in good agreement with studies further South (PORAT and WINTLE 1994, RITTE *et al.* 1997) and also an earlier study of the section (ENGELMANN *et al.* 2001).

FRECHEN *et al.* (2004) correlate the hamra above the Kurkar-C1-type aeolianite at the northernmost sections at the motorway in the Carmel coastal plain with the upper part of the pedocomplex at Habonim Quarry and also with the red-brown grumosolic palaeosol at the section Givat Olga in the Sharon coastal plain (dark grey colour in Table 7.2.5a). They further correlate the Kurkar-C2-type aeolianite formation above the hamra with the oldest aeolianite in the Sharon coastal plain underneath the red-brown palaeosol. Although for parts of the Kurkar-C2-type aeolianite similar luminescence ages were obtained as for the aeolianite in the Sharon, this is, however, a cross-correlation (middle grey colour in Table 7.2.5a). The reworked hamra at the section Atlit Railroad Bridge in the Carmel coastal plain is interpreted as the depositional product of an equivalent of the red hamra at the section Givat Olga and hamras further South (light grey colour in Table 7.2.5a).

Table 7.2.5a: Comparison of stratigraphical models for the Carmel and Sharon coastal plain after NEBER (2002), FRECHEN *et al.* (2002) and FRECHEN *et al.* (2004).

Carmel coastal plain (NEBER 2002, FRECHEN *et al.* 2004)		**Sharon coastal plain ([1]FRECHEN *et al.* 2002, [2]FRECHEN *et al.* 2004)**	
		Aeolian sand	5 – 2 ka
		Aeolianite (calcareous sandstone)	7 – 5 ka
Hamra reworked at Atlit Railroad Bridge	12 ± 2 ka	Red hamra at Givat Olga	19 – 12 ka
Aeolianite formation (Kurkar-C2-type)	74 – 35 ka (MIS 3)		
Hamra development, upper part pedocomplex	57 – 46 ka	Red-brown palaeosol at Givat Olga	56 – 33 ka
Aeolianite formation (Kurkar-C1-type)	59 – 46 ka (MIS 3)	Oldest aeolianite in Sharon[2]	65 – 50 ka[1] Mean 53.9 ± 9.1 (60 – 50) ka[2]
Hamra development	95 – 67 ka		
Aeolianite formation (Kurkar-A-type)	95 ± 15 ka and 57 ± 10 ka		
Lower part of pedocomplex at Habonim	130 – 100 ka		
Beach rock	MIS 5e		
Aeolianite formation (Kurkar-B-type)	143 – 120 ka MIS 6		
Hamra development	MIS 6		
Aeolianite formation (Kurkar-A-type)	153 – 126 ka MIS 6		

The synopsis of the data obtained from the different study sites at the latitudes of Habonim, Hadera and Netanya South and also from the sites dated by PORAT and WINTLE (1994), RITTE *et al.* (1997) and FRECHEN *et al.* (2001, 2004) provides general and detailed information about the dated deposits in the Carmel and Sharon coastal plains (cp. Figure 7.2.5a).

Generally it can be confirmed from the comparison of the discussed dating studies that the deposits exposed in the Carmel coastal plain are older than in the Sharon coastal plain and the deposits become younger towards the South. An East – West gradient in age cannot be observed at the dated East – West transects Habonim Quarry – Dor-Habonim Nature Reserve Middle Ridge – Dor-Habonim Nature Reserve Coast, Hadera Power Station Quarry – South of Power Station – Seashore Power Station and Wadi

Netanya South – Netanya South Cliff. Further no aeolianite formation in MIS 2 could be observed in the Carmel or the Sharon coastal plains at the investigated sites (cp. Figure 7.2.5a).

Aeolianites

At the dated sites aeolianite formation took place during MIS 6, MIS 5, MIS 4, MIS 3 and also in MIS 1. Glacial – interglacial changes are much more pronounced in the Eastern Mediterranean than is recorded in the SPECMAP marine isotopic curve (cp. MARTINSON *et al.* 1987, KALLEL *et al.* 2000, BAR-MATTHEWS *et al.* 2003).

The conditions in Israel and the eastern Mediterranean during MIS 6 were generally cold and arid (KALLEL *et al.* 2000, WELDEAB *et al.* 2002) after high rainfall in the eastern Mediterranean region during MIS 7 (BAR-MATTHEWS *et al.* 2003). KALLEL *et al.* (2000) documented two strong coolings in MIS 6 at about 180 – 170 ka and at circa 140 ka of up to 10 °C. For the cold sapropel S6 during that time no counterpart sapropel was found in the Tyrrhenian Sea but high organic carbon contents were similar to interglacial sapropels (S5, S4, S3). KALLEL *et al.* (2000) documented that general humid and wet conditions associated with the timing of the interglacial sapropel events were also the case for the glacial sapropel S6. This is confirmed by findings of WELDEAB *et al.* (2002) who found that Saharan dust input was drastically reduced during the time of sapropel S6 and S5 and that this was most likely due to denser vegetation cover during more humid conditions which would have reduced physical erosion and sediment removal in source areas. EMEIS *et al.* (2003) document an increase in monsoon strength at 150 ka, although this insolation maximum is not expressed as sapropel owing to cold SSTs. During the glacial maximum at the end of MIS 6 (MIS 6.2) marked increases of Saharan dust and also detrital flux from the Aegean region point towards arid conditions in the catchment areas. During sapropel S6 and during MIS 6.2 in the Levantine basin, a predominance of terrigeneous sediments of the Nile river can be observed. The aeolian contribution of terrigeneous sediments was significantly enhanced through the glacial aridity and intensified wind speeds (WELDEAB *et al.* 2002).

During the time of the Last Interglacial (MIS 5) the conditions in the eastern Mediterranean were generally warmer. KALLEL *et al.* (2000) state mean sea surface temperatures (SST) of 22.5 °C differing with 1 °C lower than modern SSTs. The

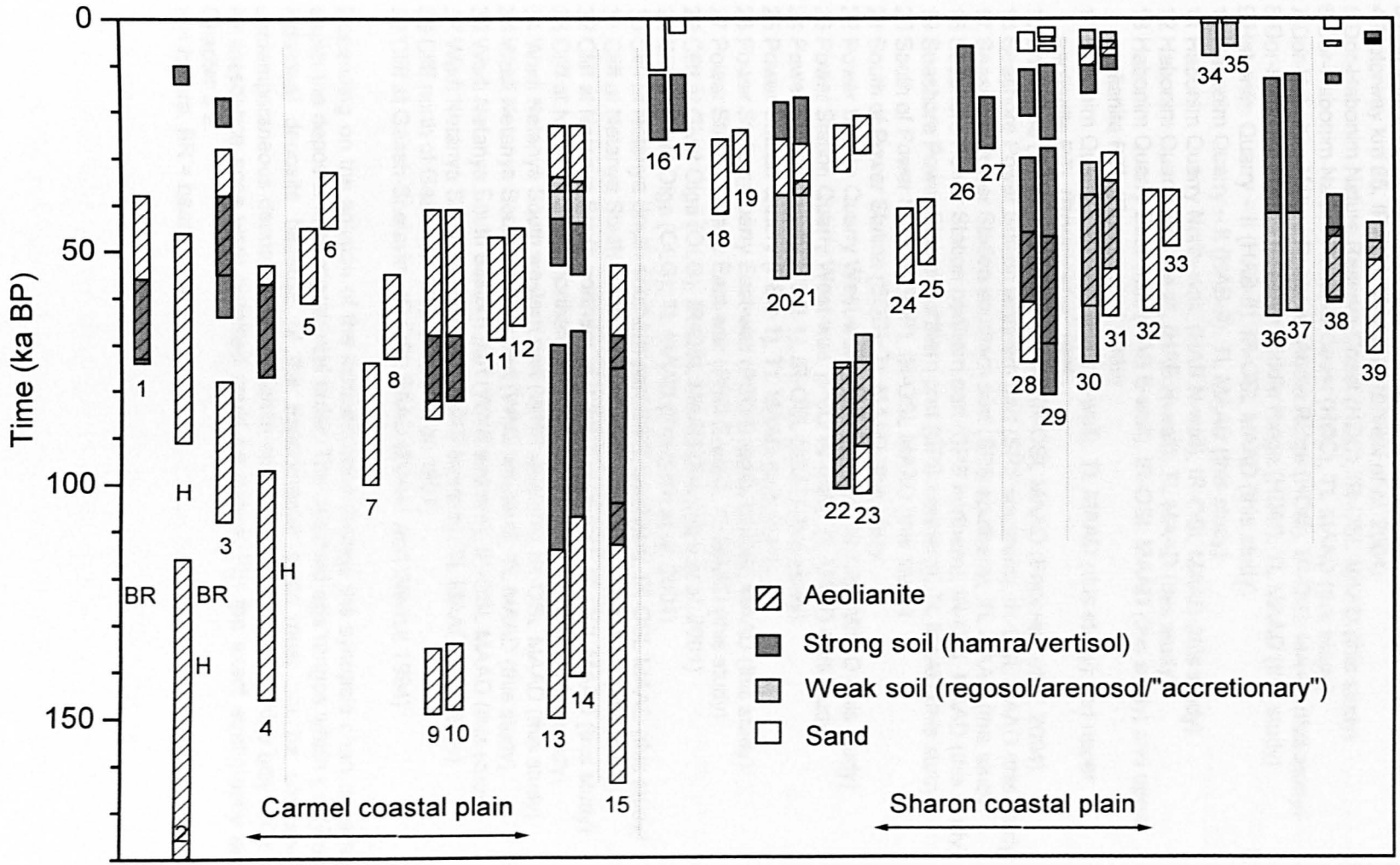

Figure 7.2.5a: Synopsis chart of aeolianites, strong soils, weak soils and sand according to their luminescence ages. Explanatory notes.

Explanatory notes to Figure 7.2.5a

1 Motorway km 93, IR-OSL MAAD (FRECHEN *et al.* 2004)
2 Atlit Railroad Bridge (ARB), motorway km 90, IR-OSL MAAD (FRECHEN *et al.* in press)
3 Atlit Junction (AJU), motorway km 90, IR-OSL MAAD (FRECHEN *et al.* 2004)
4 Motorway km 85, IR-OSL MAAD (FRECHEN *et al.* 2004)
5 Dor-Habonim Nature Reserve Coast (HDC), IR-OSL MAAD (this study)
6 Dor-Habonim Nature Reserve Coast (HDC), TL MAAD (this study)
7 Dor-Habonim Nature Reserve Middle Ridge (HDM), IR-OSL MAAD (this study)
8 Dor-Habonim Nature Reserve Middle Ridge (HDM), TL MAAD (this study)
9 Habonim Quarry – II (HAB-II), IR-OSL MAAD (this study)
10 Habonim Quarry – II (HAB-II), TL MAAD (this study)
11 Habonim Quarry North-wall, (HAB N-wall), IR-OSL MAAD (this study)
12 Habonim Quarry North-wall, (HAB N-wall), TL MAAD (this study)
13 Habonim Quarry East-wall, (HAB E-wall), IR-OSL MAAD (this study) and upper aeolianite RTL (RONEN *et al.* 1999)
14 Habonim Quarry East-wall, (HAB E-wall), TL MAAD (this study) and upper aeolianite RTL (RONEN *et al.* 1999)
15 En Ayyala (EAY), motorway km 80, IR-OSL MAAD (FRECHEN *et al.* 2004)
16 Seashore Power Station southern part (SPS southern), IR-OSL MAAD (this study)
17 Seashore Power Station southern part (SPS southern), TL MAAD (this study)
18 Seashore Power Station northern part (SPS northern), IR-OSL MAAD (this study)
19 Seashore Power Station northern part (SPS northern), TL MAAD (this study)
20 South of Power Station (SOP), IR-OSL MAAD (this study)
21 South of Power Station (SOP), TL MAAD (this study)
22 Power Station Quarry West-wall, (PSQ W-wall), IR-OSL MAAD (this study)
23 Power Station Quarry West-wall, (PSQ W-wall), TL MAAD (this study)
24 Power Station Quarry (PSQ 1), IR-OSL MAAD (this study)
25 Power Station Quarry (PSQ 1), TL MAAD (this study)
26 Power Station Quarry East-wall (PSQ E-wall), IR-OSL MAAD (this study)
27 Power Station Quarry East-wall (PSQ E-wall), TL MAAD (this study)
28 Cliff at Givat Olga (OLG), IR-OSL MAAD (FRECHEN *et al.* 2001)
29 Cliff at Givat Olga (OLG), TL MAAD (FRECHEN *et al.* 2001)
30 Cliff at Netanya South southern part (NET southern), IR-OSL MAAD (this study)
31 Cliff at Netanya South southern part (NET southern), TL MAAD (this study)
32 Cliff at Netanya South northern part (NET northern), IR-OSL MAAD (this study)
33 Cliff at Netanya South northern part (NET northern), TL MAAD (this study)
34 Wadi Netanya South western part (WNS western), IR-OSL MAAD (this study)
35 Wadi Netanya South western part (WNS western), TL MAAD (this study)
36 Wadi Netanya South eastern part (WNS eastern), IR-OSL MAAD (this study)
37 Wadi Netanya South eastern part (WNS eastern), TL MAAD (this study)
38 Cliff north of Gaash, IR-OSL (RITTE *et al.* 1997)
39 Cliff at Gaash-Shefayim, IR-OSL SAAD (PORAT and WINTLE 1994)

Depending on the solution of the luminescence datings the synopsis chart does not always depict the deposits in stratigraphical order. The obtained age ranges which partly overlap for individual deposits because of the experimental error must not be confused with a contemporaneous deposition of aeolianite and soil parent material. Also only units for which luminescence ages were obtained could be drawn. For the exact stratigraphy see text or Chapter 3.2.
H = hamra, BR = beach rock.

sapropel events in this isotopic stage, S5, S4 and S3, were associated with warm and humid conditions over the whole Mediterranean deriving from increased monsoon-like precipitation connected with strong Indian summer monsoon events and peaks in summer insolation in northern latitudes (KALLEL *et al.* 2000). The warm conditions during MIS 5 were interrupted by coolings of 2 °C of the SST during sapropel S5 and of 6 °C of the SST during sapropel S4. WELDEAB *et al.* (2002) recognised that the carbonate-free Saharan dust flux during MIS 5.4 (5d) was composed isotopically similar to the present-day Saharan dust flux in the Mediterranean and that therefore the climatic conditions during MIS 5.4 were comparable to the present climate. BAR-MATTHEWS *et al.* (2003) compared marine isotopic information from *Globigerinae* in eastern Mediterranean deep sea records with terrestrial oxygen isotope signatures from speleothems of the Soreq and Peqiin caves in Israel. They confirmed that climatic variations causing changes of the SSTs were also recorded in both of the terrestrial speleothems, establishing a direct link between marine and terrestrial isotope records of the area and also confirming that palaeoclimatic events and conditions in the eastern Mediterranean area were controlled by the rain source and that changes in SSTs could be used as proxy for terrestrial temperature variations (BAR-MATTHEWS *et al.* 2003). The palaeorainfall-values and temperature calculations by BAR-MATTHEWS *et al.* (2003) showed also that climatic conditions during sapropel formations were structured into highest rainfalls and lowest temperatures at the beginning of sapropel formation which then changed into decreasing rainfalls and increasing temperatures leading to arid conditions.

For MIS 4 the Levantine SSTs were 4° C lower than today, indicating a similar terrestrial variation (KALLEL *et al.* 2000, cp. BAR-MATTHEWS *et al.* 2003). LANDMANN *et al.* (2002) report on the lake level status of Lake Lisan (Dead Sea predecessor). They claim that after an initially high stand the water table sank because of reduced water input in the period between 70 – 45 cal ka. MACHLUS *et al.* (2000) report minor fluctuations for Lake Lisan in the time between 55 – 35 cal ka, but indicate also that the lake low stand during most of this period indicates drier climatic conditions.

In MIS 3 two low water stands which are identified through higher salt concentrations are correlated with the time between 45 – 36 cal ka (LANDMANN *et al.* 2002).

After further level oscillations and also a lake high stand that is not dated, Lake Lisan ceased in MIS 2 at around 16 cal ka indicating a strong drought (LANDMANN *et al.* 2002). The latter is also supported by climatic reconstructions from plant fossils and other data

for the maximum cooling of the Last Glaciation at about 20 – 18 ka which indicate for the area of the eastern Mediterranean strong annual precipitation decreases of –500 to –250 mm/a deviations from present-day values (cp. FRENZEL *et al.* 1992). VAN ZEIST and BOTTEMA (1991) show that during the interval 18 – 16 ka, which corresponds for them to the maximum cooling in the southern Levant, because the near eastern mountains show a maximum snow line depression during that time of 1000 – 1200 m, large areas had become deserts or semi-deserts. The vegetation in coastal areas existed of xeromorphic dwarf-shrublands dominated by *Artemisia* communities. The vegetation covered as little as 10 – 40 % of the steppe-like landscape leaving wide areas unprotected (VAN ZEIST and BOTTEMA 1991).

During MIS 1 enhanced pluvial conditions are recorded during the sapropel S1 formation at around 8 – 7 ka (cp. KALLEL *et al.* 2000, BAR-MATTHEWS *et al.* 2003). Dry conditions prevailed in Israel with low precipitation values of about 200 – 300 mm/a at around 5 ka and 2.5 ka (BAR-MATTHEWS *et al.* 2003).

Generally the information above confirms that aeolianite formation took place throughout different prevailing climatic conditions from the Penultimate Glacial over the Last Interglacial, the Last Glacial with the exception of MIS 2 and also during the Holocene (cp. Figures 7.2.1a, 7.2.2a, 7.2.3a and 7.2.5a). FRECHEN *et al.* (2004) assign to the stratigraphically older Kurkar-A-type aeolianites in the Carmel coastal plain, at the sections Atlit Railroad Bridge, Motorway km 85 and Habonim, ages between 153 – 126 ka, not considering the margins of error of the ages estimates (cp. Table 7.2.5a).

Regarding the errors of the age estimates, it cannot be decided if these aeolianites were deposited during MIS 6 or MIS 5. But considering the stratigraphical position of the beach rock deposits at Atlit Railroad Bridge a deposition of MIS 6 is very likely (cp. FRECHEN *et al.* 2004). The correlation of these aeolianites is made on lithological grounds following the characterisation by NEBER (2002).

The Kukar-A-type aeolianites at Motorway km 93, stratigraphically above the beach rock, and also exposed at Atlit Junction (cp. Figure 7.2.4a) are correlated with each other as one sedimentational phase (cp. FRECHEN *et al.* 2004), although, according to the luminescence ages the Kurkar-A-type aeolianite at Atlit Junction would have been deposited immediately after or during the ceasing sapropel S4 conditions during the Last Interglacial MIS 5 and the Kurkar-A-type aeolianite at Motorway km 93 during colder and drier conditions in the time of MIS 4 towards MIS 3. These aeolianites are again

correlated on lithological grounds of the Kurkar-type-characterisation by NIEBER (2002) as one sedimentational phase (cp. FRECHEN *et al.* 2004) (cp. Table 7.2.5a).

The Kurkar-C-type aeolianites at the Carmel coastal plain (cp. Figure 7.2.4a) cannot be distinguished age-wise but lithologically in Kurkar-C1-type and Kurkar-C2-type aeolianites and also through the intercalated soil development (cp. NIEBER 2002). The deposition of these aeolianites is correlated with the climatic conditions during MIS 3 (cp. FRECHEN *et al.* 2004) (cp. Table 7.2.5a).

Further South in the Sharon coastal plain at the section Power Station Quarry West-wall aeolianite formation took place during the Last Interglacial most likely in-between the sapropel formations S4 and S3 indicating deposition during the warmer and relatively dry conditions.

The aeolianite formations further South exposed at the cliff sections in the Sharon, and also at Power Station Quarry (PSQ 1) range with their luminescence ages between *circa* 70 – 35 ka indicating deposition ages from MIS 4 to MIS 3 during somewhat colder and drier glacial conditions (cp. KALLEL *et al.* 2000, LANDMANN *et al.* 2002).

Other aeolianites from the Sharon coastal plain at the sections Power Station Quarry, South of Power Station and at the Seashore Power Station seem in phase with the upper aeolianite at Habonim Quarry (cp. Figure 7.2.5a) and their deposition took place according to the luminescence ages during the end of MIS 3 during the period of Lake Lisan fluctuations which indicate varying precipitation over the area (cp. LANDMANN *et al.* 2002). The youngest aeolianite formation is observed at the coastal cliff in the Sharon (cp. Figure 7.2.5a). Ages correspond to the more arid post-sapropel S1 conditions (cp. BAR-MATTHEWS *et al.* 2003) (cp. Table 7.2.5a).

From the datings of the aeolianites in the Carmel and Sharon coastal plains it becomes clear that the deposition and consolidation of the aeolianites takes place during various climatic conditions during glacial and interglacial periods, during warmer and colder periods, but relatively dry. This is in itself remarkable, as it shows that sand accumulation in the coastal plains seems to be relatively independent of climatic temperature changes in the Eastern Mediterranean. It also shows that despite the climatic changes, a seasonality between summer and winter precipitation is maintained, which is necessary for the carbonaceous lithification of the aeolianites (cp. Chapter 1.1). The climatic reconstructions by FRENZEL *et al.* (1992) suggest, though their

geochronological frame might not be exact for the Eastern Mediterranean area, that precipitation seasonality remained during changing climatic conditions.

One reason for the missing aeolianite formations during the time of the LGM could be that because of the extremely arid and also colder conditions the necessary seasonality in precipitation and/or temperatures between winters and summers had ceased and sufficient solution or precipitation of carbonates could not take place to consolidate the dunes. Apart from the climatic conditions, other environmental conditions are necessary for aeolianite formation, such as sand and carbonate availability, transport through prevailing onshore winds and a windward position to that wind. Therefore other reasons for the missing aeolianites during LGM could be a shortage of sand availability connected with the distant LGM shoreline from the investigated localities, possibly associated with changed wind conditions (cp. SAARONI *et al.* 1998). Also a shortage in carbonaceous clasts, necessary to provide the carbonate for the cementation of the dunes, could perhaps be caused by a decreased amount of nutrients connected with the lessened run-off during these arid times. On the other hand MIS 2 aeolianites were perhaps deposited and consolidated further West on the exposed shore, as aeolianites are known today from drillings up to several kilometres off-shore. To summarise the conditions for aeolianite formation see Table 7.2.5b.

Table 7.2.5b: Climatic and environmental condition model for aeolianite formation.

Climatic conditions for the formation of aeolianites	Environmental conditions for the formation of aeolianites
Strong seasonality between Winter and Summer precipitation	Sand availability
Wet Winters	Sufficient carbonate content (bioclasts) in the sand
	On-shore (westerly) winds
	Windward position of deposition location (morphology)

Strong soils (hamras/vertisols)

Two distinctive differences can be observed in the Carmel and Sharon coastal plains regarding the development of strong soils. Some strong soils (hamra) develop on top of aeolianites at levelling or slope surfaces, whereas others develop in interdune (interaeolianite) depressions. A strong pedogenesis is generally observed in depressions

where, apart from hamras, vertisols also develop. Vertisols, in connection with aeolianites, were only observed in interdune depressions.

The oldest hamras at the dated sites of the Carmel coastal plain are exposed between the stratigraphically oldest Kurkar-A-type aeolianites and succeeding Kurkar-B-type aeolianites (NEBER 2002) (cp. Figure 7.2.4a). Regarding the dating of these aeolianites (cp. FRECHEN *et al.* 2004), the parent material of the soils was deposited in a time span which covers perhaps 6 – 10 ka during general cold climate conditions of MIS 6 (cp. Table 7.2.5a).

The parent material of other hamras above, which are intercalated in the aeolianites along the motorway in the Carmel coastal plain, at the sections Motorway km 93, Atlit Railroad Bridge and Motorway km 85, with luminescence ages (cp. FRECHEN *et al.* 2004) ranging around the time of MIS 4 seemed to have been deposited similarly, under the more arid, and also colder, climatic conditions post-sapropel S3 (cp. BAR-MATTHEWS *et al.* 2003, KALLEL *et al.* 2000).

The hamra horizons at the section En Ayyala were according to their mean ages probably deposited in a matter of 10 ka (cp. FRECHEN *et al.* 2004) (cp. Figure 7.2.4a). FRECHEN *et al.* (2004) seem to correlate these hamra horizons with the deposition phase mentioned directly above, although the obtained ages of the hamra horizons at En Ayyala would point towards a sedimentation post-sapropel S4 and pre-sapropel S3 (cp. Figure 7.2.4a). The latter would indicate a sedimentation of the parent material of the pedohorizons during a drier and also somewhat cooler inter-sapropel phase during MIS 5.

For the intercalated hamra horizons at the section Atlit Junction ages between 57 – 46 ka were obtained (FRECHEN *et al.* 2004). This could indicate a post-sapropel S2 deposition (cp. LOURENS *et al.* 1996). For the same time period, reduced water input in Lake Lisan is reported (LANDMANN *et al.* 2002). However, the climatic conditions during that time are not entirely clear and from Lake Lisan the signals reported are mixed (cp. MACHLUS *et al.* 2000, LANDMANN *et al.* 2002).

The deposition of the parent material of the so-called Epi-Palaeolithic hamra in the Sharon coastal plain seems to correlate with the time of MIS 2 and the LGM (cp. Figure 7.2.5a, Table 7.2.5a) for which various climate proxies indicate pronounced arid conditions.

For all these hamras the parent materials were, according to the luminescence dating, deposited during arid rather than pluvial climate conditions, but for which in most cases succeeding rainfall episodes are recorded in the Eastern Mediterranean (cp. Table 7.2.5c).

Table 7.2.5c: Comparison of hamra parent material deposition and rainfall episodes in the Eastern Mediterranean.

Hamra location	Luminescence ages	Deposition event parent material	Rainfall episodes after BAR-MATTHEWS *et al.* (2000) and other events
Seashore Power Station, South of Power Station, Power Station Quarry, Givat Olga, Netanya South, Wadi Netanya South, North of Gaash	Epi-Palaeolithic hamra between 28 – 8 ka (RITTE *et al.* 1997, FRECHEN *et al.* 2001, this study)	MIS 2	Rainfall episode # I Sapropel S1
Atlit Junction	46 ± 8 ka 57 ± 7 ka (FRECHEN *et al.* 2004)	Post sapropel S2 ?	Lake Lisan high stands
Motorway km 93, Atlit Railroad Bridge, Motorway km 85	65 ± 9 ka 76 ± 7, 64 ± 9 ka 67 ± 10 ka (FRECHEN *et al.* 2004)	MIS 4	Rainfall episode # II Sapropel S2
En Ayyala	85 ± 17 ka 80 ± 12 ka 95 ± 18 ka (FRECHEN *et al.* 2004)	MIS 5a	Rainfall episode # III Sapropel S3
Motorway km 85	Between126 ± 29 ka and 120 ± 23 ka (FRECHEN *et al.* 2004)	Transition MIS 6 to MIS 5	Rainfall episode # III Sapropel S5
Atlit Railroad Bridge	Between 153 ± 31 ka and 143 ± 27 ka (FRECHEN *et al.* 2004)	MIS 6	Insolation maximum at 150 ka

BAR-MATTHEWS *et al.* (2003) describe the changing nature of rainfall episodes in the Eastern Mediterranean. The episodes start with maximum rainfall and minimum temperature conditions which are followed during the episode by decreasing rainfall and increasing temperatures, finishing with arid conditions (BAR-MATTHEWS *et al.* 2003).

The deposition of the parent material during arid and also colder conditions followed by the above characterised rainfall episodes leads to the assumption that the pedogenesis of hamra soils intercalated in aeolianites could be connected with the rainfall episodes.

Whether the soil developments of the pedocomplexes in the observed interdune depressions at the Carmel and Sharon coastal plains contradict the above, shall now be discussed.

The calculated ages for the lower part of the Habonim Quarry pedocomplex range from the beginning of MIS 5 to its end (cp. RONEN *et al.* 1999, this study) covering the climatic oscillations during the whole of MIS 5 including the three sapropel events S5, S4 and S3. The vertisol in the upper part of the pedocomplex is superimposed over a hiatus onto the upper horizon of the lower part. The parent material for the vertisol shows deposition ages post-sapropel S2 (<~ 55 ka, LOURENS *et al.* 1996), similar to the deposition ages of the parent material of the hamra horizons at Atlit Junction. TSATSKIN and RONEN (1999) identified periods of soil formation and also sedimentary processes within the pedocomplex although the soil horizons were not separated by non-soil deposits. The succession of the soil horizons at Habonim evidences increasing water logging through restrained drainage and also the accumulation of fines resulting in clear catenary changes in the pedocomplex. TSATSKIN and RONEN (1999) also emphasise that in contrast to a constant aeolian influx of fine particles, it would be more probable that periods of discrete palaeosol development alter with sediment accumulation and an enhanced input of fines. The end of the catena shows a mixing of increasing aeolian and colluvial activity indicating landscape instability prior to 45 ka (TSATSKIN and RONEN 1999) (40 ka, this study). The microphological features of the pedocomplex at Habonim confirm rather than contradict the above suggested connection between palaeosol development and rainfall episodes in the area.

The pedocomplex at the section Givat Olga is more simply structured than the pedocomplex at Habonim Quarry and consists of a lower red-brown palaeosol unit and an upper red palaeosol (hamra) in a shallow depression (cp. FRECHEN *et al.* 2002). For the deposition of the parent material of the lower unit two clusters of luminescence ages were determined. For the lower part of the lower unit the deposition ages cover the time of MIS 4 (cp. Table 7.2.4h). For the upper part of the lower unit deposition ages (~ 40 – 30 ka) corresponding with the second half of MIS 3 were determined (cp. Table 7.2.4h). FRECHEN *et al.* (2002) used micromorphological methods to distinguish for the lower unit at the section Givat Olga two distinct palaeosols. The lower palaeosol shows characteristics of hamra and also grumusolic pedogenesis which indicate that the soil developed under climatic conditions of increased precipitation which was amplified by geomorphological factors (cp. FRECHEN *et al.* 2002). According to the deposition ages the increase in precipitation could have coincided with rainfalls of the sapropel S2 event. The upper palaeosol of the lower unit is characterised as a dark brown sandy loam with a prismatic structure and weakly expressed slickensides. Some small carbonate

concretions are described mostly at the top of this soil (cp. FRECHEN *et al.* 2002). As slickensides generally evidence cracks in soil surfaces during dry seasons and the filling of these cracks with fine colluvial material during wet seasons, the development of this soil could be connected with moister seasonal climate conditions during Lake Lisan high stands towards the end of MIS 3 (cp. LANDMANN *et al.* 2002).

The upper unit of the pedocomplex at the section Givat Olga consists of a red palaeosol characterised as rhodoxeralf (hamra) (FRECHEN *et al.* 2002). An AB horizon has developed from the surface to about 1 m below on bedded loamy sand. Below the AB horizon, layered yellowish-red sand with some small secondary carbonate nodules is described and at the base of the unit occur brown bands of 1-2 cm thickness which are thought to be possibly of erosional origin (FRECHEN *et al.* 2002). The authors also point out, that the two units of the pedocomplex at Givat Olga developed on different parent material and also under different environmental conditions (FRECHEN *et al.* 2002). The obtained ages for these horizons (cp. FRECHEN *et al.* 2002) would confirm deposition in the second half of MIS 3, post 30 ka. The brown bands of possibly erosional origin most likely correspond with the climatic fluctuations during that time (cp. LANDMANN *et al.* 2002). The deposition ages for most of the upper unit are clearly in phase with the arid conditions during MIS 2 during which the sand material of the upper part of the unit on which the AB horizon developed was most likely deposited followed by pedogenesis during the increased moister climate conditions around sapropel S1.

Overall the deposition ages of the parent material and the soil developments of the pedocomplex at the section Givat Olga confirm the above suggested thesis, that soil development in the Carmel and Sharon coastal plains is closely connected with Eastern Mediterranean rainfall episodes.

A further pedocomplex was observed at the Hadera Power Station Quarry over hamra horizons, for which ages between *circa* 30 – 20 ka were determined, indicating the deposition of the parent material during the late MIS 3 and the beginning of MIS 2. The following hiatus corresponds most likely to the time of the LGM in the Eastern Mediterranean (cp. VAN ZEIST and BOTTEMA 1991). The development of a vertisol above is superimposed over the hiatus onto the upper parts of the hamra. The deposition of the parent material in the upper part of the pedocomplex is dated to around 11 – 10 ka (cp. Table 3.2.2a). Both sediment depositions are centred around MIS 2. The hamra soil developed according to the obtained ages most likely in the increasingly moist climatic conditions shortly after the LGM. The upper part of the

pedocomplex was deposited just before the humid conditions of the sapropel S1 event that most likely caused the development of the vertisol.

All strong soil developments (hamras/vertisols) discussed here, seem to be congruent with the assumption that strong pedogenesis observed in the Carmel and Sharon coastal plains is connected with the occurrence of Eastern Mediterranean rainfall episodes. While in morphological depressions soil development is more probable, caused by the relatively sheltered from desiccation morphological position and the depression also acting as catchment for moisture, the intercalated hamra soils between aeolianites developed most probably post-sedimentary during succeeding humid climate events. The conditions for the development of hamras are summarised below (Table 7.2.5d).

Table 7.2.5d: Climatic and environmental condition model for hamra developments.

Climatic conditions for the development of hamras	Environmental conditions for the development of hamras
Moist climate conditions (rainfall episodes)	Low or ceased sand accumulation rates
	Precipitation and temperature seasonality

The observed vertisols in connection with aeolianites in the Carmel and Sharon coastal plains have developed in depressions, which most likely acted as catchment for excess water and fine particles. Vertisols also develop under increased humid conditions which are climatically but also morphologically controlled. The development of vertisols also requires a strong seasonality. The climatic and environmental conditions necessary for the pedogenesis of vertisols is summarised below (Table 7.2.5e).

Table 7.2.5e: Climatic and environmental condition model for vertisol development.

Climatic conditions for the development of vertisols	Environmental conditions for the development of vertisols
Strong seasonality between Winter and Summer precipitation	Availability of fines
Moist Winters	Low or ceased sand accumulation

Weak soils (regosols/arenosols)

Apart from one exception in the Carmel coastal plain, weak soils observed in this study are solely confined to exposures at the Sharon coastal plain (cp. Figure 7.2.5a). The exception in the Carmel coastal plain is the weak accretionary soil at the top of the pedocomplex at Habonim Quarry. Whether this soil could be characterised as regosol or arenosol is not clear (cp. TSATSKIN and RONEN 1999). The exposures further south in the Sharon coastal plain are either intercalated between aeolianite deposits or form soils intercalated or on top of loose sand, forming also the present-day soil.

Weak soils intercalated in aeolianites are found at the coastal cliff between Netanya and Gaash and also at the Hadera Power Station Quarry West-wall and at the section South of Power Station. The oldest observed weak soil in the Sharon at the Hadera Power Station Quarry West-wall (Figure 1.1g) shows deposition ages correlating with MIS 5a. With the obtained luminescence ages the soil cannot be distinguished from the underlaying aeolianite. The deposition of the parent material of the soil would correlate with the deposition of the parent material of the hamra soil at the section En Ayyala in the Carmel coastal plain.

Other weak soils in the Sharon coastal plain are intercalated between aeolianites at the sections South of Power Station, Netanya South, North of Gaash and Gaash-Shefayim. At the latter three sections a relatively pronounced weak soil is developed on top of the Nasholim Sands identified by GVIRTZMAN *et al.* (1998). For the deposition of the sands ages correlating with the time of the early MIS 3, most likely post-sapropel S2, were determined. Further weak soils, which are lens-like and intercalated in the aeolianites above at the coastal cliff in the Sharon (cp. ENGELMANN *et al.* 2001, NEBER 2002) and also at the section South of Power Station, developed on sediments deposited during MIS 3 and cannot be correlated with soil developments in the Carmel coastal plain and age-wise not be distinguished from the associated aeolianites. It is assumed that these soils result during pauses or strongly reduced sand accumulation not documented in the Carmel coastal plain.

Weak soils that are developed on sand not intercalated between aeolianites are found in the Wadi Netanya South section and on top of the coastal cliff. The weak soils developed in the eastern-most section at the Wadi Netanya South are most probably time equivalents of the weak soils at the cliff during MIS 3. Younger weak soils developed during MIS 1 on loose sands documented at the western-most section in the

wadi and also on top of the cliff for example at the section Netanya South or Gaash-Shefayim.

The contrast between the development of strong soils in the Carmel coastal plain and the development of weak soils in the Sharon coastal plain can be explained with the very strong North-South-decreasing precipitation gradient prominent in Israel and the Near East. Also variations of the carbonate contents of the soil-substrates could add to differentiated developments, as weak soils (regosols) are particularly known to form on carbonate depleted substrates and from the recent coastal sediments such differences in the abundance of carbonate are known. While in the Sharon coastal plain nearly pure quartz-sand is deposited, the coastal sediments further north in the Carmel coastal plain are furnished with an increased amount of carbonaceous bioclasts. That the lens-like less pronounced weak soils in the Dor Kurkar of the Sharon coastal cliff are not documented in the deposits of the Carmel coastal plain is explained by the higher sedimentation rates at the Sharon coastal cliff in comparison with the aeolianites in the Carmel coastal plain and also the stronger cementation of the aeolianites in the Carmel caused by higher precipitation in contrast to the Sharon. These lens-like intercalated weak soils probably reflect minor climatic fluctuations causing changes in sand accumulation. Some of these palaeosols document through rizoliths and the remains of landsnails well established plant growth and bioactivity. The conditions for the development of weak soils are summarised in Table 7.2.5f.

Table 7.2.5f: Climatic and environmental condition model for weak soil development.

Climatic conditions for the development of weak soils	Environmental conditions for the development of weak soils
Moist climate (winters)	Low or ceased sand accumulation
	Lens-like weak soils in surface dents with slightly moister conditions than surroundings
	Pronounced weak soils on horizontal surfaces with an evenly moisture distribution owing to missing relief

Sand

At the southern part of the section Seashore Power Station and the western part of the Wadi Netanya South section loose sands are deposited as the uppermost lithological unit. It is only a matter of time until these deposits are superimposed by a weak soil under the present climate conditions. The formation of recent aeolianites was not observed.

7.2.6 Climate controlled model for the cyclical formation of aeolianites and soils in the Eastern Mediterranean

Most of the Eastern Mediterranean rainfall episodes are now successfully linked with an increase in strength of the Indian summer monsoon which also affects East Africa and the Sahara (African monsoon) or the Near East and the Eastern Mediterranean (cp. KALLEL *et al.* 2000, BAR-MATTHEWS *et al.* 2003, LARRASOAÑA *et al.* 2003). The major part of information derives from marine cores taken for example from the Eastern Mediterranean, the Arabian Sea and the Bay of Bengal (e.g. KALLEL *et al.* 2000, EMEIS *et al.* 2003, LARRASOAÑA *et al.* 2003). Early cores from the Mediterranean showed dark organic-rich sediments, sapropels, which had developed under anoxic conditions (c.p. ROHLING 1994). Dating and time correlations of these horizons showed them in phase with orbital precession minima and also with periods of low dust supply from the Sahara (cp. LOURENS *et al.* 1996, LARRASOAÑA *et al.* 2003). It is meanwhile well established that sapropels develop under anoxic conditions at the sea-bottom. The anoxic conditions are caused by substantial amounts of monsoon-like freshwater supplies to the sea-surface which cause through varied salt concentrations a stratification of the water column. The stratification prevents an even exchange of oxygen between different layers. At the same time the increased precipitation generates a higher run-off from the adjacent lands, supplying high amounts of nutrients to the sea (e.g. LARRASOAÑA *et al.* 2003, EMEIS *et al.* 2003).

The monsoon-precipitation increases also affect East Africa. The Ethiopian plateau acts as the catchment area for the Blue Nile and the Atbara river. Both rivers are responsible for 80 – 90 % of the main Nile river discharge (cp. IBRAHIM 1995, SUTCLIFFE and PARKS 1999). Increases in monsoonal precipitation over the catchment areas of the Blue Nile and the Atbara cause also higher amounts of sediment to be discharged from the main Nile river into its littoral cell in the Eastern Mediterranean (cp. LARRASOAÑA *et al.* 2003).

From the luminescence dating studies discussed in this thesis for the different deposits in the Carmel and Sharon coastal plains, and also the climatic information available for the Eastern Mediterranean area and Israel in particular (cp. Chapter 7.2.4), it seems to emerge that there is evidence for a possible cyclical climatic interpretation of the coastal deposits which is directly connected with the mechanisms of monsoon-like precipitation in the Eastern Mediterranean described above. A climatically controlled model of cyclical aeolianite formation and soil pedogenesis is suggested.

BAR-MATTHEWS *et al.* (2003) were able to show that during the recession of monsoon-like rainfall over the Eastern Mediterranean, temperature increases are noted which are the reason for the increasingly arid conditions at the end of sapropel events. These changing conditions would allow at some point sand accumulation and the formation of dunes, specifically with higher accumulation rates shortly after the rainfall episode, where through the increased precipitation higher sediment input into the Eastern Mediterranean takes place. The consolidation of dunes would be possible through the precipitation seasonality which was maintained in the Eastern Mediterranean during the changing climates of the last interglacial-glacial cycle (cp. FRENZEL *et al.* 1992). Sedimentation rates would most likely be lowered over time, according to the available supplies, and temperatures would adjust relatively to non-sapropelitic conditions. The next rainfall episode (sapropel formation) would have started with a sudden increase in average precipitation values, providing the necessary moisture for enhanced plant growth and pedogenesis. The soil development would continue until disrupted through the next post-sapropel arid conditions and newly increased sediment accumulation. A schematic example of three cycles is demonstrated below (Figure 7.2.6a).

The model is supported by some findings of GVIRTZMAN and WIEDER (2001) who describe that each cycle of soil formation they studied in the Mediterranean coastal plain of Israel has two signatures of climatic proxy events. First the parent material is deposited and then soil formation takes place. Soil formation would come to an abrupt end if a new cycle of sand accumulation begins. Most of the studies of GVIRTZMAN and WIEDER (2001) were concerned with Holocene deposits in the Sharon coastal plain which they linked to climatic signatures. They also correlated older parts of various palaeosol horizons, which they summarised as "Netanya Palaeosols" (similar to the stratigraphical name of "Netanya Hamra" of GVIRTZMAN *et al.* 1998), with climate events. They do not find a signature in the deposits for the cold and extremely arid period in the Eastern Mediterranean equivalent to the time of the LGM, but find the dry phase of the Younger Dryas well represented in the deposits. However, their correlations are different from the ones in this study, as some stratigraphical units they summarise are differently expressed in sections futher North.

In HOROWITZ (1979) the rubification of hamras is associated with humid periods, which also supports the correlation in the suggested model - that pedogenesis is in phase with rainfall episodes in the Eastern Mediterranean.

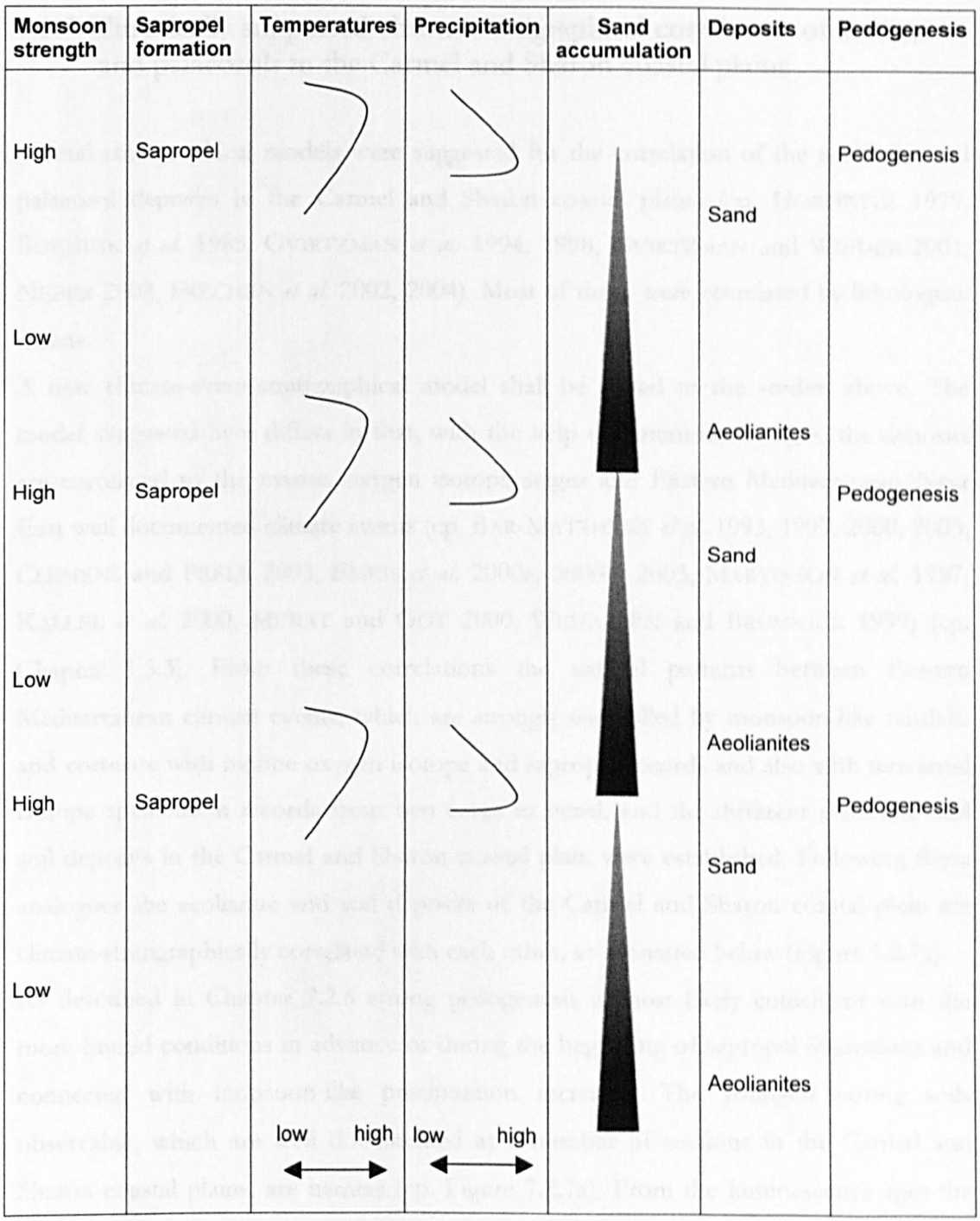

Figure 7.2.6a: Climatically controlled model of cyclical aeolianite formation and soil pedogenesis (schematic).

The majority of the observed hamras superimposed on aeolianites and exposed in the Carmel and Sharon coastal plains show a gradual transition towards the underlying horizon, indicating *in situ* soil development after a phase of sand accumulation through changing climatic and environmental conditions. The upper contact to the stratigraphical younger aeolianite is usually sharp and distinct, documenting a sudden onset of sand accumulation that buries the underlying soil (cp. e.g. Figure 1.1d).

7.2.7 Climatically supported chronostratigraphical correlation of aeolianites and palaeosols in the Carmel and Sharon coastal plains

Several stratigraphical models were suggested for the correlation of the aeolianite and palaeosol deposits in the Carmel and Sharon coastal plains (cp. HOROWITZ 1979, BOENIGK *et al.* 1985, GVIRTZMAN *et al.* 1994, 1998, GVIRTZMAN and WIEDER 2001, NEBER 2002, FRECHEN *et al.* 2002, 2004). Most of these were correlated by lithological means.

A new climate-event-stratigraphical model shall be added to the studies above. The model suggested here differs in that, with the help of luminescence ages, the deposits are correlated to the marine oxygen isotope stages and Eastern Mediterranean/Near East well documented climate events (cp. BAR-MATTHEWS *et al.* 1993, 1997, 2000, 2003, CLEMENS and PRELL 2003, EMEIS *et al.* 2000a, 2000b, 2003, MARTINSON *et al.* 1987, KALLEL *et al.* 2000, MURAT and GOT 2000, WEHAUSEN and BRUMSACK 1999) (cp. Chapter 1.3.3). From these correlations the natural patterns between Eastern Mediterranean climate events, which are strongly controlled by monsoon-like rainfalls and correlate with marine oxygen isotope and sapropel records and also with terrestrial isotope speleothem records from two caves in Israel, and the different aeolianite and soil deposits in the Carmel and Sharon coastal plain were established. Following these analogues the aeolianite and soil deposits of the Carmel and Sharon coastal plain are climate-stratigraphically correlated with each other, as presented below (Figure 7.2.7a).

As described in Chapter 7.2.6 strong pedogenesis is most likely coincident with the more humid conditions in advance or during the beginning of sapropel formations and connected with monsoon-like precipitation increases. The youngest strong soils observable, which are well documented at a number of sections in the Carmel and Sharon coastal plains, are hamras (cp. Figure 7.2.7a). From the luminescence ages the deposition of the parent materials took place under the generally arid conditions of MIS 2 and the time of the LGM. Therefore it is likely that pedogenesis was initiated in advance of and during the commencing sapropel S1 event. The pedocomplex at Power Station Quarry East-wall shows different pedogenic phases that partly document the rainfall fluctuations during that time (cp. BAR-MATTHEWS *et al.* 2003). Above these soil horizons strongly cemented carbonaceous whitish aeolianites are exposed at the sections of the cliff in the Sharon coastal plain which were most probably deposited and

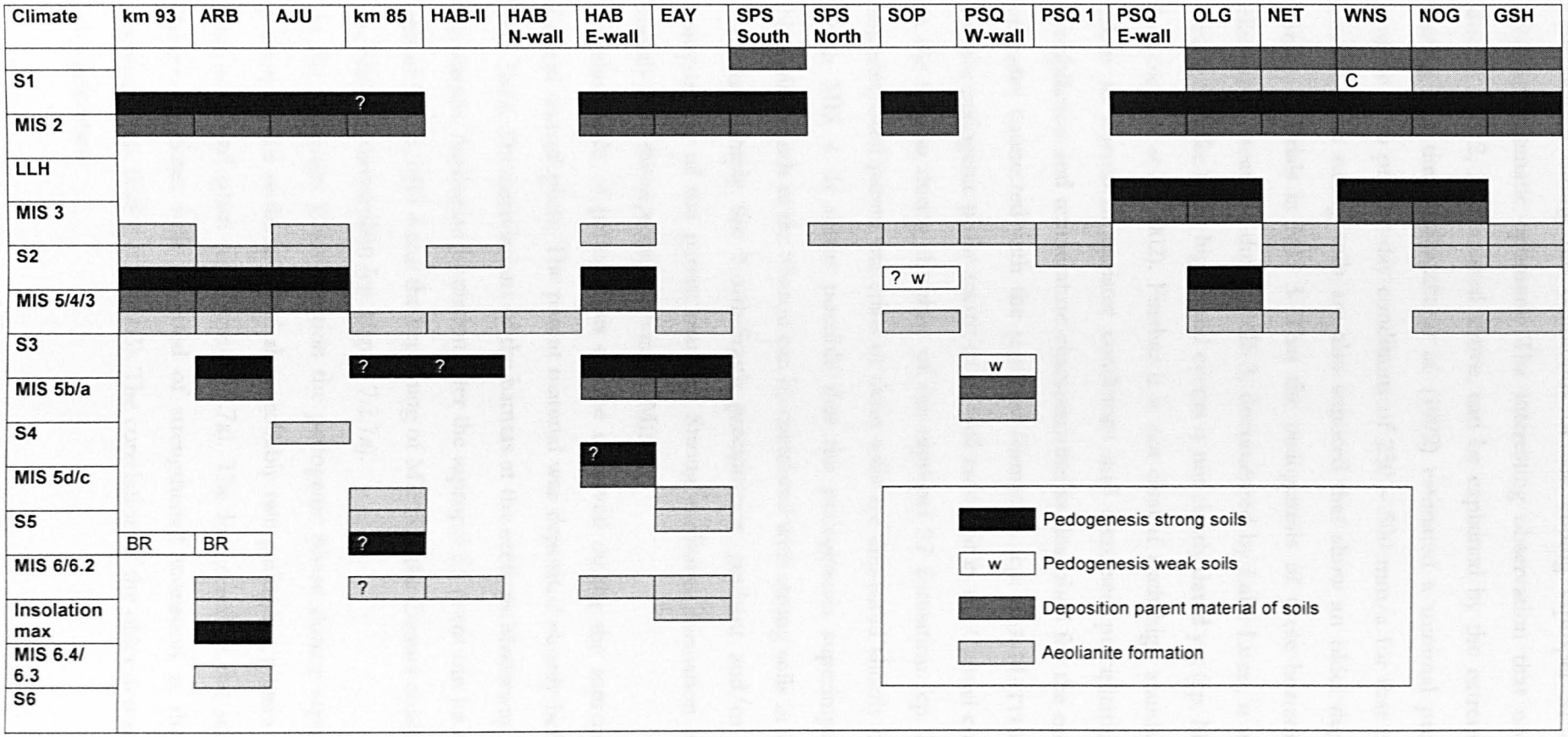

Figure 7.2.7a: Climate-event-stratigraphical model for the correlation of aeolianites and palaeosols in the Carmel and Sharon coastal plain. LLH = Lake Lisan high stands, NOG = North of Gaash, GSH = Gaash Shefayim, C = caliche-like carbonaceous horizon, BR = beach rock.

consolidated during the conditions of the ending sapropel S1 event towards the Holocene climatic optimum. The interesting observation that no aeolianite formed during MIS 2, as discussed above, can be explained by the extremely arid conditions during that time. FRENZEL *et al.* (1992) estimated a minimal precipitation decrease compared to present-day conditions of 250 – 500 mm/a for that time. In the Sharon coastal plain strong soils are also exposed that show an older deposition age of the parent materials in MIS 3. That the pedogenesis of these horizons was initiated by climatic fluctuations during MIS 3, documented by Lake Lisan, is assumed. The exact timing of Lake Lisan high stand events is not clearly dated yet (cp. MACHLUS *et al.* 2000, LANDMANN *et al.* 2002). Further it is not clear if such high stands, which are usually taken to document moister conditions and increased precipitation, have the same precipitation and temperature characteristics as described for the monsoon-like rainfall episodes connected with the sapropel formation (cp. BAR-MATTHEWS *et al.* 2003). A further pedogenic phase seems to be well recorded in the Carmel coastal plain and also in the Sharon during the time of the sapropel S2 formation (cp. Figure 7.2.7a). The superimposed parent materials of these soils are deposited shortly before the S2 event or in MIS 4. It seems possible that the pedogenesis superimposing the so-called Nasholim Sands in the Sharon can be correlated with strong soils in the Carmel, perhaps reflecting simply the North-South precipitation gradient and/or differences in the composition of the parent material. Strong aeolianite formation is also documented shortly after the sapropel S2 event in MIS 3.

Another cycle of pedogenesis can be observed during the sapropel S3 event in the Carmel coastal plain. The parent material was deposited shortly before the event or in MIS 5b/a. The correlations of the hamras at the sections Motorway km 85 and HAB-II are unsure. Aeolianite formation after the sapropel S3 event can be observed during the end of MIS 5, MIS 4 and the beginning of MIS 3 in the Carmel coastal plain as well as in the Sharon coastal plain (cp. Figure 7.2.7a).

At the Habonim E-wall section the pedogenic phase during sapropel S4 also seems present. Older aeolianites and also probably two pedogenic phases are recorded in the Sharon coastal plain (cp. Figure 7.2.7a). The lower soil at the section Atlit Railroad Bridge correlates with a period of strengthened monsoon at the 150 ka insolation maximum (cp. EMEIS *et al.* 2003). The correlation of the older deposits at Motorway km 85 is uncertain.

The above model should not be seen as a final correlation of the deposits in the Carmel and Sharon coastal plain. As the exposures are complex and detailed, further studies concerning the dating of sediments and also of the amplitudes of Eastern Mediterranean climates, will enhance the understanding of the deposits and their correlation to each other and climatic events. Therefore the model can be seen as an initial suggestion of how to correlate the cycles of pedogenesis and aeolianite formation with the rainfall episodes in the area. Its flexible and open form allows one to add information from additional deposits easily or to correlate differently according to other chronological and geological information.

CONCLUSION

The data obtained in this study add to the geochronological information on aeolianites and palaeosols in the Carmel and Sharon coastal plains in Israel. While at the outset of this study sparse geochronological information was available (PORAT and WINTLE 1994, RITTE *et al.* 1997), during the time of the study other datings on late Pleistocene deposits in the Carmel and Sharon coastal plains were added (e.g. RONEN *et al.* 1999, ENGELMANN *et al.* 2001, FRECHEN *et al.* 2001, 2002, 2004). Additionally, intensive pedological and sedimentological studies were carried out by TSATSKIN and RONEN (1999) and NEBER (2002) respectively. Through the above-mentioned studies it was possible to suggest detailed stratigraphical models for the Carmel and Sharon coastal plains based mainly on lithology but assisted by luminescence dating (NEBER 2002, FRECHEN *et al.* 2002, 2004). These models differ from stratigraphies suggested by HOROWITZ (1979), GVIRTZMAN *et al.* (1984, 1998) and GVIRTZMAN and WIEDER (2001) mainly for the Sharon coastal plain. All stratigraphical models suggested are based on the assumption that aeolianite formation and soil development are alternating processes. In early studies the deposition was mainly attributed to sea-level fluctuations during glacial-interglacial cycles (cp. Chapter 1.4). In this study it is also suggested that aeolianite formation and pedogenesis of strongly developed soils are alternating, but that they correspond to Eastern Mediterranean climate events such as episodes of enhanced rainfall in the area. The chronologies of the deposits were investigated with luminescence dating.

Geochronological results

The ages of the sections dated in this study showed that deposition of the horizons took place mainly during the last glacial – interglacial cycle and also during the Holocene. From the dating it can be confirmed that the so-called kurkar ridges are composed of polycyclic deposits as suggested by FARRAND and RONEN (1974) or NEBER (2002).

The dated East – West transects over the kurkar ridges at the sections Habonim Quarry – Dor-Habonim Nature Reserve Middle Ridge – Dor-Habonim Nature Reserve Coast, Hadera Power Station Quarry – South of Power Station – Seashore Power Station and Wadi Netanya South – Netanya South Cliff did not reveal age increases or decreases

(gradients) towards the East or the West as had been suggested by some authors. The ages of the deposits confirm that all ridges are polycyclic, evidencing the deposition of sand most likely in palaeo-dunefields and soil formation during phases of lower or ceased accumulation.

The synopsis of the data from this study with the data from other luminescence dating studies on these deposits reveal clearly that in the Carmel coastal plain older deposits are exposed than in the Sharon (cp. Figure 7.2.5a). In the Carmel the oldest sediments are dated along the Tel Aviv – Haifa motorway at the section Atlit Railroad Bridge, which were deposited during MIS 6 (cp. FRECHEN *et al.* 2004), while in the Sharon the oldest sediments dated are exposed at the section Power Station Quarry West-wall and deposited during MIS 5. Whether these differences are connected with uplift in the Carmel in contrast to the Sharon is not certain. Through the synopsis it is also clear, that there is no aeolianite formation during MIS 2 at the investigated longitudes, and this is most likely connected with the extreme arid and also colder conditions during that time. Whether the distance to the sediment source and the lower sea level during the time of the LGM played a role in the cause for the missing aeolianites is not clear. It is also uncertain whether MIS 2 aeolianites can be found in offshore successions. Overall the data obtained in this study fitted well with the established ages of other studies in the Carmel coastal plain (FRECHEN *et al.* 2004) and in the Sharon (PORAT and WINTLE 1994, RITTE *et al.* 1997, ENGELMANN *et al.* 2001 and FRECHEN *et al.* 2001, 2002).

The ages calculated for sections at the Hadera Power Station Quarry and also more western sections in the vicinity of the Power Station at Hadera showed that the deposits revealed a transition from the older deposits in the Carmel coastal plain to the younger deposits in the Sharon (cp. Figure 7.2.5). The upper part of the pedocomplex at the section Hadera Power Station East-wall can be considered as Epi-Palaeolithic hamra *sensu* RONEN (1983) with deposition ages during MIS 2 and soil development during the sapropel S1 conditions. Apart from older deposits exposed in the Carmel compared to the Sharon, there is also a difference in the development of soils observable between the two coastal plains. In the Sharon coastal plain there are in addition to hamras also weak soils (regosols/arenosols), while in the Carmel coastal plain strong soils are prominent.

Apart from the differences or joint characteristics of the Carmel and Sharon coastal plains it was possible through the obtained luminescence ages of this study and also the luminescence ages of other studies carried out in the Carmel and Sharon coastal plains,

to compare the deposition ages of aeolianites and palaeosols with Eastern Mediterranean climates during the Penultimate Glacial and the last glacial-interglacial cycle. The Eastern Mediterranean climate during this period is well documented through isotopic and sedimentological studies of marine cores and also speleothems of two caves in Israel (e.g. KALLEL *et al.* 2000, LARRASOAÑA *et al.* 2003, BAR-MATTHEWS *et al.* 2003) and is strongly structured by episodes with enhanced rainfall and phases with much less precipitation. The episodes with enhanced rainfall cause the formation of sapropels in the Mediterranean and appear in interglacial periods (sapropels S5, S4, S3, S1) but also during glacial times (S6, S2). But these rainfall episodes do not always cause sapropel formation; this is documented by the precipitation episode at about 150 ka BP during MIS 6 (EMEIS *et al.* 2003). During the end of MIS 3 and the transition to MIS 2 Lake Lisan (Dead Sea predessesor) high stands are reported which point also towards humid climatic phases (cp. LANDMANN *et al.* 2002).

The comparison of the deposition ages of the aeolianites and the palaeosols with the climatic events in the Eastern Mediterranean (marine cores) and Israel in particular (speleothems from the Soreq and Pequiin caves) seem to suggest that both the deposition of aeolianites and parent materials of soils, as well as the pedogenesis of the soils, are connected with the cyclicity of recurring enhanced rainfall. The rainfall episodes are characterised by sudden rises in precipitation connected with precession minima and increases in monsoon strength; during the event the amounts of precipitation decrease, while temperatures increase, leading towards arid conditions at the end. At the beginning the increased precipitation during such events leads to a higher run-off and the supply of nutrients to the sea, which increases bioactivity. The sediment discharge of the river Nile also increases with the monsoon strength through higher precipitation and run-off from the Ethiopian plateau.

According to the luminescence data aeolianite formation took place closely after or at the end of enhanced rainfall episodes, but also generally between two such episodes. At the end of enhanced rainfall episodes aeolianite formation is most probable as high amounts of sediment are available and increasing arid climate conditions further sand accumulation, but also increased amounts of carbonate are available through increased bioactivity, which is necessary for the carbonaceous consolidation of the dunes. Initially high accumulation rates probably adjust according to supply of sediment. At the end of periods in between rainfall episodes sand accumulation rates are most likely low. With the sudden onset of the next episode of enhanced precipitation, accumulation probably

fully ceases and pedogenesis takes place forming the strong soils observed between aeolianites in the Carmel and the Sharon coastal plains. The soil development continues until the climatic conditions again become drier and a new phase of strong sediment accumulation commences (cp. Figure 7.2.6a).

It was possible to correlate the deposits of the sites dated in this study and also the sections in the Carmel and Sharon coastal plains dated by others, with the above outlined model of aeolianite formation, parent material sedimentation and soil pedogenesis. The horizons of the different sites were correlated according to the luminescence ages and the above-presented model. A new climate-event stratigraphical model for the correlation of the aeolianite and palaeosol deposits in the Carmel and Sharon coastal plains is suggested, in which at least four pedogenic phases can be correlated with episodes of enhanced rainfall in the area (cp. Chapter 7.2.7).

Limitations

The limitations of the study are already evident in the choice of the sampling points. It was only possible to sample on-shore aeolianite and soil successions and the sampling of East-West transects was limited. Also it must be noted that most of the samples dated in other studies are either from sections from the main ridge along the motorway in the Carmel coastal plain (cp. FRECHEN et al. 2004) or from the coastal cliff in the Sharon coastal plain (cp. PORAT and WINTLE 1994, RITTE *et al.* 1997, ENGELMANN *et al.* 2001, FRECHEN *et al.* 2001, 2002), so that in a comparison with these data the longitudinal situation along the coastal plains is reflected. It is not clear if deposits of aeolianites several kilometres offshore seen in seismic profiles and also known offshore from drillings (e.g. PORAT *et al.* 2003) would contain additional information.

Methodically, certain aspects like the somewhat higher IR-OSL equivalent doses compared to the TL equivalent doses could not be explained satisfactoryly. Also radioactive disequilibria are uncertain. Fading ratios could be higher in individual samples than in the tested ones and overall the tests carried out can only be spot checks. A major factor in the age calculation is the palaeowater content, which is specifically difficult to estimate in Mediterranean climates with strong precipitation seasonalities between winters and summers and also alternating with the monsoon strength. Also the internal potassium contents could not be determined and the theoretical value by HUNTLEY and BARIL (1997) was used for the age calculations. Further, cosmic dose

rates can only be coarsely assessed in sections with large hiatuses of 30 to 50 ka and unknown erosion rates.

Chronologically the relatively large errors of the age estimates do not allow correlation exactly and certain horizons could not be distinguished from others by the obtained luminescence ages.

Future research

Future research could therefore entail the sampling of off-shore aeolianite deposits in transects with on-shore deposits, to establish whether off-shore successions are similarly composed and show comparable ages to on-shore deposits and also to find out whether MIS 2 aeolianites exist further West.

At the coastal cliff in the Sharon different sections apart from the so-called Epi-Palaeolithic hamra also show older horizons with strongly developed soils, but whether in the Sharon older interglacial deposits are exposed and how they would correlate with pedogenic horizons in the Carmel coastal plain and also with interglacial rainfall episodes is uncertain. It could therefore be worth dating sections with multiple hamra, aeolianite and sand successions, as exposed in quarries by Nordiyya. For example, quarry Nordiyya B lies East of Netanya and is reached from the petrol station by Pardessiya Junction over a track that leads to the section (directions from field book entry). From the bottom to the top a hamra, sand, hamra, aeolianite, sand and another hamra are exposed. Quarry Nordiyya A can be reached over road number 57 in the direction of Nordiyya, Ganot and Hader and lies shortly before Netanya is reached in the so-called second ridge (directions from field book entry). The succession of deposits consists of an aeolianite, a hamra, sand and another hamra. At other places with a different succession of deposits perhaps a further hamra is exposed.

A key for the understanding of the deposition and development history of pedocomplexes and multiphased soils is pedo-micromorphology. It could therefore be helpful if further soils were investigated by this method.

Deposits of key sections could be dated with the method introduced by VOGEL *et al.* (1999) which overcomes changes in the environmental dose rate caused by disequilibria or varying moisture content (cp. Chapter 4.13.5). The method could be particularly useful for dating the strongly lithified aeolianites of the Carmel coastal plain where disequilibria cannot be excluded. Also the method seems generally suited to date

deposits from a strongly precipitation seasonal environment. The precise internal dose rate determination required for this approach could be carried out with the methods advanced by DÜTSCH and KRBETSCHEK (1997) (cp. Chapter 4.13.1). Further methods for comparison could be the SAR protocol applied to quartz (MURRAY and WINTLE 2000) or to K-feldspar (WALLINGA 2000a).

REFERENCES

ADLER, A. (1934) Zur Morphologie der Küste von Palästina. Inaugural-Dissertation zur Erlangung der Doktorwürde der Hohen Mathematisch-Naturwissenschaftlichen Fakultät der Thüringischen Landesuniversität Jena, G. U. Koenig, Erfurt, pp.70. (PhD thesis, published)

AITKEN, M. J. (1985) Thermoluminescence dating. Academic Press, London, pp. 359.

AITKEN, M. J. (1992) Optical dating. *Quaternary Science Reviews*, 11: 127-131.

AITKEN, M. J. (1994) Optical dating: A non-specialist review. *Quaternary Geochronology (Quaternary Science Reviews)*, 13: 503-508.

AITKEN, M. J. (1998) An Introduction to Optical Dating. The Dating of Quaternary Sediments by the Use of Photon-stimulated Luminescence. Oxford University Press, Oxford, pp. 267.

AITKEN, M. J., TITE, M. S. and REID, J. (1964) Thermoluminescent dating of ancient ceramics. *Nature*, 202: 1032-1033, In: AITKEN, M. J. (1985) Thermoluminescence dating. Academic Press, London, pp. 359.

AITKEN, M. J., ZIMMERMAN, D. W. and FLEMING, S. J. (1968) Thermoluminescent dating of ancient pottery. *Nature*, 219: 442-444, In: AITKEN, M. J. (1985) Thermoluminescence dating. Academic Press, London, pp. 359.

AKTAS, A. and FRECHEN, M. (1991) Mittel- bis Jungpleistozäne Sedimente der Hochterrassen in der nördlichen Iller-Lech-Platte. *Geologisches Institut der Universität zu Köln, Sonderveröffentlichungen*, 82: 19-41.

ANDRUSCHKEWITCH, I. (1996) Zur Entwicklung und Verbreitung tonangereicherter und pseudovergleyter (Hamra and Nazaz) Böden der israelischen Küstenebene. Diplomarbeit (Unpublished MSc thesis), Universität Stuttgart, pp. 101.

AVNIMELECH, M. (1962) The main trends in the Pleistocene-Holocene history of the Israelian Coastal Plain. *Quaternaria*, 6: 479-495.

BARAY, M. M. and ZÖLLER, L. (1994) Methodological aspects of thermoluminescence dating of Late Glacial and Holocene dune sands from Brandenburg, Germany. *Quaternary Geochronology (Quaternary Science Reviews)*, 13: 477-480.

BAR-MATTHEWS, M., AYALON, A., MATTHEWS, A., HALICZ, L. and SASS, E. (1993) The Soreq Cave speleothems as indicators of paleoclimate variations Geological. *Survey of Israel Current Research*, 8: 1-3.

BAR-MATTHEWS, M., AYALON, A. and KAUFMAN, A. (1997) Late Quaternary paleoclimate in the eastern Mediterranean region from stable isotope analysis of speleothems at Soreq Cave, Israel. *Quaternary Research*, 47: 155-168.

BAR-MATTHEWS, M., AYALON, A., KAUFMANN, A. und WASSERBURG, G. J. (1999) The eastern Mediterranean palaeoclimate as a reflection of regional events: Soreq cave, Israel. *Earth and Planetary Science Letters*, 166: 85-95.

BAR-MATTHEWS, M., AYALON, A. and KAUFMAN, A. (2000) Timing and hydrological conditions of Sapropel events in the Eastern Mediterranean, as evident from speleothems, Soreq cave, Israel. *Chemical Geology*, 169: 145-156.

BAR-MATTHEWS, M., AYALON, A., GILMOUR, M., MATTHEWS, A. and HAWKESWORTH, C. J. (2003) Sea-land oxygen isotopic relationships from planktonic foraminifera and speleothems in the Eastern Mediterranean region and their implication for palaeorainfall during interglacial intervals. *Geochimica et Cosmochimica Acta*, 67: 3181-3199.

BARTOV, J. (1974) A structural and palaeogeographic study of the Central Sinai faults and domes. Unpublished Ph.D. dissertation, Department of Geology, Hebrew University, Jerusalem (in Hebrew, English summary). In: HOROWITZ, A. (1979) The Quaternary of Israel. Academic Press, London, pp. 394.

BEER, J., MUSCHELER, R., WAGNER, G., LAJ, C., KISSEL, C., KUBIK, P. W. and SYNAL, H. A. (2002) Cosmogenic nuclides during Isotope Stages 2 and 3. *Quaternary Science Reviews*, 21: 1129-1139.

BELKNAP, D. F. and MART, Y. (1999) Sea-level lowstand in the Eastern Mediterranean: Late Pleistocene coastal terraces offshore Northern Israel. *Journal of Coastal Research*, 15: 399-412.

BELL, C. M. (1991) The relationships between sedimentary structures, transport directions and dune types in Mesozoic aeolian sandstones, Atacama Region, Chile. *Sedimentology*, 38: 289-300.

BENTOR, Y. K. and VROMAN, A. J. (1951) The geological map of Israel, 1:100,000, Sheet 18, Avdat. Jerusalem, Geological Survey Israel. In: HOROWITZ, A. (1979) The Quaternary of Israel. Academic Press, London, pp. 1-394

BODET, F. and SCHÄRER, U. (2001) Pb isotope systematics and time-integrated Th/U of SE-Asian continental crust recorded by single K-feldspar grains in large rivers. *Chemical Geology*, 177: 265-285.

BOENIGK, W., BRUNNACKER, K., TILLMANNS, W. and RONEN, A. (1985) Die Äolianite in der nördlichen Küstenzone von Israel. Genese, Stratigraphie und Klimageschichte. *Quartär*, 35/36: 113-140.

BORUCKI, H., GRÖTSCH, E. and WENZEL, B. (eds) (1974) Lexikon der Physik. Bibliographisches Institut, Mannheim, pp. 490.

BØTTER-JENSEN, L. (1997) Luminescence techniques: Instrumentation and methods. *Radiation Measurements*, 27: 749-768.

BØTTER-JENSEN, L. and MEJDAHL, V. (1985) Determination of potassium in feldspars by beta counting using a GM multicounter system. *Nuclear Tracks*, 10: 663-666.

BØTTER-JENSEN, L. and MEJDAHL, V. (1988) Assessment of beta dose-rate using a GM multicounter system. *Nuclear Tracks and Radiation Measurements*, 14: 187-191.

BRADLEY, R. S. (1999) Palaeoclimatology. Reconstructing Climates of the Quaternary. Harcourt Academic Press, London, pp. 613.

BROOKE, B. (2001) The distribution of carbonate aeolianite. *Earth-Science Reviews*, 55: 135-164.

BRUNNACKER, K., RONEN, A. and TILLMANNS, W. (1982) Die jungpleistozänen Äolianite in der südlichen Küstenzone von Israel. Ein Beitrag zur zeitlich-räumlichen Klimaentwicklung. *Eiszeitalter und Gegenwart*, 32: 23-48.

CARMEL, Z., INMAN, D. L. and GOLIK, A. (1984) Transport of Nile sand along the southeastern Mediterranean coast. *Coastal Engineering*, 19: 1282-1290.

CERLING, T. E. and QUADE, J. (1993) Stable carbon and oxygen isotopes in soil carbonates. In: SWART, P. K., LOHMANN, K. C., MCKENZIE, J. and SAVIN, S. (eds.) Climate change in continental isotopic records, American Geophysical Union, Washington DC, pp. 217-231.

CLEMENS, S. C. and PRELL, W. L. (2003) A 350,000 year summer-monsoon multi-proxy stack from the Owen Ridge, Northern Arabian Sea. *Marine Geology*, 201: 35-51.

CE (2003) Columbia Encyclopedia. (Online) (cited 17 January 2004) URL: http://www.encyclopedia.com

DAN, J. and YAALON, D. H. (1971) On the origin and nature of the paleopedological formations in the coastal desert fringe areas of Israel. In: YAALON, D. H. (ed.) *Paleopedology-Origin, Nature and Dating of Paleosols*. International Society of Soil Science and Israel University Press, Jerusalem, pp. 245-260.

DAN, J. and KOYUMDJISKI, H. (1979) *The classification of Israel soils*. Institute of Soils and Water, Special Publication No. 137, Division of Scientific Publications, The Volcani Center, Bet Dagan, Israel (in Hebrew, English summary 9 p.).

DAN, J., YAALON, D. H. and KOYUMDJISKI, H. (1968) Catenary relationships in Israel, 1. The Netanya catena on coastal dunes of the Sharon. *Geoderma*, 2: 95-120.

DANIELS, F., BOYD, C. A. and SAUNDERS, D. F. (1953) Thermoluminescence as a research tool. *Science*, 117: 343-349.

DARWIN, C. R. (1851) Geological observations on coral reefs, volcanic islands and on South America, being the geology of the voyage of the Beagle, under the command of Captain Fitzroy during the years 1832 to 1836. Smith, Elder and Company, London. In: BROOKE, B. (2001) The distribution of carbonate eolianite. *Earth-Science Reviews*, 55: 135-164.

DAYBREAK NUCLEAR (2004) Radioluminescence measurements. (Online) (cited 1 January 2004) URL: http://www.daybreaknuclear.com/radioluminescence.html

DÜTSCH, C. and KRBETSCHEK, M. R. (1997) New methods for a better internal ^{40}K dose rate determination. *Radiation Measurements*, 27: 377-381.

DULLER, G. A. T. (1991) Equivalent dose determination using single aliquots. *Nuclear Tracks and Radiation Measurements*, 18: 371-378.

DULLER, G. A. T. (1994) Luminescence dating of sediments using single aliquots: New procedures. *Quaternary Geochronology (Quaternary Science Reviews)*, 13: 149-156.

DULLER, G. A. T. (1995) Luminescence dating using single aliquots: Methods and applications. *Radiation Measurements*, 24: 217-226.

DULLER, G. A. T. (1997) Behavioural studies of stimulated luminescence from feldspars. *Radiation Measurements*, 27: 663-694.

DUPLESSY, J.-C., LALOU, C. and VINOT, A. C. (1970) Differential isotopic fractionation in benthic foraminifera and palaeotemperatures re-assessed. *Science*, 168: 250-251.

DUPLESSY, J.-C., LABEYRIE, J., LALOU, C. and NGUYEN, H. V. (1971) La mésure des variations climatique continentales : application a la période comprise entre 130 000 et 90000 ans BP. *Quaternary Research*, 1 : 162-174.

DURRANCE, E. M. (1986) Radioactivity in geology: Principles and applications. Ellis Horwood Series in Geology, Chichester, 441 pp.

DÜTSCH, C. and KRBETSCHEK, M. R. (1997) New methods for a better internal ^{40}K dose rate determination. *Radiation Measurements*, 27: 377-381.

EB (1997) Encyclopaedia Britannica. Encyclopaedia Britannica Inc., CD97 Version1.1.

EMEIS, K.-C., SCHULZ, H.-M., STRUCK, U., SAKAMOTO, T., DOOSE, H., ERLENKEUSER, H., HOWELL, M., KROON, D. and PATERNE, M. (1998) Stable isotope and temperature records of sapropels from ODP sites 964 and 967: Constraining the physical environment of sapropel formation in the eastern Mediterranean Sea. In: ROBERTSON, A. *et al.* (eds.) *Proceedings of the Ocean Drilling Program*, ODP 160, pp. 309-331.

EMEIS, K.-C., STRUCK, U., SCHULZ, H.-M., ROSENBERG, R., BERNASCONI, ST., ERLENKEUSER, H., SAKAMOTO, T. and MARTINEZ-RUIZ, F. (2000a) Temperature and salinity variations of Mediterranean Sea surface waters over the last 16,000 years from records of planktonic stable oxygen isotopes and alkenone unsaturation ratios. *Palaeogeography, Palaeoclimatology, Palaeoecology*, 158: 259-280.

EMEIS, K.-C., SAKAMOTO, T., WEHAUSEN, R. and BRUMSACK, H.-J. (2000b) The sapropel record of the eastern Mediterranean Sea – results of Ocean Drilling Program Leg 160. *Palaeogeography, Palaeoclimatology, Palaeoecology*, 158: 371-395.

EMEIS, K.-C., SCHULZ, H., STRUCK, U., ROSSIGNOL-STRICK, M., ERLENKEUSER, H., HOWELL, M. W., KROON, D., MACKENSEN, A., ISHIZUKA, S., OBA, T., SAKAMOTO, T. and KOIZUMI, I. (2003) Eastern Mediterranean surface water temperatures and δ^{18}O composition during deposition of sapropels in the late Quaternary. *Paleoceanography*, 18 (1): 1005, doi: 10.1029/2000PA000617.

EMERY, K. O. and NEEV, D. (1960) Mediterranean beaches of Israel. *Geological Survey of Israel Bulletin*, 26: 1-23.

EMILIANI, C. (1972) Quaternary palaeotemperatures and the duration of high temperature intervals. *Science*, 178: 398-401.

ENGELMANN, A. (1997) Kombinierte Lumineszenz-Datierungen an äolischen und kolluvialen Sedimenten aus Saint Sauflieu (Picardie, Nord-Frankreich), Diplom-Arbeit (Master thesis), Geological Institute, University of Cologne, pp. 123.

ENGELMANN, A., FRECHEN, M. and ANTOINE, P. (1999) Chronostratigraphie frühweichselzeitlicher kolluvialer Sedimente von Bettencourt-Saint-Ouen (Nord-Frankreich). In: BECKER-HAUMANN, R and FRECHEN, M (eds). *Terrestrische Quartärgeologie*. Logabook, Köln, pp. 12-22.

ENGELMANN, A., NEBER, A., FRECHEN, M., BOENIGK, W. and RONEN, A. (2001) Luminescence chronology of Upper Pleistocene and Holocene aeolianites from Netanya South – Sharon Coastal Plain, Israel. *Quaternary Science Reviews*, 20: 799-804.

ERFURT, G. (2003a) Radiolumineszenzspektroskopie und –dosimetrie an Feldspäten und synthetischen Luminophoren für die geochronometrische Anwendung. Fakultät für Chemie und Physik, Technische Universität Bergakademie Freiberg, Gemany, pp. 129, (PhD thesis).

ERFURT, G. (2003b) Infrared luminescence of Pb^+ centres in potassium-rich feldspars. Physica Status Solidi, 200: 429-438.

ERFURT, G. and KRBETSCHEK, M. R. (2003a) IRSAR – A single-aliquot regenerative-dose dating protocol applied to the infrared radiofluorescence (IR-RF) of coarse-grain K-feldspar. *Ancient TL*, 21 (1): 35-42.

ERFURT, G. and KRBETSCHEK, M. R. (2003b) Studies on the physics of the infrared radioluminescence of potassium feldspar and on the methodology of its application to sediment dating. *Radiation Measurements*, 37: 505-510.

ERFURT, G., KRBETSCHEK, M. R., BORTOLOT, V. J. and PREUSSER, F. (2003) A fully automated multi-spectral radioluminescence reading system for geochronometry and dosimetry. *Nuclear Instruments and Methods in Physics Research B*, 207: 487-499.

EUROPEAN COMMUNITIES JOINT RESEARCH CENTRE (1999) The Radioactive decay of the nuclide ^{60}Co. (Online) (cited 28 Jul 2003) URL: http://www.nuclides.net/NUCLIDES_2000/co-60.htm

EYTAM, Y. and BEN-AVRAHAM, Z. (1992) Morphology and sediments of the inner shelf off northern Israel. *Israel Journal of Earth Science*, 41: 27-44.

FARRAND, W. R. and RONEN, A. (1974) Observations on the Kurkar-Hamra succession on the Carmel Coastal Plain. *Tel Aviv*, 1: 45-54.

FITZPATRICK, E. A. (1980) Soils, their formation, classification and distribution. Longman, London, pp. 353.

FOLZ, E. and MERCIER, N. (1999a) Use of a new procedure to determine paleodose in the OSL dating of quartz: The MARA protocol. *Quaternary Science Reviews*, 18: 859-864.

FOLZ, E. and MERCIER, N. (1999b) A single-aliquot OSL protocol using bracketing regenerative doses to accurately determine equivalent doses in quartz. *Radiation Measurements*, 30: 477-485.

FONTUGNE, M. and CALVERT, S. E. (1992) Late Pleistocene variability of the carbon isotopic composition of organic matter in the Eastern Mediterranean: Monitor of changes in carbon sources and atmosphere CO_2 concentrations. *Paleoceanography*, 7: 1-20.

FRECHEN, M. (1991) Thermolumineszenz-Datierungen an Lössen des Mittelrhein-Gebietes. *Sonderveröffentlichungen Geologisches Institut der Universität zu Köln*, 79: 1-137.

FRECHEN, M. (1992) Systematic thermoluminescence dating of two loess profiles from the Middle Rhine area (F. R. G.). *Quaternary Science Reviews*, 11: 93-101.

FRECHEN, M. (1994) Thermolumineszenz-Datierungen an Lössen des Tönchesberges aus der Osteifel. *Eiszeitalter und Gegenwart*, 44: 79-93.

FRECHEN, M. (1999a) Upper Pleistocene loess stratigraphy in Southern Germany. *Quaternary Geochronology*, 18: 243-269.

FRECHEN, M. (1999b) Luminescence dating of loessic sediments from the Loess plateau, China. *Geologische Rundschau*, 87: 675-684.

FRECHEN, M. and PREUSSER, F. (1996) Kombinierte Lumineszenz-Datierungen am Beispiel des Lößprofils Mainz-Weisenau. *Frankfurter Geowissenschaftliche Arbeiten*, 20: 53-66.

FRECHEN, M. and DODONOV, A. E. (1998) Loess chronology of the Middle and Upper Pleistocene in Tadjikistan. *Geologische Rundschau*, 87: 2-20.

FRECHEN, M. and YAMSKIKH, A. F. (1999) Upper Pleistocene loess stratigraphy in the southern Yenisei Siberia area. *Journal of the Geological Society London*, 156: 515-525.

FRECHEN, M., BOENIGK, W. and WEIDENFELLER, M. (1995) Chronostratigraphie des „Eiszeitlichen Lößprofils" in Koblenz-Metternich. *Mainzer geowissenschaftliche Mitteilungen*, 24: 155-180.

FRECHEN, M., HORVÁTH, E. and GÁBRIS, G. (1997) Geochronology of Middle and Upper Pleistocene loess sections in Hungary. *Quaternary Research*, 48: 291-312.

FRECHEN, M., ZANDER, A., CÍLEK, V. and LOŽEK, V. (1999) Loess chronology of the Last Interglacial/Glacial cycle in Bohemia and Moravia, Czech Republic. *Quaternary Science Reviews*, 18: 1467-1493.

FRECHEN, M., DERMANN, B., BOENIGK, W. and RONEN, A. (2001) Luminescence chronology of aeolianites from the section at Givat Olga – coastal plain of Israel. *Quaternary Science Reviews*, 20: 805-809.

FRECHEN, M., NEBER, A., DERMANN, B., TSATSKIN, A., BOENIGK, W. and RONEN, A. (2002) Chronostratigraphy of aeolianites from the Sharon Coastal Plain of Israel. *Quaternary International*, 89: 31-44.

FRECHEN, M., NEBER, A., TSATSKIN, A., BOENIGK, W. and RONEN, A. (2004) Chronology of Pleistocene sedimentary cycles in the Carmel coastal plain of Israel. *Quaternary International*, 121: 41-52.

FRENZEL, B., PÉCSI, M. and VELICHKO, A. A. (1992) Atlas of paleoclimates and paleoenvironments of the northern hemisphere, Late Pleistocene – Holocene. Geographical Research Institute, Hungarian Academy of Science, Budapest and Gustav Fischer Verlag, Stuttgart, pp. 153.

FREUND, R. and ZAK, I. (1973) Migration of folding and faulting along geological structures. Teva Ve'aretz, 16: 264-270 (in Hebrew). In: HOROWITZ, A. (1979) The Quaternary of Israel. Academic Press, London, pp. 394.

FREUND, R., GOLDBERG, M., WEISSBROD, T., DRUCKMAN, Y. and DERIN, B. (1975) The Triassic-Jurassic structure of Israel and its relation to the origin of the Eastern Mediterranean. *Bulletin Geological Survey Israel*, 65: 1-26. In: HOROWITZ, A. (1979) The Quaternary of Israel. Academic Press, London, pp. 1-394

FRIEDMAN, G. M. (1964) Early diagenesis and lithification in carbonate sediments. *Journal of Sedimentary Petrology*, 34: 777-813.

FRIHY, O. E. (1994) Discrimination of accreted and eroded coasts using heavy mineral compositions of the Nile Delta beach sands, Egypt. *Sedimentology*, 41: 905-912.

GALILI, E. and SHARVIT, J. (1998) Ancient coastal installations and the tectonic stability of the Israeli coast in historical times. In: STEWART, I. S. and VITA-FINZI, C. (eds) *Coastal Tectonics*. Geological Society, London, Geological Society Special Publications, Volume 146, pp. 147-163.

GALILI, E., WEINSTEIN-EVRON, M. and RONEN, A. (1988) Holocene sea-level changes based on submerged archaeological sites off the Northern Carmel Coast in Israel. *Quaternary Research*, 29: 36-42.

GALILI, E., WEINSTEIN-EVRON, M., HERSHKOVITZ, I., GOPHER, A., KISLEV, M., LERNAU, O., KOLSKA-HORWITZ, L. and LERNAU, H. (1993) Atlit-Yam: A prehistoric site on the sea floor off the Israeli coast. *Journal of Field Archaeology*, 20: 133-157.

GALLOWAY, R. B. (1996) Equivalent dose determination using only one sample: Alternative analysis of data obtained from infrared stimulation of feldspars. *Radiation Measurements*, 26: 103-106.

GAMMEL, B. M. (1997) Nuclides. (Online) (cited 17 January 2004) URL: http://www1.muenchen.de/~gammel/matpack/html/Nuclear/Nuclids

GARFUNKEL, Z. and HOROWITZ, A. (1966) The Upper Tertiary and Quaternary morphology of the Negev, Israel. Israel Journal of Earth Science, 15: 101-117. In: HOROWITZ, A. (1979) The Quaternary of Israel. Academic Press, London, pp. 394.

GODFREY-SMITH, D. I., HUNTLEY, D. J. and CHEN, W. H. (1988) Optical dating studies of quartz and feldspar sediment extracts. *Quaternary Science Reviews*, 7: 373-380.

GÖKSU, H. Y., FREMLIN, J. H., IRWIN, H. T. and FRYXELL, R. (1974) Age determination of burnt flint by a thermoluminescent method. *Science*, 183: 651-654.

GOLDBERG, P. (1986) Late Quaternary environmental history of the Southern Levant. *Geoarchaeology: An International Journal*, 1: 225-244.

GOLDSMITH, V. and GOLIK, A. (1980) Sediment transport model of the southeastern Mediterranean coast. *Marine Geology*, 37: 147-175.

GOLIK, A. (1992) Sand balance along the southeastern Mediterranean coastline – Review. *MBSS Newsletter*, 14, 99-102.

GOLIK, A. (1993) Indirect evidence for sediment transport on the continental shelf of Israel. *Geo-Marine Letters*, 13: 159-164.

GOLIK, A. (1997) Dynamics and management of sand along the Israeli coastline. *Bulletin de l'Institut océanographique, Monaco*, 18: 97-110.

GOODALL, T. M. and AL-BELUSHI, J. D. (1998) A glossary of Arabic desert terminology used in southeastern Arabia. In: ALSHARHAN, A. S., GLENNIE, K. W., WHITTLE, G. L. and KENDALL, C. G. ST. C. (eds) *Quaternary deserts and climatic change*., Balkema, Rotterdam, pp. 611-619.

GORING-MORRIS, A. N. and GOLDBERG, P. (1990) Late Quaternary dune incursions in the southern Levant: Archaeology, chronology and palaeoenvironments. *Quaternary International*, 5: 115-137.

GRÖGLER, N., HOUTERMANS, F. G. and STAUFFER, H. (1960) Über die Datierung von Keramik und Ziegel durch Thermolumineszenz. *Helvetica Physica Acta*, 33: 595-596, In: AITKEN, M. J. (1985) Thermoluminescence dating. Academic Press, London, pp. 359.

GUÉRIN, G. and VALLADAS, G. (1980) Thermoluminescence dating of volcanic plagioclases. *Nature*, 286: 697-699.

GVIRTZMAN, G. (1970) The Saqiye Group (Late Eocene to Early Pleistocene) in the coastal plain and Hashefela regions, Israel. Unpublished Ph.D. dissertation, Department of Geology, Hebrew University, Jerusalem (in Hebrew, English summary). In: HOROWITZ, A. (1979) The Quaternary of Israel. Academic Press, London, pp. 394.

GVIRTZMAN, G. and KLANG, A. (1972) A structural and depositional hinge line along the coastal plain of Israel, evidenced by magneto-tellurics. *Bulletin Geological Survey Israel*, 55: 1-18. In: HOROWITZ, A. (1979) The Quaternary of Israel. Academic Press, London, pp. 394.

GVIRTZMAN, G. and WIEDER, M. (2001) Climate of the last 53,000 years in the eastern Mediterranean, based on soil-sequence stratigraphy in the coastal plain of Israel. *Quaternary Science Reviews*, 20: 1827-1849.

GVIRTZMAN, G., SHACHNAI, E., BAKLER, N. and ILANI, S. (1984) Stratigraphy of the Kurkar Group (Quaternary) of the coastal plain of Israel. *Geological Survey of Israel Current Research*, 1983-84: 70-82.

GVIRTZMAN, G., NETSER, M. and KATSAV, E. (1998) Last-Glacial to Holocene kurkar ridges, hamra soils, and dune fields in the coastal belt of central Israel. *Israel Journal of Earth Science*, 47: 29-46.

GVIRTZMAN, G., WIEDER, M. and CARMI, I. (2000) Climate changes during the Late Holocene of the coastal plain of Israel according to Carbon 14 dating of land snails. 17th International Radiocarbon Conference, Judean Hills, Israel, p. 82.

HARVEY, E. N. (1957) A history of luminescence. *Memoirs of the American Philosophical Society*, 44: 1-351, In: AITKEN, M. J. (1998) An Introduction to Optical Dating. The Dating of Quaternary Sediments by the Use of Photon-stimulated Luminescence. Oxford University Press, Oxford, pp. 267.

HOROWITZ, A. (1975) The Pleistocene palaeoenvironments of Israel. In: In: WENDORF, F. and MARKS, A. E. (eds). *Problems in Prehistory: North Africa and the Levant*. SMU Press, Dallas, pp. 207-227.

HOROWITZ, A. (1979) The Quaternary of Israel. Academic Press, London, pp. 1-394.

HUNTLEY, D. J. and CLAGUE, J. J. (1996) Optical dating of tsunami-laid sands. *Quaternary Research*, 46: 127-140.

HUNTLEY, D. J. and BARIL, M. R. (1997) The K content of the K-feldspars being measured in optical dating or in thermoluminescence dating. *Ancient TL*, 15/1: 11-13.

HUNTLEY, D. J. and LAMOTHE, M. (2001) Ubiquity of anomalous fading in K-feldspars and the measurement and correction for it in optical dating. *Canadian Journal of Earth Science*, 38: 1093-1106.

HUNTLEY, D. J., GODFREY-SMITH, D. I. and THEWALT, M. L. W. (1985) Optical dating of sediments. *Nature*, 313: 105-107.

HÜTT, G. and JAEK, I. (1989) Infrared stimulated photoluminescence dating of sediments. *Ancient TL*, 7: 48-51.

HÜTT, G., JAEK, I. and TCHONKA, J. (1988) Optical dating: K-feldspars optical response stimulation spectra. *Quaternary Science Reviews*, 7: 381-386.

IBRAHIM, G. A. M. (1995) Application and comparison of rainfall-runoff models on the Blue Nile basin. The Sultanate of Oman international conference on water resources management in arid countries, 12-16 March, Volume 2, Sultanate of Oman, Muscat, pp. 751-755.

ICHIKAWA, Y. (1965) Dating of ancient ceramics by thermoluminescence. *Bulletin of the Institute of Chemical Research, Kyoto University*, 43: 1-6, In: AITKEN, M. J. (1985) Thermoluminescence dating. Academic Press, London, pp. 359.

ISSAR, A. (1980) Stratigraphy and paleoclimates of the Pleistocene of central and northern Israel. *Palaeogeography, Palaeoclimatology, Palaeoecology*, 29: 261-280.

ISSAR, A., TSOAR, H. and LEVIN, D. (1989) Climatic changes in Israel during historical times and their impact on hydrological, pedological and socio-economic systems. In: LEINEN, M. and SARNTHEIN, M. (eds). *Paleoclimatology and Paleometeorology: Modern and Past Patterns of Global Atmospheric Transport.* Kluwer Academic Publishers, Dordrecht/Netherlands, pp. 525-541.

ITZHAKI, Y. (1955) Outlines of the geology of Shefelat Pleshet (southern coastal plain of Israel). Geological Survey Israel, Jerusalem. In: HOROWITZ, A. (1979) The Quaternary of Israel. Academic Press, London, pp. 394.

ITZHAKI, Y. (1961) Contributions to the study of the Pleistocene in the coastal plain of Israel. Pleistocene shore-lines in the coastal plain of Israel. *Geological Survey of Israel Bulletin*, 32: 1-9.

IVANOVICH, M. (1992) The phenomenon of radioactivity. In: IVANOVICH, M. and HARMON, R. S. (eds). *Uranium-series disequilibrium: Applications to Earth, Marine and Environmental Science.* Clarendon Press, Oxford, pp. 1-33.

IVANOVICH, M. and HARMON, R. S. (1992). Uranium-series disequilibrium: Applications to Earth, Marine and Environmental Science. Clarendon Press, Oxford, p. 910.

IVY-OCHS, S. D. (1996) The dating of rock surfaces using *in situ* produced ^{10}Be, ^{26}Al and ^{36}Cl, with examples from Antarctica and the Swiss Alps. Ph.D. thesis, ETH, Zürich, Diss. ETH No. 11763, pp. 196.

JUVIGNÉ, E. H. and WINTLE, A. G. (1988) A new chronostratigraphy of the late Weichselian loess units in Middle Europe based on thermoluminescence dating. *Eiszeitalter und Gegenwart*, 38: 94-105.

KALLEL, N., PATERNE, M., DUPLESSY, J. C., VERGNAUD-GRAZZINI, C., PUJOL, C., LABEYRIE, L., ARNOLD, M., FONTUGNE, M. and PIERRE, C. (1997) Enhanced rainfall on Mediterranean region during the last sapropel event. *Oceanologica Acta*, 20: 697-712.

KALLEL, N., DUPLESSY, J.-C., LABEYRIE, L., FONTUGNE, M., PATERNE, M. and MONTACER, M. (2000) Mediterranean pluvial periods and sapropel formation over the last 200 000 years. *Palaeogeography, Palaeoclimatology, Palaeoecology*, 157: 45-58.

KARMELI, D., YAALON, D. H. and RAVINA, I. (1968) Dune sand and soil strata in Quaternary sedimentary cycles of the Sharon Coastal Plain. *Israel Journal of Earth Science*, 17: 45-53.

KENNEDY, G. C. and KNOPF, L. (1960) Dating by thermoluminescence. *Archaeology*, 13: 147-148, In: AITKEN, M. J. (1998) An Introduction to Optical Dating. The Dating of Quaternary Sediments by the Use of Photon-stimulated Luminescence. Oxford University Press, Oxford, pp. 267.

KIDRON, G. J. and YAIR, A. (1997) Rainfall – runoff relationship over encrusted dune surfaces, Nizzana, Western Negev, Israel. *Earth Surface Processes and Landforms*, 22: 1169-1184.

KRBETSCHEK, M. R. and TRAUTMANN, T. (2000) A spectral radioluminescence study for dating and dosimetry. *Radiation Measurements*, 32: 853-857.

KRBETSCHEK, M. R., RIESER, U., ZÖLLER, L. and HEINICKE, J. (1994) Radioactive disequilibria in palaeodosimetric dating of sediments. *Radiation Measurements*, 23: 485-489.

KRBETSCHEK, M. R., GÖTZE, J., DIETRICH, A. and TRAUTMANN, T. (1997) Spectral information from minerals relevant for luminescence dating. *Radiation Measurements*, 27: 695-748.

KRBETSCHEK, M. R., TRAUTMANN, T., DIETRICH, A. und STOLZ, W. (2000) Radioluminescence dating of sediments: methodological aspects. *Radiation Measurements*, 32: 493-498.

KUNTZE, H, ROESCHMANN, G. and SCHWERDTFEGER, G. (1994) Bodenkunde. Verlag Eugen Ulmer, Stuttgart, pp. 424.

LANDMANN, G., ABU QUDAIRA, G. M., SHAWABKEH, K., WREDE, V. and KEMPE, S. (2002) Geochemistry of the Lisan and Damya Formations in Jordan, and implications for palaeoclimate. *Quaternary International*, 89: 45-57.

LARRASOAÑA, J. C., ROBERTS, A. P., ROHLING, E. J., WINKELHOFER, M. and WEHAUSEN, R. (2003) Three million years of monsoon variability over the northern Sahara. *Climate Dynamics*, 21: 689-698.

LEMARCHAND, P. and RADI, L. (1997) Israel und Palästina – geopolitischer Atlas. Westermann, Braunschweig, pp. 144.

LI, S.-H. (1991) Removal of the thermally unstable signal in optical dating of K-feldspar. *Ancient TL*, 9: 26-29.

LIETZ, J. and SCHWARZBACH, M. (1971) Quartäre Sedimente auf der Atlantik-Insel Porto Santo (Madeira-Archipel) und ihre paläoklimatische Deutung. *Eiszeitalter und Gegenwart*, 22: 89-109.

LOURENS, L. J., ANTONARAKOU, A., HILGEN, F. J., VAN HOOF, A. A. M., VERGNAUD GRAZZINI, C. and ZACHARIASSE, W. J. (1996) Evaluation of the Plio-Pleistocene astronomical timescale. *Paleoceanography*, 11: 391-413.

LÖWENGART (1928) Zur Geologie der Küstenebene Palästinas. *Correspondenzblatt Mineralogie*, 9B: 498-519.

MACHLUS, M., ENZEL, Y., GOLDSTEIN, S. L., MARCO, S. and STEIN, M. (2000) Reconstucting low levels of Lake Lisan by correlating fan-delta and lacustrine deposits. *Quaternary International*, 73/74: 137-144.

MAGARITZ, M. and GOODFRIEND, G. A. (1987) Movement of desert boundary in the Levant from Latest Pleistocene to Early Holocene. In: BERGER, W. H. and LABEYRIE, L. D. (eds). *Aprupt Climatic Change*. D Reidel Publishing Company, Dortrecht/Netherlands, pp. 173-183.

MART, Y. and PERECMAN, I. (1996) Neotectonic activity in Caesarea, the Mediterranean coast of central Israel. *Tectonophysics*, 254: 139-153.

MARTINSON, D. G., PISIAS, N. G., HAYS, J. D., IMBRIE, J., MOORE, T. C. and SHACKLETON, N. J. (1987) Age dating and the orbital theory of the ice ages: Development of a high-resolution 0 to 300,000-year chronostratigraphy. *Quaternary Research*, 27: 1-29.

MAZESS, R. B. and ZIMMERMAN, D. W. (1966) Pottery dating from thermoluminescence. *Science*, 152: 347-348, In: AITKEN, M. J. (1998) An Introduction to Optical Dating. The Dating of Quaternary Sediments by the Use of Photon-stimulated Luminescence. Oxford University Press, Oxford, pp. 267.

MCGARRY, S., BAR-MATTHEWS, M., MATTHEWS, A., VAKS, A., SCHILMAN, B. and AYALON, A. (2004) Constraints on hydrological and palaeotemperatures variations in the Eastern Mediterranean region in the last 140 ka given by δD values of speleothem fluid inclusions. *Quaternary Science Reviews*, 23: 919-934.

MCNAMARA, K. (1986) The Pinnacles Desert: A geological masterpiece. *Australian Natural History*, 22/1: 12-16.

MCNISH, A. (1936) Geomagnetic coordinates for the entire earth. *Terra Magha*, 41: 37 43.

MEJDAHL, V. (1969) Thermoluminescence dating of ancient Danish ceramics. *Archaeometry*, 11: 99-104, In: AITKEN, M. J. (1985) Thermoluminescence dating. Academic Press, London, pp. 359.

MEJDAHL, V. and BØTTER-JENSEN, L. (1994) Luminescence dating of archaeological materials using a new technique based on single aliquot measurements. *Quaternary Geochronology (Quaternary Science Reviews)*, 13: 551-554.

MERCIER, N. and VALLADAS, H. (1994) Thermoluminescence dates for the Paleolithic Levant. In: BAR-YOSEF, O. and KRA, R. S. (eds). *Late Quaternary Chronology and Paleoclimates of the Eastern Mediterranean by Radiocarbon*. University of Arizona, Tucson, USA, pp. 13-20.

MERCIER, N., VALLADAS, H., JORON, J. L., SCHIEGL, S., BAR-YOSEF, O. and WEINER, S. (1995) Thermoluminescence dating and the problem of geochemical evolution of sediments – a case study: The Mousterian levels at Hayonim. *Israel Journal of Chemistry*, 35: 137-141.

MIMRAN, Y. (1972) The Tayasir Volcanics, a Lower Cretaceous formation in the Shomeron, central Israel. *Bulletin Geological Survey Israel*, 52: 1-9. In: HOROWITZ, A. (1979) The Quaternary of Israel. Academic Press, London, pp. 394.

MOROZOV, G. V. (1968) The relative dating of Quaternary Ukrainian sediments by the thermoluminescence method. 8th International Quaternary Association Congress, Paris, U.S. Geological Survey Library, Washington, D.C., Cat. No. 208M8280, p. 167, In: AITKEN, M. J. (1998) An Introduction to Optical Dating. The Dating of Quaternary Sediments by the Use of Photon-stimulated Luminescence. Oxford University Press, Oxford, pp. 267.

MÜLLER, P. J., KIRST, G., RUHLAND, G., VON STORCH, I. and ROSELL-MELÉ, A. (1998) Calibration of the alkenone palaeotemperature index $U^{k'}_{37}$ based on the core tops from the eastern South Atlantic and the global ocean (60° N – 60° S). *Geochimica Cosmochimica Acta*, 62: 1757-1771.

MUNYIKWA, K. (2000) Cosmic ray contribution to environmental dose rates with varying overburden thickness. *Ancient TL*, 18: 27-34.

MURAT, A. and GOT, H. (2000) Organic carbon variations of the eastern Mediterranean Holocene sapropel: a key for understanding formation processes. *Palaeogeography, Palaeoclimatology, Palaeoecology*, 158: 241-257.

MURRAY, A. S. and ROBERTS, R. G. (1998) Measurement of the equivalent dose in quartz using a regenerative-dose single-aliquot protocol. *Radiation Measurements*, 29: 503-515.

MURRAY, A. S. and MEJDAHL, V. (1999) Comparison of regenerative-dose single aliquot and multiple-aliquot (SARA) protocols using heated quartz from archaeological sites. *Quaternary Science Reviews*, 18: 223-229.

MURRAY, A. S. and WINTLE, A. G. (2000) Luminescence dating of quartz using an improved single-aliquot regenerativ-dose protocol. *Radiation Measurements*, 32: 57 73.

MURRAY, A. S., ROBERTS, R. G. and WINTLE, A. G. (1997) Equivalent dose measurement using a single aliquot of quartz. *Radiation Measurements*, 27: 171 184.

NEBER, A. (2002) Sedimentological properties of Quaternary deposits on the Central coastal plain, Israel. Department of Archaeology, University of Haifa, pp.217 (unpublished Ph.D. thesis).

NEEV, D. (1975) Tectonic evolution of the Middle East and the Levantine Basin (easternmost Mediterranean). *Geology*, 1975: 683-686.

NEEV, D., BAKLER, N., MOSHKOVITZ, S., KAUFMAN, A., MAGARITZ, M. and GOFNA, R. (1973) Recent faulting along the Mediterranean coast of Israel. *Nature*, 245: 254-256.

NEEV, D., BAKLER, N. and EMERY, K. O. (1987) Mediterranean Coasts of Israel and Sinai. Taylor & Francis, New York, Philadelphia, London, pp. 130.

NIR, Y. (1973) Geological history of the recent and subrecent sediments of the Israel Mediterranean shelf and slope, Geological Survey of Israel, unpublished report. In: NIR, Y. (1985) Israel. In : BIRD, E. C. F. and SCHWARTZ, M. L. (eds). *The world's coastline*. Van Nostrand Reinhold Company, New York, pp. 505 511.

NIR, Y. (1985) Israel. In : BIRD, E. C. F. and SCHWARTZ, M. L. (eds). *The world's coastline*. Van Nostrand Reinhold Company, New York, pp. 505 511.

NIR, Y. (in press) The Israel Mediterranean kurkar sandstone cliff and its retreat during the Holocene. *Journal of Coastal Research*, In: STANLEY, D. J., NIR, Y. and GALILI, E. (1998) Clay mineral distributions to interpret Nile cell provenance and dispersal: III. Offshore margin between Nile delta and northern Israel. *Journal of Coastal Research*, 14: 196-217.

NGDC (National Geophysical Data Center) (2004) Cosmic ray shower. (Online) (cited 17 January 2004) URL: http://web.ngdc.noaa.gov/stp/SOLAR/COSMIC_RAYS/shower.gif

NRA (Nature Reserve Authority) (2004) Dor-Habonim (Israel). (Online) (cited 17 January 2004) URL: http://www.rac-spa.org.tn/SPA/Israel/DORHAB.htm

O'NEIL, J. R., CLAYTON, R. N. and MAYEDA, T. K. (1969) Oxygen isotope fractionation of divalent metal carbonates. *Journal of Chemical Physics*, 30: 5547-5558.

OSMOND, J. K. and IVANOVICH, M. (1992) Uranium-series mobilisation and surface hydrology. In: IVANOVICH, M. and HARMON, R. S. (eds). *Uranium series disequilibrium: Applications to Earth, Marine and Environmental Science*. Clarendon Press, Oxford, pp. 259-289.

PERATH, I. and ALMAGOR, G. (2000) The Sharon escarpment (Mediterranean coast, Israel): Stability, dynamics, risks and environmental management. *Journal of Coastal Research*, 16: 225-228.

PICARD, L. and AVNIMELECH, M. (1937) On the geology of the central coastal plain. *The Journal of the Palestine Oriental Society*, 17: 255-298.

PISIAS, N. G., MARTINSON, D. G., MOORE, T. C., SHACKLETON, N. J., PRELL, W., HAYS, J. and BODEN, G. (1984) High resolution stratigraphic correlation of benthic oxygen isotope records spanning the last 300,000 years. *Marine Geology*, 56: 119-136.

PORAT, N. and WINTLE, A. G. (1994) IRSL dating of kurkar and hamra from the Givat Olga Member in the Sharon Coastal Cliff, Israel. In: AMIT, R., ARKIN, Y. and HIRSCH, F. (eds.) *Israel Geological Society Annual Meeting, 28 February - 2 March, Abstracts*, Nof Ginosar, p. 85.

PORAT, N. and RONEN, A. (2002) Luminescence and ESR age determinations of the Lower Palaeolithic site Evron Quarry, Israel. *Advances in ESR Applications*, 18: 123-130.

PORAT, N., HORWITZ, L., ZHOU, L. P., CHAZAN, M., SARAGOSTI, I. and NOY, T. (1996) ESR and luminescence dating of the Paleolithic site at Holon, the coastal plain, Israel. In: AMIT, R., AVIAD, D., HITZOR, Y., FELDMAN, L., SHAMIR, G., SHTIVELMAN, V., VANGOSH, A. and WEINSTEIN-EVRON, M. (eds.) *Israel Geological Society Annual Meeting, 18-21 March, Abstracts*, Eilat, p. 76.

PORAT, N., ZHOU, L. P., CHAZAN, M., NOY, T. and HORWITZ, L. K. (1999) Dating the Lower Paleolithic open-air site of Holon, Israel by luminescence and ESR techniques. *Quaternary Research*, 51: 328-341.

PORAT, N., AVITAL, A., FRECHEN, M. and ALMOGI-LABIN, A. (2003) Chronology of upper Quaternary offshore successions from the southeastern Mediterranean Sea, Israel. *Quaternary Science Reviews*, 22: 1191-1199.

PRESCOTT, J. R. and STEPHAN, L. G. (1982) The contribution of cosmic radiation to the environmental dose for thermoluminescent dating. Latitude, altitude and depth dependences. *PACT*, 6: 17-25.

PRESCOTT, J. R. and HUTTON, J. T. (1994) Cosmic ray contributions to dose rates for luminescence and ESR dating: Large depth and long-term time variations. *Radiation Measurements*, 23: 497-500.

PREUSSER, F. (1999) Lumineszenzdatierung fluviatiler Sedimente; Fallbeispiele aus der Schweiz und Norddeutschland. *Kölner Forum für Geologie und Paläontologie*, 3: 1-62.

PREUSSER, F. and KASPER, H. U. (2001) Comparison of dose rate determination using high-resolution gamma spectrometry and inductively coupled plasma mass spectrometry. *Ancient TL*, 19: 19-23.

RABAN, A. (1983) Submerged prehistoric sites off the Mediterranean coast of Israel. In: MASTERS, P. M. and FLEMMING, N. C. (eds) *Quaternary coastlines and marine archaeology: Towards the prehistory of land bridges and continental shelves*. Academic Press, London, pp. 115-232.

RALPH, E. K. and HAN, M. C. (1966) Dating of pottery by thermoluminescence. *Nature*, 210: 245-247, In: AITKEN, M. J. (1985) Thermoluminescence dating. Academic Press, London, pp. 359.

RHODES, E. J. (1988) Methodological considerations in the optical dating of quartz. *Quaternary Science Reviews*, 7: 395-400.

RIEHL, N. (1971) Einführung in die Lumineszenz. Karl Thiemig, München/Germany, pp.1-350.

RIESER, U., KRBETSCHEK, M. R. and STOLZ, W. (1994) CCD-camera based high sensitivity TL/OSL-spectrometer. *Radiation Measurements*, 23: 523-528.

RITTE, M., PORAT, N. and GVIRTZMAN, G. (1997) Stratigraphy of the coastal cliff of the Sharon: Environments of deposition and luminescence dating. In: SIVAN, D., HATZOR, Y., RON, H., MARCO, S. and EYAL, Y. (eds.) *Israel Geological Society Annual Meeting, 15-17 April, Abstracts*, Kefar Gil'adi, pp. 92-93.

ROHLING, E. J. (1994) Review and new aspects concerning the formation of eastern Mediterranean sapropels. *Marine Geology*, 122: 1-28.

RONEN, A. (1975a) Réflexions sur l'origine, la genèse et la chronologie des grès dunaires calcifiés dits « première » et « deuxième » chaînes côtières sur le littoral israélien. *Bulletin de la Société Préhistorique Française*, 72: 72-77.

RONEN, A. (1975b) The Palaeolithic archaeology and chronology of Israel. In: WENDORF, F. and MARKS, A. E. (eds). *Problems in Prehistory: North Africa and the Levant*. SMU Press, Dallas, pp. 229-248.

RONEN, A. (1977) Mousterian sites in red loam in the coastal plain of Mount Carmel. *Eretz-Israel Archaeological, Historical and Geographical Studies*, 13: 183-190.

RONEN, A. (1983) Late Quaternary sea levels inferred from coastal stratigraphy and archaeology in Israel. In: MASTERS, P. M. and FLEMMING, N. C. (eds) *Quaternary coastlines and marine archaeology: Towards the prehistory of land bridges and continental shelves*. Academic Press, London, pp. 121-134.

RONEN, A. (1991) The lower palaeolithic site Evron-Quarry in western Galilee, Israel. *Sonderveröffentlichungen Geologisches Institut der Universität zu Köln*, 82: 187-212.

RONEN, A. and WINTER, Y. (1997) Eyal 23 – a Lower Palaeolithic site in the Eastern Sharon, Israel. *Quartär*, 47/48: 177-188.

RONEN, A., KAUFMAN, D., GOPHNA, R., BAKLER, N., SMITH, P. and AMIEL, A. (1975) The Epi-Palaeolithic site Hefziba, Central Coastal Plain of Israel. *Quartär*, 26: 53-72.

RONEN, A., BURDUKIEWICZ, J.-M., LAUKHIN, ST. A., WINTER, Y., TSATSKIN, A., DAYAN, T., KULIKOV, O. A., VLASOV, V. K. and SEMENOV, V. V. (1998) The Lower Palaeolithic site Bizat Ruhama in the Northern Negev, Israel. *Archäologisches Korrespondenzblatt*, 28: 163-173.

RONEN, A., TSATSKIN, A. and LAUKHIN, ST. A. (1999) The genesis and age of Mousterian palaeosols in the Carmel Coastal Plain, Israel. In: DAVIES, W. and CHARLES, R. (eds). *Dorothy Garrod and the Progress of the Palaeolithic*. Oxbow Books, Oxford, pp. 135-151.

SAARONI, H., ZIV, B., BITAN, A. and ALPERT, P. (1998) Easterly wind storms over Israel. *Theoretical and Applied Climatology*, 59: 61-77.

SAID, R. (1975) The geological evolution of the river Nile. In: WENDORF, F. and MARKS, A. E. (eds). *Problems in Prehistory: North Africa and the Levant*. SMU Press, Dallas, pp. 7-44.

SANDLER, A. and HERUT, B. (2000) Composition of clays along the continental shelf off Israel: contribution of the Nile versus local sources. *Marine Geology*, 167: 339-354.

SHOSHANY, M., GOLIK, A., DEGANI, A.., LAVEE, H. and GVIRTZMAN, G. (1996) New evidence for sand transport direction along the coastline of Israel. *Journal of Coastal Research*, 12: 311-325.

SHUKRI, N. M. and PHILIP, G. (1956a) The geology of the Mediterranean coast between Rosetta and Bardia: Part I – Recent Sediments – Mechanical analyses and mineral composition. *Bulletin de l'Institut d'Egypte*, 37: 377-386. In: EMERY, K. O. and NEEV, D. (1960) Mediterranean beaches of Israel. *Geological Survey of Israel Bulletin*, 26: 1-23.

SHUKRI, N. M. and PHILIP, G. (1956b) The geology of the Mediterranean coast between Rosetta and Bardia: Part III – Pleistocene Sediments – Mineral analysis. *Bulletin de l'Institut d'Egypte*, 37: 445-455. In: EMERY, K. O. and NEEV, D. (1960) Mediterranean beaches of Israel. *Geological Survey of Israel Bulletin*, 26: 1-23.

SINGHVI, A. K. and KRBETSCHEK, M. R. (1996) Luminescence dating: A review and perspective for arid zone sediments. *Annals of Arid Zone*, 35: 249-279.

SINGHVI, A. K., SHARMA, Y. P. and AGRAWAL, D. P. (1982) Thermoluminescence dating of sand dunes in Rajasthan, India. *Nature*, 295: 313-315.

SIVAN, D., GVIRTZMAN, G. and SASS, E. (1999) Quaternary stratigraphy and palaeogeography of the Galilee coastal plain, Israel. *Quaternary Research*, 51: 280-294.

SIVAN, D., WDOWINSKI, S., LAMBECK, K., GALILI, E. and RABAN, A. (2001) Holocene sea-level changes along the Mediterranean coast of Israel, based on archaeological observations and numerical model. *Palaeogeography, Palaeoclimatology, Palaeoecology*, 167: 101-117.

SMITH, B. W., AITKEN, M. J., RHODES, E. J., ROBINSON, P. D. and GELDARD, D. M. (1986) Optical dating: Methodical aspects. *Radiation Protection Dosimetry*, 17: 229-233.

SPOONER, N. A. (1992) Optical dating: Preliminary results on the anomalous fading of luminescence from feldspars. *Quaternary Science Reviews*, 11: 139-145.

SPOONER, N. A. (1994) The anomalous fading of infrared-stimulated luminescence from feldspars. *Radiation Measurements*, 23: 625-632.

STANLEY, D. J., NIR, Y. and GALILI, E. (1998) Clay mineral distributions to interpret Nile cell provenance and dispersal: III. Offshore margin between Nile delta and northern Israel. *Journal of Coastal Research*, 14: 196-217.

SURVEY OF ISRAEL (1999a) Topographic Map 1 : 100,000, Sheet 3, Haifa. Survey of Israel, Tel Aviv.

SURVEY OF ISRAEL (1999b) Topographic Map 1 : 100,000, Sheet 5, Netanya. Survey of Israel, Tel Aviv.

SUTCLIFFE, J. V. and PARKS, Y. P. (1999) The hydrology of the Nile. IAHS Special Publication No. 5, IAHS Press, Institute of Hydrology, Wallingford, pp. 179.

TERNOIS, Y., SICRE, M.-A., BOIREAU, A., CONTE, M. H. and EGLINTON, G. (1997) Evaluation of long-chain alkenones as palaeotemperature indicators in the Mediterranean Sea. *Deep Sea Research*, 1: 271-286.

TRAUTMANN, T. (1999) Radiolumineszenzuntersuchungen an Feldspat. *Published thesis for the degree of Dr. rer. nat. (doctor rerum naturalium).* Fakultät für Chemie und Physik, Technische Universität Bergakademie Freiberg, Germany, pp. 95.

TRAUTMANN, T. (2000) A study of radioluminescence kinetics of natural feldspar dosimeters: experiments and simulations. *Journal of Physics D: Applied Physics*, 33: 2304-2310.

TRAUTMANN, T., KRBETSCHEK, M. R., DIETRICH, A. and STOLZ, W. (1998) Investigations of feldspar radioluminescence: Potential for a new dating technique. *Radiation Measurements*, 29: 421-425.

TRAUTMANN, T., KRBETSCHEK, M. R., DIETRICH, A. and STOLZ, W. (1999) Feldspar radioluminescence: A new dating method and ist physical background. *Journal of Luminescence*, 85: 45-58.

TRAUTMANN, T., KRBETSCHEK, M. R., DIETRICH, A. and STOLZ, W. (2000a) The basic principle of radioluminescence dating and a localized transition model. *Radiation Measurements*, 32: 487-492.

TRAUTMANN, T., KRBETSCHEK, M. R. and STOLZ, W. (2000b) A systematic study of the radioluminescence properties of single feldspar grains. *Radiation Measurements*, 32: 685-690.

TSATSKIN, A. and RONEN, A. (1999) Micromorphology of a Mousterian paleosol in aeolianites at the site Habonim, Israel. *Catena*, 34: 365-384.

USDA (1975) *Soil taxonomy. A basic system of soil classification for making and interpreting soil surveys.* U.S. Department of Agriculture, Soil Conservation Service, Agriculture Handbook No. 436, U.S. Government Printing Office, Washington, D. C., pp. 754.

VALLADAS, H., MERCIER, N., JORON, J.-L. and REYSS, J.-L. (1998) GIF laboratory dates for Middle Paleolithic Levant. In: AKAZAWA, T., AOKI, K: and BAR-YOSEF, O. (eds). *Neandertals and Modern Humans in Western Asia.* Plenum Press, New York, pp. 69-75.

VAN ZEIST, W. and BOTTEMA, S. (1991) Late Quaternary Vegetation of the Near East. *Beihefte zum Tübinger Atlas des Vorderen Orients. Reihe A, Naturwissenschaften, Nr. 18.* Dr. Ludwig Reichert Verlag, Wiesbaden, pp. 155.

VENKATARATHNAM, K., BISCAYE, P. E. and RYAN, W. B. F. (1972) Origin and Dispersal of Holocene Sediments in the Eastern Mediterranean Sea. In: STANLEY, D. J. (ed.). *The Mediterranean Sea: A Natural Sedimentation Laboratory.* Dowdon, Hutchinson & Ross Inc. Publishers, Stroudsburg, Pennsylvania, pp. 455-469.

VISOSEKAS, R (1985) Tunnelling radiative recombination in labradorite: its association with anomalous fading of thermoluminescence. *Nuclear Tracks and Radiation Measurements*, 10: 521-529.

VISOCEKAS, R. and ZINK, A. (1999) Use of the far red TL emission band of alkali feldspars for dosimetry and dating. *Quaternary Science Reviews*, 18: 271-278.

VISOCEKAS, R., SPOONER, N. A., ZINK, A. and BLANC, P. (1994) Tunnel afterglow, fading and infrared emission in thermoluminescence of feldspars. *Radiation Measurements*, 23: 377-385.

VLASOV, V. K. and KULIKOV, O. A. (1989) Radiothermoluminescence dating and applications to Pleistocene sediments. *Physics and Chemistry of Minerals*, 16: 551-558.

VOGEL, J. C., WINTLE, A. G. and WOODBORNE, S. M. (1999) FOCUS: Luminescence dating of coastal sands: Overcoming changes in environmental dose rate. *Journal of Archaeological Science*, 26: 729-733.

WALLINGA, J., MURRAY, A. and WINTLE, A. (2000a) The single-aliquot regenerative dose (SAR) protocol applied to coarse-grain feldspar. *Radiation Measurements*, 32: 529-533.

WALLINGA, J., MURRAY, A. and DULLER, G. A. T. (2000b) Underestimation of equivalent dose in single-aliquot optical dating of feldspars caused by preheating. *Radiation Measurements*, 32: 691-695.

WEHAUSEN, R. and BRUMSACK, H.-J. (1999) Cyclic variations in the chemical composition of eastern Mediterranean Pliocene sediments: a key for understanding sapropel formation. *Marine Geology*, 153: 161-176.

WELDEAB, S., EMEIS, K. C., HEMLEBEN, C., VENNEMANN, T. W. and SCHULZ, H. (2002) Sr and Nd isotope composition of Late Pleistocene sapropels and nonsapropelic sediments from the Eastern Mediterranean Sea: Implications for detrital influx and climatic conditions in the source areas. *Geochimica et Cosmochimica Acta*, 66: 3585-3598.

WILLEMS, N. (1994) Erläuterung der gammaspektrometrischen Analysenergebnisse. Interne Mitteilung des Geologischen Institutes der Universität zu Köln, pp. 7, Köln (unpublished).

WINTLE, A. G. (1973) Anomalous fading of thermoluminescence in mineral samples. *Nature*, 245, 143-144.

WINTLE, A. G. (1981) Thermoluminescence dating of late Devensian loess in southern England. *Nature*, 289: 479-480.

WINTLE, A. G. (1987) Thermoluminescence dating of loess at Rocourt, Belgium. *Geologie en Mijnbouw*, 66: 35-42.

WINTLE, A. G. (1990) A review of current research on TL dating of loess. *Quaternary Science Reviews*, 9: 385-397.

WINTLE, A. G. (1997) Luminescence dating: Laboratory procedures and protocols. *Radiation Measurements*, 27: 769-817.

WINTLE, A. G. and HUNTLEY, D. J. (1979) Thermoluminescence dating of a deep sea sediment core. *Nature*, 279: 710-712.

WINTLE, A. G. and BRUNNACKER, K. (1982) Ages of volcanic tuff in Rheinhessen obtained by thermoluminescence dating of loess. *Die Naturwissenschaften*, 69: 181 182.

WINTLE, A. G. and HUNTLEY, D. J. (1982) Thermoluminescence dating of sediments. *Quaternary Science Reviews*, 1: 31-52.

WINTLE, A. G. and PACKMAN, S. C. (1988) Thermoluminescence ages for three sections in Hungary. *Quaternary Science Reviews*, 7: 315-320.

WINTLE, A. G., SHACKLETON, N. J. and LAUTRIDOU, J. P. (1984) Thermoluminescence dating of periods of loess deposition and soil formation in Normandy. *Nature*, 310: 491-493.

WRESCHNER, E. E. (1983) The submerged Neolithic village "Newe Yam" on the Israeli Mediterranean coast. In: MASTERS, P. M. and FLEMMING, N. C. (eds) *Quaternary coastlines and marine archaeology: Towards the prehistory of land bridges and continental shelves*. Academic Press, London, pp. 325-333.

YAALON, D. H. (1967) Factors affecting the lithification of eolianite and interpretation of its environmental significance in the coastal plain of Israel. *Journal of Sedimentary Petrology*, 37: 1189-1199.

YAALON, D. H. (1971) Soil-forming processes in time and space. In: YAALON, D. H. (ed.) *Paleopedology-Origin, Nature and Dating of Paleosols*. International Society of Soil Science and Israel University Press, Jerusalem, pp. 29-39.

YAALON, D. H. (1992) Pedogenesis on the Mediterranean Coastal Plain of Israel. *MBSS Newsletter*, 14: 95-99.

YAALON, D. H. and LARONNE, J. (1971) Internal structures in eolianites and paleowinds, Mediterranean coast, Israel. *Journal of Sedimentary Petrology*, 41: 1059 1064.

YAIR, A., LAVEE, H. and GREITSER, N. (1997) Spatial and temporal variability of water percolation and movement in a system of longitudinal dunes, Western Negev, Israel. *Hydrological Processes*, 11, 43-58.

ZANDER, A. M. (2000) Vergleich verschiedener Lumineszenzmethoden zur Datierung von Löss. *Kölner Forum für Geologie und Paläontologie*, 6: 1-92.

ZANDER, A. M., DULLER, G. A. T. and WINTLE, A. G. (2000) Multiple and single aliquot luminescence dating techniques applied to quartz extracted from Middle and Upper Weichselian loess, Zemechy, Czech Republic. *Journal of Quaternary Science*, 15: 51-60.

ZILBERMAN, E. (1993) The Late Pleistocene sequence of the northwestern Negev flood plains – A key to reconstructing the paleoclimate of southern Israel in the Last Glacial. *Israel Journal of Earth Science*, 41: 155-167.

ZILBERMAN, E., AMIT, R. and PORAT, N. (1994) Tel Sharuhen – A Quaternary type section of the western Negev, Israel. *Geological Survey of Israel Current Research*, 9: 81-86.

ZINK, A. J. C. and VISOCEKAS, R. (1997) Datability of sanidine feldspars using the near infrared TL emission. *Radiation Measurements*, 27: 251-261.

ZÖLLER, L., STREMME, H. and WAGNER, G. A. (1988) Thermolumineszenz-Datierung an Löß-Paläoboden-Sequenzen von Nieder-, Mittel und Oberrhein/Bundesrepublik Deutschland. *Chemical Geology*, 73: 39-62.

ZÖLLER, L., OCHES, E. A. and MCCOY, W. D. (1994) Toward a revised chronostratigraphy of loess in Austria with respect to key sections in the Czech Republic and in Hungary. *Quaternary Science Reviews*, 13: 465-472.

APPENDICES

Appendices of this study

In the appendices the calculations for the cosmic dose rates of the Israeli samples and the results for any one depth are given (cp. Chapter 5.5.2).

Appendix 1: Calculation of the cosmic dose rates for the Israeli samples

Considering the depth dependence, the cosmic ray dose rate D_0 at sea level at 55° geomagnetic latitude was calculated after PRESCOTT and HUTTON (1994) with the experimentally estimated bulk density (cp. Chapter 5.5.2) (Equation App 1a).

$$D_0 = \frac{C}{\left((x+d)^{\alpha}+a\right)(x+H)}\, e^{(-\beta x)} \qquad \text{(Equation App 1a)}$$

The depth l in a sediment column is expressed in this equation as x in hg cm^{-2}, considering the bulk density ρ of the sediment in hg cm^{-3} (Equation App 1b).

$$x\left(\frac{hg}{cm^2}\right) = \rho\left(\frac{hg}{cm^3}\right) * l(cm) \qquad \text{(Equation App 1b)}$$

The constants are used as given in PRESCOTT and HUTTON (1994) (Equation App 1c).

$$D_0 = \left(\frac{6072}{\left((x+11.6)^{1.68}+75\right)(x+212)}\right) e^{\left(-5.5*10^{-4}*x\right)} \qquad \text{(Equation App 1c)}$$

To find out the geomagnetic latitude λ, used in the calculations for the cosmic ray dose rate of the Israeli samples, a theoretical point was chosen with the geographic latitude θ = 32° 29' (32.48°) and the geographic longitude ϕ = 34° 54' (34.90°). This point lies longitude-wise about half way between the sampled sections and is latitude-wise in the north-western part of the Sharon coastal plain.

The geomagnetic latitude λ for this point was calculated over Equation App 1d given by PRESCOTT and HUTTON (1994) based on MCNISH (1936).

$$\sin\lambda = 0.203\ \cos\theta\ cos(\phi - 291) + 0.979\ sin\theta \qquad \text{(Equation App 1d)}$$

$$\sin\lambda = 0.203\ \cos 32.48\ cos(34.90 - 291) + 0.979\ sin 32.48$$

$$\lambda = 29.00°$$

With Equation (App 1e) dose rate D for the geomagnetic latitude λ = 29.00° can be determined after PRESCOTT and HUTTON (1994).

$$D = D_0\left(F + J * e^{\left(\frac{h}{H}\right)}\right) \qquad \text{(Equation App 1e)}$$

The values for F, J and H are graphically determined from PRESCOTT and HUTTON (1994, Figure 2) (cp. PRESCOTT and STEPHAN 1982) using the above calculated geomagnetic latitude λ.

$$F = 0.28$$

$$J = 0.69$$

$$H = 4.18\ km$$

Further was in Equation 5.3.9e h = 0 km inserted as altitude, as all the sections in this study are just above sea level and the difference is negligible.

In the case of the Israeli samples one calculates with h = 0 km as follows (Equation App 1f).

$$D = 0.20995539 * \left(0.28 + 0.69 * e^{\frac{0}{4.18}}\right) \qquad \text{(Equation App 1f)}$$

$$D = 0.204\ Gy/ka = 204\ \mu Gy/a$$

The results of the calculations for a depth l are given in Appendix 2. Uncertainties of ± 10 % were considered for the age calculation.

Appendix 2: Cosmic dose rate D_{cos} for sample depth

Depth (cm)	Cosmic dose rate D_{cos} (Gy/ka)
0	0.204
1-4	0.203
5-7	0.202
8-11	0.201
12-14	0.200
15-18	0.199
19-21	0.198
22-25	0.197
26-29	0.196
30-32	0.195
33-36	0.194
37-40	0.193
41-43	0.192
44-47	0.191
48-51	0.190
52-55	0.189
56-58	0.188
59-62	0.187
63-66	0.186
67-70	0.185
71-74	0.184
75-78	0.183
79-82	0.182
83-86	0.181
87-90	0.180
91-94	0.179
95-98	0.178
99-102	0.177
103-106	0.176
107-110	0.175
111-114	0.174
115-119	0.173
120-123	0.172
124-127	0.171
128-131	0.170
132-136	0.169
137-140	0.168
141-144	0.167
145-149	0.166
150-153	0.165
154-158	0.164
159-162	0.163
163-167	0.162
168-172	0.161
173-176	0.160
177-181	0.159
182-185	0.158
186-190	0.157
191-195	0.156
196-200	0.155
201-205	0.154
206-210	0.153
211-214	0.152
215-219	0.151
220-224	0.150
225-230	0.149
231-235	0.148
236-240	0.147
241-245	0.146
246-250	0.145
251-255	0.144
256-261	0.143
262-266	0.142
267-272	0.141
273-277	0.140
278-283	0.139
284-288	0.138
289-294	0.137
295-300	0.136
301-305	0.135
306-311	0.134
312-317	0.133
318-323	0.132
324-329	0.131
330-335	0.130
336-341	0.129
342-347	0.128
348-353	0.127
354-360	0.126
361-366	0.125
367-372	0.124
373-379	0.123
380-385	0.122
386-392	0.121
393-399	0.120
400-406	0.119
407-412	0.118
413-419	0.117
420-426	0.116
427-433	0.115
434-441	0.114
442-448	0.113
449-455	0.112
456-463	0.111
464-470	0.110
471-478	0.109
479-486	0.108
487-493	0.107
494-501	0.106
502-509	0.105
510-518	0.104
519-526	0.103
527-534	0.102
535-543	0.101
544-551	0.100
552-560	0.099
561-569	0.098
570-578	0.097
579-587	0.096
588-596	0.095
597-605	0.094
606-615	0.093
616-624	0.092
625-634	0.091
635-644	0.090
645-654	0.089
655-664	0.088
665-675	0.087
676-685	0.086
686-696	0.085
697-707	0.084
708-718	0.083
719-729	0.082
730-741	0.081
742-753	0.080
754-764	0.079
765-777	0.078
778-789	0.077
790-801	0.076
802-814	0.075
815-827	0.074
828-841	0.073
842-854	0.072
855-868	0.071
869-882	0.070
883-896	0.069
897-911	0.068
912-926	0.067
927-941	0.066
942-957	0.065
958-973	0.064
974-989	0.063
990-1006	0.062
1007-1023	0.061
1024-1041	0.060
1042-1059	0.059
1060-1077	0.058
1078-1096	0.057
1097-1115	0.056
1116-1135	0.055
1136-1155	0.054
1156-1176	0.053
1177-1198	0.052
1199-1220	0.051
1221-1242	0.050
1243-1266	0.049
1267-1290	0.048
1291-1315	0.047
1316-1340	0.046
1341-1367	0.045
1368-1394	0.044
1395-1422	0.043
1423-1451	0.042
1452-1481	0.041
1482-1512	0.040
1513-1545	0.039
1546-1578	0.038
1579-1613	0.037
1614-1649	0.036
1650-1687	0.035
1688-1727	0.034
1728-1768	0.033
1769-1811	0.032
1812-1856	0.031
1857-1903	0.030
1904-1952	0.029
1953-2004	0.028
2005-2059	0.027
2060-2117	0.026
2118-2178	0.025
2179-2243	0.024
2244-2312	0.023
2313-2385	0.022
2386-2464	0.021
2465-2548	0.020
2549-2638	0.019
2639-2736	0.018
2737-2842	0.017
2843-2958	0.016
2959-3085	0.015
3086-3225	0.014
3226-3380	0.013
3381-3510	0.012

Thesis submitted 9 February 2004

Viva 14 May 2004

External Examiner: Prof. Ann Wintle, Institute of Geography and Earth Sciences, Aberystwyth, UK

Internal Examiner: Dr. Mike Bell, School of Environment, University of Gloucestershire, Cheltenham, UK

Corrections submitted 15 December 2004

Award of PhD 26 January 2005